

MAX '91

Flare Research at the
Next Solar Maximum

■ Workshop #1: Scientific Objectives ■

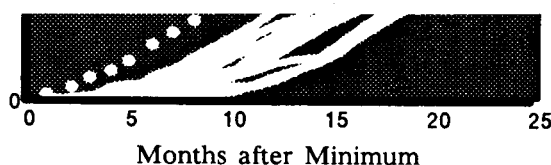
Kansas City, 9-10 June 1988



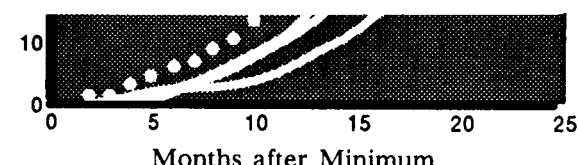
(NASA-TM-101259) MAY 1991: FLARE RESEARCH
AT THE NEXT SOLAR MAXIMUM. WORKSHOP 1:
SCIENTIFIC OBJECTIVES (NASA) 316 pCSCL 03B



N89-15854
---THRU---
N89-15880
Unclassified
0188346

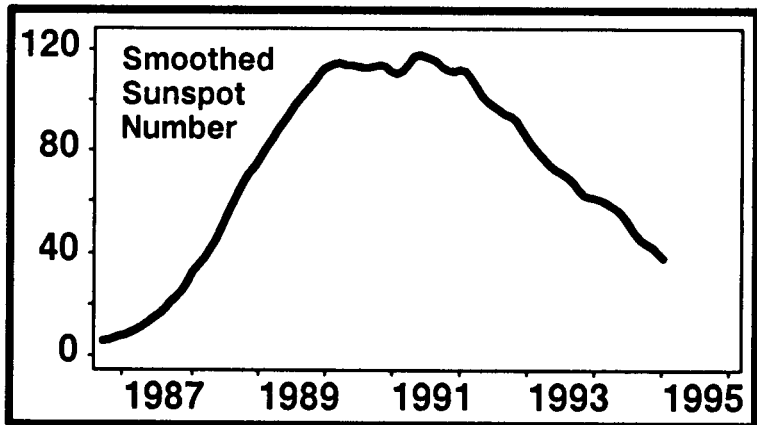


Months after Minimum



Months after Minimum

Summary and Reports



MAX '91

Flare Research at the Next Solar Maximum

Workshop #1: Scientific Objectives
Kansas City, 9-10 June 1988

Summary and Reports

Edited by
Richard C. Canfield
Institute for Astronomy
Honolulu, Hawaii

Brian R. Dennis
NASA Goddard Space Flight Center
Greenbelt, Maryland

TABLE OF CONTENTS

	<i>Page</i>
PARTICIPANTS	vii

PREFACE.....	ix
--------------	----

STRAWMAN MAX '91 PLANS

ORGANIZATION (E. Hildner)	1
OPERATIONS (D. Speich)	3
WORKSHOPS AND MEETINGS (B. Dennis)	7
NATIONAL SOLAR OBSERVATORY (D. Neidig)	8

ADVICE FROM THE LEADERS OF SMY

SOLAR MAXIMUM YEAR (C. De Jager)	10
SMM COORDINATION (D. Rust)	11

REPORTS FROM THE WORKSHOP GROUP LEADERS

ENERGY STORAGE (T. Tarbell)	14
ENERGY RELEASE (R. Moore)	18
PARTICLE ACCELERATION (R. Lin)	22
ENERGY TRANSPORT (D. Neidig)	24

CONTRIBUTED PAPERS

ACTIVE REGION EVOLUTION IN THE CHROMOSPHERE AND TRANSITION REGION	29
R.A. Shine, and C. J. Schrijver	

FULL-DISK MAGNETOGRAMS OBTAINED WITH A Na MAGNETO-OPTICAL FILTER AT THE MOUNT WILSON OBSERVATORY	33
E. J. Rhodes, A. Cacciani, G. Garneau, T. Misch, D. Progovac, T. Shieber, S. Tomczyk, and R. K. Ulrich	

OBSERVATIONS OF PHOTOSPHERIC MAGNETIC FIELDS AND SHEAR FLOWS IN FLARING ACTIVE REGIONS.....	50
T. Tarbell, S. Ferguson, Z. Frank, A. Title, and K. Topka	
FLARE ONSET AT SITES OF MAXIMUM MAGNETIC SHEAR.....	61
M. J. Hagyard, and J. B. Smith, Jr.	
AN IMAGING VECTOR MAGNETOGRAPH FOR THE NEXT SOLAR MAXIMUM.....	81
R. Canfield, and D. L. Mickey	
DEVELOPMENT OF THE SAMEX VECTOR MAGNETOGRAPH AT THE MARSHALL SPACE FLIGHT CENTER	86
E. A. West, Jr., M. J. Hagyard, and G. A. Gary	
THE DRIVER IN FLARES AND CORONAL MASS EJECTIONS: MAGNETIC EXPANSION.....	97
R. L. Moore	
PLANNED IMPROVEMENTS TO THE OWENS VALLEY FREQUENCY-AGILE INTERFEROMETER FOR MAX '91.....	98
G. J. Hurford, and D. E. Gary	
MILLIMETER WAVELENGTH OBSERVATIONS OF SOLAR FLARES FOR MAX '91	107
M. R. Kundu, N. Gopalswamy, N. Nitta, E. J. Schmahl, S. M. White, and W. J. Welch	
SOLAR VECTOR MAGNETOGRAPH FOR MAX '91 PROGRAMS	113
D. M. Rust, J. W. O'Byrne, and T. J. Harris	
MECHANISMS FOR FAST FLARE RECONNECTION	121
G. Van Hoven, D. Deeds, and T. Tachi	
RADIATIVE RECONNECTION-SUMMARY	132
G. Van Hoven, T. Tachi, and D. D. Schnack	
ARCHES SHOWING UV FLARING ACTIVITY	141
J. M. Fontenla	
THE NEED FOR HARD X-RAY IMAGING OBSERVATIONS AT THE NEXT SOLAR MAXIMUM.....	145
A. G. Emslie	

THE FOURIER IMAGING X-RAY SPECTROMETER (FIXS) FOR THE ARGENTINIAN, SCOUT-LAUNCHED SATELITE DE APLICACIONES CIENTIFICAS - 1 (SAC - 1)	153
B. R. Dennis, C. J. Crannell, U. D. Desai, L. E. Orwig, A. L. Kiplinger, R. A. Schwartz, G. J. Hurford, A. G. Emslie, M. Machado, and K. Wood	
IMAGING SOLAR FLARES IN HARD X-RAYS AND GAMMA RAYS FROM BALLOON-BORNE PLATFORMS	164
C. J. Crannell	
HIGH SPATIAL RESOLUTION AND HIGH SPECTRAL RESOLUTION DETECTORS FOR USE IN THE MEASUREMENT OF SOLAR FLARE HARD X-RAYS.....	177
U. D. Desai, and L. E. Orwig	
A COSMIC AND SOLAR X-RAY AND GAMMA-RAY INSTRUMENT FOR A SCOUT LAUNCH.....	193
D. J. Forrest, W. T. Vestrand, and E. L. Chupp	
FLARE OBSERVATION DURING MAX'91 BALLOON CAMPAIGNS.....	201
D. J. Forrest	
SOLAR RESPONSE OF THE BATSE INSTRUMENT ON THE GAMMA-RAY OBSERVATORY	204
G. J. Fishman, C. A. Meegan, T. A. Parnell, R. B. Wilson, W. Paciesas, T. Cline, B. Teegarden, B. Schaefer, and H. S. Hudson	
DEVELOPMENT OF A HIGH SPEED H-ALPHA CAMERA SYSTEM FOR THE OBSERVATION OF RAPID FLUCTUATIONS IN SOLAR FLARES....	214
A. L. Kiplinger, B. R. Dennis, L. E. Orwig, and P. C. Chen	
DOES THE RESISTIVE TEARING INSTABILITY NONLINEARLY EVOLVE TO A FAST RECONNECTION MODE?	224
R. S. Steinolfson	
MODELLING A C-TYPE FLARE OBSERVED IN MICROWAVES AND HARD X-RAYS	246
E. J. Schmahl, M. R. Kundu, and B. R. Dennis	
A HIGH RESOLUTION GAMMA-RAY AND HARD X-RAY SPECTROMETER FOR SOLAR FLARE OBSERVATIONS IN MAX '91	262
R. P. Lin, D. W. Curtis, P. Harvey, K. Hurley, J. H. Primbsch, D. M. Smith, R. M. Pelling, and F. Duttweiler	

COORDINATED VIDEOMAGNETOGRAPH OBSERVATIONS BY THE BIG BEAR AND HUAIROU OBSERVATORIES	279
H. Wang, A. Patterson, H. Zirin, G. Ai, and H. Zhang	
HIGH-RESOLUTION DIGITAL MOVIES OF EMERGING FLUX AND HORIZONTAL FLOWS IN ACTIVE REGIONS ON THE SUN	283
K. Topka, S. Ferguson, Z. Frank, T. Tarbell, and A. Title	
STATISTICAL PROPERTIES OF SOLAR GRANULATION FROM THE SOUP INSTRUMENT ON SPACELAB 2.....	294
K. Topka, A. Title, T. Tarbell, S. Ferguson, and R. Shine	

PARTICIPANTS

NAME	INSTITUTION
Chang-Hyuk An	Univ. of Alabama
M. Aschwanden	Univ. of Colorado
W. Berning	New Mex. State U.
J. David Bohlin	NASA Hq.
Pat Bornmann	NOAA/SEL
Richard C. Canfield	Univ. of Hawaii
Anne Cannon	Univ. of Sydney
Peter Cargill	Univ. of Maryland
S. Chandrashekhar	Univ. of Alabama
Gary Chapman	San Fernando Obs.
Edward W. Cliver	AFGL
John Cook	Naval Research Lab.
Carol Jo Crannell	NASA/GSFC
John Davis	NASA/MSFC
Cornelius de Jager	Utrecht
Brian Dennis	NASA/GSFC
Upendra Desai	NASA/GSFC
Murray Dryer	NOAA/SEL
Gordon Emslie	Univ. of Alabama
George Fisher	Univ. of Hawaii
Juan Fontenla	NRC/MSFC
Dave Forrest	Univ. of N.H.
G. Allen Gary	NASA/MSFC
Dale Gary	Caltech
Chris Godfrey	Missouri Western State College
N. Gopalswamy	Univ. of Maryland
Mona Hagyard	NASA/MSFC
John Harvey	National Solar Obs.
Adil Hassam	Univ. of Maryland
William Henze	Teledyne Brown/MSFC
Ernie Hildner	NOAA/SEL
Gordon Holman	NASA/GSFC
Hugh Hudson	UCSD
Gordon Hurford	Caltech
Stephen Kahler	Emmanuel College
Alan Kiplinger	NASA/GSFC & STX
James Klimchuk	Stanford University
Mukul R. Kundu	Univ. of Maryland
Barry LaBonte	IFA/UH
Theodore LaRosa	Univ. of Alabama

Peng Li	Univ. of Alabama
Paulett Liewer	JPL/Caltech
Robert Lin	Univ. of CA/Berkeley
Charles Lindsey	Univ. of Hawaii
James Ling	Jet Propulsion Lab.
Bruce Lites	HAO/NCAR
Alexander McClymont	Univ. of Hawaii
J. McTiernan	Stanford
Zoran Mikic	Science Applications
Ron Moore	NASA/MSFC
J. Daniel Moses	AS&E
Donald Neidig	AFGL/Sac Peak
Werner Neupert	NASA/GSFC
Larry Orwig	NASA/GSFC
William Parkinson	Center for Astrophysics
Dennis Peacock	NSF
Matthew Penn	IFA/Univ. of Hawaii
Jason Porter	NASA/MSFC
Edward Rhodes	Univ. of S. Calif.
David Rust	JHU APL
Edward Schmahl	Univ. of Maryland
Richard Schwartz	NASA GSFC & STX
K. Shibata	Inst. Fusion Studies
Richard A. Shine	LPARL
David Sime	High Altitude Obs.
Dean Smith	Berkeley Res. Assoc.
Dave Speich	NOAA
Philip A. Stahl	Harry Bayley Obs. (Barbados)
Richard Steinolfson	Univ. of Texas
Theodore Tarbell	LPARL
Kenneth Topka	LPARL
Gerald Van Hoven	Univ. Cal, Irvine
David F. Webb	Emmanuel Col.
Donat Wentzel	NSF
Edward West	NASA/MSFC
L. Wilkinson	Univ. of Alabama
Ying Cai Xiao	Univ. of Alabama
Harold Zirin	Caltech

PREFACE

Approximately 80 scientists attended the inaugural workshop of the Max '91 program on the "Scientific Objectives of Flare Research at the Next Solar Maximum", which was held on June 9 and 10 in conjunction with the Kansas City meeting of the Society. The success of the workshop was due in large part to the excellent support provided by the AAS Director of Society Programs, Pam Hawkins, and by the local organizing committed chaired by Stephen Shawls of the University of Kansas.

The purpose of the Max '91 program is to gather coordinated sets of solar flare and active region data and to perform interpretive and theoretical research aimed at understanding flare energy storage and release, particle acceleration, flare energy transport, and the propagation of flare effects to Earth. Instruments for long-duration balloon flights will be funded by NASA and ground-based instruments will be funded by NSF. Coordination of Max '91 with similar national programs in other countries will be provided by the International FLARES 22 program lead by Marcos Machado (Argentina) and Ernest Hildner (USA).

The workshop participants were divided into four groups according to their main scientific interests: energy storage, energy release, particle acceleration, and energy transport. In each group the workshop participants identified the major research issues and their observational approach from space, balloons, rockets, and the ground, as well as promising lines of theoretical study, modeling, and analysis. These proceedings of the workshop contain the group leaders' summaries of the discussions that took place within these groups at the workshop, copies of the poster papers that were presented there, as well as outlines of talks that were presented by invited speakers on topics such as coordination and operations during the workshop, successes and failures of the Solar Maximum Year Program (the equivalent to the Max '91 program at the previous solar cycle), and coordination during the Solar Maximum Mission.

A need was established for workshops before 1991 on coordination, data exchange formats, and operations (1989); a vector and longitudinal magnetograph co-observing campaign (1989); and a "hare and hounds" test of methods for extrapolating photospheric vector field measurements into the corona (1990). A planning workshop will be held prior to the August 1991 launch of Solar-A and the first long-duration balloon flights. Workshops in subsequent years will address coordinated balloon, space, and ground-based campaigns centered on various specific scientific objectives.

ORGANIZATION OF MAX '91

To act as executives and spokesmen

Chairmen-R. Canfield

B. Dennis

To give guidance to Chairmen

Steering Committee-

R. Canfield -Co-Chairman

B. Dennis -Co-Chairman, IAU's repr. to FLARES 22

A. Kiplinger-Coordinator

E. Hildner -Liaison with FLARES 22

TBD -Leaders of currently active workshops

TBD -Leaders of currently active meetings

TBD -Leaders of currently active campaigns

TBD -NSF Discipline Chief

J. D. Bohlin-NASA Discipline Chief

To coordinate and implement MAX '91 activities, distribute (with NOAA help) real-time information about the Sun during campaigns, etc.:

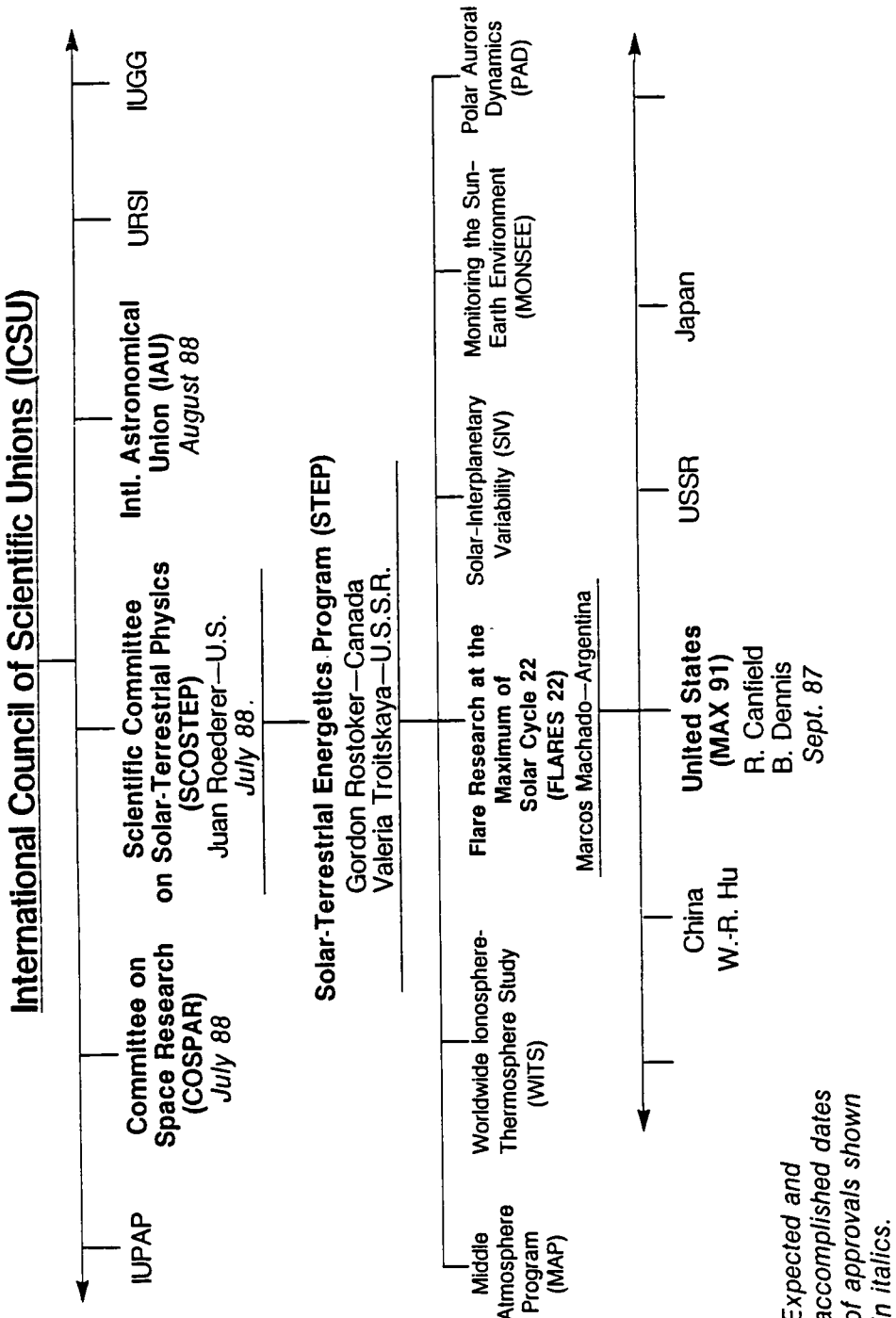
Coordinator-A. Kiplinger (located at NOAA-SEL, Boulder)

The Executive Committee of the Max '91 program will consist of the co-chairmen, the coordinator, and the liaison with FLARES 22.

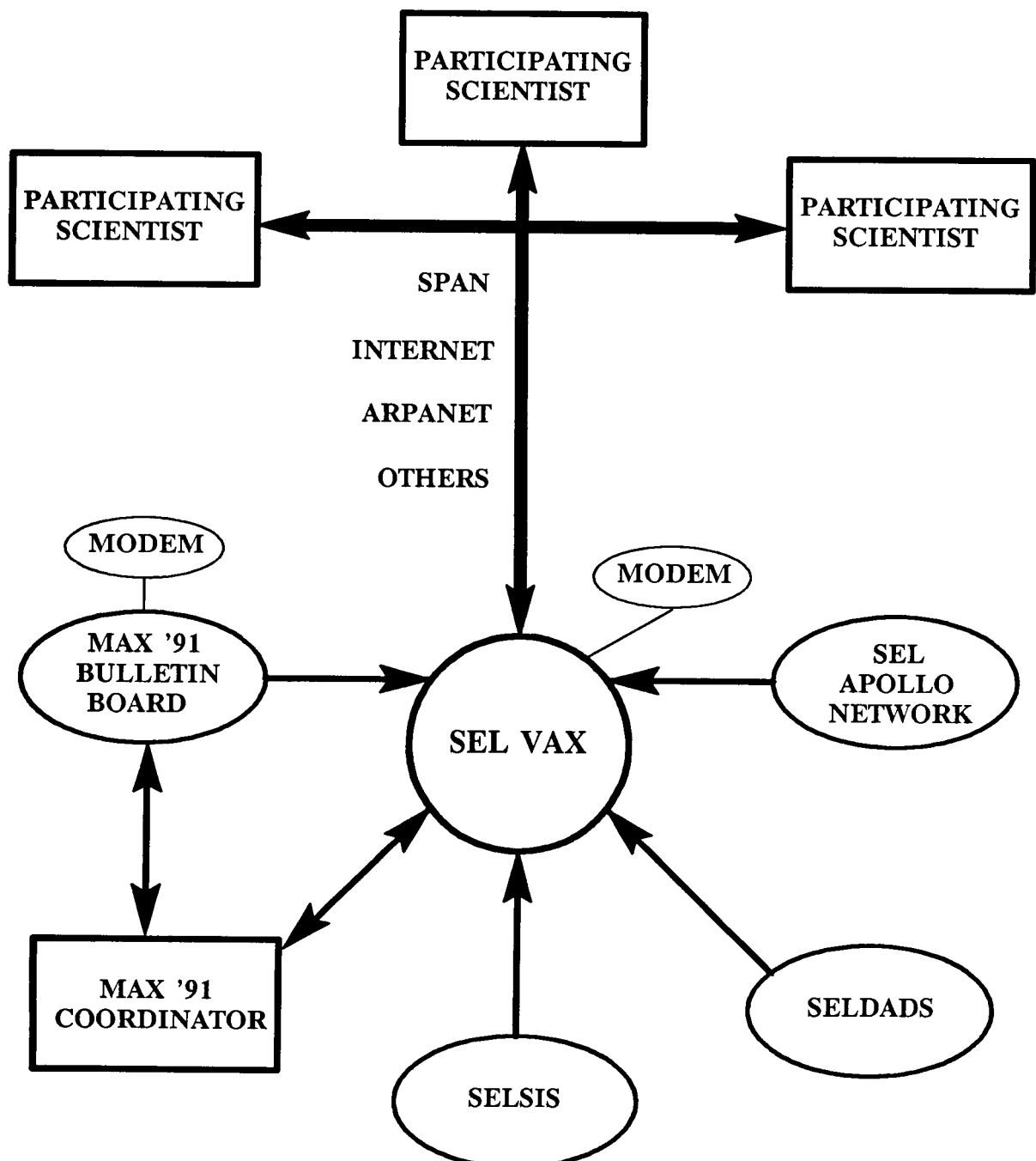
To supply enthusiasm, ideas, and labor

Beneficiaries and Workers-U.S. research community members

INTERNATIONAL ORGANIZATION FOR FLARE RESEARCH PROGRAMS



MAX '91 COMMUNICATIONS (STRAWMAN)



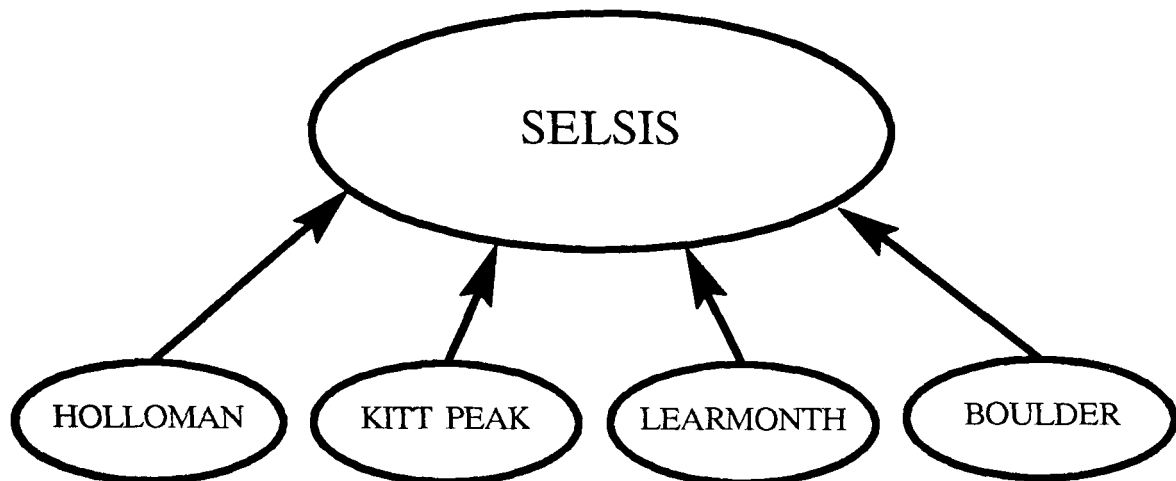
SEL RESOURCES AVAILABLE

1. Extensive and preexisting communications network (SPAN, INTERNET, and others to be added).
2. Geosynchronous full disk x-ray and energetic particle detectors.
3. Geophysical monitors for terrestrial effects.
4. 24 hours/day operation.
5. Knowledge in solar event manipulation – expert system.
6. Experience in participating in, and operating, similar operations (SKYLAB, SPACELABS 1 & 2, SMY, SMM).
7. Interface for SOON/RSTN operations.

ACRONYMS

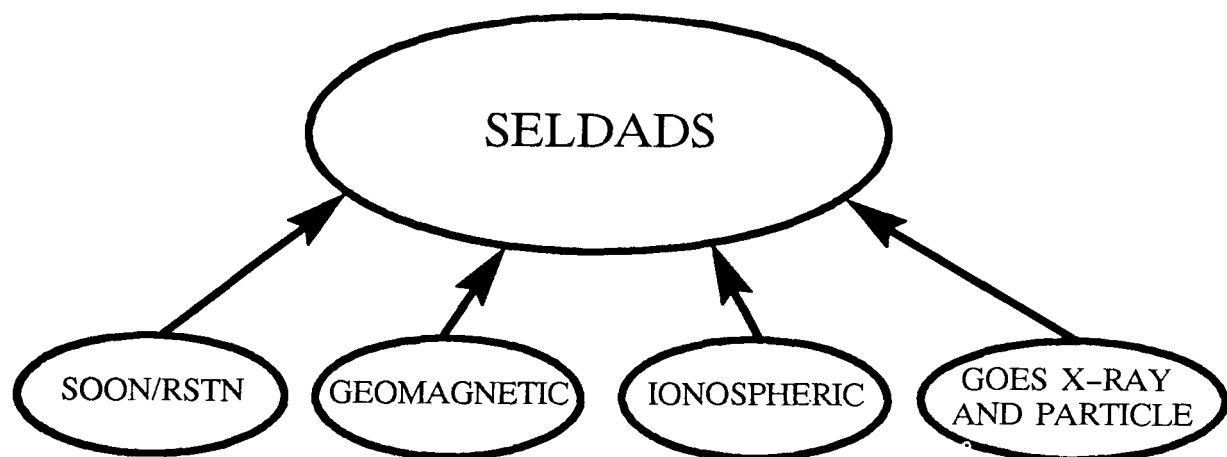
AUTODIN	AUTomatic DIgital Network
COMEDS	COntinental MEterological Data System
GOES	Geosynchronous Operational Environmental Satellite
IUWDS	International Ursigram and World Days Service
MSFC	Marshall Space Flight Center
RSTN	Radio Solar Telescope Network
SELDADS	Space Environment Laboratory Data Acquisition and Display System
SELSIS	Space Environment Laboratory Solar Imaging System
SMM	Solar Maximum Mission
SMY	Solar Maximum Year
SOON	Solar Observing Optical Network

SPACE ENVIRONMENT LABORATORY SOLAR IMAGING SYSTEM



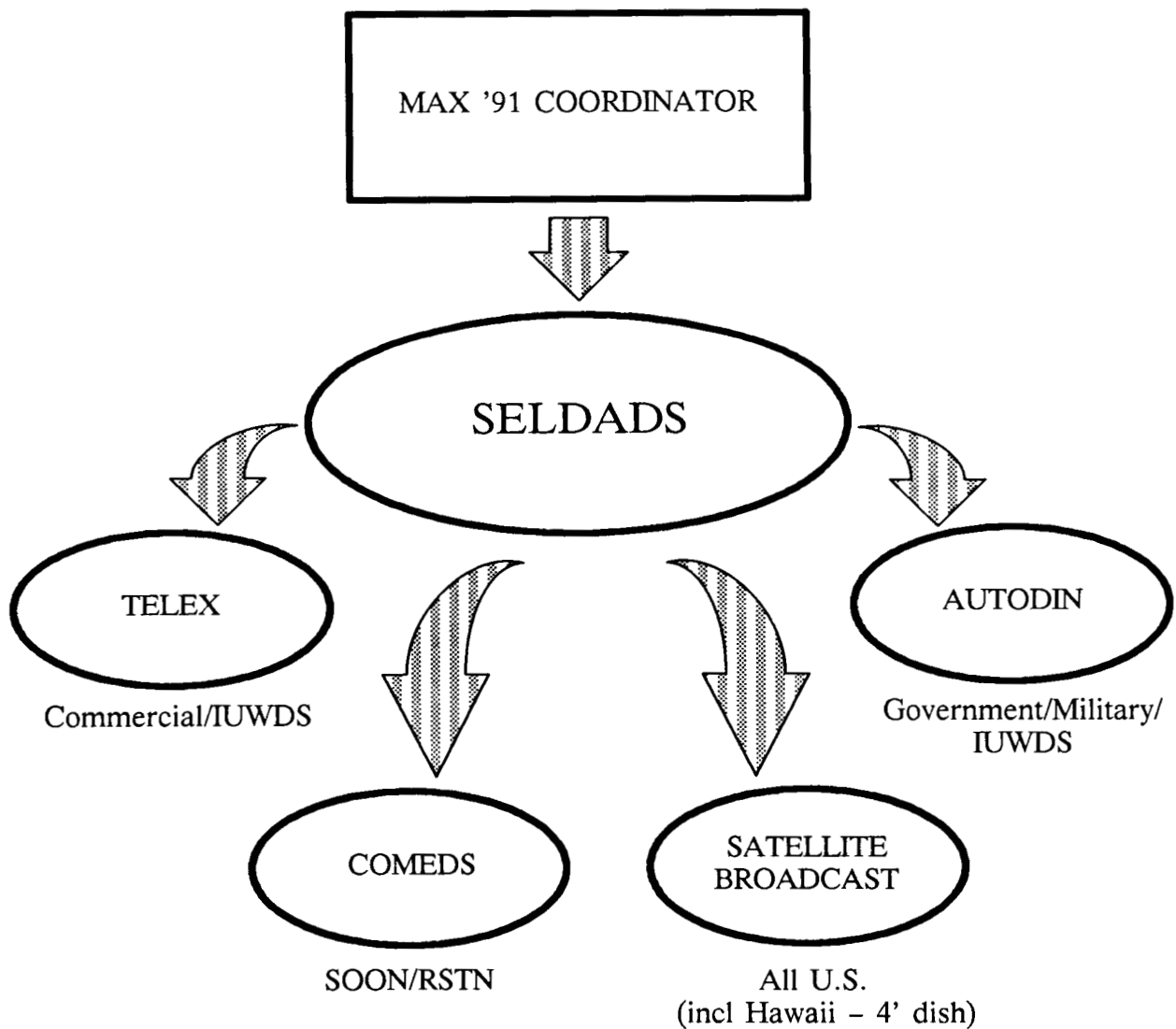
In 1990 add: Big Bear, San Vito, Ramey, and MSFC

SPACE ENVIRONMENT LABORATORY DATA ANALYSIS AND DISPLAY SYSTEM



Over 1400 separate data sets

MAX '91 COMMUNICATIONS THROUGH SELDADS



MAX '91

WORKSHOPS AND MEETINGS

	Location	Date	Subject
1.	Kansas City	June 1988	Scientific Objectives
2.	Boulder?	Summer 1989	Coordination Data Exchange Formats Planning Operations
3.	TBD	Summer 1989	Vector and Longitudinal Magnetograph Coobserving Campaigns
4.	TBD	Summer 1990	"Hare and Hounds"
5.	TBD	TBD 1991	Preceeding Launch of Solar-A in August 1991
6, 7,...	TBD	Summer 1992, '93, '94...	1 Workshop following each Max '91 Campaign, Coordinate with Solar-Terrestrial Workshops

INTERNATIONAL MEETINGS

1.	Helsinki, Finland	July 1988	COSPAR-Marcos Machado "The Next Solar Maximum and Beyond"
2, 3,...	TBD	TBD	FLARES 22

Note: It is strongly recommended that proceedings of the workshops and meetings be published in some form, either as refereed papers in Solar Physics, as a NASA Conference Proceeding, or in Advances in Space Research as done during the previous solar maximum.

NSO Participation in MAX '91
NSO Contacts for MAX '91: H. Jones and D. Neidig

The National Solar Observatory strongly supports the MAX '91 program and is enthusiastic about participating in MAX '91 observing campaigns. To this end, we welcome members of the flare research community to NSO's facilities. NSO's potential for flare research resides in present or nearly completed instrumentation, including both synoptic facilities (which, by nature of their operations, can be substantially dedicated to supporting MAX '91) and general purpose instruments. NSO has accumulated considerable observing-campaign experience at both the Kitt Peak and the Sacramento Peak sites, and has policies in place for accommodating observing proposals which cannot be precisely scheduled in advance. As for effective utilization of NSO's facilities, it would be desirable for MAX '91 investigators to engage in collaborations with NSO scientific staff, whenever possible.

In addition to presently existing facilities (see below), NSO is vigorously pursuing the development of new instrumentation that will find application in MAX '91 activities. Examples include an infrared spectrograph and detector package, an adaptive optics system, an advanced Stokes polarimeter (in collaboration with the High Altitude Observatory), a new longitudinal and/or vector magnetograph (in collaboration with JHU/APL), a near-limb emission-line coronagraph with array detector, an improved multi-band flare patrol, and improved capability for rapid data acquisition during flares. We solicit advice from potential users about which of these, as well as other, facilities improvements would be most useful during MAX '91.

KITT PEAK SYNOPTIC FACILITIES

- A. Vacuum Telescope/Diode Array Magnetograph
 - 1. Daily Full-Disk Magnetograms (1 arcsec pixels)
 - 2. Daily Full-Disk He I 10830 Spectroheliograms
 - 3. Area Scan Magnetograms: intensity, velocity, magnetic field – 1 arcsec pixels; variable FOV; typical cadence 2.5 minutes; can be formatted as a digital movie
 - 4. Area Scan He 10830 Spectroheliograms – same specifications as Item 3 above
 - 5. Semi-dedicated operation to support NASA flight missions (e.g. MAX '91)
- B. Vacuum Telescope/Spectromagnetograph (nearing completion)
 - 1. Same imaging/operational capabilities as above
 - 2. Magnetic, velocity, intensity data derived in "real time" from line profiles – well calibrated and free from crosstalk
 - 3. Possible additional data products – line widths, continuum intensity, differential continuum, line wing intensities; interactions of magnetic fields, flows and thermodynamic state of plasma
 - 4. Video-rate spectral polarimetry for flare observing
- C. Razdow H-Alpha Telescope: Visual reference; patrol mode data recording on film or video tape

KITT PEAK GENERAL FACILITIES

- A. McMath/Main Spectrograph
- B. McMath/FTS
- C. Image Stabilizer
- D. IR Spectrograph (being refurbished)
- E. IR Detector Packages (under development)

SACRAMENTO PEAK SYNOPTIC FACILITIES

- A. H-Alpha Full Disk Patrol
- B. White-Light Full Disk Patrol
- C. Multi-Band Polarimeter (upgrade proposed): active region FOV; photographic recording in five broad (40 Å) bands; simultaneous recording in two orthogonal linear polarization planes
- D. One-Shot (Full Limb) Coronagraph: red and green emission-line, H-alpha; recorded on 70 mm film
- E. Vector Magnetograph (APL instrument; uses Fabry-Perot etalon; may be in operation during MAX '91)
- F. Twin 40-cm Coronagraphs, providing:
 - 1. Daily photoelectric limb scans in red, green, and yellow emission lines
 - 2. Realtime and post-facto maps of corona against the disk, including coronal holes
 - 3. Daily large-scale spectropheliograms in H-alpha and K-line

SACRAMENTO PEAK GENERAL FACILITIES

- A. Vacuum Tower Telescope, with the following instrumentation:
 - 1. Universal Birefringent Filter: recording on 35 mm film or CCD array; UBF may be used in series with 0.05 Å Fabry-Perot etalon, or in parallel with tunable H-alpha filter or K-line filter
 - 2. Echelle Spectrograph: recording on 35 or 70 mm film, or multiple arrays; capable of providing imaging spectroscopy in several lines simultaneously
 - 3. Universal Spectrograph: recording of entire optical spectrum on 35 mm film; H-alpha slit jaw images
 - 4. Adaptive Optics System (under development): will feed all of the above instruments, providing higher spatial resolution
- B. Twin 40-cm Coronagraphs, with the following instrumentation:
 - 1. Coronal emission line photometer (CCD array imaging in planning, will allow study of coronal transients)
 - 2. Littrow spectrograph
 - 3. Universal spectrograph
 - 4. Spectropheliograph

SOLAR MAXIMUM YEAR/SOLAR MAXIMUM ANALYSIS (SMY/SMA)

C. de Jager
Laboratory for Space Research
National Institute for Space Research
Utrecht, The Netherlands

The *Final SMY/SMA Report* has just been published (Solar Physics, 114, 387-414, 1988).

Looking backward, I think that the following seven requirements should be satisfied to guarantee success for an international cooperative scientific program.

1. The availability of novel observational instruments and/or techniques.
2. A complete try-out, to take place at least two years before the start of the campaign.
3. A precise and clearly defined observational program.
4. A clear and unambiguous observational structure, with a well-defined hierarchy, which prevents duplications or counter-actions.
5. Regular workshops, symposia to ascertain the state of the project.
6. An occasional redefinition of the program, in order to bring it in line with the progress made.
7. A well defined and well-structured analysis phase.

SOCIOLOGY OF THE SMY

D. M. Rust
Applied Physics Laboratory
The Johns Hopkins University
Laurel, MD 20707

Since Professor de Jager has described the history and organization of the Solar Maximum Year (SMY) (these proceedings), and since the scientific highlights were summarized in *Solar Physics*, Vol. 114, and in the published proceedings of the SMY and SMA (Solar Maximum Analysis) workshops, I hope you will allow me to reflect on the sociology of the SMY. I served as the SMY science coordinator and as the Solar Maximum Mission (SMM) observatory coordinator in 1979 - 81.

The SMY was invented for the same reason one invents a new instrument or observing technique: to accomplish a scientific goal. Our primary motivation was to obtain a better understanding of solar flares and their interplanetary effects. In 1979, the Solar Maximum Mission was nearly ready for launch and most of the other instrumentation that we could think of for studying solar flares was in place. But, many of us were concerned that the opportunity offered by the onrushing solar maximum would be frittered away with disjointed, incommensurate flare reports. Stories about "the great flare of (fill in date)" for which only one observer had good data were clogging the literature and giving flare research a bad name. We had to try to insure that comprehensive data sets would be obtained on as many flares as possible and that meaningful physical analyses could be carried out with these data. And in this, we achieved a modest success, I think. Present day understanding of solar flares seems much better rooted in physical theory than prior to the SMY.

Because a flare is a short-lived phenomenon that affects only a tiny fraction of the solar disk, we set out to coordinate the observers' work so that telescopes operating from the gamma ray band to radio wavelengths as well as interplanetary particle and field detectors would all be aimed appropriately at the same time, to provide full coverage of as many flares as possible. It was a problem in dealing with people - about 400 headstrong, independent scientists at about 60 institutions in 17 countries around the world. I will try to summarize what seemed to work with them and what seemed not to work. Some of the things that did not work might work yet for the Max '91 program if handled more adroitly.

We tried to increase the resources available for flare observations and in this we were only partially successful. The National Science Foundation solicited proposals for increased support of observations, but the response from the community was disappointing. Here was the first lesson: the elasticity of the community of researchers is very low. It takes several years and a very clear and early commitment from the funding agencies to effect a significant increase in observing capability. The SMA was more successful in this regard because people expected that support for data analysis would be available, and it is an easier activity to expand. I believe that the community did not lack resources for analysis of the observations.

Efforts to increase the solar time available at the VLA and to involve the Air Force Solar Observing Optical Network (SOON) were quite successful, primarily because the

SMY program was sold early-on directly to the highest officials. In the case of the SOON, we came away armed with a supportive letter from an Assistant Secretary of Defense. The SMY also helped keep the radio observatory at Fort Davis operating after plans had been made to cease funding it. Here was a second lesson: the SMY was accepted as an important program when the benefits and purposes were explained to the officials who controlled the resources. Our colleagues in many countries were also quite successful in increasing resources when they tried. Max '91 offers similar opportunities. In the U.S., NASA and NSF are poised to help, but they must have proposals. Think big, send in your proposals.

One way to reach the powers that be and even to elevate the consciousness of your fellow researchers is to publicize the program. The press loves sunspots and solar flares and each eleven years there is a new crop of reporters who want to tell our story. A press release from NSF about the SMY generated stories in many national publications such as The Wall Street Journal, Discover, The New York Times, People Magazine. It made our sponsors feel good and it fulfilled one of our sacred duties: to inform the public about our work. Press releases from government agencies or major observatories should be encouraged. Cooperate with the press. Get on The Today Show.

Remember we are talking about sociology here. Even our jaded colleagues will respond to the drama of a rocket shot or a balloon launch or a special campaign. I found that daily observing schedules were duly posted on bulletin boards and ignored, but telexes and telephone calls about special events elicited strong efforts to get complementary observations. The Max '91 program of balloon missions should bring out a strong response if each flight is well publicized and its objectives explained. It is good to have a trial run well in advance of the first balloon flight. The Max '91 coordinator should establish personal contact with each observer who wants to contribute.

Workshops are also special events, of course. Plan on about one workshop each year, appoint topic leaders, publish the proceedings. This may be gray literature, but the workshops can be specialized enough so they do not tie up all the good people each time. They cement the personal commitments that will motivate your headstrong, independent colleague to cancel his vacation, leave his wife in the hospital, let his car maintenance go, skip his staff meeting and go out and fight for the observations he needs.

The coordinator should be provided with adequate resources to telephone, telex and e-mail without restraint. He should have travel funds so that he can attend the workshops and visit the observatories. He is a respected scientist and his visit at an observatory will almost guarantee a concerted effort there in the next campaign. He should not be expected to be on call 24 hours a day and, in fact, he must not be burdened with daily message distribution or activity forecasting. The NOAA forecasters did a fine, authoritative job during the SMY. All that daily prognosticating at the SMM experimenter operations facility should have been abandoned and the job turned over to NOAA much earlier than it was. Daily reporting of SMM observing plans was largely wasted effort.

Speaking of things that didn't work, I have to mention the Joint Observing Sequences of SMM and the Coordinated Observing Sequences that the ground-based observers were supposed to follow. A great deal of effort went into planning these JOS's and COS's, but in the heat of battle, they were ignored. When he (or she) is at the telescope, no one can tell the solar observer what to do. The best you can hope for is to get data of some kind

from each observatory at the right time and place on the sun. Through the workshops and the published literature, our colleagues will come to their private conclusions about what kind of observations are best.

Other efforts that didn't seem to pan out were the SMY Newsletter and various compilations of data obtained. We published about six newsletters per year during the SMY, but possibly aside from raising consciousness about the SMY, they seemed to have had little effect. The GONG approach of issuing one or two newsletters per year, largely reporting on people and meeting activities, seems to be more appropriate. The SMY Newsletters are not remembered and neither are the lists that I compiled and distributed about who obtained what H-alpha, UV, gamma-ray, white-light, X-ray, etc. data in each major event recorded during the SMY. Here was a real sociological lesson: if someone wants to share his data and to look at another's data, he wants to do it on a person-to-person basis. The solar flare data of Max '91 will be neither more voluminous nor catalogable than those of the SMY. Most participants will still find it more efficient and more satisfying to work directly with the principal investigators than with an impersonal data bank.

Before the launch of SMM, there were sober agreements reached on common formats for display of light curves, for maps of UV emission and magnetic fields, for spectra, etc. None were adhered to. The reason for this, I think, is that each spectrogram, each map will be constructed by the observer according to aesthetic principles: the desired feature will be centered, offset, shaded and scaled to emphasize whatever he thinks is important. Is there a standard format for masterpieces?

Considering the above paragraph, one may ask if we really want to compare and combine flare observations to achieve a higher synthesis. However, I suggest you assume the best, namely, that it is only the rugged independence and personal artistry of the scientific animal that drives him to produce something incommensurate with what has gone before. Here is where the workshops and meetings are so important. In order to participate most honestly and satisfactorily, our friends will eventually want to compare data in a meaningful way. The theorist will eventually want to offer a testable conclusion. A successful Max '91 program will produce enough data for a physical analysis of flares. When these data are presented at the Max '91 workshops, the stage will be set for the confrontations of divergent views that are the stuff of progress in a mature science.

ENERGY STORAGE

Ted Tarbell

The energy storage group had a productive meeting, developing several ideas for campaigns and workshops. These proposed activities are scientifically important and reasonable in scope, and some can be started before the major observing campaigns of Max '91 begin. Approximately twenty people took part in the discussions, which were chaired by Ted Tarbell of Lockheed.

Scientific Objectives

The group quickly agreed on the major scientific objective in this area: to measure the magnetic energy content of active regions and changes between the pre- and post-flare states. Although it is universally believed that flares are powered by energy stored in the coronal magnetic field, this has never been demonstrated by observations. Convincing evidence for non-potential field configurations has certainly been found. However, the uncertainty in magnetic free energy even for the best-observed active regions is comparable to the energy released in a large flare. Therefore, the build-up of magnetic energy and its release in the course of a flare have not been measured. The major limitations of previous measurements, low spatial resolution and uncertainty in the estimation of vector fields from polarization measurements, can potentially be removed in observations during the next solar maximum.

An important secondary goal is the ability to calculate the vector magnetic field in the corona from magnetograph measurements and other tracers. Additional observations beyond the vector field in the photosphere can be used as inputs to a coronal field computation or as checks on its accuracy. In particular, the connectivity of field lines may be seen in H-alpha or soft X-ray images. Connectivity may also be inferred from the time evolution of longitudinal magnetograms showing emergence and cancellation of flux and from horizontal flow measurements made in white light. Another approach is to measure the vector field at two heights (photosphere and temperature minimum) for additional constraints on field extrapolations into the corona. Finally, microwave imaging spectroscopy can provide direct measurements of the magnetic field strength at the base of the corona.

The effects of fine structure in the photospheric magnetic field must be better understood. It is a controversial question at this time whether it is possible to measure meaningful averages of the magnetic field vector using observations with low spatial resolution. Comparisons between high resolution polarization measurements from balloons or satellites and ground-based observations will be very illuminating.

Magnetograph Observing Campaigns

Group participants discussed observing plans for many existing or proposed magnetographs. Vector magnetographs included those at MSFC, HAO, Hawaii, APL-JHU, Lockheed (SOUP), and perhaps NSO (in the 12 micron lines); longitudinal magnetographs of NSO, BBSO, San Fernando, Lockheed (HRSO engineering model), and GONG were also represented. Two campaigns involving ground-based magnetographs observing the same

region during overlapping time intervals were proposed. One motivation is to compare measurements of the same quantities from different instruments, including magnetic flux, linear polarizations (Stokes parameters Q and U), vector B components, field strengths, and computed active region energy content. The importance of reporting basic polarization measurements as well as inferred field properties was stressed. A comparison campaign of this type was performed for longitudinal magnetographs in the 1970's, and the results were constructive and "very sobering," to quote one of the participants. Coordinated magnetograph campaigns can be attempted before 1991, and they would be excellent rehearsals for the expected balloon, rocket, and spacecraft campaigns. The third project is an exercise for theoreticians using a benchmark problem.

1) Longitudinal Magnetograph Co-observing. The minimal version would be a repeat of the previous comparison campaign, with (nearly) simultaneous observations of the chosen region followed by comparison of flux maps. A far more interesting campaign would have observatories around the world providing 24 hour coverage of a changing region near central meridian for several days. Then scientific questions concerning the evolution of flux of both polarities could be studied: for example, the relative roles of cancellation in place vs. dispersal by diffusion might be estimated.

2) Vector Magnetograph Co-observing. Because of the much greater technical difficulties of making vector measurements, this campaign would be devoted to instrumental comparisons. Simultaneous microwave observations would also be encouraged.

3) "Hare and Hounds" Exercise. In this campaign, one theoretician (the "hare") constructs a self-consistent vector field configuration for the half-space bounded by the photosphere. The vector field on the photospheric surface (and perhaps some information on connectivity as well) is provided to the other participants ("hounds"), who compute the coronal field and total energy content using their favorite algorithms. Results are submitted by the hounds in standard format and compared with each other and with the hare's model, with the goal of assessing model dependence and theoretical uncertainty in field extrapolations and energy content. This approach has been used very successfully in the GONG project, where the problem was inversion of global oscillation periods to infer the rotation of the solar interior.

Flare Campaigns

1) Search for Flare Trigger. Although strong shear is a thought to be necessary for a region to flare, it is not a sufficient condition. The goal of this campaign is to identify the missing factor(s) which trigger the flare. The approach is to choose regions about to flare and observe them intensively until they do. Desired observations are vector magnetic fields, longitudinal magnetograms with high time resolution, H-alpha, and photospheric Doppler and transverse velocities.

2) Energy Buildup Study. This approach squarely addresses the basic issue of energy storage in the magnetic field. Choose a young, growing region, situated a few days before central meridian transit and measure the same quantities as above with 24 hour coverage for several days. From these observations, we can deduce the energy content as a function of time in the region and any release by flares, reconnections, or other mechanisms.

3) Flare Energetics. This campaign attempts to survey the gross energetics of a large sample of regions, perhaps all regions in one chosen rotation, for example. Instead of

following detailed evolution with high time resolution, the observations should concentrate on periodic measurements of energy content and release rate from X-rays, H-alpha, white light, and vector magnetograms.

4) Balloon, Rocket, and Spacecraft Campaign Support. Scientific support for these campaigns by ground-based observatories is taken for granted, with the principal (or primary guest) investigator setting the detailed goals. However, the logistics and funding needed by the observatories are not at all trivial. Program plans for Max '91 must allocate these resources.

Support of Real-Time Operations

A significant amount of real-time support must be provided for these campaigns to be successful. Most of the ground-based instruments represented have fields-of-view limited to a single active region. Therefore, the discussion focussed almost entirely on selection of the region for coordinated observations. At the start of a campaign observing day, observers must be alerted to the promising regions available. This means that reliable communications must be maintained from the Canary Islands to MSFC and Ottawa River to the Western US to Hawaii (and then to Japan to China to India to Israel and to the Canary Islands). E-mail links with all the observatories are a logical approach to providing this coverage. This type of early warning is essential for the Flare Trigger Campaign. For other campaigns, choosing the region is not so time-critical, but once the choice is made it must be "broadcast" to all the observatories. More than just coordinates are desired by many observers for region identification: annotated white light images or sunspot drawings are preferred.

In campaigns based on balloon, rocket, or spacecraft observations, information must flow from the ground observers to the launch site or control center. A convenient source of information on target regions is essential for the principal investigator, who may be faced with making launch decisions under heavy stress. Twenty-four hour support should be possible, for limited periods of time in exceptional circumstance.

Coordination of Observations

The group listed some obvious responsibilities which belong on the "job description" for the Max '91 Coordinator. These include: 1) advance notification of campaign dates to all relevant observatories; 2) compilation afterwards of data taken during each campaign; 3) maintenance of electronic bulletin boards; 4) encouraging observers to report their observations routinely, even during normal (i.e., non-campaign) periods, to provide a useful though not exhaustive listing of what data has been taken.

Workshops

Each of the magnetograph campaigns would logically have a dedicated workshop afterwards. We hope that initiation and coordination of the observations (or theoretical work) would not require meetings solely for that purpose. This should be done if possible via E-mail, newsletters, and splinter sessions at other meetings.

The Hare and Hounds Exercise could start soon, if a large enough group of theorists are willing to try it. It needs a leader and a hare, not necessarily the same person. The Longitudinal Magnetograph Co-observing Campaign could also begin fairly soon, perhaps in the summer of 1989, after the new NSO spectromagnetograph at Kitt Peak is in routine operation. Possible candidates were identified at the workshop and will be approached for leading both of these campaigns. Vector Magnetograph Co-Observing should wait until the next generation instruments are ready in a few years.

The flare campaigns also deserve a workshop each, after the data has been collected and initially digested. These could be merged with other workshops as appropriate, to avoid saturation of the community.

ENERGY RELEASE

Ron Moore

The Energy Release group discussion had 20 participants. The ratio of observers and data analysts to theorists was about 2 to 1, a healthy ratio for the topic of energy release in solar flares.

Overall Science Objectives

The overall scientific objective of the Flare Energy Release Group, simply put, is to find out how flares work. The specific science objectives of each member were motivated partly by that member's concept of the general nature of flares and how they work. In our Group it was widely, perhaps unanimously, held that a flare is an explosive release of free magnetic energy from the preflare nonpotential magnetic field at the site of the flare. That is, we took the standard view that the essential flare process is a conversion of magnetic energy into the other forms of energy that suddenly increase in flares. Beginning with this precept, to further draw out the underlying ideas that guide our flare research, we discussed the following broad question: what is the main sequence of energy conversion in flares and coronal mass ejections? The consensus of the Group was that the answer probably lies somewhere within the span of the three alternatives presented in Figure 1.

In each of the flare energy conversion sequences in Figure 1, the energy flow is from magnetic energy to other forms of energy. The other forms of energy are plasma particle energy (thermal and nonthermal), radiation, and mechanical energy. Radiation is the ultimate form of all of the flare energy that is not carried away in the form of the mechanical energy of a coronal mass ejection. In all three alternative schemes, the flare radiation energy comes from particle energy via collisions. The three alternatives differ in the flow of magnetic energy into particle energy and mechanical energy. In the first alternative, all of the released magnetic energy passes through the form of plasma particle energy via current dissipation (perhaps at reconnection sites). The mechanical energy of any coronal mass ejection generated in the event comes from work done by the pressure of flare-heated plasma. The third alternative is an extreme opposite of the first. Here, the first step in the conversion sequence is work by magnetic stress, rather than current dissipation. The magnetic work directly generates the mechanical energy and indirectly generates the particle energy by driving current dissipation (perhaps at sites of driven reconnection). The second alternative is a blend of the first and third alternatives. Here, the particle energy comes from the magnetic energy via current dissipation that is not driven by magnetic stress, but the mechanical energy is generated through magnetic work.

After considerable discussion to clarify the three alternative conversion sequences of Figure 1, the Group members were polled for their preference, given these three choices. Of the 19 participants present at that time, only 1 chose the first sequence, 6 chose the second, 8 the third, and 4 abstained, being unwilling or unable to decide which of these three alternatives was closer to the truth for real flares. This exercise demonstrated that, beyond the basic idea that the energy comes from the preflare magnetic field, the nature of the energy release in flares, even in broadest outline, is still a wide open problem. The general feeling in our Group was that the question of the main sequence of energy release

posed in Figure 1 is one of the broad questions to be addressed by the Max '91 program and for which there are good prospects for progress during Max '91.

Specific Objectives

The specific Max '91 research plans of each of the theorists focused on one or more of the following topics: (1) reconnection, (2) MHD stability of sheared magnetic field configurations, and (3) MHD of coronal mass ejections. Work on these topics is well motivated by our broad objective of determining the main processes and cause-and-effect linkages in flare energy release. In nearly all of the proposed theoretical work, the basic approach is to use computer modeling. The top priority observational input requested by the theorists was observation of the magnetic field configuration and its evolution. Vector magnetograms were recognized as most important in this regard, followed by observations of magnetic structure in the corona and observations of the location of concentrations of energy release within the field configuration.

The specific research plans of the observers and data analysts were based on the following types of observations: (1) vector magnetograms, (2) X-ray imaging from SOLAR A and from rockets, (3) imaging in microwave and millimeter-wave radio emission, (4) imaging of the UV chromosphere and transition region from rockets and from the Ultraviolet Spectrometer and Polarimeter on SMM, (5) measurement of the UV and X-ray spectral irradiance of flares from the Argentine SAC-1 satellite, (6) high-resolution imaging of the visible chromosphere and photosphere from balloons and from the ground, and (7) ground-based coronagraph imaging of active regions in coronal line emission. The main themes of the specific observational objectives were (1) the magnetic field structure in active regions and its evolution leading to flares, (2) change and motion of the magnetic field as the flare occurs and/or a coronal mass ejection is launched, and (3) the total energy output of a flare and comparison of this with the change of magnetic energy computed from the observed vector magnetic field. Again, vector magnetograms were strongly favored as the most important complement to the other observations of active regions and flares.

Campaigns

The perception in our Group was that the centerpiece of the Max '91 observational program will be the balloon flights. So, it is expected that the greatest effort to obtain a full range of coordinated observations from space and from the ground will be during intense campaigns that coincide with Max '91 balloon flights. Similarly, there should be observing campaigns in support of rocket flights and observing runs at the VLA. It is also expected that SOLAR A will be the lead observatory for some Max '91 campaigns. A less intense level of supporting observations should continue in coordination with SOLAR A during the intervals between full-up campaigns.

Coordination of Observations

Our main conclusion in this area was that procedures and standards for coordinated observations and uniform data formats need to be worked out and tested before the main

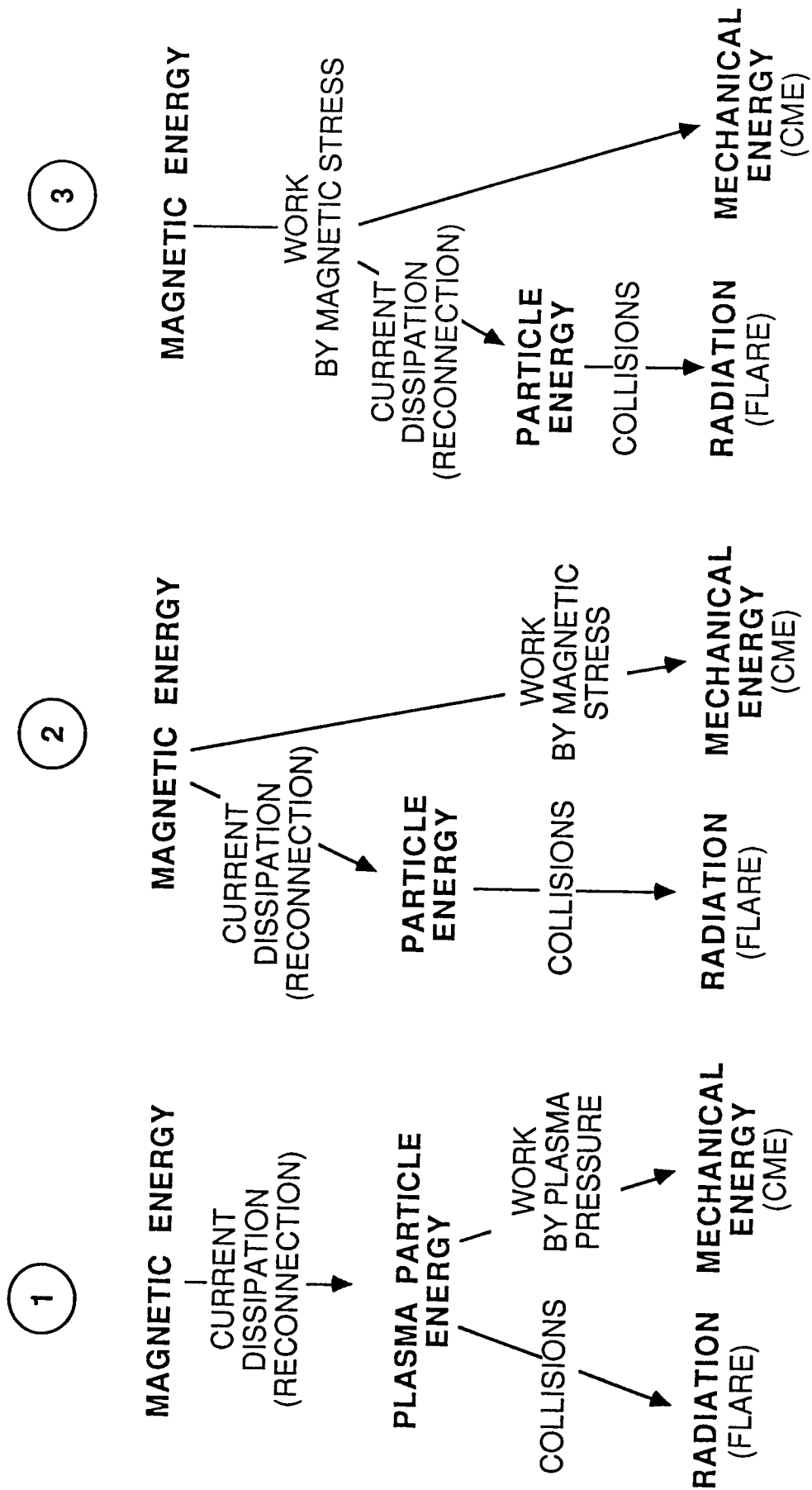
phase of Max '91, i.e., before the launch of SOLAR A or the first Max '91 balloons. It was pointed out that some rocket and VLA campaigns will take place before the main phase of Max '91 and should be used as training runs to work out the coordination in practice. We hope that the Max '91 Coordinator will be a vigorous leader of this effort.

Workshops

Although some were of the opinion that the solar community has been having too many workshops, most felt that there should be about one Max '91 workshop per year between now and the main phase of Max '91. One purpose of these workshops should be to involve the Japanese side of SOLAR A in Max '91. Another good reason to have a workshop is to stimulate and increase the science yield from a successful observing campaign such as we hope will occur in connection with a rocket flight or VLA run.

Figure 1. Three physically possible alternatives for the main sequence of energy conversion in flares and coronal mass ejections. The major forms of energy are in bold lettering. The arrows indicate the sequence of conversion from one form of energy to another; each arrow is labeled by the conversion process in that step of the sequence.

WHAT IS THE MAIN SEQUENCE OF ENERGY CONVERSION IN FLARES AND CME'S?



PARTICLE ACCELERATION

Robert Lin

Scientific Objectives

The ability to accelerate particles appears to be a common characteristic of cosmic plasmas. Solar flares offer a near ideal laboratory for the study of particle acceleration; the sun is close enough to obtain detailed measurements over the entire wavelength band as well as to directly detect the accelerated particles which escape, and far enough away to observe the overall structure of the phenomenon. Flares are known to release a large fraction of their energy in the form of accelerated particles, and often the particles are accelerated to tens to hundreds of MeV energies on very short time scales. Thus one of the primary goals of Max '91 is to understand the acceleration processes both for the 10-102 keV electrons, which may carry a significant portion of the flare energy, and the ions, which are accelerated up to energies as high as several GeV.

Campaigns

The combination of balloon-borne and ground-based instrumentation planned for MAX '91 will provide orders of magnitude improvement over that available in the previous solar cycle, and will permit for the first time, probing of the physics of the acceleration mechanisms. For example, high spectral resolution measurements of hard X-ray and gamma-ray continuum can identify the thermal, superhot component and separate it from power-law-like components produced by the accelerated electrons. Sharp features in the spectrum such as breaks can be accurately measured and their temporal evolution studied. Since the X-rays result from the well understood bremsstrahlung process, the parent electron spectrum can be obtained. The acceleration and loss processes can then be studied in detail.

Very high sensitivity hard X-ray measurements are needed to detect very weak microflares and determine whether they are a primary contribution to the heating of the active corona. Good spectral resolution can indicate whether they are thermal or non-thermal in character.

Hard X-ray imaging measurements will provide the size and location of the electron acceleration, propagation and loss regions. Microwave measurements with good spectral and spatial resolution can then provide the plasma density, magnetic field, and temperature in these regions, as well as images of the energetic electrons in the corona. H α and other optical observations will show the effect of the accelerated electrons in producing heating and mass motion of the atmosphere and delineate the detailed chromospheric structure of the region. Soft X-ray images will show the structure at higher temperatures in the corona. Hard X-ray polarization measurements can provide information on the beaming of the energetic electrons. The measurements can provide, for the first time, the detailed, quantitative diagnostic information about the environment of the acceleration required to evaluate various acceleration mechanisms.

In a similar manner, nuclear gamma-ray line spectroscopy can provide information on energetic ions, their numbers, spectrum, temporal evolution, and directivity. Very sensitive

measurements of the narrow 2.223 MeV line can answer the question: does every flare, or only large flares, accelerate ions above 10 MeV? Detailed high resolution measurements of the 511 keV positron annihilation line can give information on the temperature density and ionization state in the annihilation region. Finally, detection of a number of prompt lines can provide information on solar elemental abundances and determination of the line shapes will give information on the anisotropy of the ions. Gamma-ray continuum and millimeter wave radio measurements will provide information on the relativistic electron population, which is believed to be accelerated with the ions; images at mm wavelengths will also provide spatial information.

The high energy solar measurements are very dependent on catching a large flare event. Thus, the long observing times provided by long duration balloon flights are crucial. Mid-latitude flights, from Australia to Brazil or U.S. to China, can provide 7 days of 12 hours/day solar observations. Flights in Antarctica, however, appear to be capable of providing 14 days or longer with 24 hours/day solar observing during local summertime. One of the main advantages of Antarctic flights is that the balloon's loss of lift is only ± 0.5 latitudes, so that much less ballast per day is required, and therefore much longer flights are possible with large payloads. The possibility of "predicting" large flare events needs to be explored. It is known that following one large flare the chances of a second large flare is higher for several days following. Possibly balloon payloads could be launched following a large flare for flights of a few days.

A number of obvious scientific subjects for campaigns come to mind:

1. 10-102 keV electron acceleration. A combination of simultaneous hard X-ray continuum spectroscopy, imaging, and polarization measurements, combined with microwave, soft X-ray, and H α imaging and spectroscopy would be needed. It is extremely important to get simultaneous measurements.
2. Ion and relativistic electron acceleration processes. Gamma-ray line and continuum spectroscopy, radio observations of flare shocks, mm and microwave imaging and spectroscopy, gamma-ray imaging if available, and interplanetary ion and electron measurements, as well as supporting H α and soft X-ray observations would be required.
3. Microflares and coronal heating - very high sensitivity spectroscopy and imaging in hard X-rays, microwave, and H α are required. Also useful would be metric and kilometric radio and interplanetary electron and ion isotopic composition measurements, since ^3He and interplanetary electron events are probably coronal microflares. Soft X-ray measurements, especially in the 5-20 keV range, would be useful.

Campaigns should be scheduled around LDBF launches and access to such instruments as VLA.

ENERGY TRANSPORT

Donald Neidig

The topic for this group is centered on two major questions: (A) what are the mechanisms of flare energy transport, and (B) how do the effects of flares and other transient activity propagate to Earth? We restrict the first question to the transport of energy within the immediate vicinity of the flare energy release – especially to the solar atmosphere along field lines connected to the site of energy release. The second question, in the case of flare-associated disturbances, bears mainly on the restructuring of coronal magnetic fields surrounding, or perhaps involved with, the flare. In the case of coronal mass ejections (CMEs) or other coronal disturbances originating in the apparent absence of flares, the energy release and propagation mechanisms may occur higher in the corona and may be weakly coupled to the solar surface. These mechanisms, for which a fundamental distinction from flares has not been demonstrated, are poorly understood; yet they may represent the crucial connecting link between solar activity and subsequent geophysical disturbances. Thus the two major questions posed in Group D are quite separate and require different observational/analytical approaches.

WHAT ARE THE MECHANISMS OF FLARE ENERGY TRANSPORT?

This is a long-standing question motivated mainly by the conventional belief that the low density region favored by theory as the site for energy release must be spatially separated from the higher density regions from which EUV and optical emissions originate, thus requiring one or more transport mechanisms. In addition to the heating of the lower atmosphere, transport mechanisms are doubtless active in distributing energy throughout the hot coronal regime in the flare. The candidate mechanisms include heat conduction, nonthermal particles (keV electrons, keV protons, and MeV protons), Alfvén waves, irradiation, bulk motions of mass and magnetic field, and maser activity. In principle, the role of each of these can be determined by means of coordinated observations in optical, radio, EUV and x-ray wavelengths combined with detailed modeling of the atmospheric response to the rate and form of energy input.

Science Goals

1. Identify the principal mechanisms of energy transport and determine how they vary with time and location within the flare and from one flare to another. This goal carries with it the following objectives:
 - a. Characterize the evolution of bremsstrahlung-emitting electrons
 - b. Distinguish between thermal and nonthermal processes
 - c. Determine the thermal structure and dynamics of the flare atmosphere as a function of height or density
2. Determine to what extent the flare emission in the lower atmosphere is a consequence of energy transport, and to what extent (if any) it is due to in situ heating. In the broadest sense, the issue here is to understand where the magnetic field energy is being converted into other forms, and to determine whether the heating at any location arises

from imported, as opposed to locally generated, energy. Thus, this goal challenges the traditional assumption that the initial flare energy release is confined to the corona. The attendant observational objective is:

a. Compare the total (mechanical and radiative) power output at all locations in the flare – especially in the lower atmosphere – with the total power input available from the primary energy source.

Data Types (and Sources)

- a. Optical imaging and spectroscopy in continuum, H-alpha and other lines; magnetograms (NSO, BBSO, MSFC and others)
- b. UV and EUV spectra, including the Lyman-alpha line (None expected)
- c. X-Ray and XUV spectra (SMM, but requires reboosting, regassing of XRP experiment)
- d. Imaging in both soft and hard x-rays (Solar-A; Balloon-GRID, flight possible)
- e. Soft x-ray and hard x-ray continuum spectra (GOES; GRO; SMM, possibly)
- f. Hard x-ray polarimetry (Balloon-HXP, possibly)
- g. Microwave imaging; flux profiles (NRAO, USAF/RSTN, and others)

A realistic approach assumes that only items a, d, e and g will be available during MAX '91. This would lead to substantial gains in understanding energy transport through further analysis and modeling (possibly three-dimensional) of the chromosphere and temperature minimum region, using optical imaging techniques developed during the previous solar maximum but extended now to lines in addition to H-alpha. Improved x-ray spatial resolution offered by Solar-A will provide new data on timing and spatial distributions of hot plasmas and impact points for nonthermal particles; these inputs are essential for determining the time and spatial variations of both particle and conduction fluxes. If items b,c, and f become available, Group D activities can be expanded to include studies of the role of keV protons in heating the lower atmosphere, transition region structure and energy budget, chromospheric evaporation and momentum balance, and definitive separation of effects due to particle vs. conductive heating.

Observing Campaigns

Ideally, the following campaigns would be conducted simultaneously. However, limitations in the configurations of ground-based optical instruments available at any given time may require two separate campaigns.

Campaign I (aimed at Science Goal No. 1): Combine soft x-ray and hard x-ray images and continuum spectra with ground-based optical measurements emphasizing high resolution magnetograms and spectral diagnostics of vertical temperature structure, dynamics, and filling factors in the chromosphere and temperature minimum region.

Campaign II (aimed at Science Goal No. 2): Same spacecraft measurements as in Campaign I; optical measurements emphasize imaging in several lines and continuum, to determine the temporal variation and spatial distribution of the power budget in relation to magnetic field structures.

Coordination and Planning

- (i) Achieve Group D consensus of objectives and activities (membership should be expanded before proceeding with detailed plans)
- (ii) Select steering committee (e.g. Group D leader(s), MAX '91 Coordinator, and one representative each from Solar-A, SMM, and participating ground-based observatories)
- (iii) Set up "observing seasons" for the campaigns; conduct intensive observations capturing several flares within each campaign
- (iv) Make preliminary assessment on data obtained for each flare
- (v) Hold two workshops, each combining the activities centered around Campaigns I and II; core project is to work toward Science Goals 1 and 2 (each goal concentrating on the data obtained from no more than two flares); other related topics to be included.

HOW DO THE EFFECTS OF FLARES AND OTHER TRANSIENT ACTIVITY PROPAGATE TO EARTH?

The propagation of disturbances through the interplanetary (IP) medium is fairly well understood (although perhaps not presently modeled in complete detail); therefore, we concentrate our attention on aspects which are less understood, namely, the coronal origins of energetic particles, shocks, and CMEs, and the mechanisms by which coronal disturbances are injected into the IP medium. Unlike flares, which are relatively well observed, these phenomena are sorely lacking in terms of fundamental data that provide basic inputs to theory and modeling. The most fundamental missing measurement is the coronal vector magnetic field. In addition, there presently is no capability to study the RF emission (due to Earth atmospheric cut-off) associated with disturbances as they traverse the region 5R-20R, i.e., the region where disturbances undergo significant velocity change, and where the solar wind is accelerated. Nor are much-needed meter-wave heliograph observations expected during the MAX '91 time frame. Also, the HELIOS-type data are no longer available, with the result that in situ measurements of IP disturbances subsequent to coronagraph CME observations are lacking.

Science Goals

1. Determine why only approximately two-thirds of major flares are associated with IP shocks and CMEs (note that some CMEs are associated with filament eruptions rather than flares, and some have no apparent associated surface activity; in any case the fraction 2/3 is presently under debate). The attendant observational objectives are:
 - a. Search for characteristics that distinguish between flares (or the flare environments) that are associated with IP events and those which are not.
 - b. Provide qualitative descriptions of the preflare outer corona structures for the active regions producing flares of the two types above.
2. Determine why some flares produce IP proton events, while others do not. Observational objectives are similar to those above, and place strong emphasis on understanding the role of CMEs and shocks in the coronal flare explosion and the restructuring of the overlying magnetic field.

3. Provide a physical description of a CME, including its shape, density, and embedded magnetic field, and draw inferences on the CME origin and injection based on comparisons between modeled CME parameters and in situ IP measurements. The attendant objectives are:

- a. Improve statistics of CME mass, velocity, and geometry from space coronagraph measurements
- b. Model the vector magnetic field in the pre-CME corona.
- c. Obtain measurements of CME-induced changes in the IP magnetic field, density, and solar wind velocity.

Data Types (and Sources)

- a. Wide-field coronagraph (SMM/CP, possibly, but should have new camera and tape recorder; PHOBOS, but has very low cadence)
- b. Near-limb coronagraph (NSO, HAO; cadences should be increased)
- c. Soft x-ray imager (Solar-A; GOES/SXI)
- d. Vector magnetograph (MSFC; UH; APL; may require mosaic displays in order to increase field of view)
- e. Decametric radiometer (WIND, possibly: 10 MHz - 10 KHz)
- f. Interplanetary scintillation measurements (Britain, India, Japan; cadence is 1/day)
- g. H-alpha filtergrams (NSO, BBSO, and others)
- h. HELIOS-type photometer (USAF Solar Mass Ejection Imager, presently under study)
- i. IP magnetic field, density, and solar wind velocity (IMP 8 and WIND, possibly)
- j. Meter-wave radio burst sweep (USAF/RSTN and others)

It is assumed that these data (except item h) will be collected in a patrol or patrol-like mode during MAX '91. Some adjustments in these routine operations, dictated by requirements in cadence or field of view, are indicated for items b and d. Availability of item a (which is by no means certain!) is crucial to nearly all of the Group D activities relating to phenomena occurring in the outer corona. An additional activity of interest to Group D, but which is not included in the campaign below, is three-dimensional MHD modeling of IP shock propagation out to 1 AU and beyond.

Observing and Analysis Campaign

Collect data bases for Items a-g, i, and j above for a number of flares (some producing IP protons and CMEs, and some not) located within 30 degrees of the solar east limb (east limb required because coronagraph measurements must be made of the pre-CME state; unfortunately, positive detection of IP proton event is less certain for eastern hemisphere events); look for differences in H-alpha and soft x-ray morphology, evolution in time, peak coronal gas pressure, and magnetic field structures in the flare, and combine these with observations of pre-flare outer corona structures obtained from coronagraphs during limb passage of the associated active regions; search for similarities in the outer corona and large-scale photospheric magnetic field environment in cases of flares and non-flare events that produce protons and CMEs.

Coordination and Planning

- (i) and (ii): identical to the respective points in Section A.3 above.
- (iii) Search data base and select a representative sample of events. This requires participation by a representative for each data type.
- (iv) Hold two workshops, one for presenting preliminary results and planning analysis and one for finalizing. These could be held in conjunction with the workshops dedicated to Question A above.

ACTIVE REGION EVOLUTION IN THE CHROMOSPHERE AND TRANSITION REGION

R. A. Shine

Solar and Optical Physics, Lockheed Research Laboratory

and

C. J. Schrijver

Joint Institute for Laboratory Astrophysics

ABSTRACT

Images in the C IV 1548Å and the Si II 1526Å lines taken with the Ultra-violet Spectrometer Polarimeter (UVSP) instrument on board the *Solar Maximum Mission* (SMM) satellite have been combined into movies showing the evolution of active regions and the neighboring supergranulation over several days. The data sets generally consist of 240 by 240 arc second rasters with 3 arc second pixels taken once per orbit (about every 90 minutes). The images are projected on a latitude/longitude grid to remove the foreshortening as the region rotates across the solar disk and further processed to remove jitter and gain variations. Movies have been made with and without differential rotation. Although there are occasional missing orbits, these series do not suffer from the long nighttime gaps that occur in observations taken at a single groundbased observatory and are excellent for studying changes on time scales of several hours. The longest sequence processed to date runs from 20-Oct-1980 to 25-Oct-1980. This was taken during an SMM flare buildup study on AR 2744. Several shorter sequences taken in 1980 and 1984 will also be shown. The results will be presented on a video disk which can be interactively controlled to view the movies.

One of the scientific objectives during the *Solar Maximum Mission* (SMM) observations of 1980 was to study the morphology and evolution of active regions. During some periods, a special effort was made to obtain consistent data sets on an active region for several days with a large field of view. For the Ultra-violet Spectrometer Polarimeter (UVSP) instrument, the operating mode in support of this objective was at least one 240" by 240" image of the active region every orbit. We have developed software to process these images and to record them on a random access video disk. They are projected on a latitude/longitude grid to remove the foreshortening as the region rotates across the solar disk and further processed to remove jitter and gain variations. They can then be played as movies with variable speed, blinked between images, or just viewed as a single image. We intend to eventually process all of the UVSP large rasters using these techniques.

Movies have only been made using data taken during the interval from 20-Oct-1980 to 25-Oct-1980 (in spite of the optimistic statement in the abstract). This was during an official

Flare Buildup Study (FBS) which was intended to provide a consistent data set on the development of an active region over a disk crossing (about 2 weeks). Reasonably complete coverage was achieved for 5 days as shown in figure 1. Each orbit lasted 90 minutes and this is the spacing between images when the coverage is complete since only one large raster was done per orbit. Each took about 8 minutes to complete and the remainder of the orbit was used for smaller rasters with a higher cadence. This sequence consists of 57 raster pairs in C IV and Si II. C IV is formed at about 100,000 K in the transition region and Si II is formed in the middle to upper chromosphere. Not all of these images were complete or on line center and 5 of them have been omitted in some of the movies to reduce distractions. Both of these lines were observed with a square 3" entrance slit and a 0.3 Å exit slit. The intensity range is very great, especially in C IV where the brightest points may be hundreds of time more intense than the average. The range was decreased for the displays using a gamma of 0.5 for Si II and 0.35 for C IV.

Figure 2 shows 4 frames from the movie displaying both lines. The box around each image is a latitude/longitude grid 20 degrees on a side. This is very similar to a sun center projection. These were mapped without differential rotation but there are movies with and without differential rotation and also one showing Si II results for the two cases side by side. The Stonyhurst grid in the lower right has the original image position and size marked. Figure 3 shows two "continuum" images taken during this time span which show the sunspot configuration. These were taken at about 3100Å.

It is clear from the movies that 90 minute time steps are too long to follow much of the activity in the transition region shown by C IV. The bright points and loops are generally different in adjacent frames and the movie gives the appearance of hundreds of small explosions. The details of the fainter loop structures within and outside the active region also change from frame to frame although the general configuration is often similar. Si II is much more stable on these time scales and is better for studying changes in the structure of the active region. One of the most striking things in the Si II movie is the outflow around the sunspot group. The evolution of the supergranulation is also apparent. The pattern within the active region is much more stable than in the quiet areas. The supergranules outside the active region seem to be caught up in flows which push them around on a time scale shorter than their lifetimes. We plan to track them using local correlation tracking techniques similar to those used for tracking granules to investigate possible large scale flow fields.

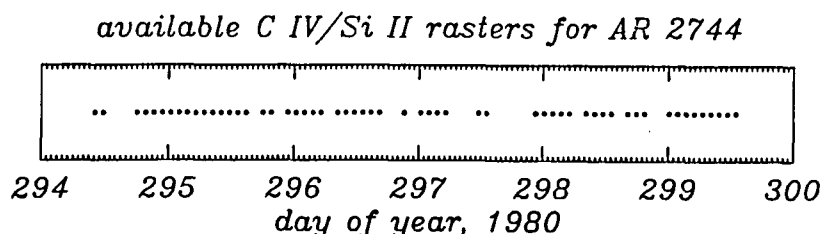


Figure 1. The dots indicate the times of the 57 C IV/Si II rasters in this sequence. Of these, 5 are sufficiently compromised (data dropouts or far off line center) to be distracting in a movie and have been omitted in edited versions of the movies.

C IV 1548

Si II 1533

C IV 1548

Si II 1533



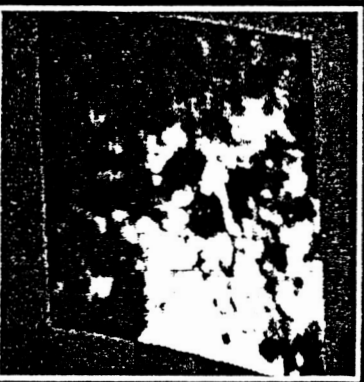
AR 2744 UVSP EXP # 14092
10:15 GMT D295 1980
DELTA T = 1.60 HOURS
SOLAR (X,Y) = (-338, -327)
SOLAR (R,T) = (0.498, -125)

1 ARC MIN 50000 KM



AR 2744 UVSP EXP # 14004
10:18 GMT D294 1980
DELTA T = 0.00 HOURS
SOLAR (X,Y) = (-519, -308)
SOLAR (R,T) = (0.629, -149)

1 ARC MIN 50000 KM



AR 2744 UVSP EXP # 14183
10:11 GMT D296 1980
DELTA T = 1.60 HOURS
SOLAR (X,Y) = (-133, -321)
SOLAR (R,T) = (0.363, -112)

1 ARC MIN 50000 KM



AR 2744 UVSP EXP # 14436
9:59 GMT D299 1980
DELTA T = 1.58 HOURS
SOLAR (X,Y) = (-489, -311)
SOLAR (R,T) = (0.597, -33)

1 ARC MIN 50000 KM

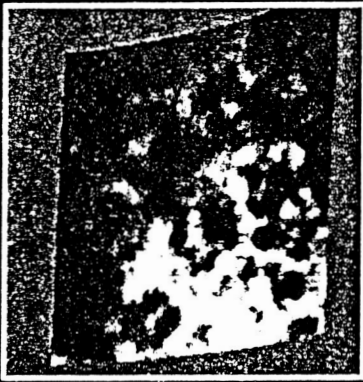


Figure 2. Four of the C IV and Si II rasters (frames 1, 13, 25, and 56 in the movies). The images are mapped onto a latitude/longitude grid 20 degrees on a side. This is very similar to a sun center projection. The Stonyhurst grid in the lower right has the original image position and size marked.

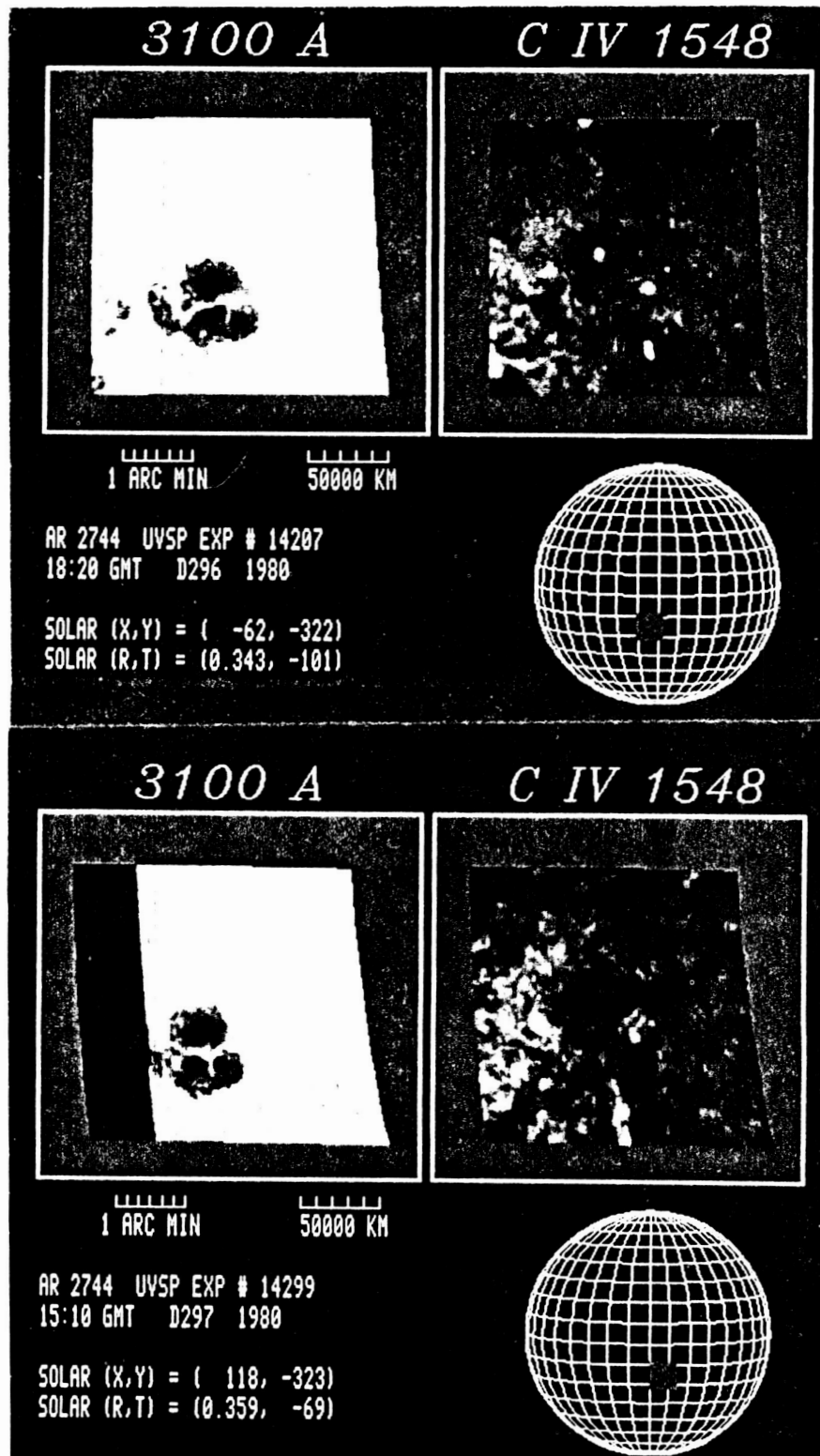


Figure 3. The 2 available long wavelength "continuum" images of the region during this time period (taken during some of the gaps in figure 1) and accompanying C IV images (taken with a different slit than the others).

Full-Disk Magnetograms Obtained with a Na Magneto-Optical Filter at
the Mount Wilson Observatory

Edward J. Rhodes, Jr. (USC and JPL)
Alessandro Cacciani (University of Rome and JPL)
Glenn Garneau (JPL)
Tony Misch (Lick Observatory)
Dusan Progovac (USC)
Tom Shieber (UCLA)
Steve Tomczyk (UCLA)
Roger K. Ulrich (UCLA)

We report here on the first full-disk magnetograms to be obtained with the Na Magneto-Optical Filter (MOF) which is located at the 60-foot solar tower of the Mount Wilson Observatory. This MOF was employed as a longitudinal magnetograph on June 18, 19, and July 1, 1987. On those three days the MOF was combined with a large format (1024x1024 pixel) virtual phase charge coupled device camera and a high-speed data acquisition system. The combined system was used to record both line-of-sight magnetograms and Dopplergrams which covered the entire visible solar hemisphere. The pixel size of these magnetograms and Dopplergrams was $2.3''$. On each of the three days a time series of nine pairs of magnetograms and Dopplergrams was obtained at the rate of one pair every two minutes. On the same three days longitudinal magnetograms having one arcsecond pixels were obtained with the vacuum telescope at Kitt Peak and provided to us by T. Duvall. We have compared the MOF and vacuum tower magnetograms both at JPL's Multi-Mission Image Processing Laboratory and at USC and have found the two sets of images to be well correlated both in spatial distribution and strength of the measured magnetic field. We have also employed the simultaneously-obtained MOF Dopplergrams to remove the cross-talk which was present between the Doppler and Zeeman shifts of the NaD lines from the magnetograms from all three days and will also describe recent improvements to the system which allow us to obtain full-disk magnetograms as rapidly as once every 25 seconds. This work was supported by NASA grant NASW-13 and by NSF grant INT 84-00213 to USC. A portion of the research was also performed by the Jet Propulsion Laboratory, California Institute of Technology, under contract with the National Aeronautics and Space Administration.

COMPONENTS OF MAGNETO-OPTICAL FILTER IN MAGNETOGRAPH MODE AND WITH Na D1/D2 SEPARATOR (IMAGING LENSES OMITTED)

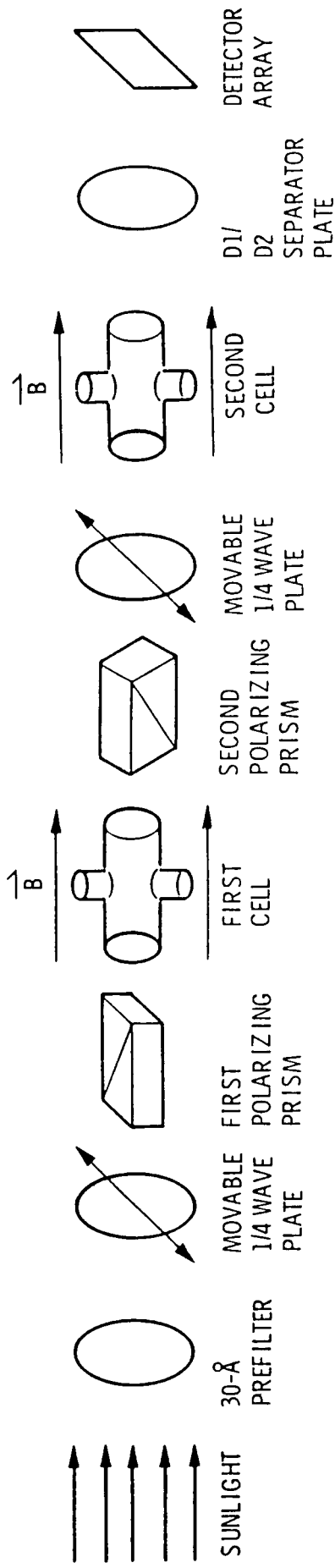
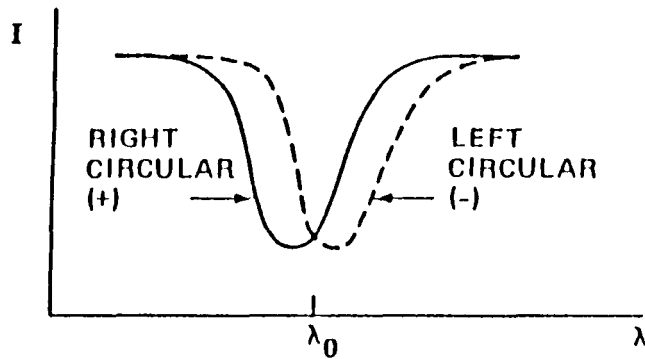


Figure 1. Schematic diagram of the MOF in the longitudinal magnetograph/Dopplergraph mode. In actual operation on objective lens, field lens, and a reimaging lens are added to the elements shown here. The lens, and a reimaging lens are added to the elements shown here. The first 1/4 wave plate is for the magnetograph, while the second is for the Dopplergraph.

~ MAGNETIC FIELD SPLITS SPECTRAL LINE:
TWO COMPONENTS
OPPOSITE POLARIZATIONS



~ LINE DISPLACEMENT DEPENDS ON FIELD STRENGTH:

$$\Delta\lambda (+) = -aH$$

$$\Delta\lambda (-) = +aH$$

$$a \cong 10 \text{ mÅ/kg} = 0.01 \text{ mÅ/g}$$

~ DOPPLER SHIFT DISPLACES BOTH COMPONENTS:

$$\Delta\lambda = bV$$

$$b \cong 20 \text{ mÅ/(km/s)} = 0.02 \text{ mÅ/(m/s)}$$

~ II, V CAN BE DERIVED:

MEASURE INTENSITY (I)

IN TWO WINGS (R = RED, B = BLUE)

IN TWO POLARIZATIONS (+, -).

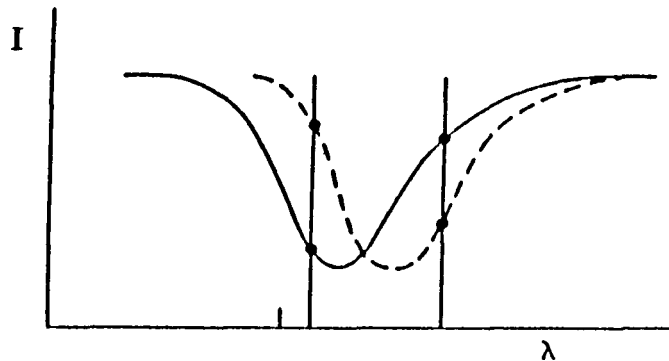


Figure 2. Schematic illustration of the method by which the simultaneous Zeeman splittings and Dopplers shifts of a solar spectral line can be determined separately.

$$B_- = I_0 + (aH + bV) (dI/d\lambda)$$

$$B_+ = I_0 + (-aH + bV) (dI/d\lambda)$$

$$R_+ = I_0 + (-aH - bV) (dI/d\lambda)$$

$$R_- = I_0 + (aH - bV) (dI/d\lambda)$$

- $\sum = B_- + B_+ + R_+ + R_- = 4I_0$

RED - BLUE GIVES V,

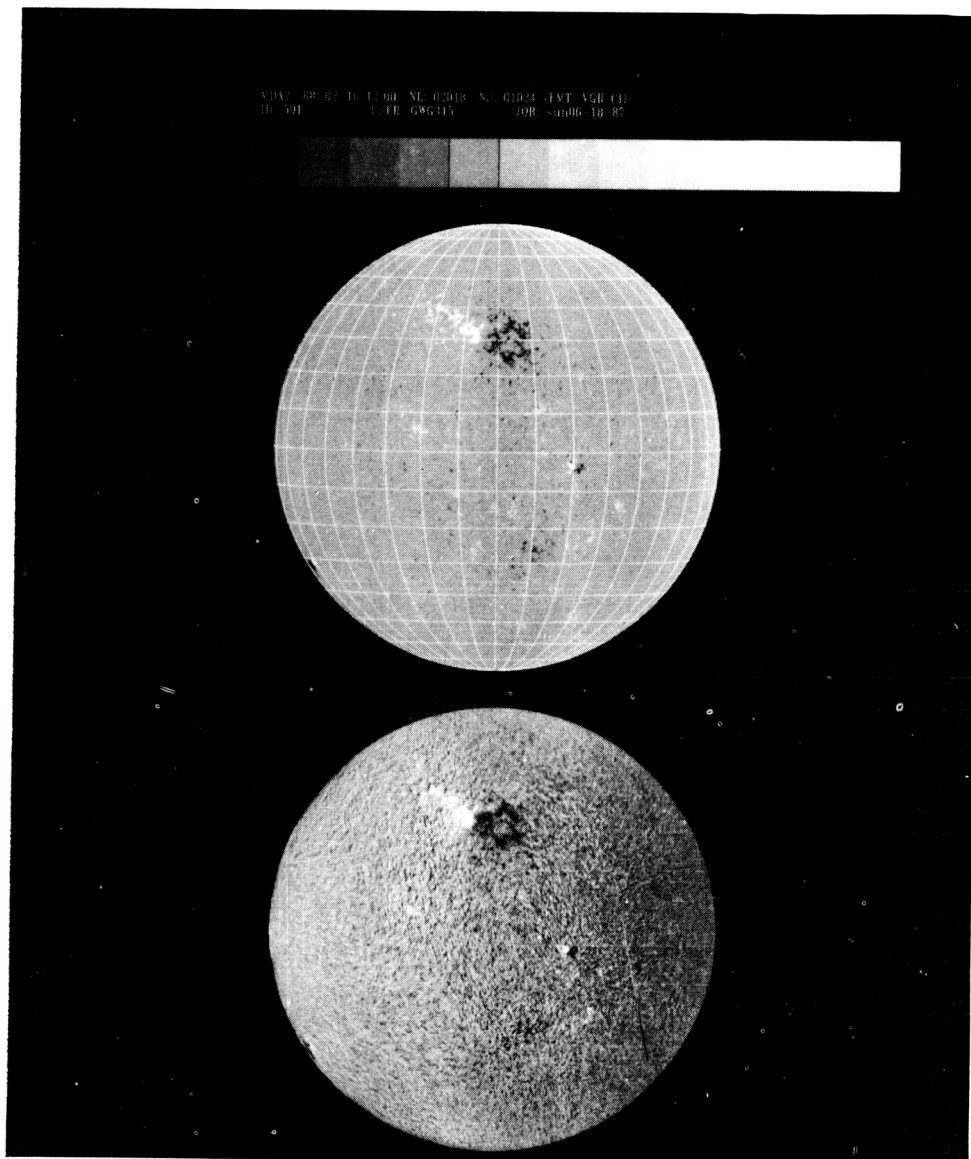
RIGHT - LEFT GIVES H:

$$V = \frac{(R_+ - B_+) + (R_- - B_-)}{\sum}$$

$$H = \frac{(R_+ - R_-) + (B_+ - B_-)}{\sum}$$

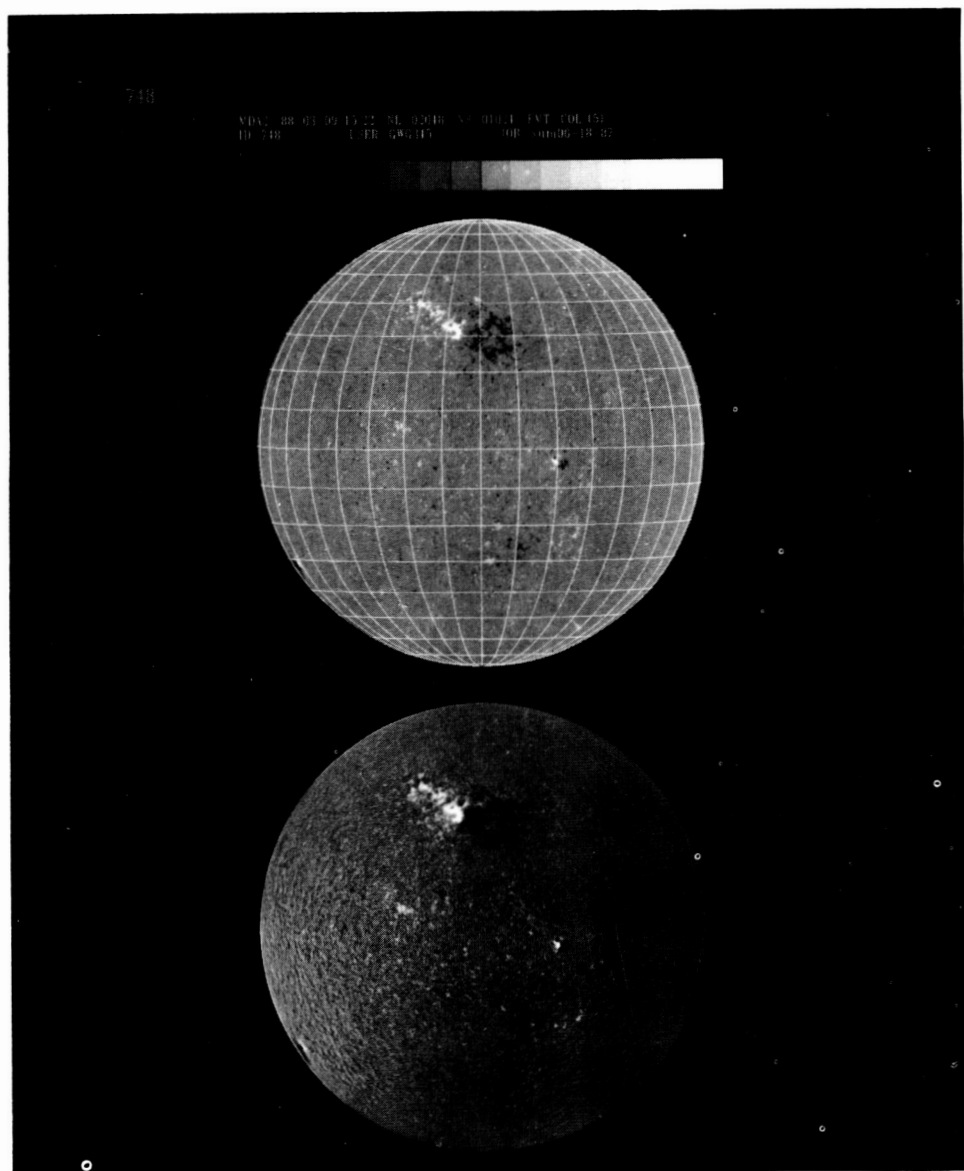
Figure 3. Formulae used for the conversion of four filtergrams into one magnetogram (H) and one Dopplergram (V).

ORIGINAL PAGE IS
OF POOR QUALITY



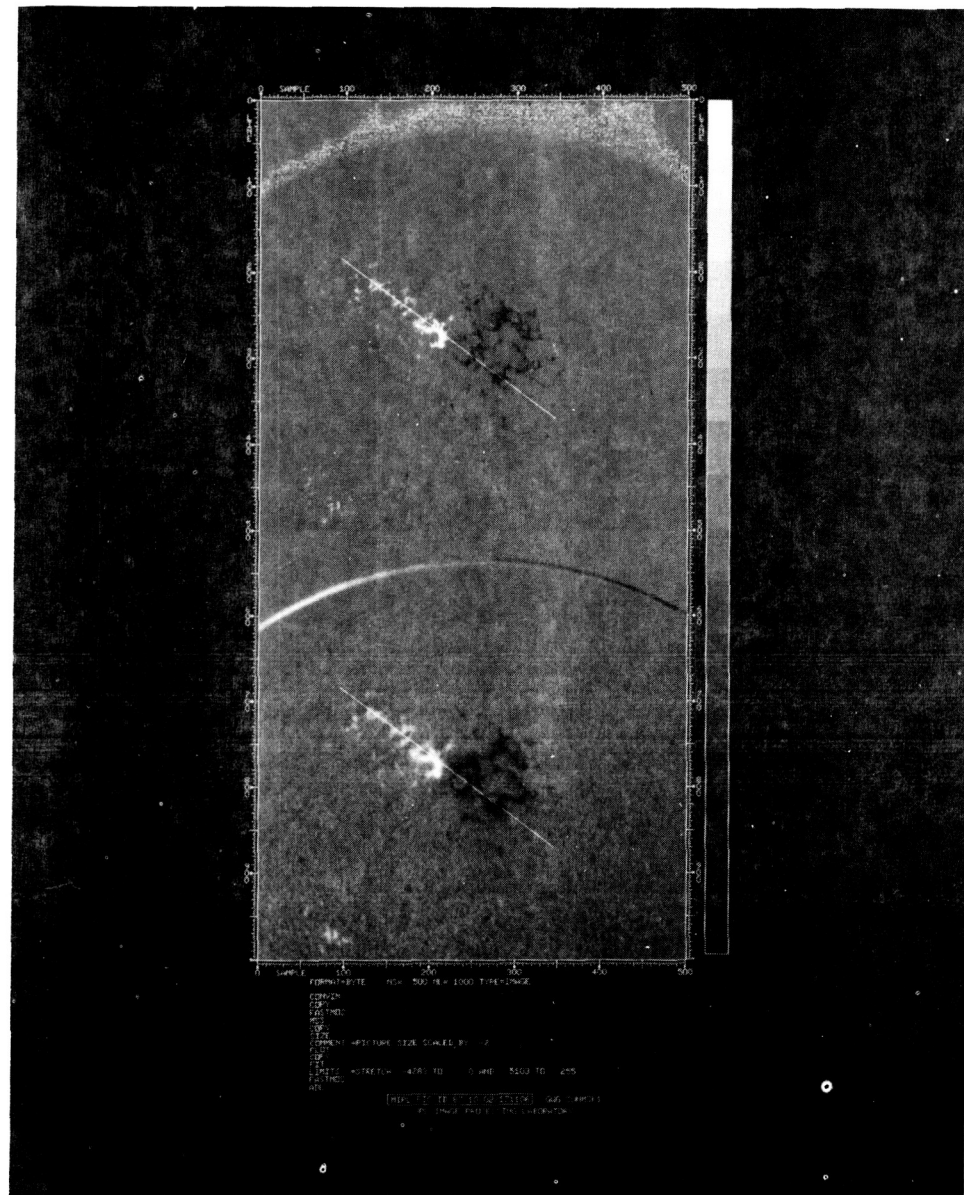
• Figure 4. KPNO magnetogram for 6/18/87 (top).
Single Mt. Wilson MOF magnetogram for 6/18/87 (bottom).

ORIGINAL PAGE IS
OF POOR QUALITY



• Figure 5. KPNO magnetogram for 6/18/87 (top).
Average of nine individual MOF magnetograms for 6/18/87 (bottom).

**ORIGINAL PAGE IS
OF POOR QUALITY**



- Figure 6. Enlargement of active region located at 30° N in Figures 4 and 5. KPNO magnetogram is shown at the top. The average of the nine MOF magnetograms is shown below. The white line is a scan line through the active region along which the magnetic field strengths are compared in Figures 7 and 8.

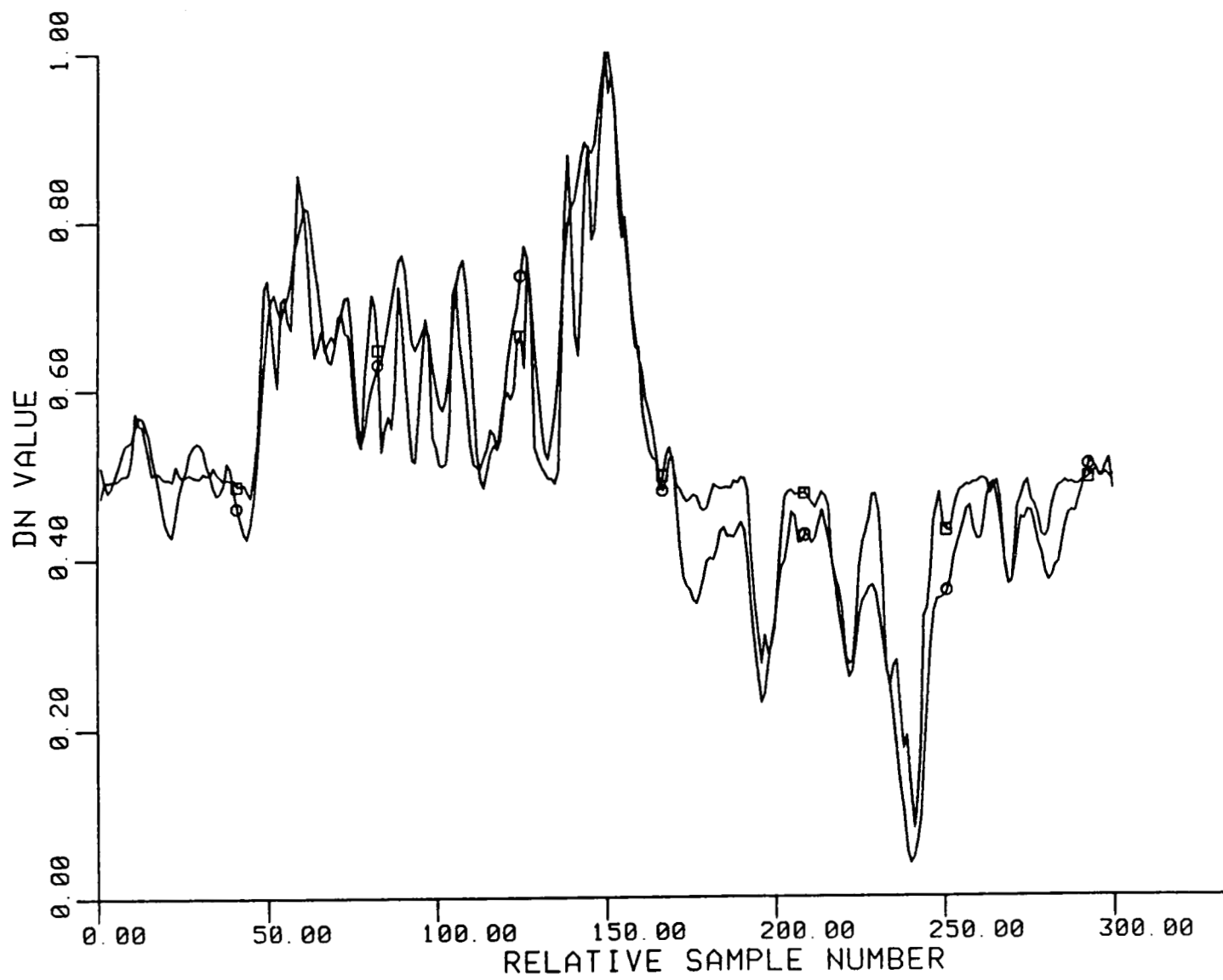
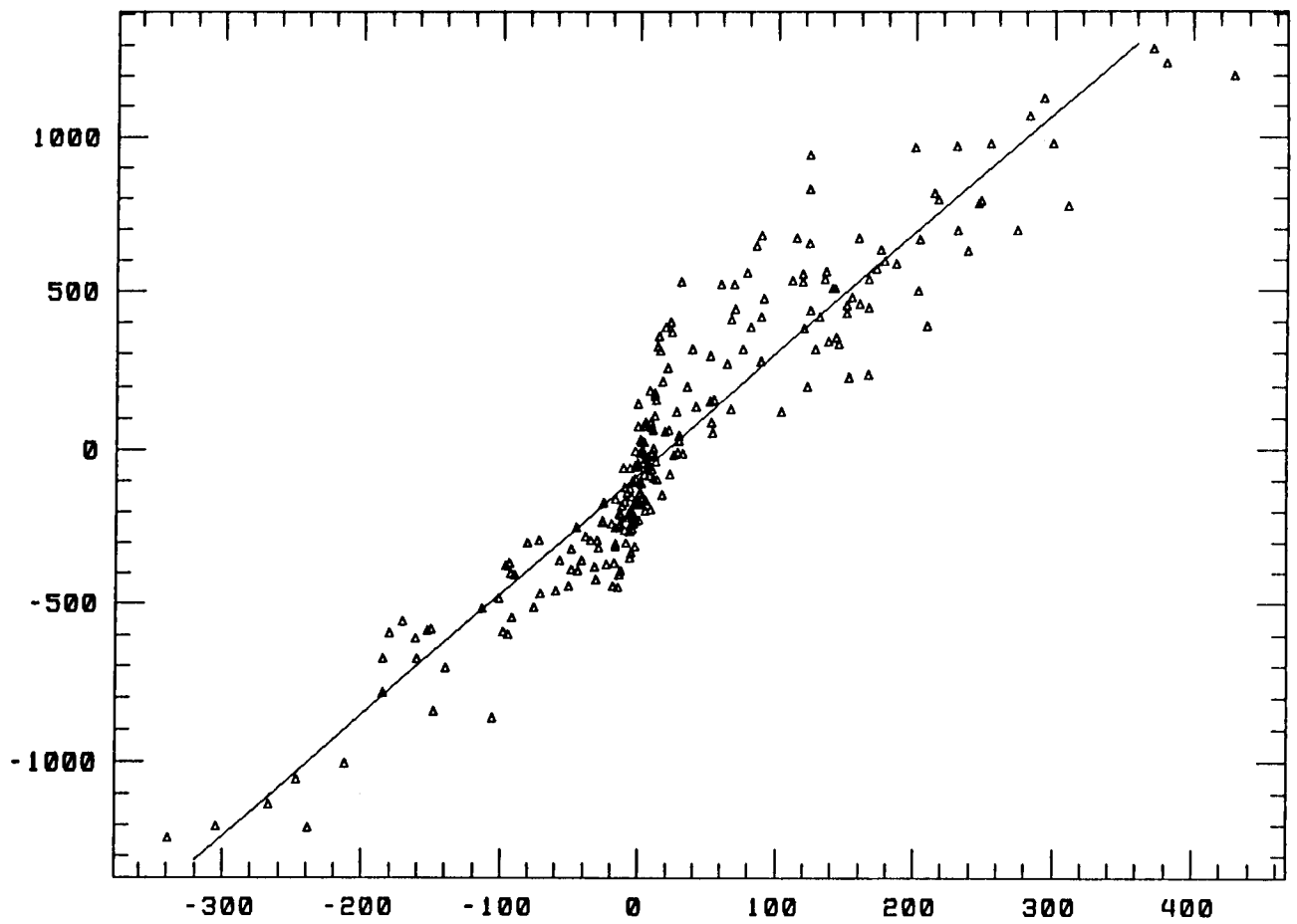
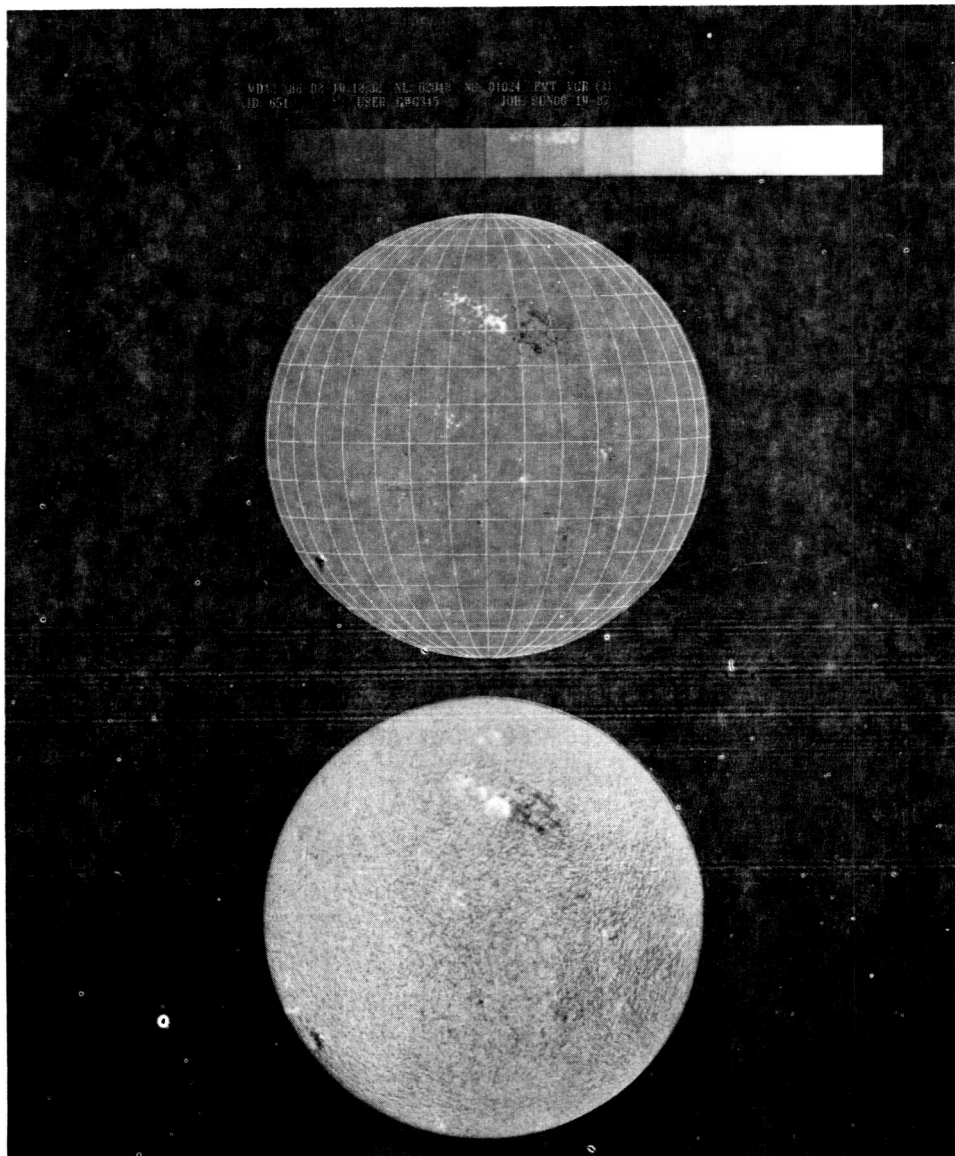


Figure 7. Comparison of measured magnetic field strengths along the scan line through the active region shown in Figure 6. The MOF data points are labeled with the open circles, while the corresponding KPNO data points are labeled with the squares.



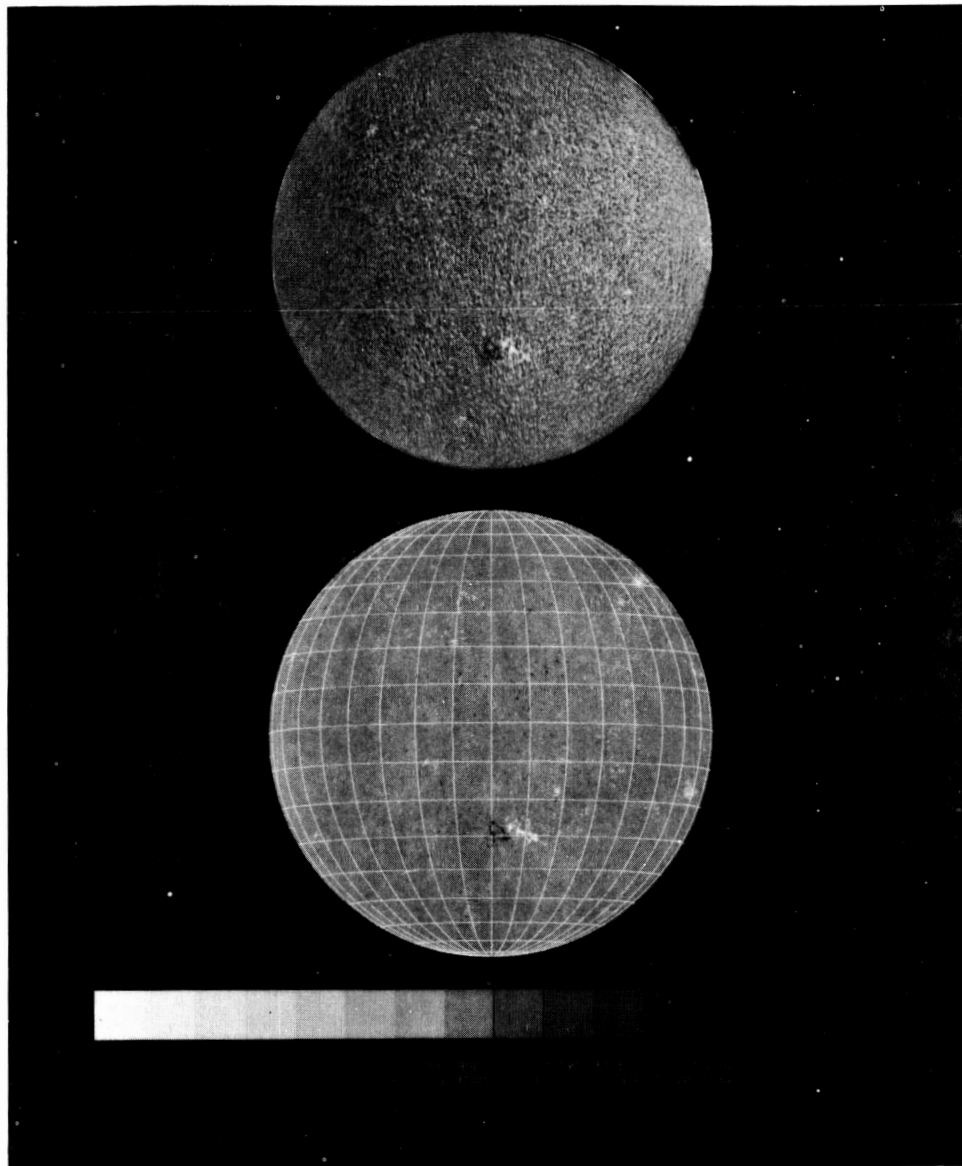
- Figure 8. Scatterplot of measured magnetic field strengths along scanline shown in Figure 6. KPNO values are plotted horizontally in gauss while corresponding values from the average MOF magnetogram shown in Figure 5 are plotted vertically. The least squares fit to the points is shown as the straight line. The correlation coefficient for this fit was 0.93.



- Figure 9. Comparison of KPNO magnetogram for 6/19/87 (top) with corresponding single Mt. Wilson MOF magnetogram (bottom). The active regions shown in Figures 4 and 5 have all rotated to the west in these images.

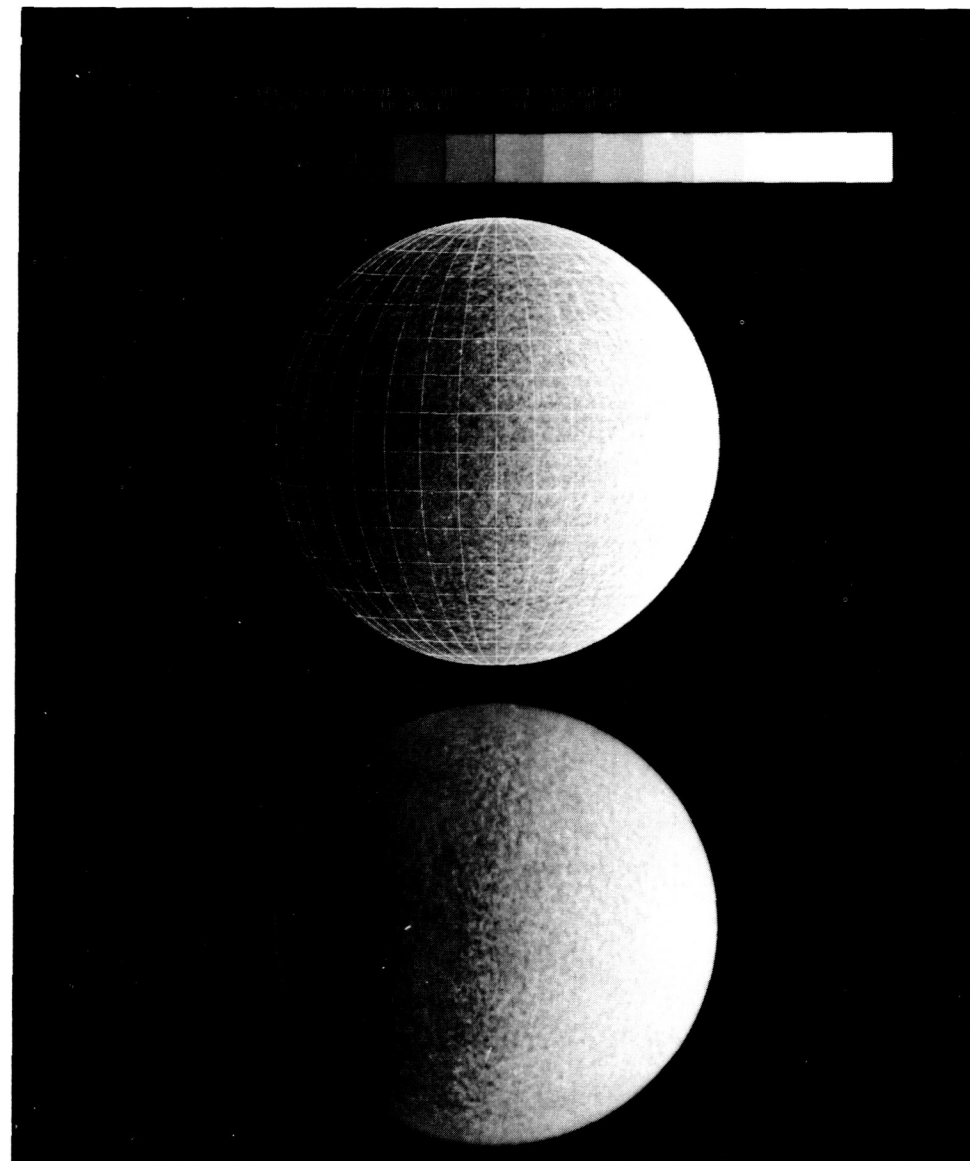
ORIGINAL PAGE IS
OF POOR QUALITY

ORIGINAL PAGE IS
OF POOR QUALITY

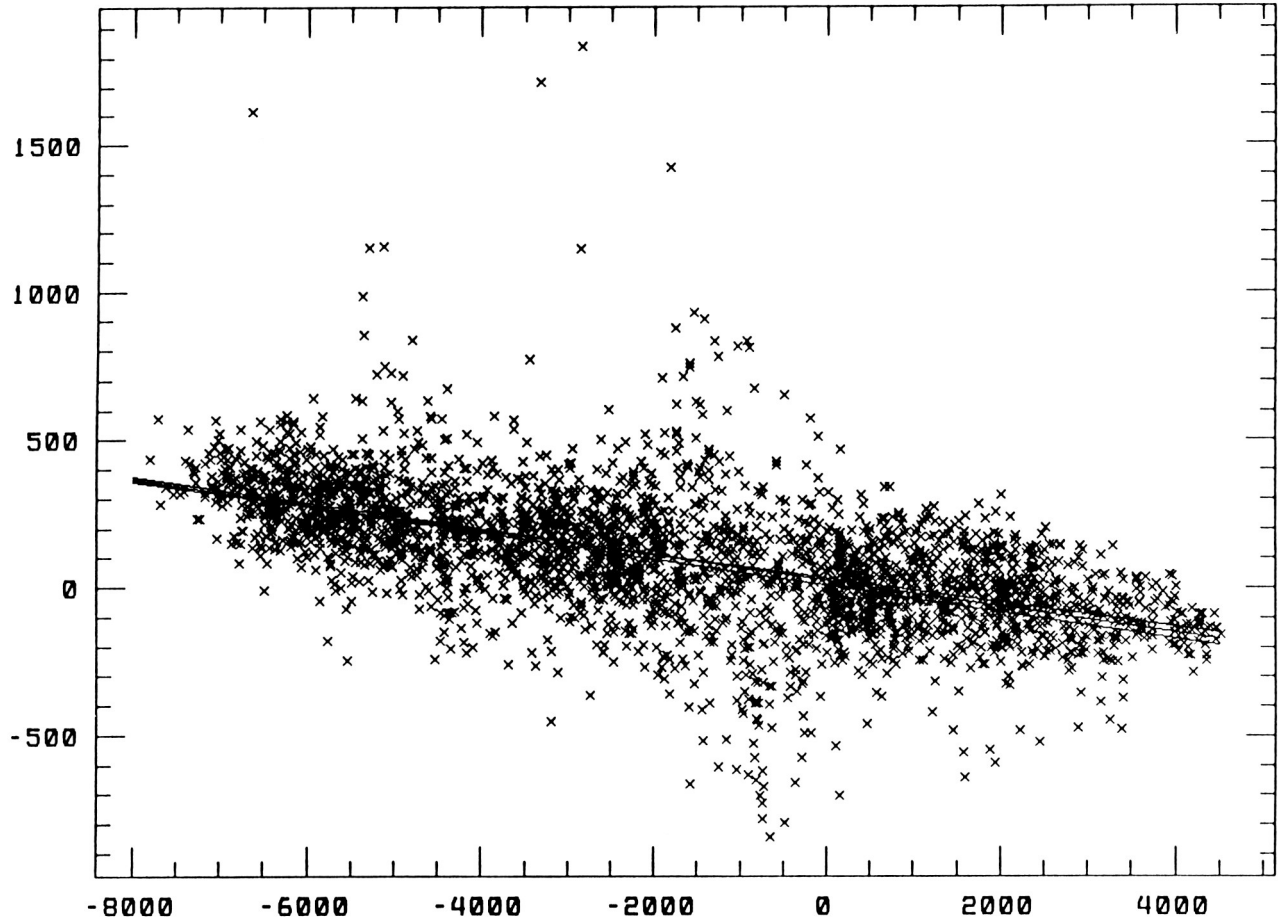


• Figure 10. Comparison of KPNO (top) and single Mt. Wilson MOF magnetogram for 7/1/87 (bottom).

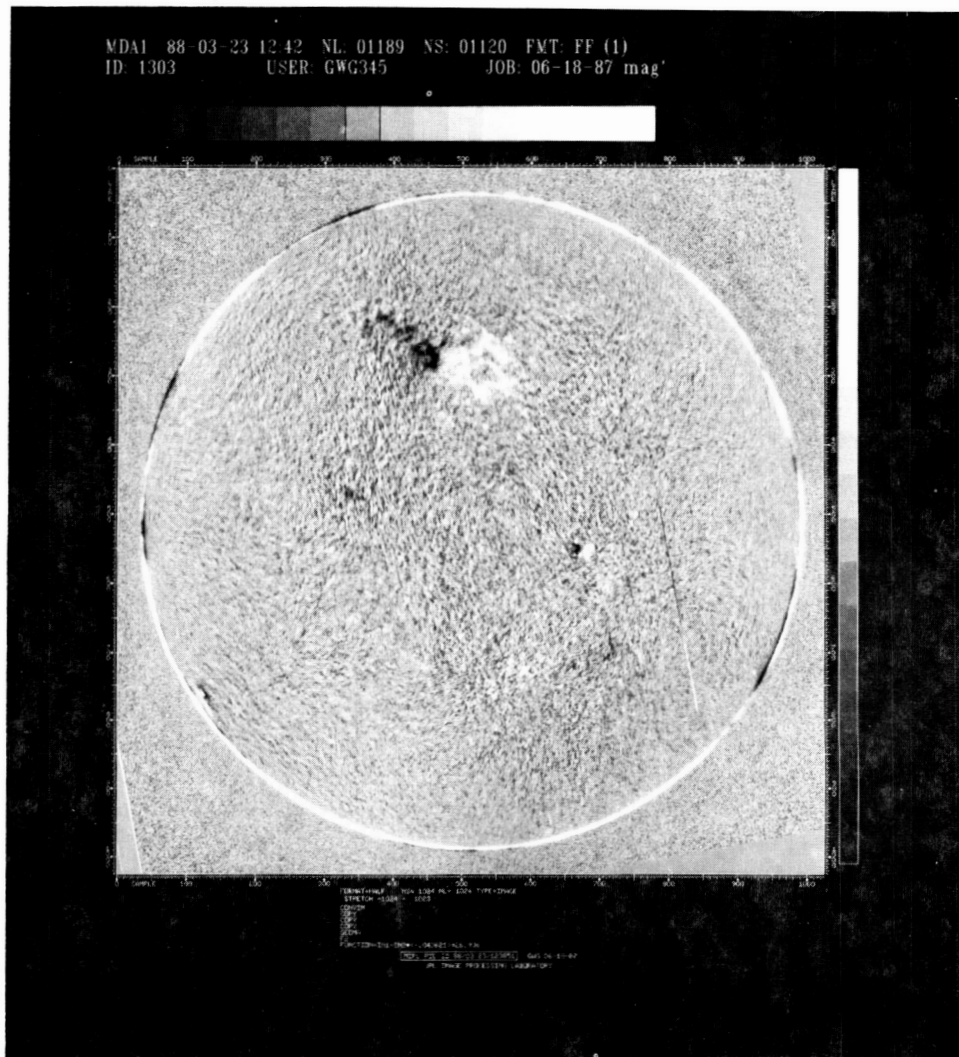
ORIGINAL PAGE IS
OF POOR QUALITY



- Figure 11. Comparison of KPNO (top) and Mt. Wilson MOF Dopplergram (bottom) for 7/1/87. Solar rotation is visible in both images as is the supergranulation. Because the two images were not obtained simultaneously, the oscillatory velocity patterns are not in phase. The Mt. Wilson Dopplergram was obtained in 1 minute while the KPNO Dopplergram required 40 minutes.

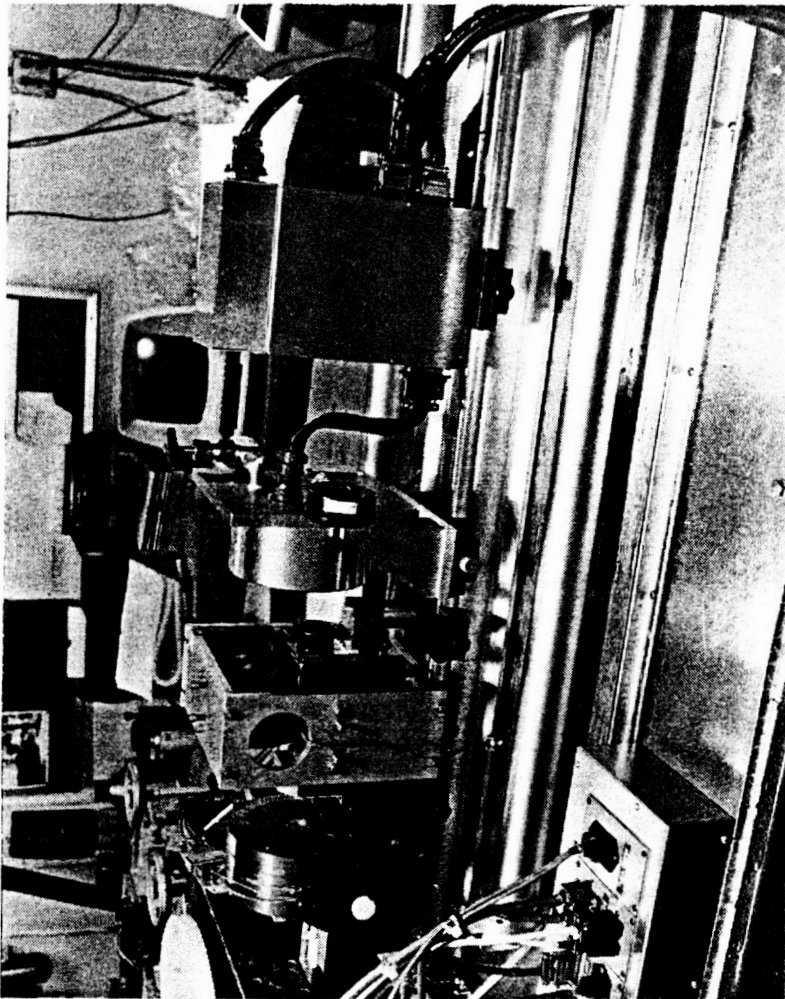
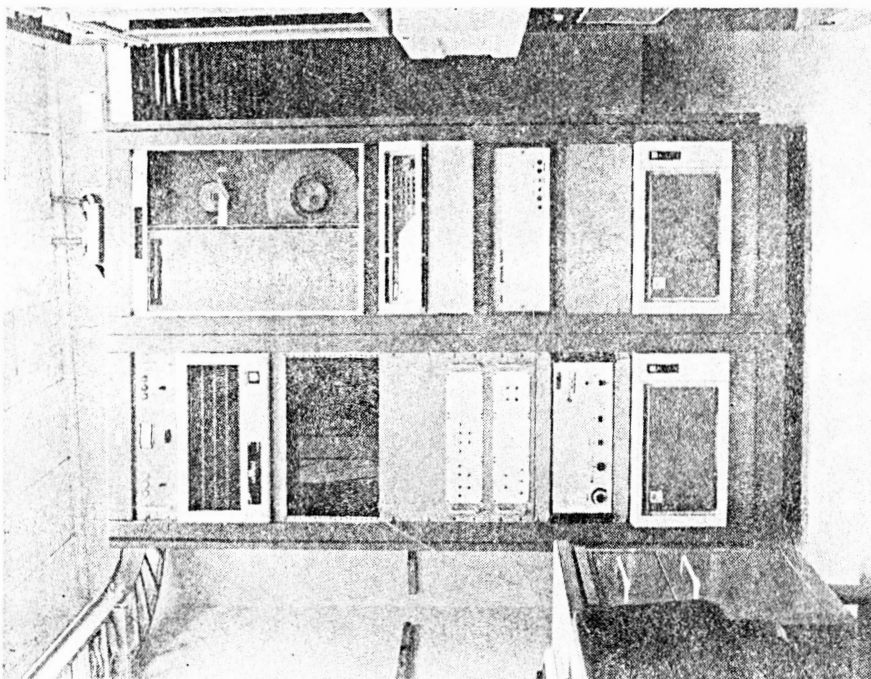


- Figure 12. Comparison of magnetic and Doppler signals from 6/18/87 raw images. Values were compared for three narrow (three-pixel high) bands which were oriented parallel to the equator. One band was in the Northern Hemisphere, one in the Southern Hemisphere, and the third was along the equator itself. The overall correlation between the two signals is evident as is a large amount of scatter. There are 3072 pairs of points included in this figure. The three straight lines are the least-squares regression fits to the 1024 pairs of points within each zone. The nearly identical regression fits indicate that a single trend is valid over the entire image (except in the active regions). The largest deviations from the regression fits correspond to the large magnetic field strengths recorded in the large active region of Figures 4 and 6. The simple correlation between the Doppler velocities and the weak magnetic background signal is masked by the large field strengths in this active region.



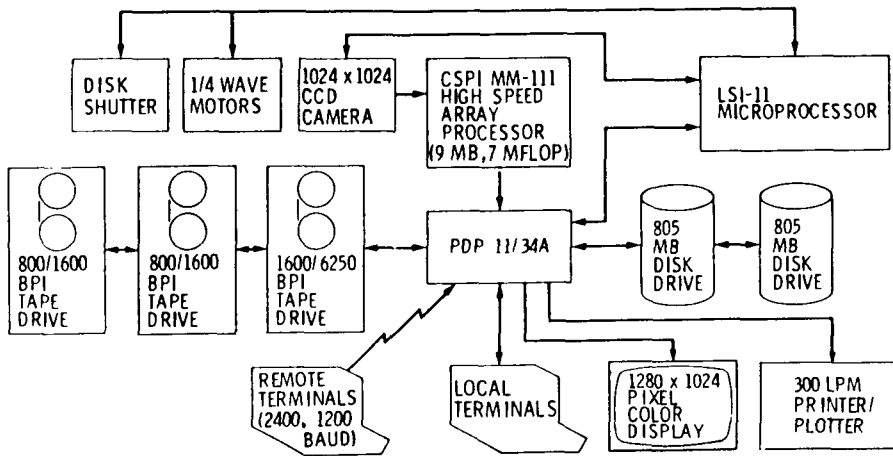
- Figure 13. A single “cleaned” magnetogram for 6/18/87. This magnetogram is the result of the removal of the Doppler-shift-induced cross-talk from the raw magnetogram of Figure 4. This cross-talk was removed using the empirical fit for the 6/18/87 magnetogram and Dopplergram which was found in Figure 12 above. This fit ($\text{MAGNETIC} = 26.94 - 0.04362x\text{DOPPLER}$) was calculated for each pixel of the raw magnetogram and then subtracted from that image. The east-west trend which was evident in Figures 4 and 5 is absent in this “cleaned” magnetogram.

ORIGINAL PAGE IS
OF POOR QUALITY



- Figure 14. (left) Photograph of the MOF (the two magnet assemblies at the left) and the CCD camera (the aluminum cylinder at the center and the electronics box at the right) as they are currently installed at Mt. Wilson. (right) The 60-foot tower CCD Data Acquisition Computer.

MT. WILSON HELIOSEISMOLOGY DATA ACQUISITION FACILITY



- Figure 15. Schematic diagram of the data acquisition system at the 60-foot tower which will be used for the magnetogram development. Since the figure was prepared an additional 800 MB of disk storage has been added at to the system. In addition to the shown here, analysis will also be conducted on the USC ALLIANT FX/8 system.

Improvements Implemented Since June 1987

- Data Acquisition Rate Sped Up to 4 frames in 66 seconds
- Guider Has Been Renovated
- Wide Acceptance Angle Polarizers Have Been Installed
- Images can be Numerically Integrated in Real Time
- Faster Disk Drives Installed

Planned Improvements for 1988

- 2x Magnification Optics to be Installed
- Efforts underway to Improve "Seeing" of 60-Foot Tower
- All-Refractive Optic System May be Implemented
- Vector Magnetograph Mode to be Tested
 - Additional Mount to be Installed for Extra Waveplates
 - Additional Array Processor Memory will Allow Rapid Acquisition of Six-Filtergram Sequence

**Observations of Photospheric Magnetic Fields and Shear Flows
in Flaring Active Regions**

T. Tarbell, S. Ferguson, Z. Frank, A. Title, K. Topka (Lockheed PARL)

Abstract

Horizontal flows in the photosphere and sub-surface convection zone move the footpoints of coronal magnetic field lines. Magnetic energy to power flares can be stored in the corona if the flows drive the fields far from the potential configuration. We show videodisk movies with 0.5 - 1 arcsecond resolution of the following simultaneous observations: green continuum, longitudinal magnetogram, Fe I 5576 Å line center (mid-photosphere), H α wings (± 600 mÅ), and H α line center. The movies show a 90×90 arcsecond field-of-view of an active region at S29, W11 (15:05 - 16:25 UT, 8/6/87). When viewed at speeds of a few thousand times real-time, the photospheric movies clearly show the active region fields being distorted by a remarkable combination of systematic flows and small eruptions of new flux. Magnetic dipoles are emerging over a large area, and the polarities are systematically flowing apart. We have mapped the horizontal flows in detail from the continuum movies, and these may be used to predict the future evolution of the region. The horizontal flows are not discernable in H α . The H α movies strongly suggest reconnection processes in the fibrils joining opposite polarities. When viewed in combination with the magnetic movies, the cause for this evolution is apparent: opposite polarity fields collide and partially cancel, and the fibrils reconnect above the surface. This type of reconnection, driven by sub-photospheric flows, complicates the chromospheric and coronal fields, causing visible braiding and twisting of the fibrils. Some of the transient emission events in the fibrils and adjacent plage may also be related. The flows in this region probably also cause some reconnections beneath the surface, leading to U-shaped magnetic loops as well as Ω -loops.

Longer sequences with more uniform seeing, as would be obtained from balloon or space flight, are sorely needed. These observations were obtained at the Vacuum Tower Telescope (NSO/Sunspot) using the SOUP tunable filter and the HRSO CCD camera. This work was supported by Lockheed Independent Research Funds and NASA contracts NAS8-32805 (SOUP) and NAS5-26813 (HRSO).

ORIGINAL PAGE IS
OF POOR QUALITY

Evolution of the Active Region

Once the fields have emerged, AR's continue to grow and deform, often increasing in magnetic complexity and in stored magnetic energy. Large scale flows have traditionally been observed using pores and sunspots as tracers. Using SOUP data, we discovered that granulation can be used to measure accurate horizontal flow velocities anywhere on the sun. More recent work at Lockheed and NSO (by November and Simon) has shown that this can also be done with ground-based data if long enough time series of approximately uniform quality are available. We have now used the same techniques on magnetograms, to separate the systematic motion of magnetic features on the sun from the random jiggling due to seeing.

The August 6 magnetic movie, after removal of the seeing jitter, shows that the polarities in the region are separating systematically over a large area. This is shown very dramatically on the video movies: white polarity features move down and to the left, and black polarities move up and to the right. This rule characterizes the proper motions throughout the region between the spots. Presumably, the magnetic features of each polarity represent the frayed ends of a large flux rope in the convection zone. As the ropes separate down below, the ends are dragged apart at the surface. With better observations, it will be interesting to see when magnetic features move "against the current" of the meso- and supergranular flows (measured from proper motion of non-magnetic granulation). This would indicate very strong buoyancy and tension forces at work to overcome the drag force of the surroundings.

We have mapped the photospheric flow of the granulation and pores by correlation tracking on the continuum movie. Some of the flow features of the magnetic movie are seen, but the flows do not agree everywhere. Future evolution of the region is simulated using the measured flows; again, the agreement is mixed. The correlation tracking technique breaks down if, for example, a pore is moving against a steady flow of granulation, and both are included in the tracking field-of-view. With better resolution and less seeing jitter, it may be possible to separate the magnetic and non-magnetic flows.

Another discovery from the August 6 magnetic movie is that flux emergence in this region does not take place at a neutral line separating separating polarities. Instead, it is occurring in small bipolar events spread over a large area between the leading and following spots. Even a snapshot shows that the polarity mixing makes it impossible to draw a neutral line. The movie shows that the opposite poles of an emerging bipole separate and then move rapidly across the "neutral zone" to flux concentrations on either side. The motions are not always at uniform speed—sudden spurts are often seen.

A very important consequence of this geometry is that many flux cancellation and recon-

nection events are forced to occur among the newly emerged magnetic elements. With opposite polarities moving in opposite directions through the same area, collisions are frequently observed. Cancellation of flux occurs, sometimes forming a temporary lane of one polarity. In some cases, dramatic reconnections of the H- α fibrils are seen when the magnetic footpoints of a set of fibrils are cancelled by intrusion of opposite polarities. This is very graphic evidence for magnetic reconnection taking place above the surface, presumably in the low chromosphere. These reconnections are driven by sub-surface flows, not by global properties of the chromospheric or coronal fields. Therefore, they have no tendency to simplify the topology of the magnetic field, and considerable twisting and braiding of the H- α fibrils is observed in our movies after a reconnection. This process can store energy in the field for coronal heating or flaring, as discussed in detail by Parker, van Ballegooijen, and others.

It is likely that some collisions between opposite polarity flux tubes occur beneath the surface. Before emerging through the surface, the field lines are nearly horizontal, and this must persist for some time afterwards as well. The inclined field lines of different flux tubes can therefore meet and reconnect below the surface, forming shallow, U-shaped tubes. These are weighted down by the gas frozen into the magnetic tube and cannot float up through the photosphere and out into the corona. U-loops have been suggested by Spruit et al. to play a role in the destruction of active region flux.

FIGURE CAPTIONS

Fig. 1. Snapshots of the active region in (a) continuum near 5576; (b) Fe I 5576, 30 mÅ blue; (c) H- α line center; (d) H- α wing, 600 mÅ red. All images in Figs. 1 and 2 were taken within 80 seconds of each other, in one cycle of the observing sequence. Field-of-view is 90 \times 80 arcseconds, and ticks are at 2 arcsecond intervals.

Fig. 2. Same as Fig. 1, showing (a) Fe I 5576 line center, compensated for the local Doppler shift; (b) Doppler velocity measured from 4 images evenly spaced through 5576 ($g=0$ line); (c) H- α wing, 600 mÅ blue; (d) magnetogram made in blue wing of Fe I 6302 ($g=2.5$).

Fig. 3. Horizontal flow vectors (measured by correlation tracking on the continuum movie) overlain on a magnetogram. Many meso- and supergranules (diverging flows) can be seen as well as magnetic concentrations in converging flows.

Fig. 4. Two frames from a "cork movie" simulation of future evolution of the region based on the measured flows of Fig. 3. The clocks show the elapsed time from the initial condition of a uniform array of markers ("corks").

Fig. 5. Collage of frames from the H- α line center movie, showing the major reconnection event, and one magnetogram. Each frame is labelled with the time. Field-of-view is 45 \times 45 arcseconds, and ticks are at 1 arcsecond intervals.

Fig. 6. Collages of frames from the H- α line center and red wing movies, showing the major reconnection event. Field-of-view is 25 \times 25 arcseconds, and ticks are at 1 arcsecond intervals.

Fig. 7. Same as Fig. 6 for H- α blue wing and magnetogram movies. Initially the fibrils connect a small white polarity feature just to the right of center to the large black-polarity sunspot above this field-of-view. The growth and encroachment of the adjacent black polarity causes the reconnection. Afterwards, the fibrils connect the black sunspot to the strong white polarity just above the time label.

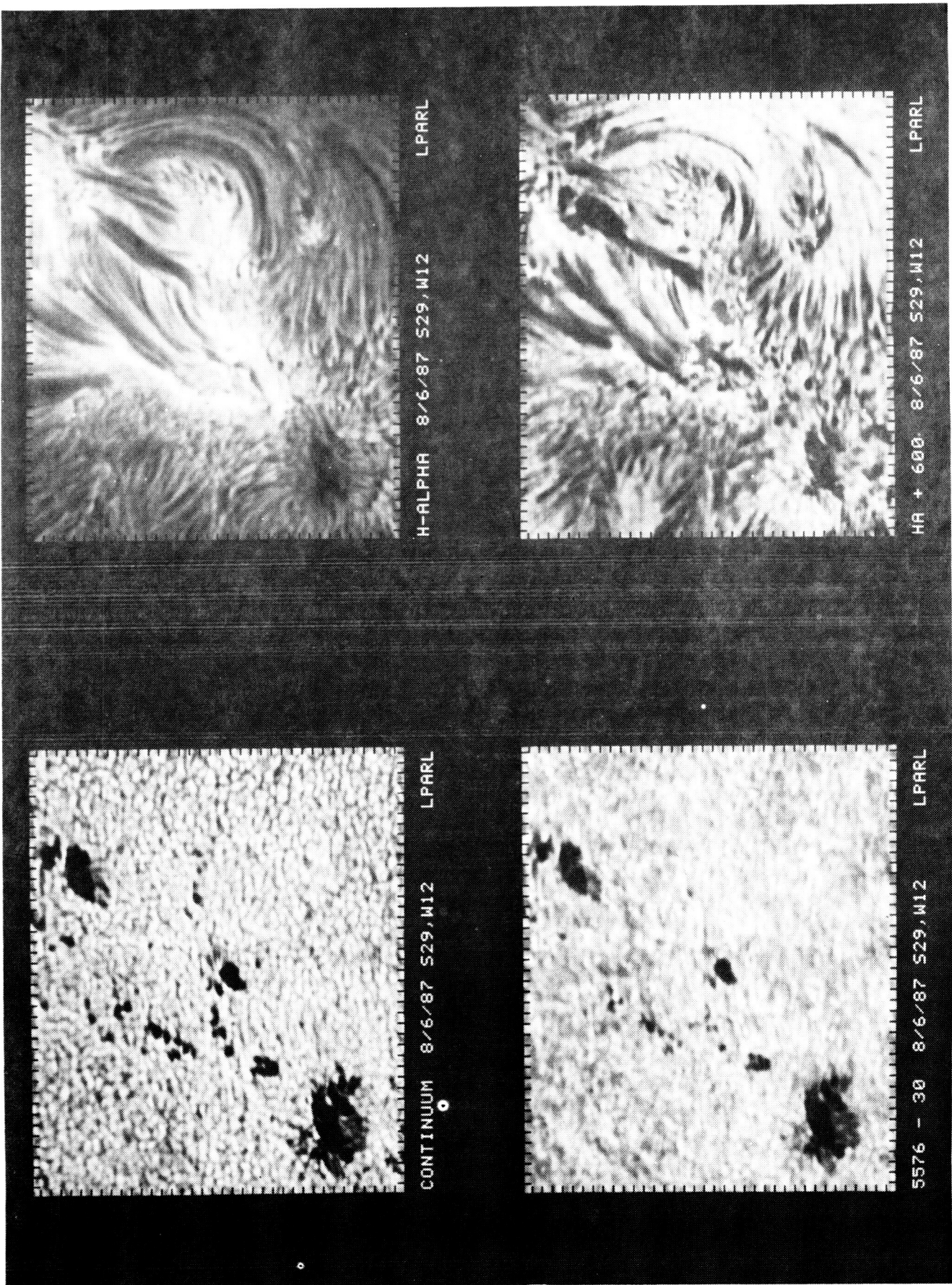


FIG. 1

ORIGINAL PAGE IS
OF POOR QUALITY

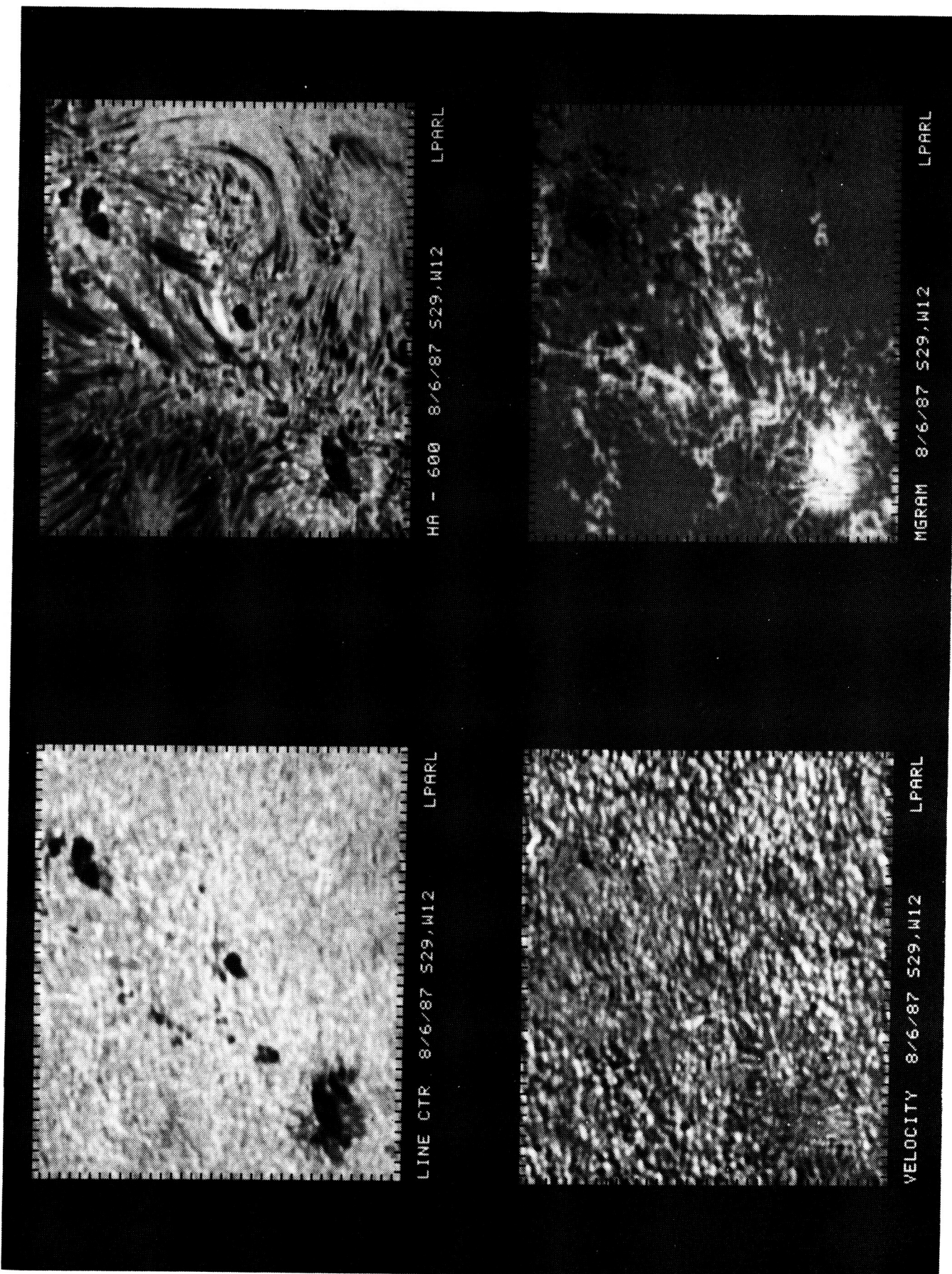
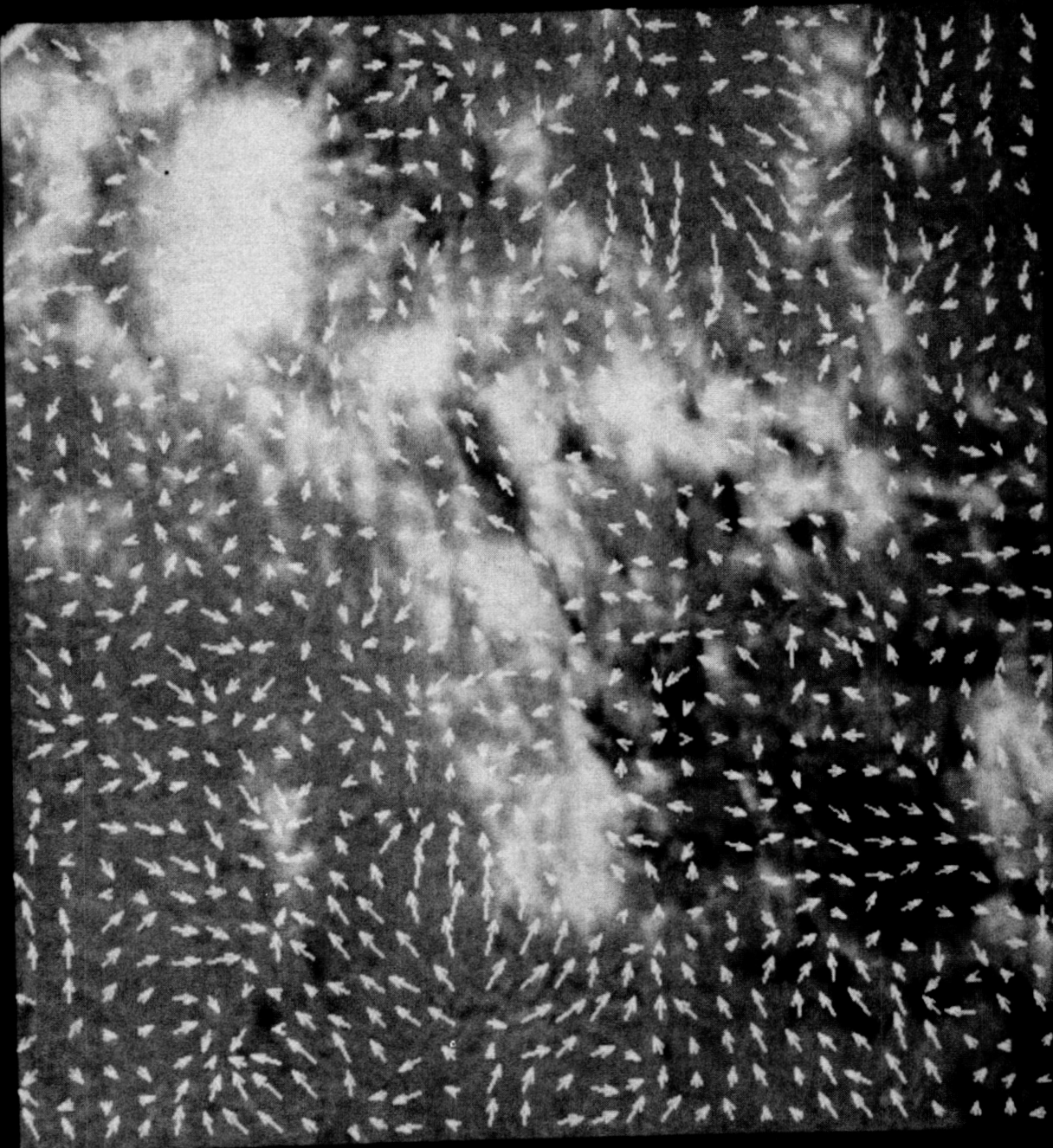


FIG. 3



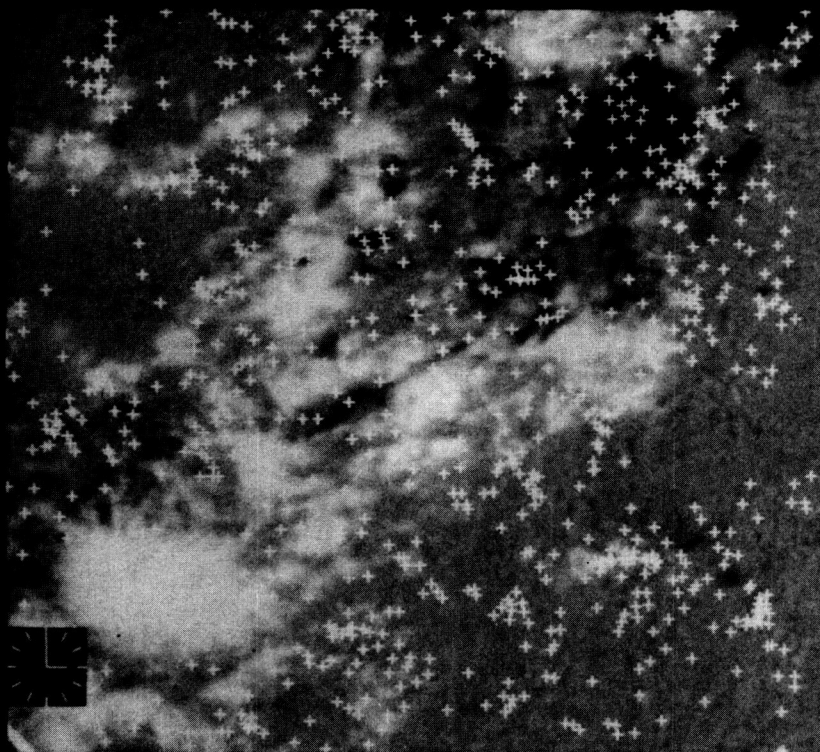
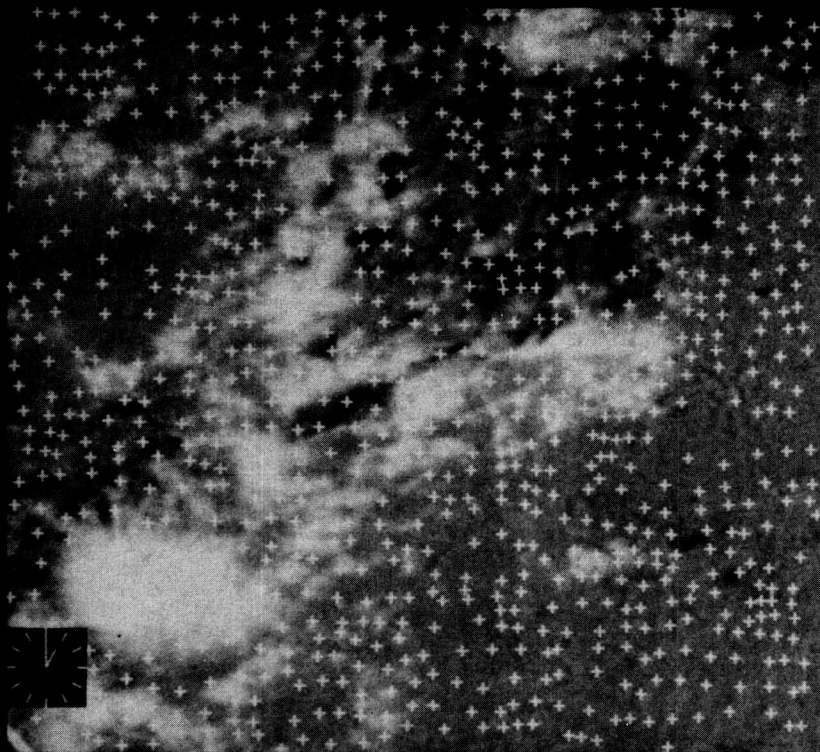


FIG. 4

57

ORIGINAL PAGE IS
OF POOR QUALITY

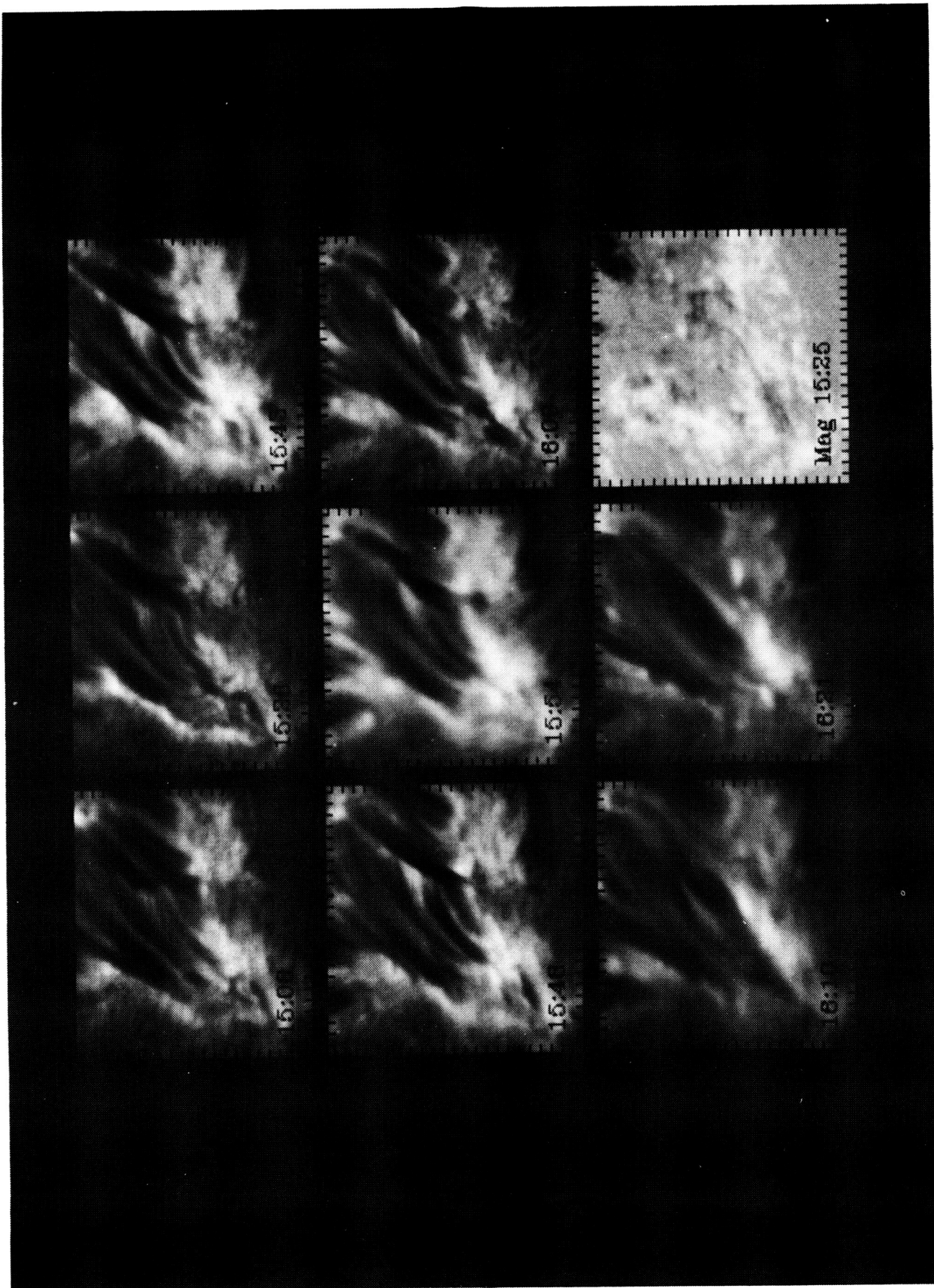
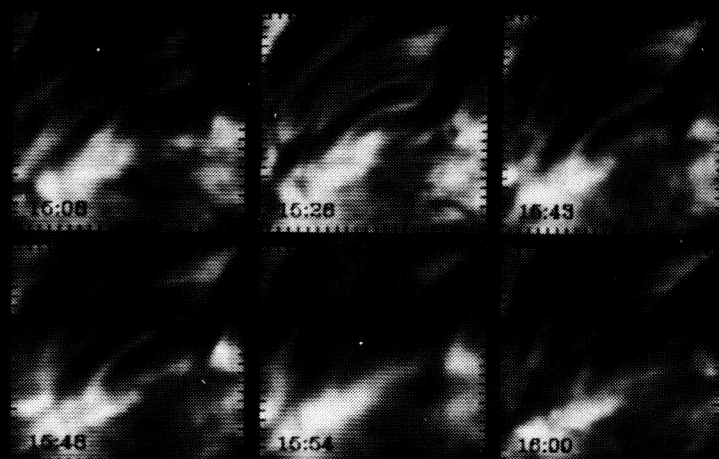
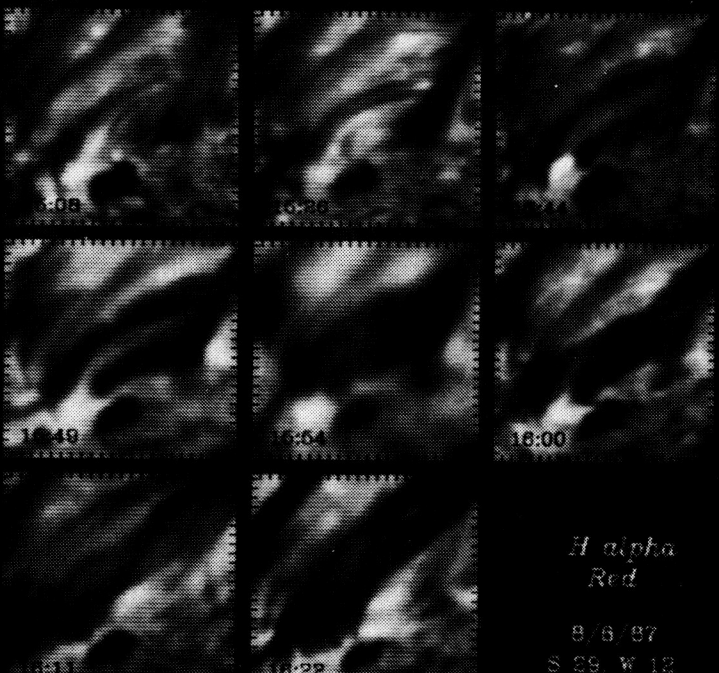


FIG. 5



H alpha
Line center

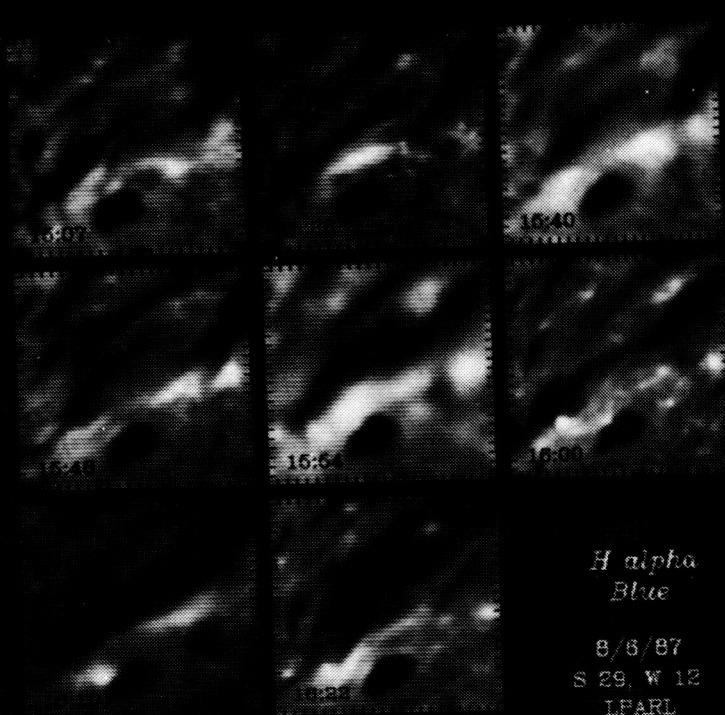
8/6/87
S 29, W 12
IPARL



H alpha
Red

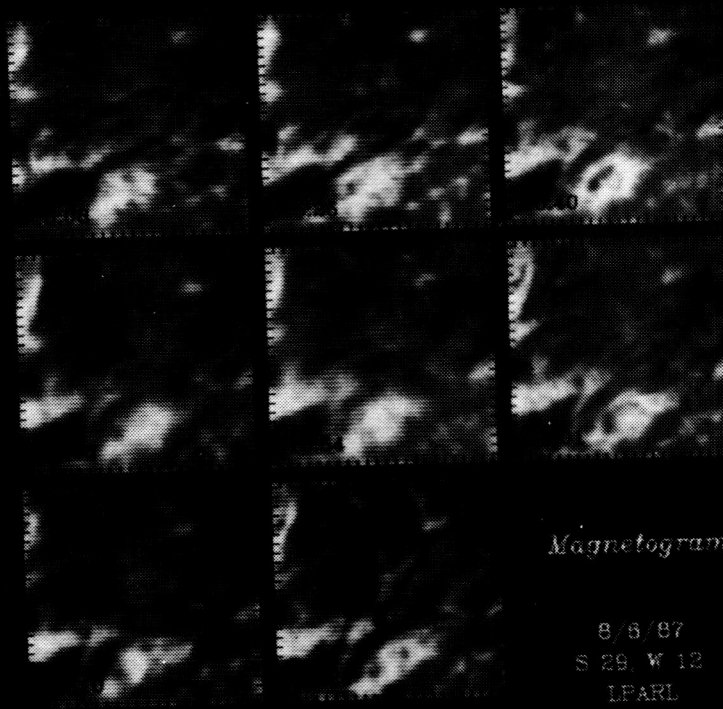
8/6/87
S 29, W 12
IPARL

FIG. 6



*H alpha
Blue*

8/6/87
S 29, W 12
LFARL



Magnetogram

8/6/87
S 29, W 12
LFARL

FIG. 7

FLARE ONSET AT SITES OF MAXIMUM MAGNETIC SHEAR

M. J. Hagyard¹ and J. B. Smith, Jr.²

NASA/Marshall Space Flight Center¹
NOAA Space Environment Laboratory²

Observations of the transverse component of the Sun's photospheric magnetic field obtained with the MSFC vector magnetograph show us where the fields are nonpotential. We have studied the correlation between locations of nonpotential fields and sites of flare onset for four different active regions. On the top panels (3-12) of this poster display we outline the details of this study for active region AR 4711 (February 1986). On the lower panels (13-20) we present results of similar studies for three other regions: AR 2372 (April 1980), AR 2776 (November 1980), and AR 4474 (April 1984). For all four regions we show that flares initiate at sites on the magnetic neutral line where the local field deviates the most from a potential field.

This result is consistent with the concept that the source of the flare energy is the free energy stored in nonpotential fields. However, it has been the advent of measurements of the transverse field that has allowed a quantitative evaluation of nonpotential fields. The line-of-sight component of the photospheric field determines the potential field structure but it gives no indication where the field has been stressed into nonpotential configurations. By comparing the observed and potential fields' transverse components, the nonpotential characteristics of the field can be determined. To obtain a quantitative measure of nonpotentiability, we use the parameter angular shear, $\Delta\Phi$, the difference between the directions of the observed and potential transverse fields. In this study we evaluate $\Delta\Phi$ and the transverse field strength B_r along the neutral line, starting with AR 4711 in panels 3 & 4.



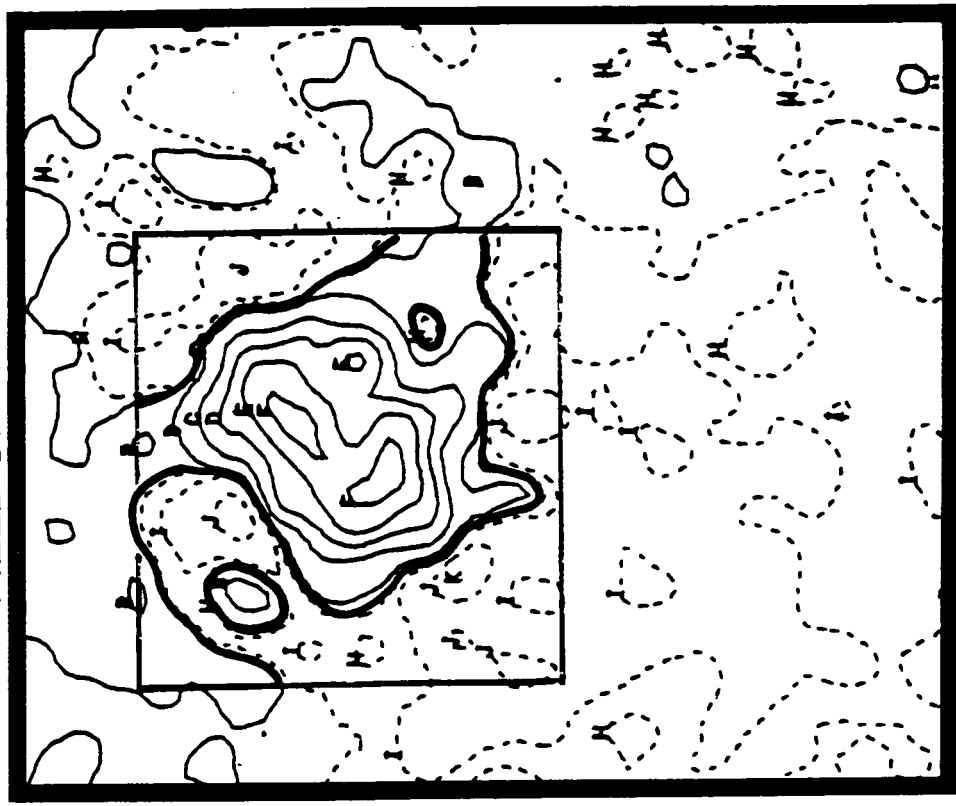
AR 4711 (PREFLARE), FEB. 3, 1986



AR 4711, (PREFLARE) H- α , FEBRUARY 03/1986 U.T. STRUCTURE AND CONFIGURATION SHOULD BE COMPARED WITH THE LONGITUDINAL, (BL) MAGNETOCRAMP IN FIGURE 4, WHERE THE AREA OF ENLARGEMENT FOR ANALYSIS (IN FIGURE 10) IS OUTLINED, AND THE BL NEUTRAL LINE IS SHOWN. (Ha is courtesy Big Bear Solar Observatory.)

LINE- OF- SIGHT MAGNETIC FIELD OF
AR 4711, FEB. 03, 1986
1642 UT

FIELD OF VIEW = 5.6×5.6 ARC MIN



CONTOURS

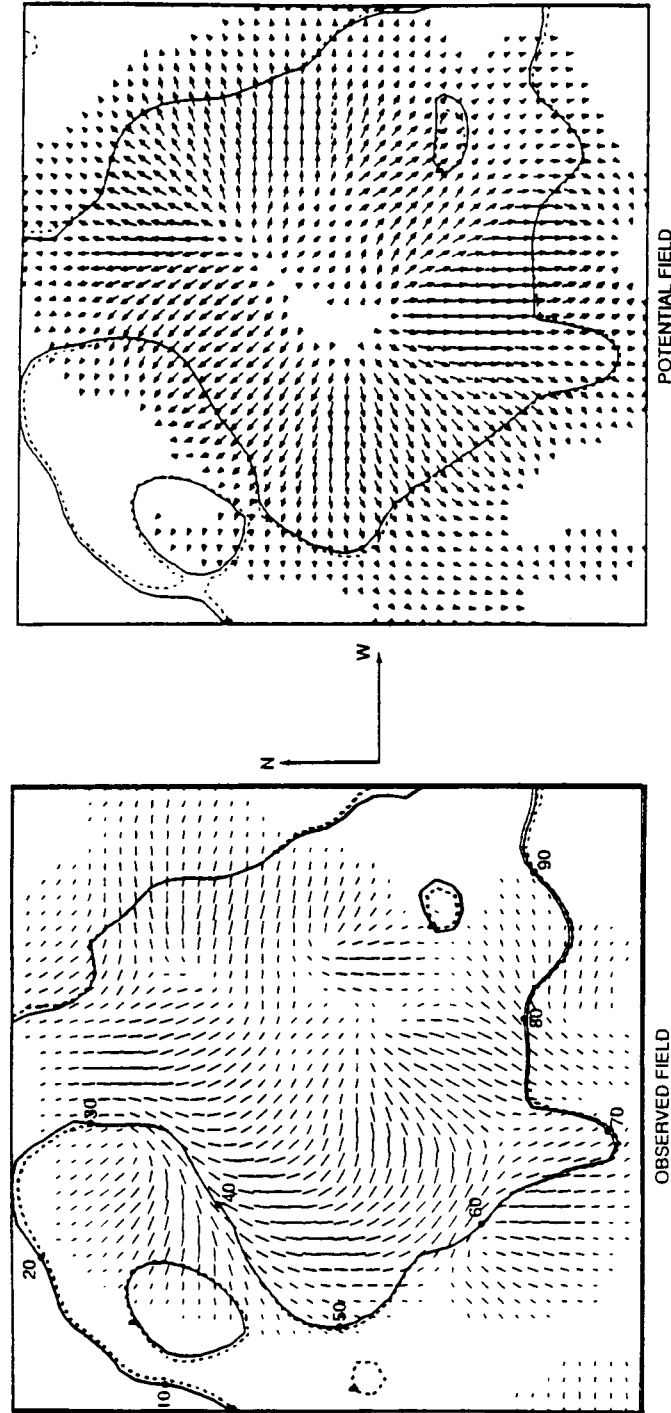
±10 G
100
500
1000
1500
2000
2250

SOLID (DASHED) CONTOURS
REPRESENT POSITIVE
(NEGATIVE) POLARITIES. THE
DARK CONTOUR OUTLINES THE
MAGNETIC NEUTRAL LINE
SEPARATING POSITIVE AND
NEGATIVE POLARITIES.
THE BOX OUTLINES THE AREA
(110×110 ARC SEC) THAT IS
ENLARGED AND SHOWN IN THE
DISPLAYS OF THE OBSERVED AND
POTENTIAL TRANSVERSE
FIELDS (PANELS 5 & 6).

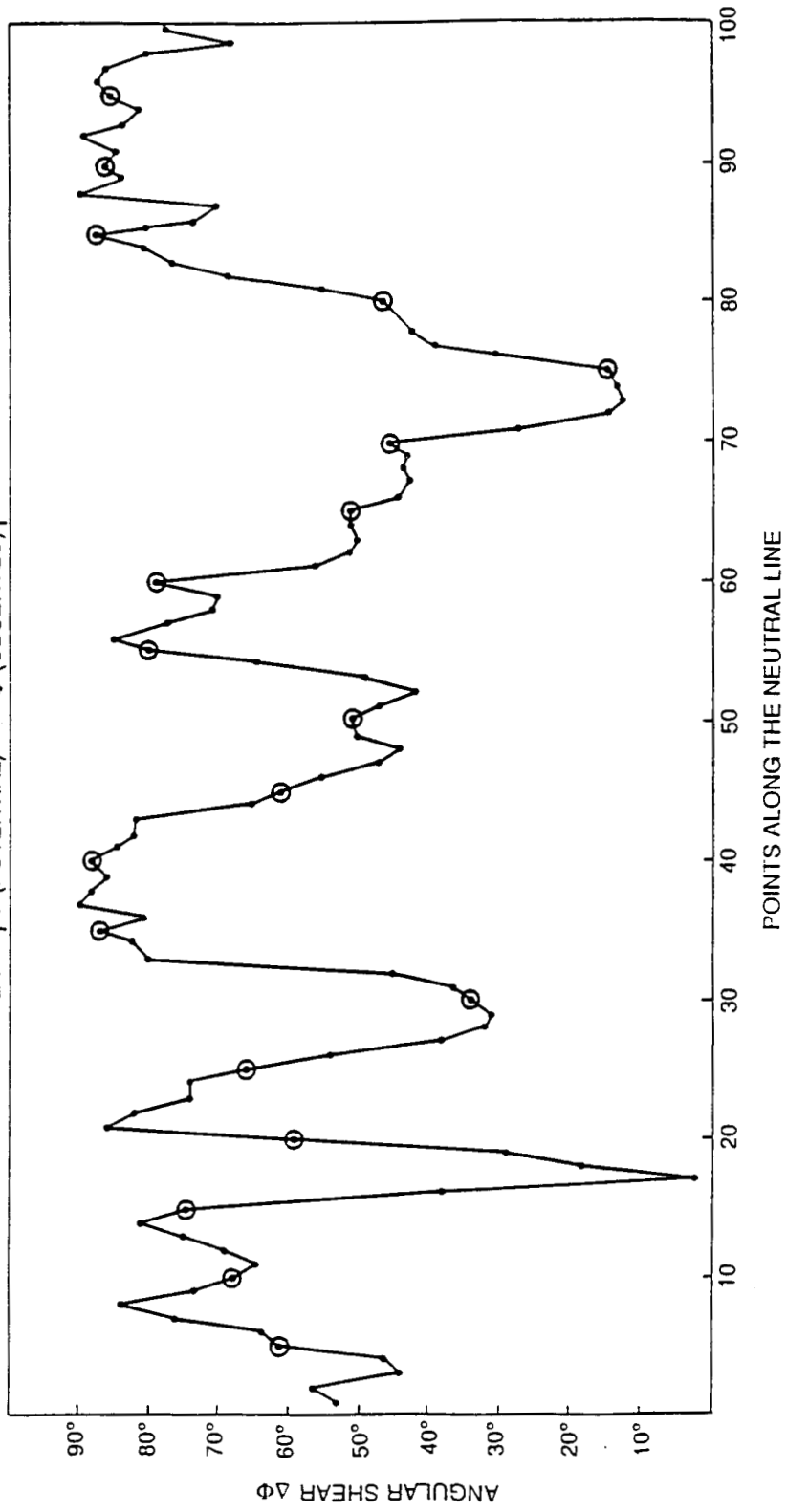
Here we show the transverse components of the observed and potential magnetic fields over the area of the box in panel 4. The length and direction of the line segments indicate the strength (scaled from 250 to 1000 G) and orientation of the transverse field. The magnetic neutral line has been superposed for reference.

Note how a comparison of these two transverse components shows directly where the photospheric field is stressed, i.e., nonpotential. We define angular shear $\Delta\Phi$ as the difference between the orientations of the potential and observed transverse components. In the next two panels (7 & 8) we plot $|\Delta\Phi|$ and the observed transverse intensity B_r for points along the neutral line. These points are located on the overlay for reference.

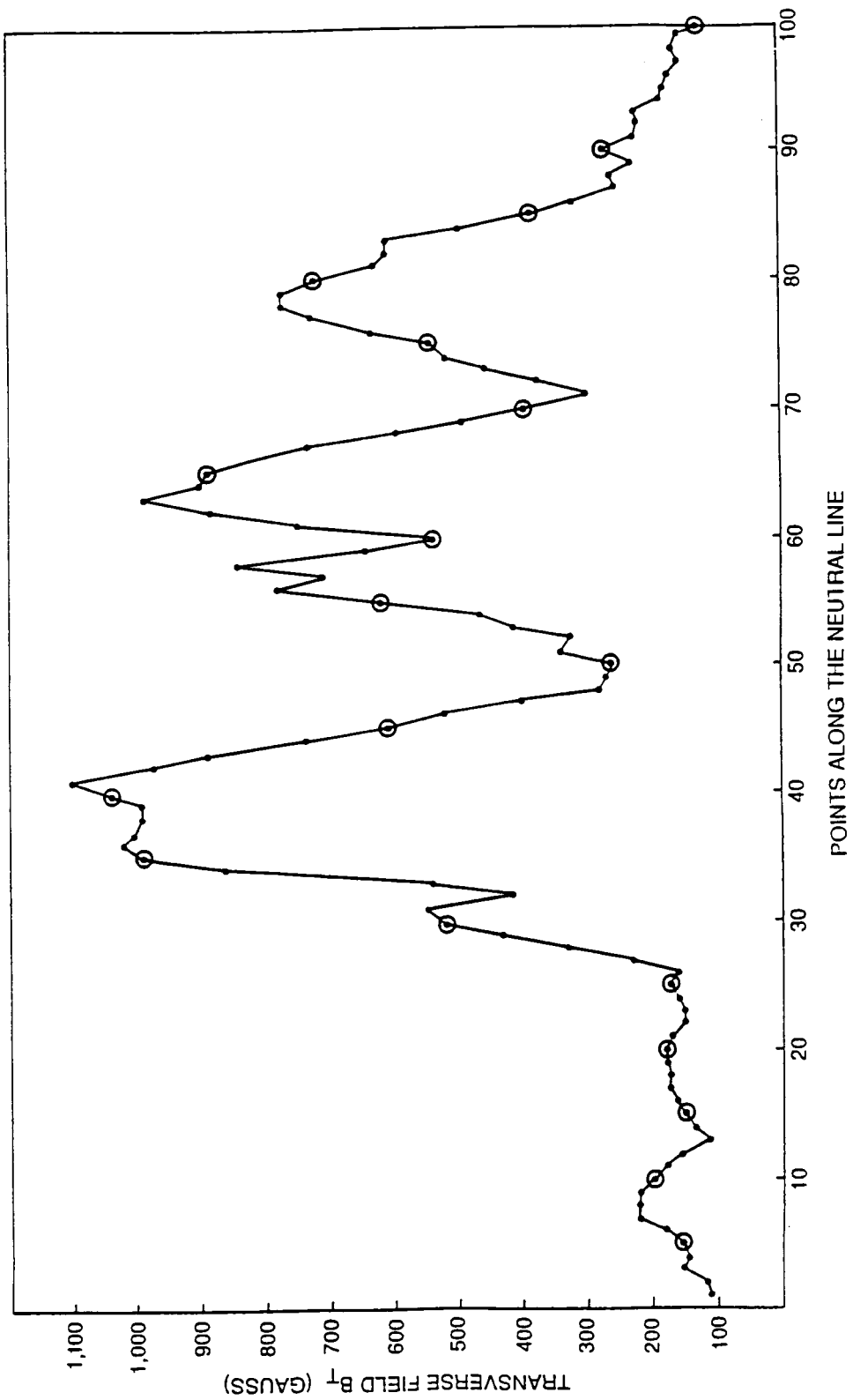
AR 4711
TRANSVERSE MAGNETIC FIELD
1642 UT FEBRUARY 3, 1986



ANGULAR SHEAR $\Delta\phi$ ALONG THE NEUTRAL LINE
 AR 4711
 $\Delta\phi = |\Phi(\text{POTENTIAL}) - \Phi(\text{OBSERVED})|$



OBSERVED TRANSVERSE MAGNETIC FIELD B_T
ALONG THE NEUTRAL LINE
AR 4711



These graphs of $\Delta\Phi$ and B_r at points along the neutral line indicate that both parameters rise to large values at various points. The “shear” $\Delta\Phi$ is $\geq 80^\circ$ over several intervals of points while $B_r \geq 550$ G (the half-maximum value) over three different intervals. However, the highest values of shear - $> 85^\circ$ - coincide with strong - > 1000 G - fields only along the interval 33 - 43 (points). All this comes together when we see where the flare starts, shown in panel 10. The overlay shows that flare onset occurs along this particular interval, where the shear is $\geq 85^\circ$ and the field is ≥ 1000 G.

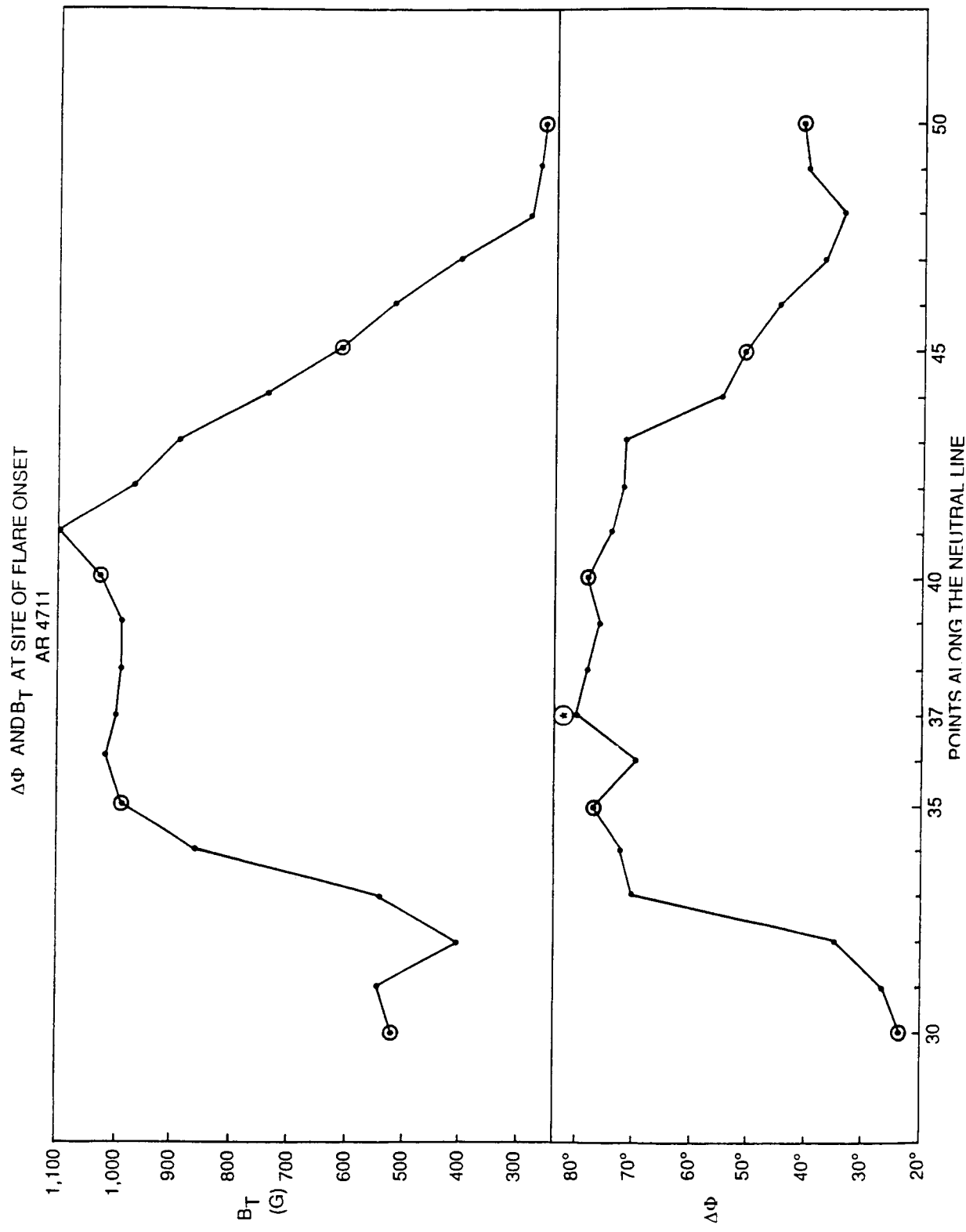
In panel 11, $\Delta\Phi$ and B_r are shown along the interval 30 - 50 (points). Initial flare points shown in panel 10 are seen to bracket the area of point 37 where $\Delta\Phi$ attains its (local) maximum value. \Rightarrow

AR 4711 (FLARE ONSET & BV), FEB. 1986



ORIGINAL PAGE IS
OF POOR QUALITY

H- α AT NEAR FLARE ONSET TIME (03/2037 UT) SCALED TO THE VECTOR MAGNETOGRAM; TRANSPARENCY OVERLAY IS THE TRANSVERSE MAGNETIC FIELD (B_T) AZIMUTH VECTOR; TORS AND THE BL NEUTRAL LINE. NUMBERS IDENTIFY ANALYSIS LOCATIONS; FLARE ONSET KERNELS (OUTLINED IN FIELD) INDICATE CONNECTING LOOPS CROSS BL NEUTRAL LINE NEAR MAXIMUM STRENGTH (POINT 37); COMPARE WITH FIGURE 11. (H- α courtesy Big Bear Solar Observatory.)

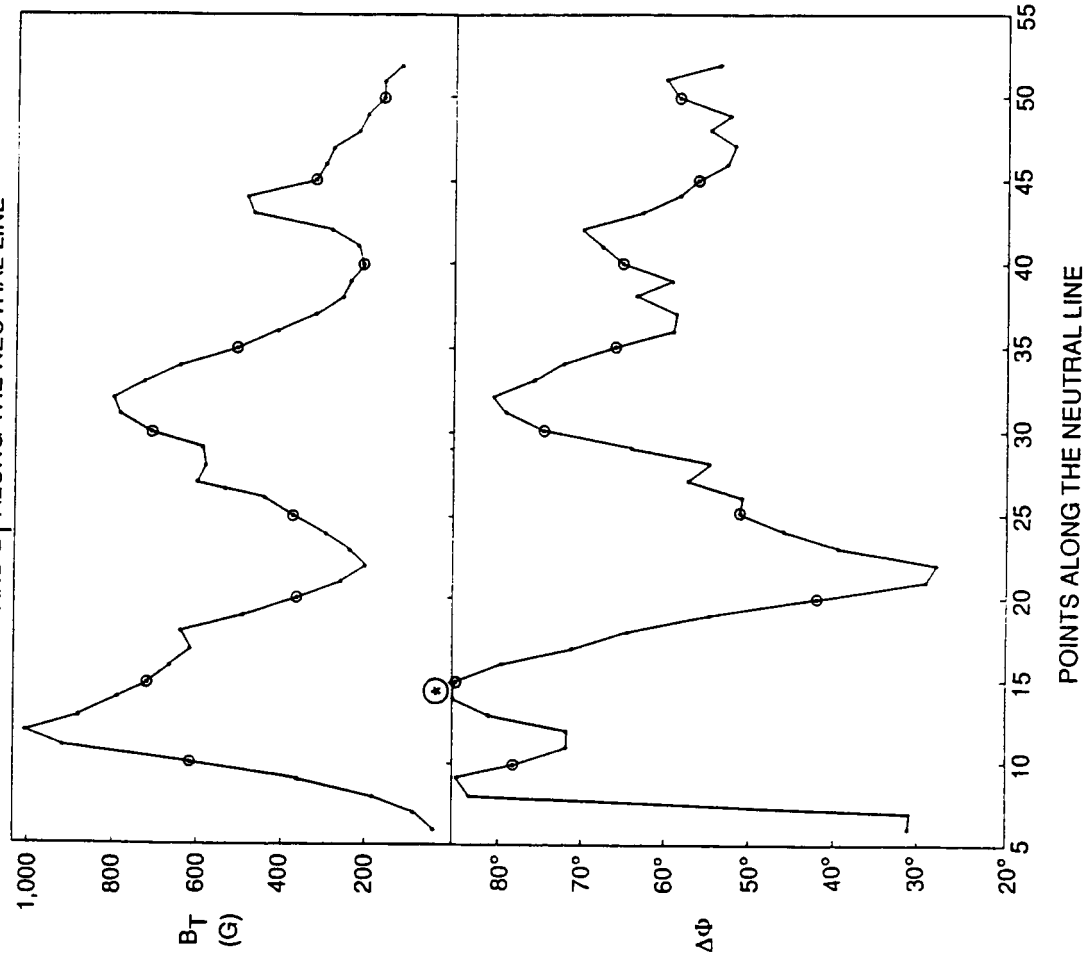


The results of this analysis of AR 4711 show that flare onset occurred at the location where the field was the most “nonpotential,” i.e., where there was a coincidence of the area of maximum shear and strong fields. Also, the initial flare brightenings occurred on either side of the neutral line at the location of maximum angular shear.

We have done the same analysis on three other active regions and found similar results. In panel 13 we show the variations of $\Delta\Phi$ and B_r along the neutral line of AR 2372, followed by an H-alpha image in panel 14 that locates the initial flare points. Similar figures follow for AR 2776 (panels 15 & 16) and AR 4474 (panels 17 & 18).
↓

AR 2372 APRIL 6, 1980

$\Delta\Phi$ AND B_T ALONG THE NEUTRAL LINE



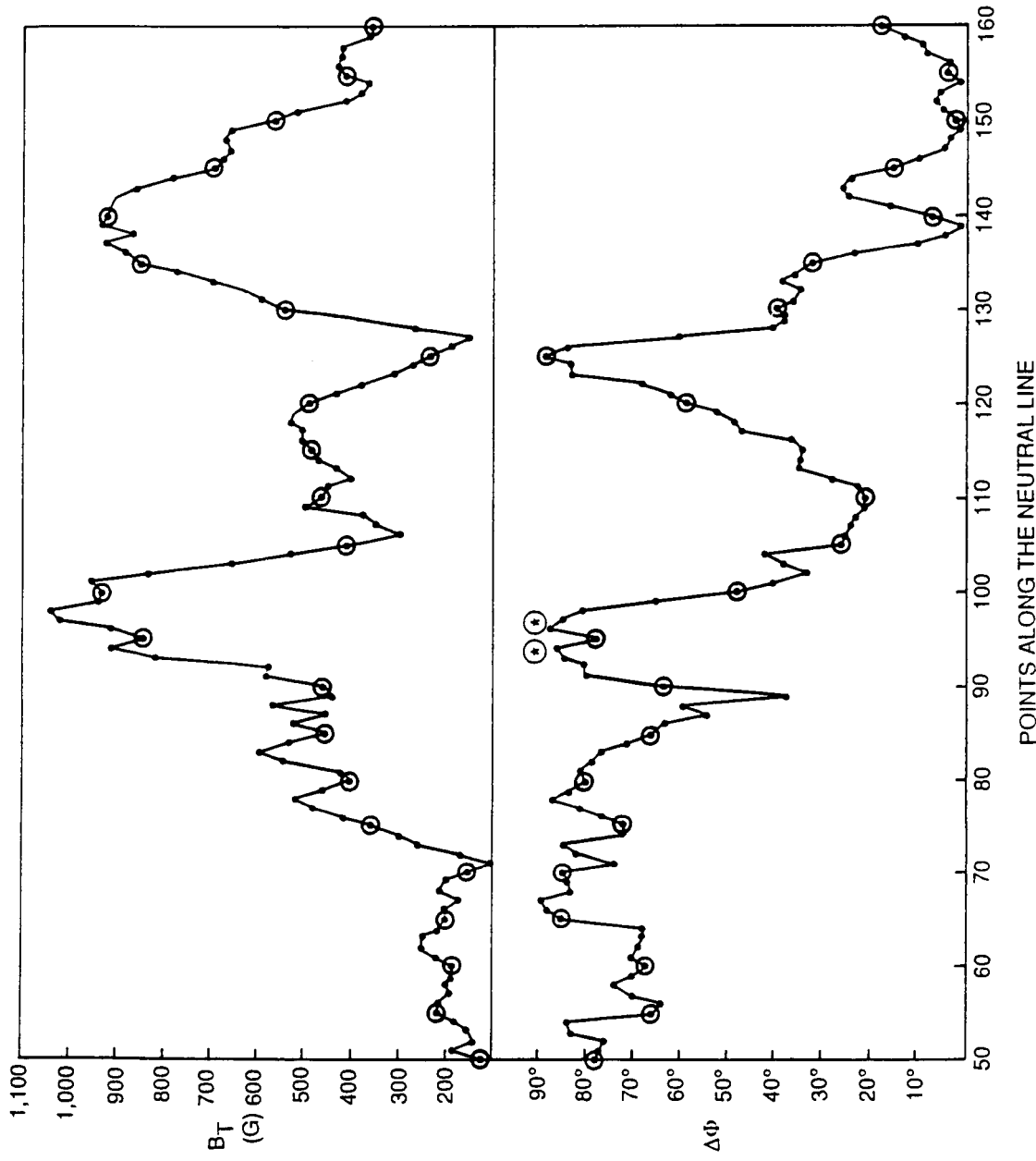
AR 2372 (EARLY FLARE), APRIL 1980



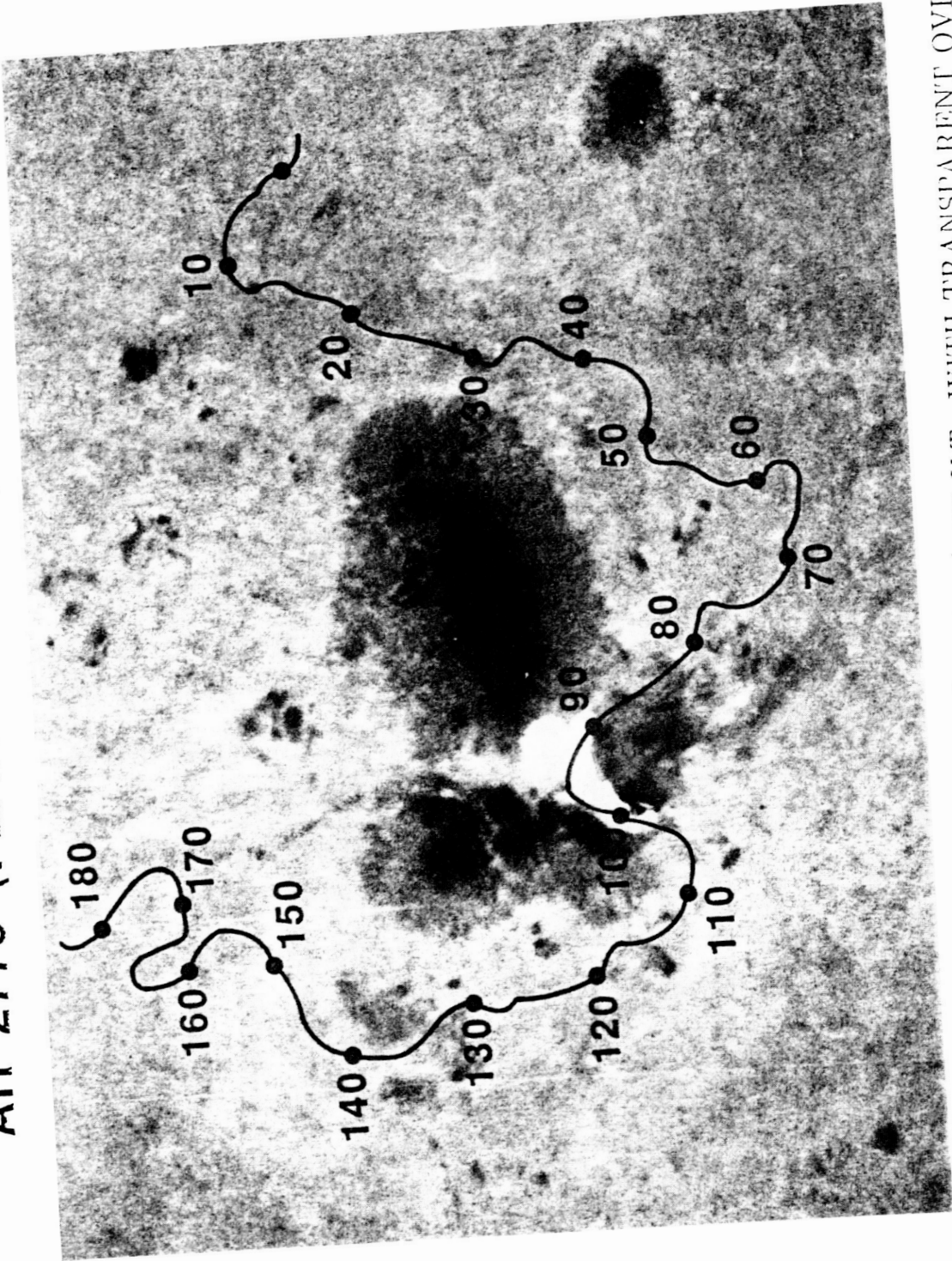
ORIGINAL PAGE IS
OF POOR QUALITY

AR2372, H_α (+.5Å), PRE-MAXIMUM (06/1423 U.T.), BUT NOT NEAR ONSET TIME. TRANSPARENT OVERLAY IS PHOTOSHIFTED BI, NEUTRAL LINE, WITH NUMBERS INDICATING ANALYSIS LOCATIONS. ONSET LOCATIONS (RED Xs) CONNECT ACROSS AREA OF MAXIMUM SHEAR (POINTS 14-15, FIGURE 13), AND WHERE STRONG TRANSVERSE FIELD IS ALSO OBSERVED. H-_α courtesy U.S.N.A./Air Weather Service (SOON).

AR 2776 NOVEMBER 5, 1980
 $\Delta\Phi$ AND B_T ALONG THE NEUTRAL LINE



AR 2776 (FLARE ONSET), NOV. 1980

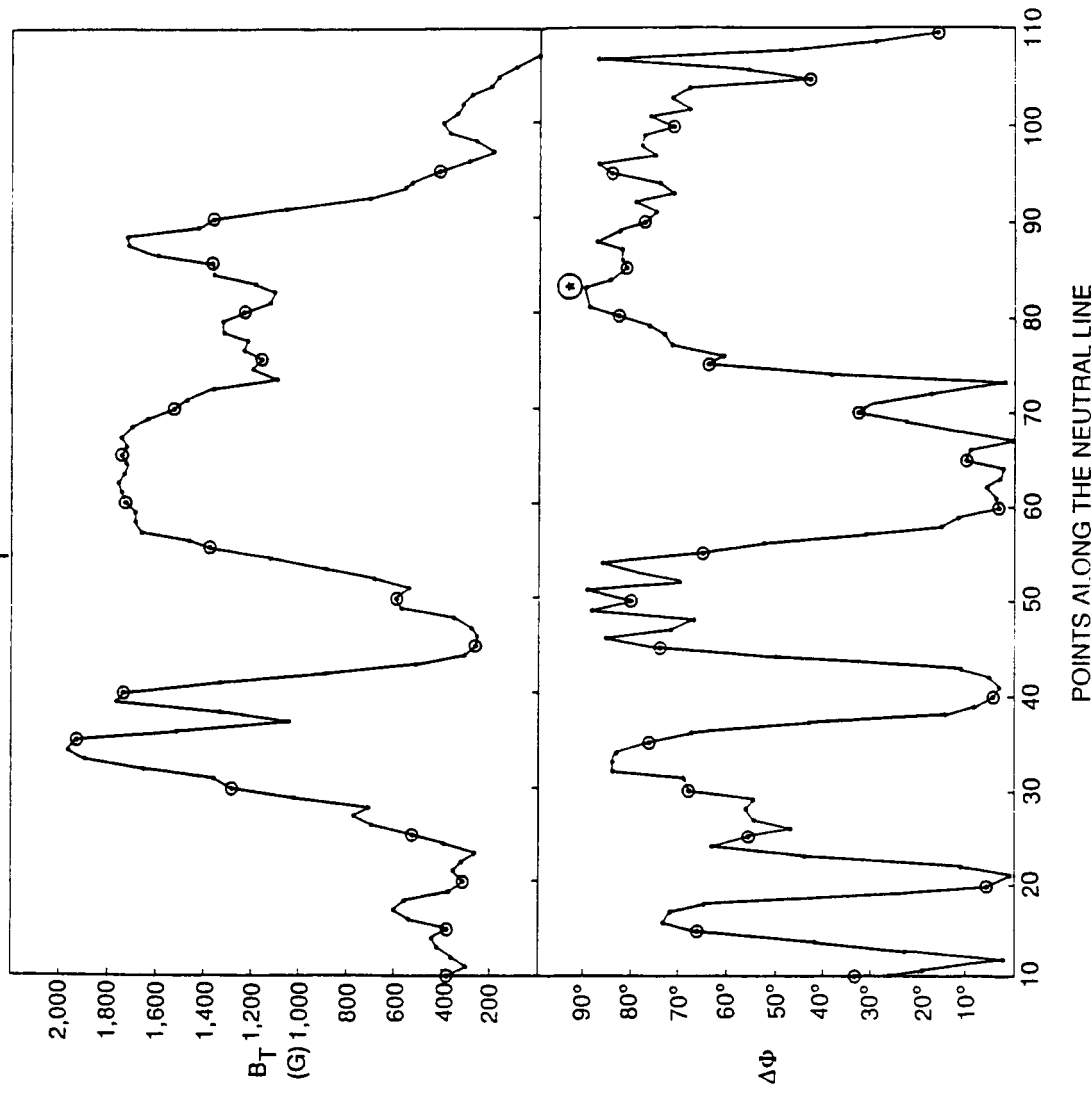


ORIGINAL PAGE IS
76 OF POOR QUALITY

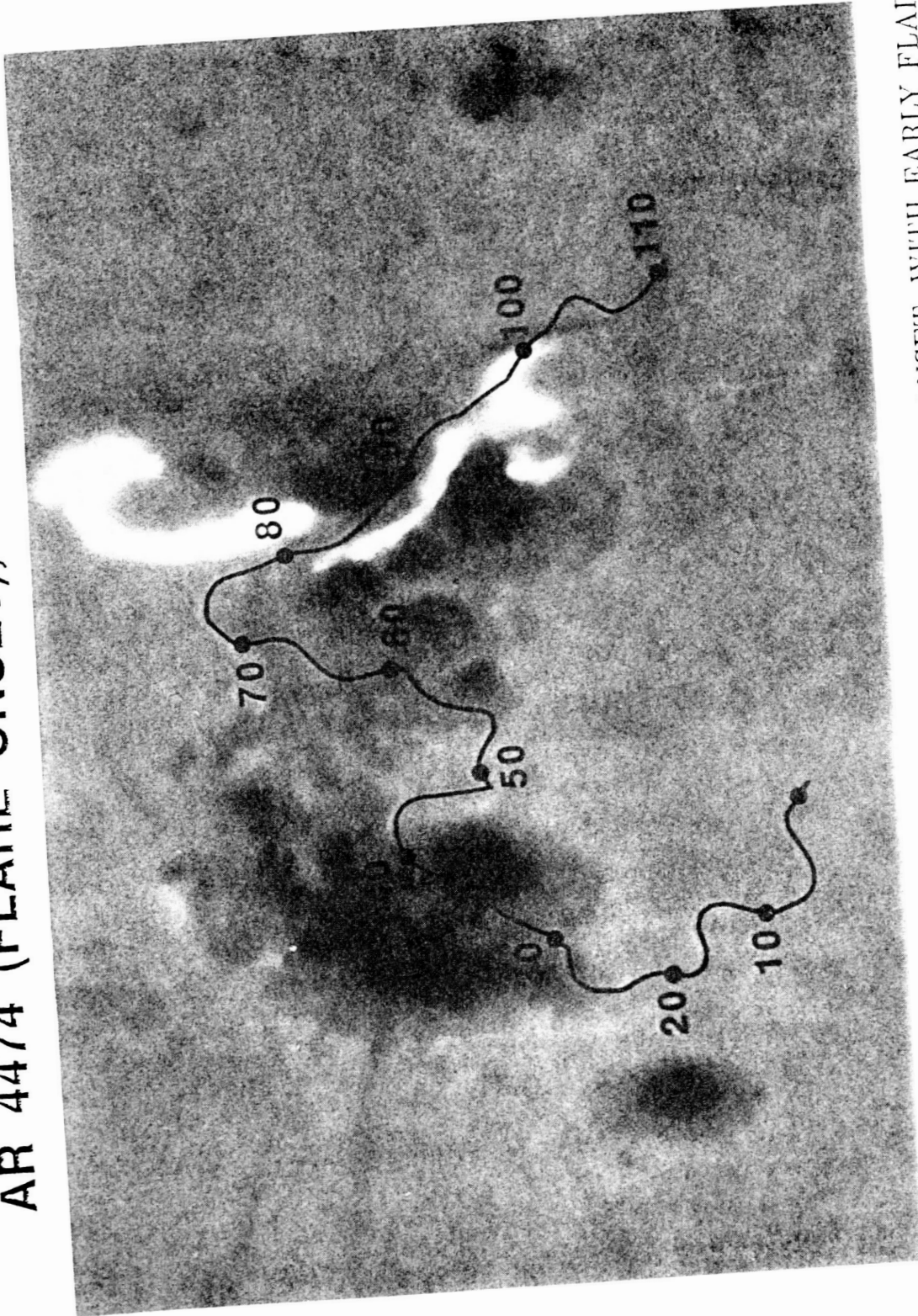
FLARE ONSET IN OFF-BAND H- α (1.07\AA) AT 05/2227 U.T., WITH TRANSPARENCE OVERLAY OF THE (PHOTOSPHERIC) BL NEUTRAL LINE AND NUMBERS INDICATING ANALYSIS LOCATIONS. OPPOSITE POLARITY FLARE ONSET KERNELS CONNECT ACROSS NEUTRAL LINE NEAR LOCATION OF MAXIMUM SHFAR (POINTS 94-96), AND WHERE STRONG BT OBSERVED (COMPARE WITH FIGURE 15). (H- α courtesy U.S. Air Weather Service/SOON.)

AF 4474 APRIL 24 1984

$\Delta\Phi$ AND B_T ALONG THE NEUTRAL



AR 4474 (FLARE ONSET), APRIL 24, 1984



ORIGINAL PAGE IS
OF POOR QUALITY

OFF BAND H- α (\pm 0.7 Å) AT 24/2350:30 U.T., NEAR FLARE ONSET, WITH EARLY FLARE RIBBONS; TRANSPARENT OVERLAY OF BL NEUTRAL LINE, WITH NUMBERS SHOWING ANALYSIS LOCATIONS OF FIGURE 16. LOCATION OF FLARE ELEMENTS INDICATES MAXIMUM SHEAR (POINTS 80-90), AND WHERE STRONG BT CONNECTION ACROSS ZONE OF MAXIMUM SHEAR (POINT 110). H- α is courtesy USAF/Air Weather Service (SOON). IS OBSERVED. COMPARE WITH FIGURE 17.

RESULTS OF THESE 3 ANALYSES:

AR 2372

The flare initiated in the area where there was a coincidence of intervals of the strongest shear (85°) and strongest fields (1000 G).

AR 2776

There were two areas of maximum shear (90°) but weak fields (< 200 G) and one area of strong field (> 900 G) but weak shear ($< 40^\circ$); none of these areas flared. The flare began where there was a coincidence of strong shear ($> 80^\circ$) and strong fields (> 900 G).

AR 4474

The strongest field (1900 G) coincided with a small area of strong shear (84°); this area was the site of a flare three days later. The 3B/X15 flare erupted at the extended area of strong shear ($> 80^\circ$) and strong fields (> 1100 G) with a maximum shear (90°) occurring at three points.



CONCLUSIONS

The results of this study suggest that flares are likely to erupt where the shear is $\geq 85^\circ$, the field is ≥ 1000 G, and there is strong shear ($\geq 80^\circ$) extending over a length ≥ 8000 km (4 points).

IMPLICATIONS FOR MAX '91 FLARE RESEARCH

We have seen that it is measurements of the transverse field that indicate probable flare sites, i.e., where the field deviates strongly from a potential state. These measurements are essential for any Max '91 flare research relative to flare buildup and onset. Thus it is crucial to have vector magnetographs operating during Max '91 and providing these data for mission planning and basic research. These instruments should have the highest possible polarimetric sensitivity, high temporal and spatial resolutions, and fields of view covering the areas of typical active regions.

AN IMAGING VECTOR MAGNETOGRAPH FOR THE NEXT SOLAR MAXIMUM

Richard C. Canfield and Donald L. Mickey
Institute for Astronomy, University of Hawaii
Honolulu, Hawaii 96822

ABSTRACT.

Measurements of the vector magnetic field in the sun's atmosphere with high spatial and temporal resolution over a large field of view are critical to understanding the nature and evolution of currents in active regions. Such measurements, when combined with the thermal and nonthermal X-ray images from the upcoming Solar-A mission, will reveal the large-scale relationship between these currents and sites of heating and particle acceleration in flaring coronal magnetic flux tubes.

We describe the conceptual design of a new imaging vector magnetograph that combines a modest solar telescope with a rotating quarter-wave plate, an acousto-optical tunable prefilter as a blocker for a servo-controlled Fabry-Perot etalon, CCD cameras, and a rapid digital tape recorder. Its high spatial resolution (1/2 arcsec pixel size) over a large field of view (4 by 5 arcmin) will be sufficient to significantly measure, for the first time, the magnetic energy dissipated in major solar flares. Its millisecond tunability and wide spectral range (5000 - 8000 Å) enable nearly simultaneous vector magnetic field measurements in the gas-pressure-dominated photosphere and magnetically-dominated chromosphere, as well as effective co-alignment with Solar-A's X-ray images.

PERFORMANCE CHARACTERISTICS

- **Spatial resolution:** one arcsec. Detector pixel spacing of approximately 0.5 arcsec over a 4 x 5 arcmin field of view. This high resolution will critically sample the high quality image typical at Mees early in the day.
- **Spectral resolution:** $70 \text{ m}\text{\AA}$ at 6000\AA . This resolution is marginal for the narrowest lines; at least three spectral samples will be required in the simplest cases, and probably quite a few more will be used for the standard program.
- **Spectral range:** $5000 - 6500 \text{ \AA}$. This range includes both photospheric (e.g. Fe I $\lambda 6302$) and chromospheric (e.g. Mg I $\lambda 5173$) lines whose use for vector magnetic field measurement is well understood.
- **Temporal resolution:** A complete magnetogram in a single line in 15 seconds. This resolution is determined primarily by the data recording speed; better resolution can be achieved over a smaller field of view.
- **Sensitivity:** 10 Gauss longitudinal fields and 200 Gauss transverse fields in a few seconds. Simultaneous velocity measurements to 10 m/s. Temporal resolution can be traded for increased sensitivity.
- **Co-alignment:** A simultaneous photospheric white-light image of the full field of view, for precise co-alignment with Solar-A images and Max'91 ground and balloon-borne experiments.

DESIGN FEATURES

- **Telescope:** 20-cm refractor. On-axis, as shown in the Figures 4 and 5. On the spar at Mees Solar Observatory, Haleakala, Maui.
- **Monochromator:** Air-spaced tunable Fabry-Perot, 70mÅ bandpass. Order-sorting using an acousto-optic tunable filter (AOTF) with bandpass of 2 Å, a contrast of 1000:1, a large field of view, rapidly tunable over the full wavelength range.
- **Polarization Modulator:** Rotating quarter-wave plate. The AOTF will double as a beam-splitting analyzer.
- **Detectors:** High-resolution commercial CCD cameras. No mechanical shutter is necessary; turning off the radio-frequency signal to the AOTF turns off the diffracted beams imaged on the cameras. 754 x 488 pixel detector arrays.
- **Data Acquisition:** 68020-based computer in a VME-bus chassis. A minimum modulation sequence consists of a half-rotation of the wave plate, i.e. eight camera reads, which are combined to derive Stokes parameters. Recording on 8mm digital video cassettes.
- **Analysis and Archiving:** Off-line analysis on a Sun workstation. Archival medium is the original 8mm video cassette. Digital optical disk for archiving working datasets. Video disk recorder for time-dependence studies.

Imaging Vector Magnetograph

Modulator Section

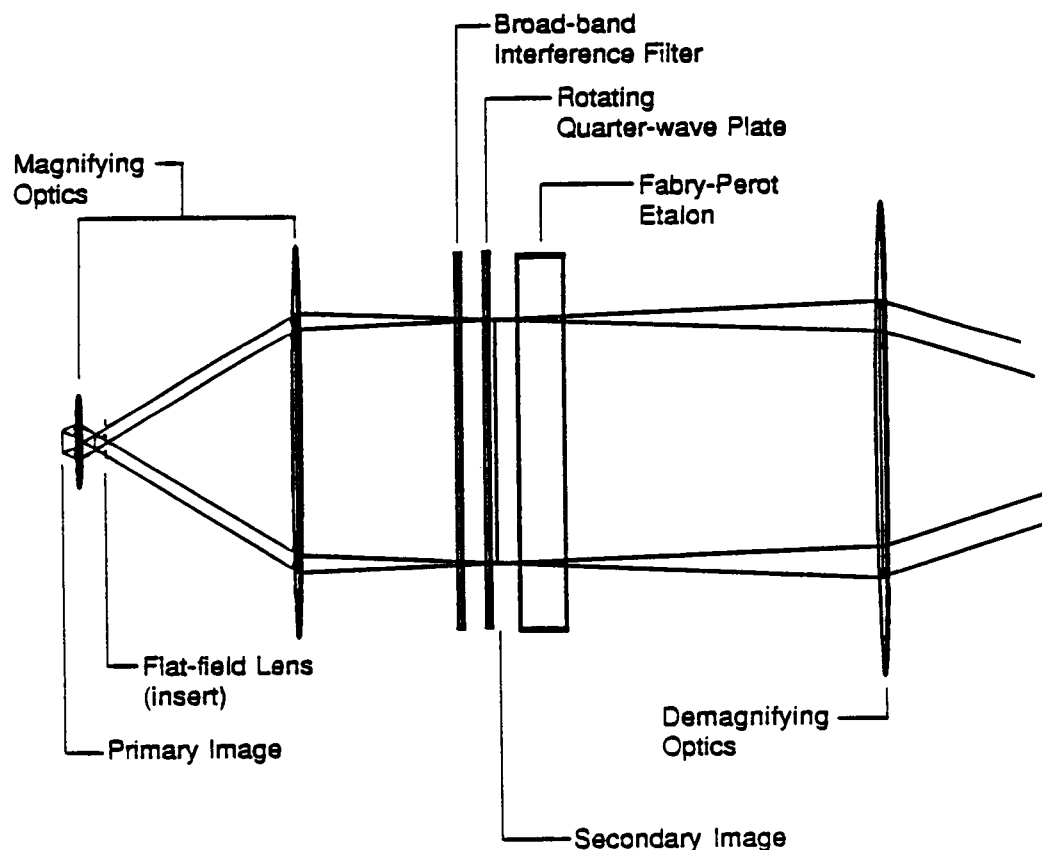


Figure 1. The modulator section of the Imaging Vector Magnetograph. Vertical exaggeration is 5:1.

c - 2

Imaging Vector Magnetograph

Analyzer Section

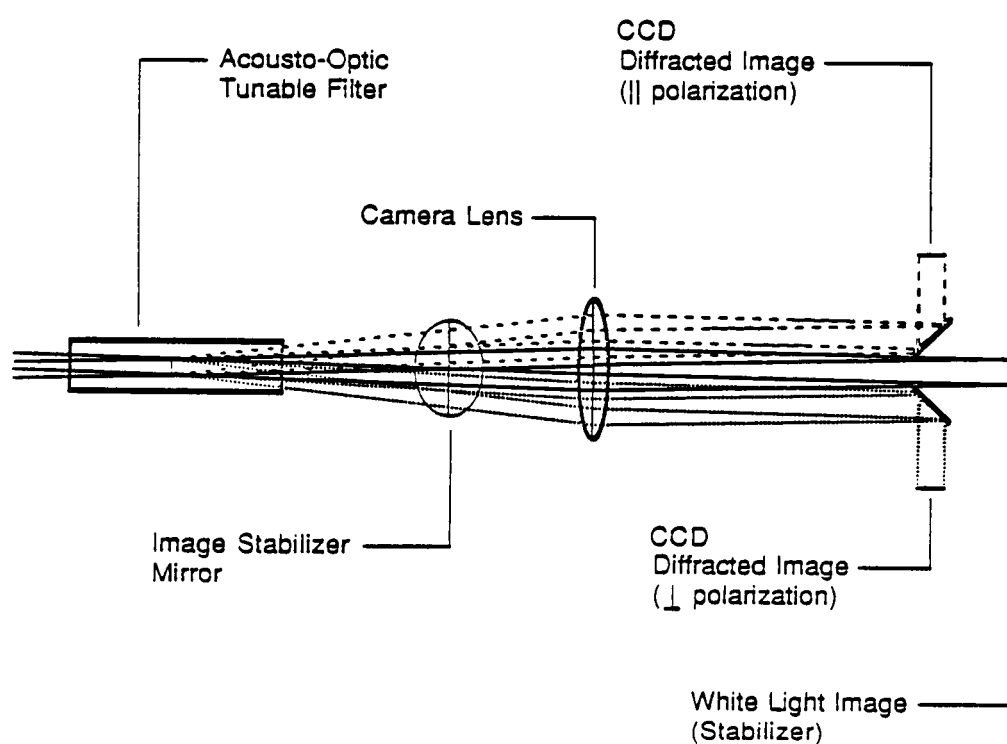


Figure 2. The analyzer section of the Imaging Vector Magnetograph.

Development of the SAMEX Vector Magnetograph at the Marshall Space Flight Center

E. A. West, M. J. Hagyard and G. A. Gary
(NASA/Marshall Space Flight Center)

G. M. Arnett
(BGB Inc., Huntsville, Al.)

Abstract

A breadboard design to prove the operational feasibility of SAMEX Vector Magnetograph is being developed at Marshall Space Flight Center (MSFC). Although the breadboard design will not include all of the elements of the original design concept, critical elements such as the large detector array and the high resolution polarimeter will be important parts of the breadboard design to study the data analysis and compression techniques that will be needed in a SAMEX instrument, to study the calibration techniques for systematic errors in the polarimeter, and to obtain high resolution vector magnetograms during the next solar maximum. Although the SAMEX polarimeter is not optimum for a groundbased patrol instrument, the design concept can be confirmed with groundbased measurements and direct comparisons with the existing MSFC vector magnetograph. The extension of the scientific objectives for this breadboard design is possible if a tunable filter can be acquired.

The SAMEX Vector Magnetograph study was supported by the Air Force Geophysical Laboratory through its Solar Research Branch of the Space Physics Division. The development of the SAMEX detector system is being supported by a NASA Small Business Innovative Research grant to BGB, Inc., Huntsville, Alabama.

Scientific Objectives of the SAMEX Vector Magnetograph

- + To observe the formation and configuration of non-potential fields in photospheric active regions
- + To quantify the non-potential characteristics of these fields (e.g., angular shear, electric currents) in flaring and non-flaring regions
- + To quantify the free magnetic energy and the force-free nature of active-region fields as they develop and evolve
- + To determine what factors lead to the destabilization of the fields and the eruption of flares

Instrumental requirements to meet Scientific Objectives

- + Temporal resolution of a few minutes
- + Field of View to contain a typical active region
- + Spatial resolution of at least $0.5''$
- + Polarization resolution of at least $10E-4$
- + Spectral resolution of approximately $1/8$ Angstrom

ORIGINAL PAGE IS
OF POOR QUALITY

DESIGN RELATIONSHIPS

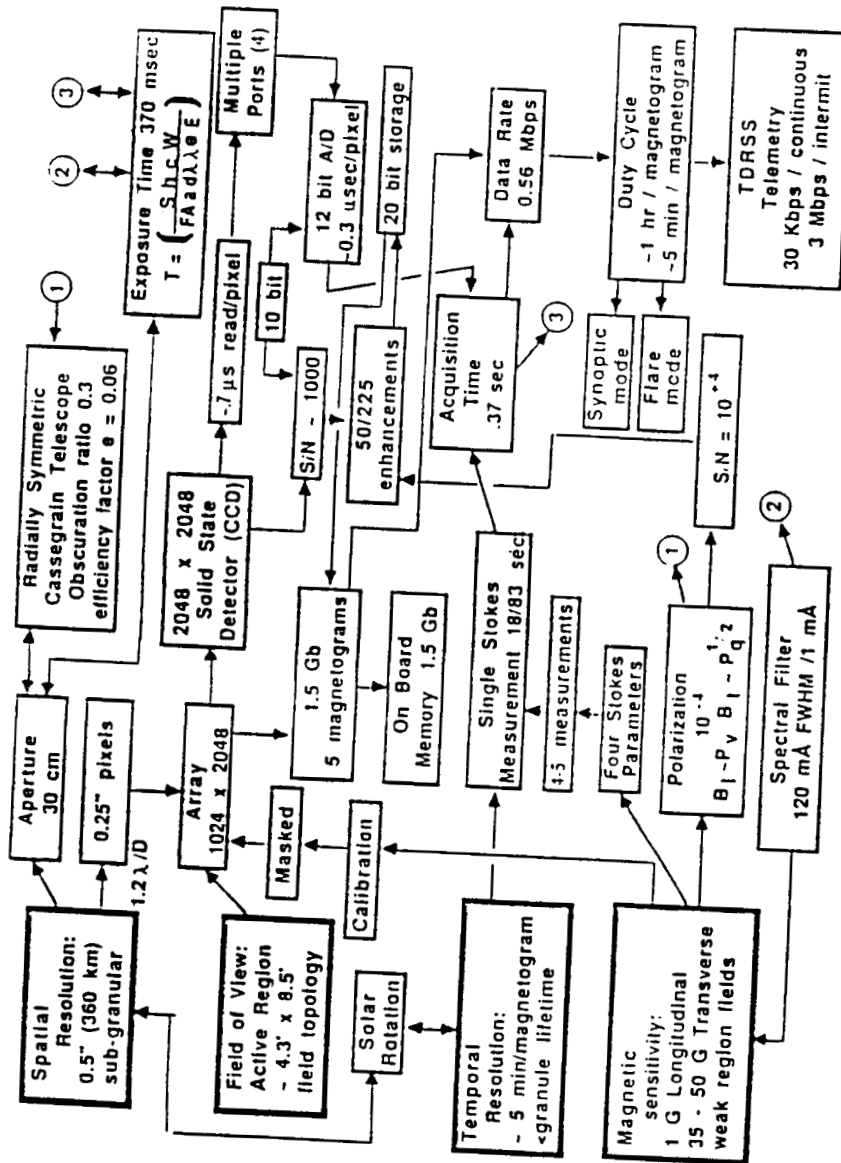


Figure 11. The overall interrelations of the SAMEX magnetograph requirements. This diagram shows how the design specifications for spatial resolution, field of view, temporal resolution, and magnetic sensitivity are interrelated with each other and produce requirements on the magnetograph instrument, onboard computers, and spacecraft systems. To satisfy most of these requirements in an optimum sense requires many different trade-offs. The details of these relationships are described in the text.

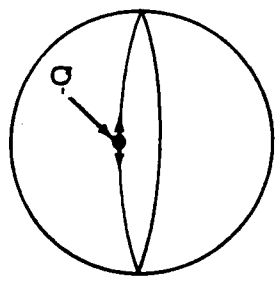
5-161-6-2C

Reasons for selecting a rotating polarizer as the active element in the polarimeter

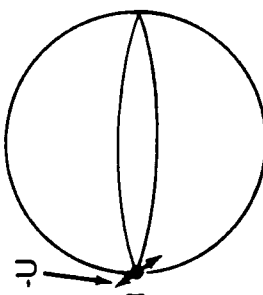
- + The transverse field (linear polarization) is more difficult to measure (the longitudinal field is related to the circular polarization), therefore the polarimeter should be optimized for the linear polarization measurement.
- + The removal of retarders in the linear polarization measurement eliminates circular cross talk (which is the stronger signal) and improves the polarization resolution.
- + Using redundant measurements, systematic errors in the remaining retarders (the rotating quarterwave plate following the analyzer and the fixed quarterwave used to measure the circular polarization) can be corrected for.

Table 1. Sequence of measurements using a rotating polarimeter and fixed quarterwave plate

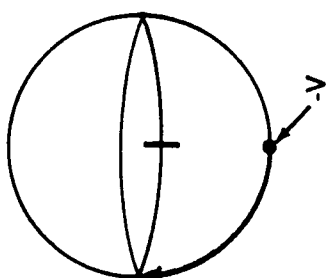
Angle of polarizer	Intensity measurement	
	Wave plate out	Wave plate in
0°	$I + Q$	$I + Q$
45°	$I + U$	$I + V$
90°	$I - Q$	$I - Q$
135°	$I - U$	$I - V$
180°	$I + Q$	$I + Q$
225°	$I + U$	$I + V$
270°	$I - Q$	$I - Q$
315°	$I - U$	$I - V$



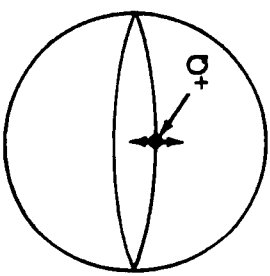
I-Q
ANALYZER
@ 90°



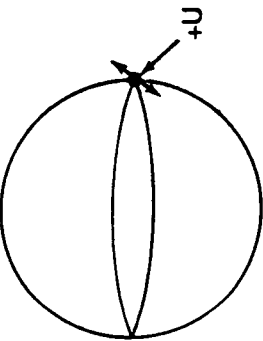
I-U
ANALYZER
@ -45°



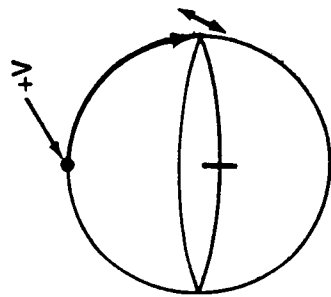
I-V
1/4 PLATE @ 0°
ANALYZER
@ -45°



I+Q
ANALYZER
@ 0°

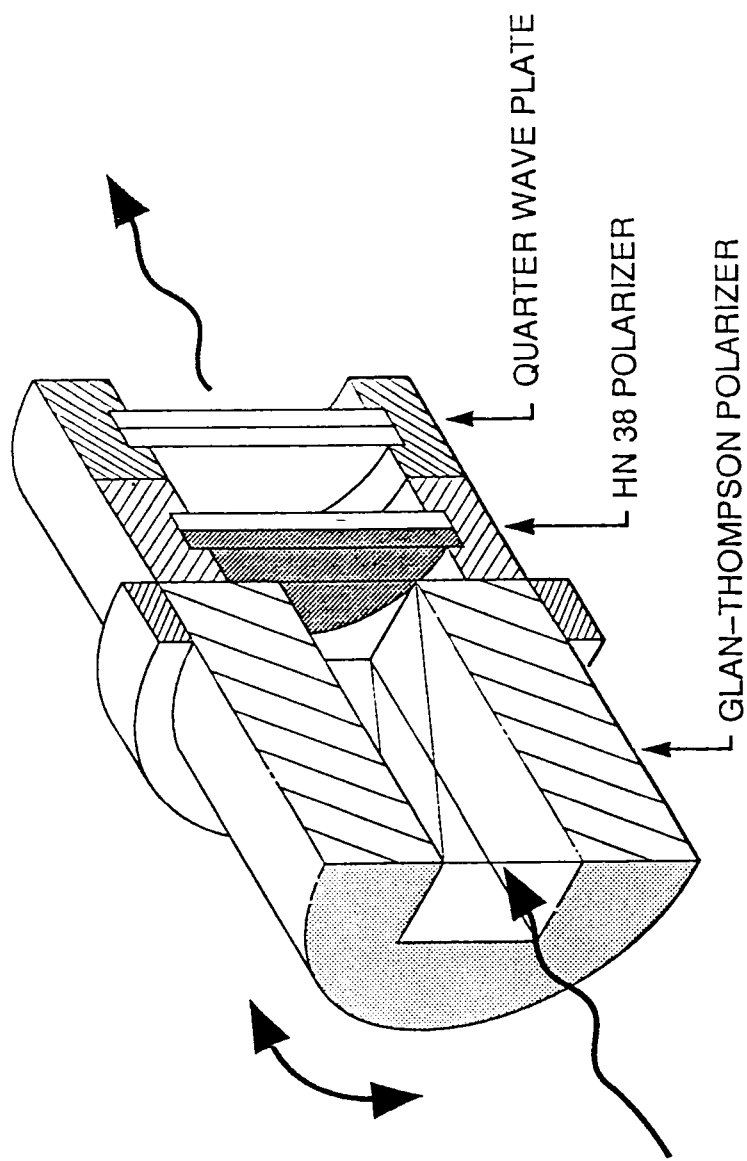


I+U
ANALYZER
@ 45°

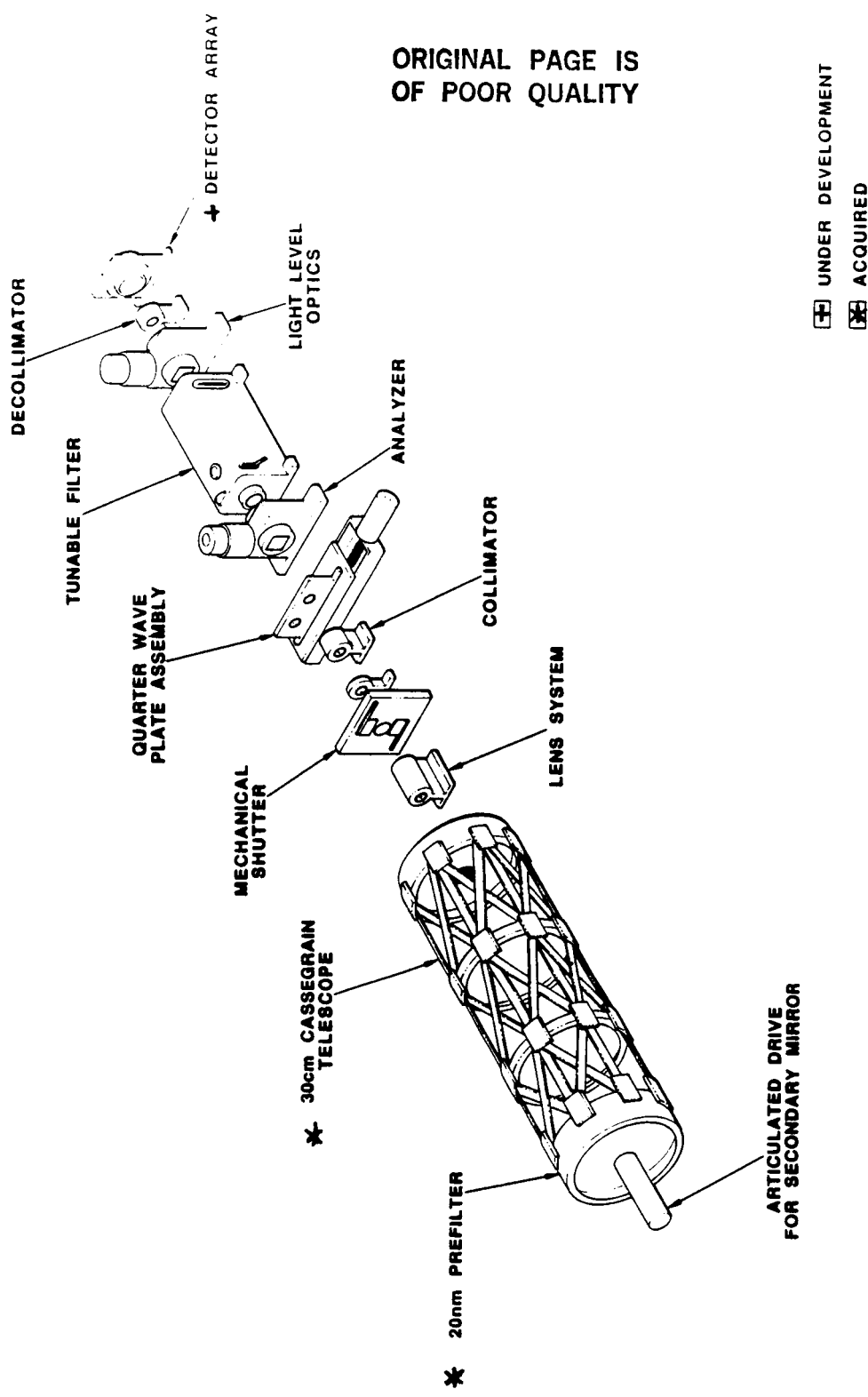


I+V
1/4 PLATE @ 0°
ANALYZER
@ 45°

Rotating Analyzer



THE SYSTEM CONFIGURATION FOR THE SOLAR VECTOR MAGNETOGRAPH

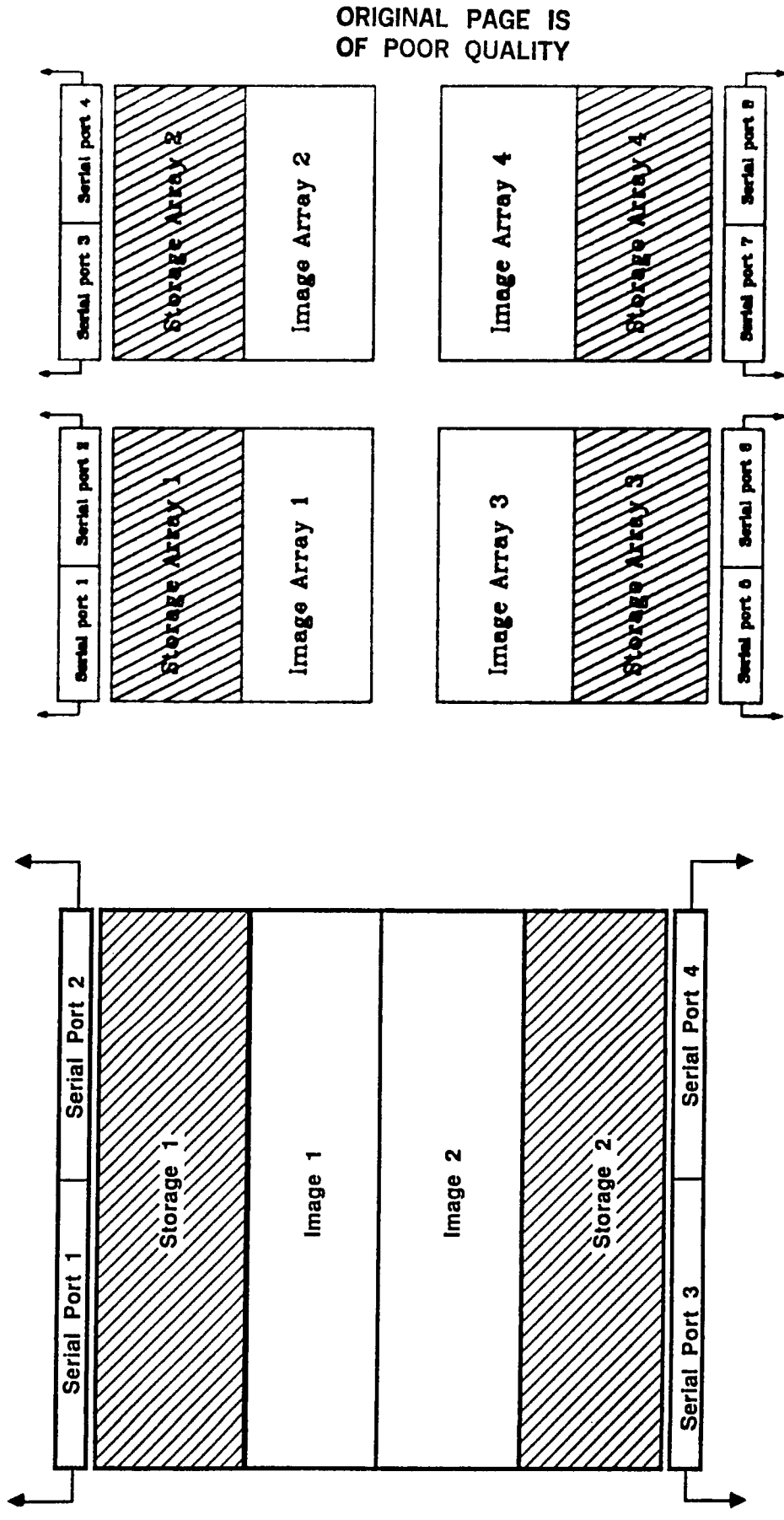


	Proposed SAMEX detector system	Preliminary breadboard design
Manufacturer:	Tektronix	Thomson
Array size:	2048 x 2048	4 (1024 x 1024)
Pixel size:	27 microns	19 microns
Well size:	750K electrons	250K electrons
Quantum Efficiency:	45 %	45 %
Proposed readout rate	4.8 Megapixels/sec.	9.6 Megapixels/sec.

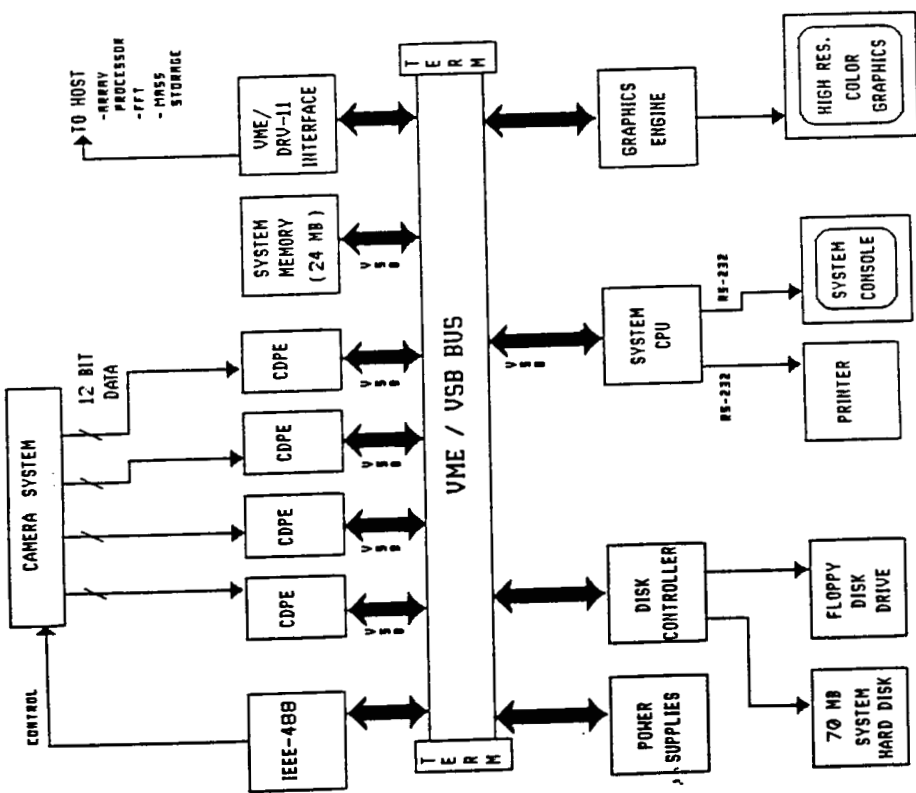
There are 4 serial ports on each Thomson CCD. The camera controller will be designed for flexibility so that it can handle CCD's developed in the future. The 2 port design (8 total) is required to match the smaller well size of the Thomson sensor with the S/N and time resolution requirements that satisfy the scientific objectives.

Proposed SAMEX detector system

Preliminary breadboard design



Preliminary Design of the Solar Vector Magnetograph Data Acquisition System



Preliminary design produced by Ralph Kimball of Echotek Inc.

THE DRIVER IN FLARES AND CORONAL MASS EJECTIONS:
MAGNETIC EXPANSION

Ronald L. Moore
Space Science Laboratory, Marshall Space Flight Center, NASA

ABSTRACT

Chromospheric filaments, and hence the sheared magnetic fields that they trace, are observed to erupt in flares and coronal mass ejections. In the eruption, the filament-traced field is seen to expand in volume. For frozen-in magnetic field and isotropic expansion, the magnetic energy in a flux tube decreases as the flux tube expands. The amount of expansion of the magnetic field and the corresponding decrease in magnetic energy in a filament-eruption flare and/or coronal mass ejection can be estimated to order of magnitude from the observed expansion of the erupting filament. This evaluation for filament-eruption events in which the filament expansion is clearly displayed gives decreases in magnetic energy of the order of the total energy of the accompanying flare and/or coronal mass ejection (Moore 1988, *Astrophys. J.* 324, 1132). This simple expanding flux tube model can also fit the observed acceleration of coronal mass ejections, i.e., the observed tracks of velocity vs height, if it is assumed that the increase in mechanical energy of the mass ejection comes from the magnetic energy decrease in the expansion. These results encourage the view that magnetic expansion such as seen in filament eruptions drives both the plasma particle energization in flares and the bulk mass motion in coronal mass ejections.

This work is supported by NASA through the Solar Physics Branch of its Space Physics Division and by the Air Force Geophysical Laboratory through the Solar Physics Branch of its Space Physics Division.

PLANNED IMPROVEMENTS
TO THE
OWENS VALLEY FREQUENCY-AGILE INTERFEROMETER
FOR MAX'91

G. J. Hurford, D. E. Gary
(Caltech)

SCIENTIFIC MOTIVATION FOR MICROWAVE SPECTROSCOPY

* MEASUREMENT OF CORONAL MAGNETIC FIELDS

Gyroresonance opacity creates spectral features that can be used to accurately measure the strength of magnetic fields at the base of the corona. (Figure 1) This provides the basis for a practical coronal magnetograph.

* DIAGNOSTICS OF SOLAR ENERGETIC ELECTRONS

Theoretical models of brightness temperature spectra show that microwaves can cleanly distinguish between thermal and nonthermal gyrosynchrotron emission on the basis of shape of the spectra. The peak brightness temperature and peak frequency then define the plasma and particle parameters. (Figure 2)

WHY HASN'T THIS BEEN DONE BEFORE ??

The diagnostic content of microwaves is in terms of their brightness temperature spectra (surface brightness).

To measure brightness temperature at any frequency, it is necessary to spatially resolve the source.

The physics of gyroresonance emission and the character of burst spectra imply that spectral resolution of about 10% is required over several octaves of frequency.

THERE IS NO EXISTING FACILITY THAT COMBINES BOTH ADEQUATE SPECTRAL COVERAGE AND HIGH SPATIAL RESOLUTION IMAGING.

(The VLA does not have the spectral coverage; the present Owens Valley interferometer does not have enough baselines to image complex sources.)

WHAT'S THE PLAN ??

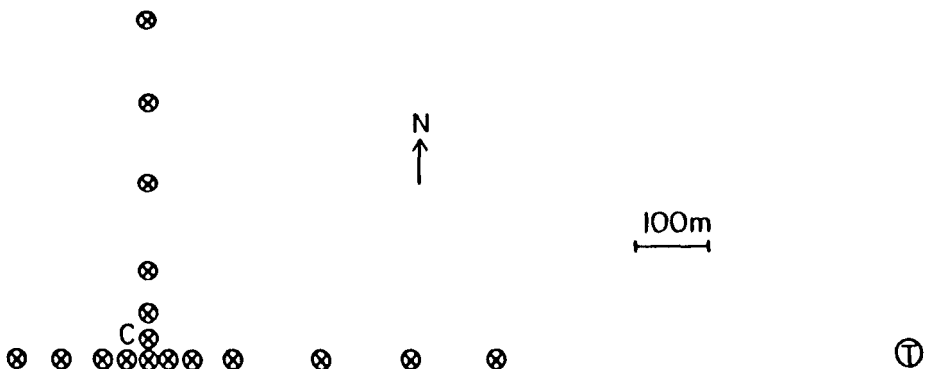
To add 3 small antennas to the OVRO interferometer to form a 5-element SOLAR-DEDICATED array.

This would provide up to 7 or 10 baselines (compared to the present 1 or 3). This would be sufficient to apply microwave diagnostics to most active region and burst sources.

By using frequency-synthesis it would also provide an imaging capability comparable to that of a ~100 baseline interferometer for morphological observations.
(See Figures.)

WHAT'S INVOLVED IN EXPANDING THE ARRAY ??

- * The present system is based on a pair of 27-meter parabolic antennas, equipped with frequency-agile receivers. By rapidly cycling in frequency the system functions effectively as a microwave spectrometer over the range 1 to 18 GHz. Baselines up to 1.25 km are available so that burst and active region sources can be resolved at all frequencies.
- * To expand the array, we will add 3 small (2 m diameter) antennas, equipped with frequency-agile receivers of essentially the current design.
- * Large antennas are not necessary because by doing interferometry between 2 meter and 27 meter diameter antennas, the effective sensitivity is the same as that with a pair of 7 meter antennas (geometric mean of 2 and 27). This is quite satisfactory.
- * Although antennas of this diameter are readily available, commercially available antenna mounts do not combine adequate sky coverage with reasonable cost. Therefore we will build the antenna mount in-house, using a simpler design well-matched to our requirements.
(See 1/4 scale model.)
- * To avoid the expense of new cabling, the small antennas will be located at existing antenna stations. (See below.)



Interferometer configuration, showing the possible locations of the 27 m antennas (x) relative to the 40 m telescope (T) and the control room (C).

- * Normally a significant expense in N-antenna arrays is the need for $N \times N$ correlators and associated systems.
- * This expense will be avoided by constructing a 5-to-3 line multiplexer and then time-multiplexing existing delay lines, amplifiers, correlators and data system.
- * The resulting system will be capable of fully sampling 5 antennas while changing frequencies up to 10 times per second.

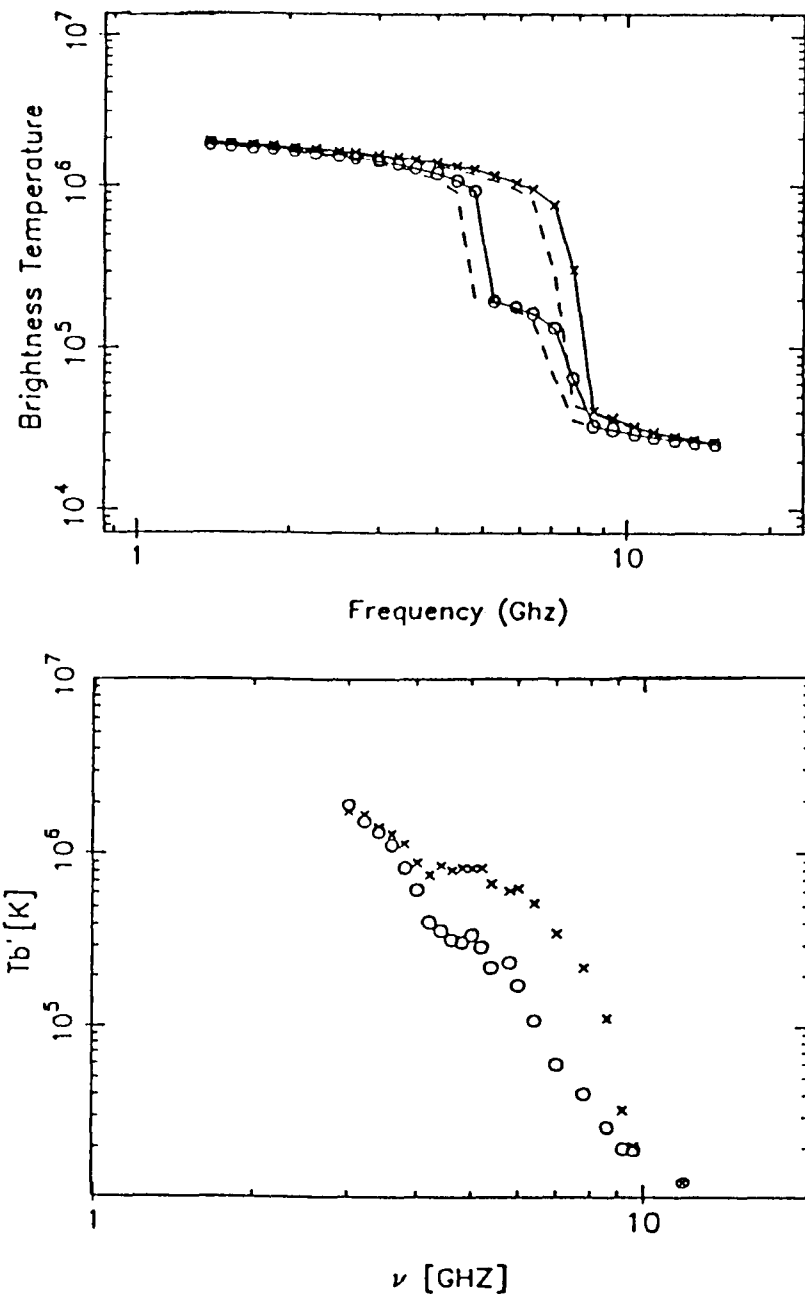


Figure 1. The upper panel shows model line-of-sight spectrum calculated using a three-dimensional potential field model of sunspot magnetic fields in a constant conductive flux modelled atmosphere. The discontinuities are a result of the interplay of gyroresonance opacity (at the 2nd and 3rd harmonics) with the sharp temperature gradient at the transition zone. x and o represent emission in the extraordinary and ordinary modes respectively. The dashed line shows the effect of increasing the model magnetic field by 10%.

The lower panel shows a typical observed line-of-sight spectrum near an isolated sunspot. As suggested by the model, the frequencies at which the spectral breaks occur (particularly in the extraordinary mode) can be readily interpreted in terms of the magnetic field where the line of sight intersects the base of the corona. For this line of sight (4000 km displaced from the center of the sunspot), at 300,000 K the 3rd harmonic of gyrofrequency corresponds to 7.6 GHz, implying a field of 900 gauss (ref Hurford and Gary, NASA-CP-2442, p317).

Universal Spectra for Homogeneous Sources

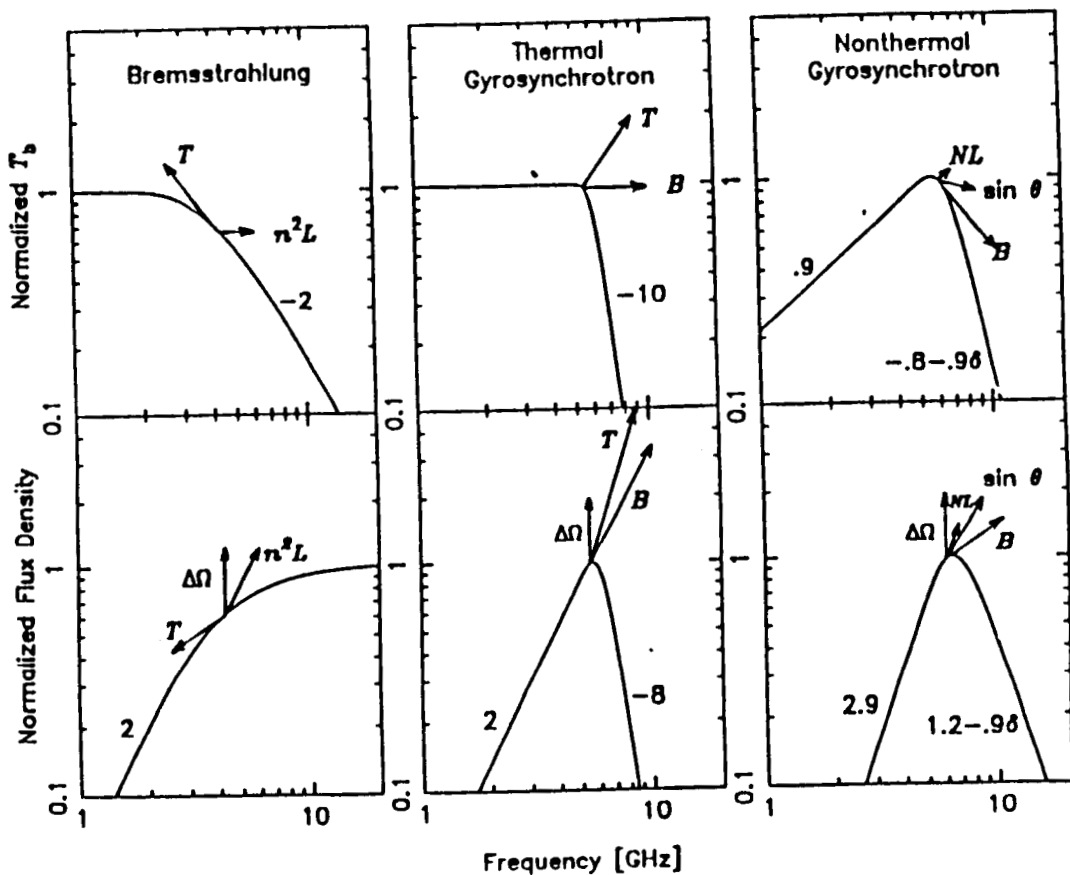


Figure 2. Universal curves, from theory, for emissions by various mechanisms from a homogeneous source. The arrows indicate the magnitude and direction in which the spectrum would shift for a factor of 2 increase of the indicated parameter. The top panels show brightness temperature spectra (requiring measurements with spatial resolution) and the bottom panels show the corresponding flux density spectra for a source of fixed size. The arrow labelled B in the thermal gyroresonance spectrum actually represents the quantity, $B (nL)^{0.11} \sin(\eta)^{0.66}$. Theta, the angle between the field line and line of sight, can be independently determined from circular polarization.

TP spectra near peak

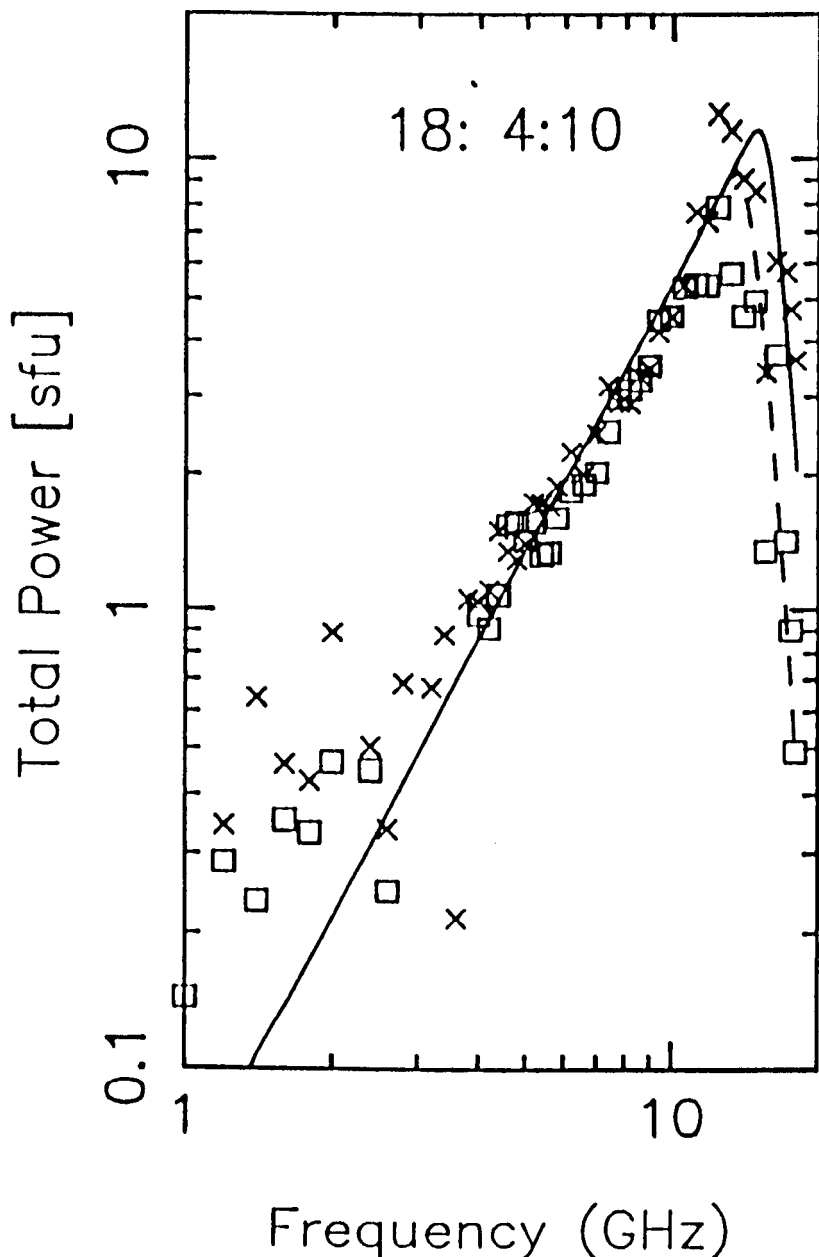


Figure 3. The microwave spectrum in right- and left-hand circular polarization for a burst with demonstrably simple spatial structure and interferometrically determined size of 8 arcseconds. The overlaid curves assume a homogeneous source with a thermal gyrosynchrotron spectrum. Thus the only degrees of freedom for the fits are the peak flux and frequency. Corresponding x-mode (solid) and o-mode (dashed) fits are shown.

FREQUENCY-SYNTHESIS IMAGING

- * EXPLOITS THE FACT THAT THE SEPARATION OF ANTENNAS IN UNITS OF WAVELENGTH IS DIFFERENT AT EACH FREQUENCY.
- * THEREFORE AN 86 FREQUENCY MEASUREMENT WITH 3 ANTENNAS CAN PROVIDE AS MANY U-V POINTS AS A 258 BASELINE INTERFEROMETER.
- * FUNDAMENTAL CONCERN IS THE EFFECT OF FREQUENCY-DEPENDENCE IN THE SOURCE GEOMETRY.
 - FOR SOURCES WHICH HAVE DIFFERENT MORPHOLOGY IN DIFFERENT FREQUENCY RANGES. THIS CAN RESTRICT THE RANGE OF FREQUENCIES USED IN A GIVEN MAP.
 - FOR SOURCES WHOSE SIZE OR FLUX VARIES SMOOTHLY WITH FREQUENCY, THE AMPLITUDES ARE WEIGHTED TO COMPENSATE FOR THE SPECTRUM, AND THEN THE SIZE VARIATION IS DETERMINED ITERATIVELY.
- * IN PRACTICE, FREQUENCY-SYNTHESIS PROVIDES A COST-EFFECTIVE AND PRACTICAL TECHNIQUE FOR OBTAINING THE LOCATION AND MORPHOLOGY OF SOLAR MICROWAVE SOURCES.

ORIGINAL PAGE IS
OF POOR QUALITY

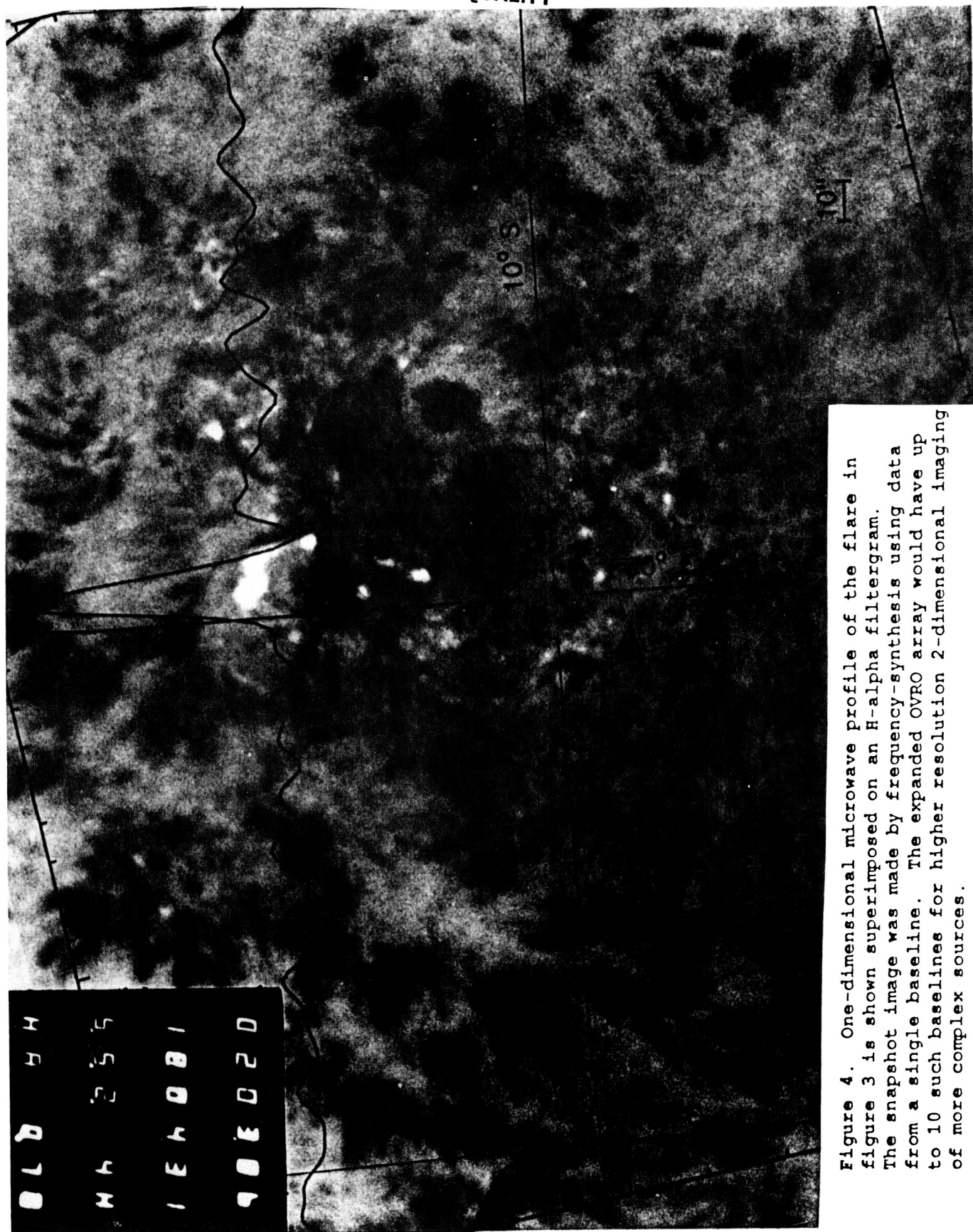


Figure 4. One-dimensional microwave profile of the flare in figure 3 is shown superimposed on an H-alpha filtergram. The snapshot image was made by frequency-synthesis using data from a single baseline. The expanded OVRO array would have up to 10 such baselines for higher resolution 2-dimensional imaging of more complex sources.

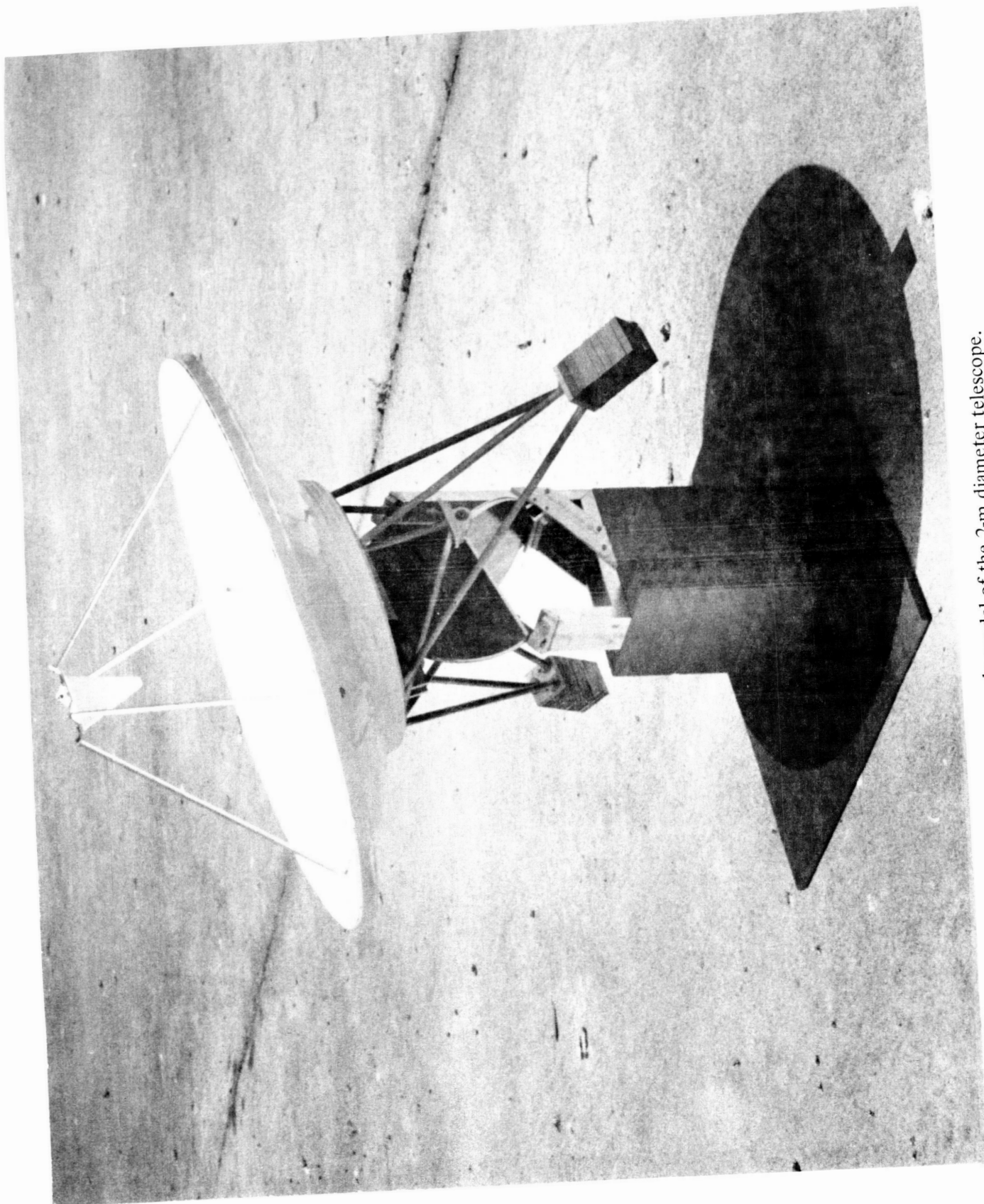


Figure 5. Quarter-scale model of the 2-m diameter telescope.

ORIGINAL PAGE IS
OF POOR QUALITY

MILLIMETER WAVELENGTH OBSERVATIONS OF SOLAR FLARES FOR MAX'91

M.R. Kundu, N. Gopalswamy, N. Nitta, E.J. Schmahl, S.M. White
(U. Maryland) and W.J. Welch (U. California, Berkeley).

BIMA Array

The Astronomy Program of the University of Maryland has recently joined the Universities of California (Berkeley) and Illinois in a consortium to upgrade the Hat Creek millimeter-wave interferometer (to be known as the Berkeley-Illinois-Maryland Array, or BIMA). The improved array (see below) will become available during the coming Solar Maximum, and we will have guaranteed time for solar observing as part of the consortium. We plan to make quasi-dedicated observations for long periods (10-15 days at a time), depending on solar activity.

The Hat Creek millimeter interferometer presently consists of three 6-m diameter antennas which can be located at various stations along a T-shaped road-way which extends 300 m East-West and 200 m North-South. Current operation is in the 2.5 - 4 mm wavelength atmospheric window. The receivers employ cooled Schottky diode mixers. The receivers can be tuned by a solid state oscillator from 70 to 115 GHz. Retuning takes about 5 - 15 minutes. Both sidebands of the first mixer are received and are separated by phase switching of the local oscillators. Thus, two frequencies separated by 2.3 GHz can be observed simultaneously. One linear polarization is received. A quarter-wave plate to produce circular polarization around 90 GHz is available. The receiver, antenna and atmosphere contribute to the system temperature. Scaled to above the atmosphere, the temperature is typically 300 to 500 K SSB over most of the band, rising to about 1000 K at 115 GHz where the opacity is greater.

The BIMA consortium has decided to expand this interferometer into a 6-element array with 15 baselines. Work is already in progress for this expansion, and it is expected to be complete in 2 years time. This array with 15 baselines will permit us to produce synthesized snapshot maps of solar flares simultaneously at 4 frequencies in the range 70 - 240 GHz. Thus, not only will the positions of mm burst sources be known, but their spectra will also be determined with reasonable accuracy. Before this expansion is completed, however, we shall use the instrument as a 3-element interferometer. This will be useful to find the positions of strongest burst sources with temporal resolution $\gtrsim 0.1$ sec. We shall be able to make these measurements at 2 frequencies separated by 2.3 GHz.

Science Objectives

The millimeter region has been perhaps the most under-utilized observing wavelength range in solar physics, due to the lack of telescopes which can match the temporal and spatial resolution available at other wavelengths. Millimeter wave observations are sensitive to both the highest-energy electrons in flares as well as to cool material in the chromosphere.

The science we shall address divides naturally into flares and chromospheric structures. Highly energetic particles accelerated in flares radiate strongly at millimeter wavelengths: in particular, since gamma-ray imaging is presently difficult, a millimeter array is the only method of imaging the most energetic particles in flares, and we propose many important studies using this fact. Using high-time-resolution, we will study particle acceleration in the impulsive phase, and the location of acceleration region in relation to other flare features. We hope to add greatly to the understanding of prompt acceleration in flares using temporal and spatial resolution previously unavailable. Delays between gamma-ray and millimeter peaks will be studied in conjunction with spatial information on the location of the millimeter sources, which, along with information in microwaves, will allow us to investigate the propagation of energy from the corona to the chromosphere during the impulsive phase. And we will establish whether gamma-rays and millimeter-waves come from identical regions by studying the anisotropy of millimeter-wave flares on the disk.

Observations of structures in the chromosphere outside of flares will place more emphasis on mapping, particularly of filament depressions and sheaths, the brightness distribution at the limb, and of active region structure. Millimeter waves can investigate the interface between filaments and the corona, the understanding of which is essential to model filaments. We will identify fine structures which we expect to find and relate them to spicules and interspicular regions inferred from limb brightness distributions. We will seek to confirm reports that coronal holes appear bright at millimeter wavelengths, and study the reason for this. Using mosaicing techniques we will map active regions and study the correspondence of optical, magnetogram and millimeter features. Finally, measurement of circular polarization will allow us to measure magnetic fields in the chromosphere.

PATROL MONITORING OF THE SUN AT MILLIMETER WAVELENGTHS

After its extension to six-elements the BIMA Array will have a seventh antenna available. This antenna, already equipped with 2-4 mm receivers, can be used for monitoring the Sun. It may be possible to use this antenna for fully dedicated observations of the Sun at a number of other wavelengths, e.g. 2 cm, 1 cm, 4mm and 2 mm. This arrangement will provide us with spectra at high frequencies not at present routinely available.

Daily monitoring of solar continuum flux at four wavelengths: 20mm, 10mm, 3mm, and 1.3mm. The receiver is located near the vertex of a 6m diameter antenna, as shown in Figures 4 and 5 below, for two different possible resolutions. In Figure 4 the receiver observes the entire sun directly with large beams at all wavelengths. In Figure 5 mirrors are inserted so that the sun is observed with the resolution of the 6m antenna (see table). Time resolution is ≥ 0.1 sec, permitting the study of flare development.

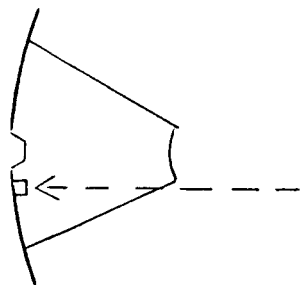


Figure 4

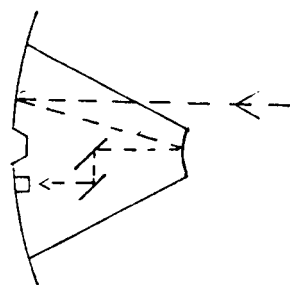


Figure 5

WAVELENGTH	RESOLUTION	
	<u>1</u>	<u>2</u>
20mm	30'	12'
10mm	30'	6'
3mm	30'	2'
1.3mm	30'	1'

ORIGINAL PAGE IS
OF POOR QUALITY

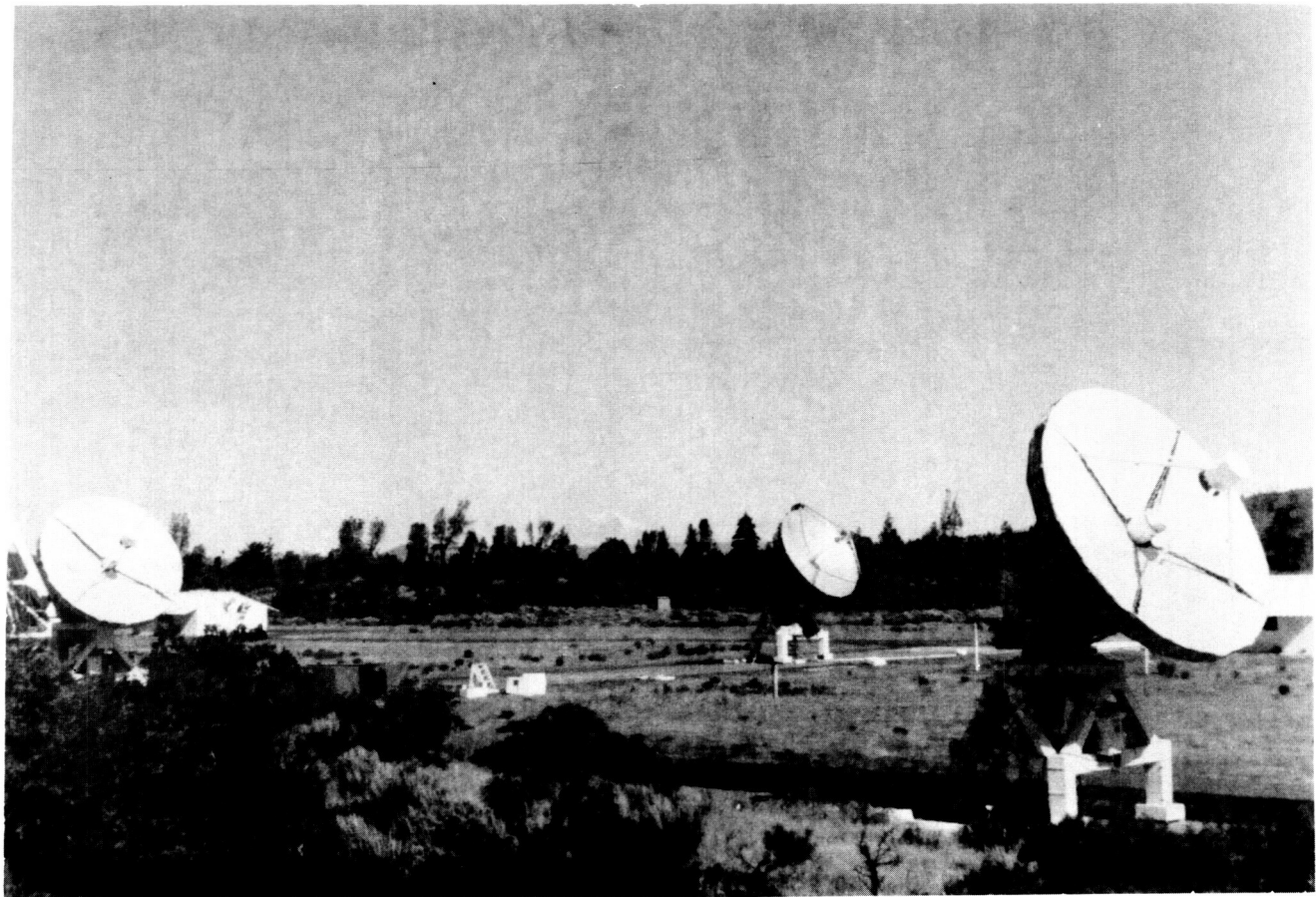


FIG. 1. THREE ELEMENT INTERFEROMETER PRESENTLY
AVAILABLE FOR SOLAR OBSERVATIONS AT MILLIMETER
(2-4MM) WAVELENGTHS. THE ARRAY IS SCHEDULED
TO BE COMPLETED BY EARLY 1991.

ORIGINAL PAGE IS
OF POOR QUALITY



FIG. 2. A SCHEMATIC DIAGRAM OF THE SIX-ELEMENT
BIMA ARRAY FOR MILLIMETER WAVELENGTH OBSERVATIONS
OF THE SUN (SEE TEXT).

ORIGINAL PAGE IS
OF POOR QUALITY

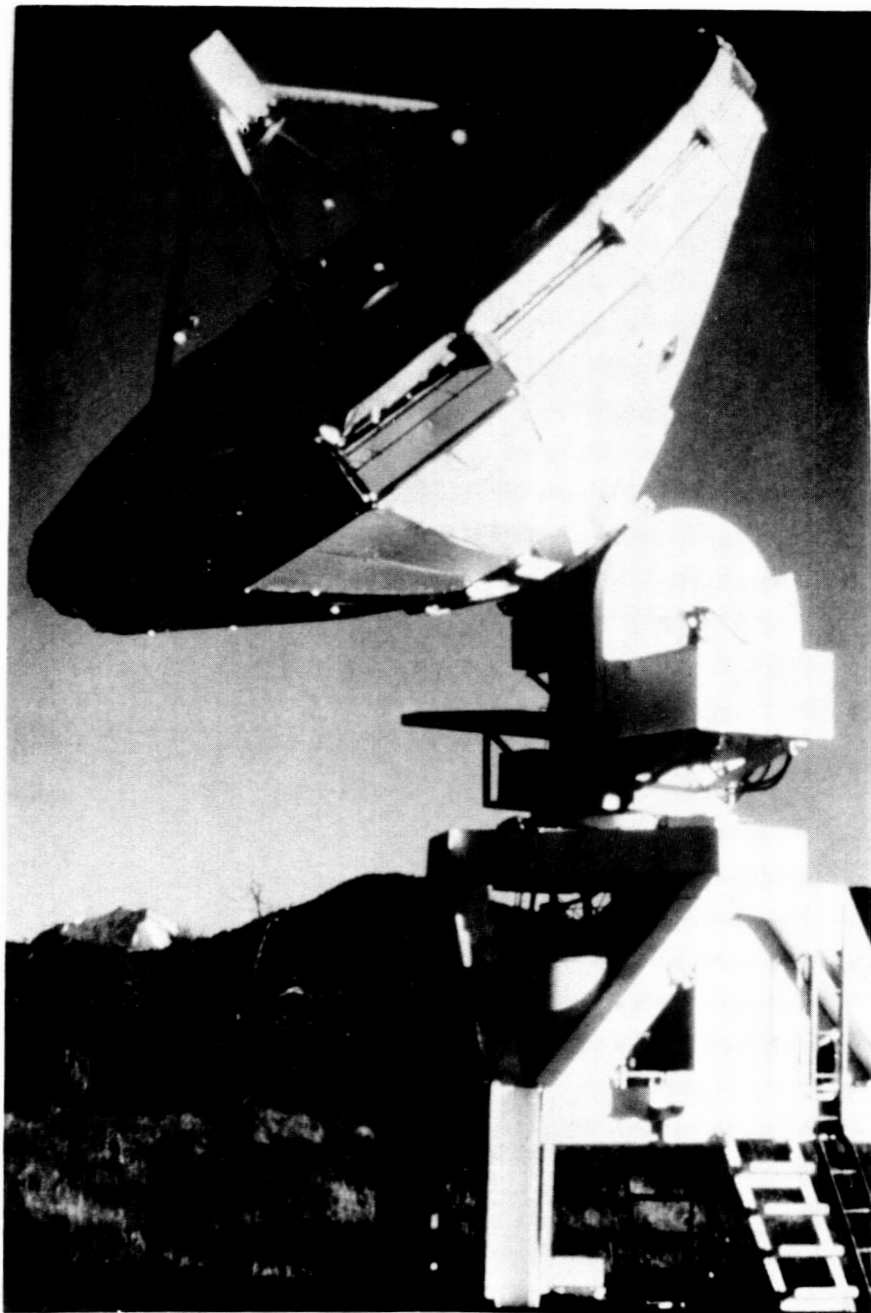


FIG. 3. THE SEVENTH ANTENNA OF THE BIMA ARRAY TO BE USED FOR DEDICATED OBSERVATIONS OF SOLAR FLARES AT FOUR WAVELENGTHS IN THE 20 - 1.3 MM RANGE.

Display paper presented at the Max '91 Workshop of the American
Astronomical Society Solar Physics Division meeting, Kansas City, MO
June 6 - 10, 1988.

SOLAR VECTOR MAGNETOGRAPH FOR MAX '91 PROGRAMS

D. M. Rust, J. W. O'Byrne, T. J. Harris

Johns Hopkins University Applied Physics Laboratory
Laurel, MD 20707

ABSTRACT

A new instrument for measuring solar magnetic fields is under construction. Key requirements for any solar vector magnetograph are high spatial resolution, high optical throughput, fine spectral selectivity and ultra-low instrumental polarization. An available 25-cm Cassegrain telescope will provide 0.5 arcsec spatial resolution. Spectral selection will be accomplished with a 150-mÅ filter based on an electrically tunable solid Fabry-Perot etalon. Filter and polarization analyzer design concepts for the magnetograph are described in detail. The instrument will be tested at JHU/APL, and then moved to the National Solar Observatory in late 1988. It will be available to support the Max '91 program. The magnetograph is being constructed at the Center for Applied Solar Physics, which is supported by the Air Force Office of Scientific Research University Research Initiative grant AFOSR-87-0077.

INTRODUCTION

The principal objective of the Center for Applied Solar Physics (CASP) is to improve solar activity observations and prediction techniques through an interdisciplinary program of instrumentation development and fundamental research on solar magnetic fields. Design and fabrication of a solar vector magnetograph is the keystone of the program, which began in January, 1987. This report summarizes activities on the VMG program. Other reports from the CASP program are available on request.

In early 1987, Rust, Appourchaux and Harris (APL/JHU preprint 87-24) studied a number of VMG design options, specifically as they relate to an instrument for operation in space. The proof-of-concept magnetograph now being assembled at APL will be operated at the Sacramento Peak Observatory, under a joint agreement with the National Solar Observatory. The major optical and electronic components for the VMG have been obtained and are described in the following paragraphs.

TELESCOPE AND CAMERA

The first optical element in the CASP magnetograph is a 25-cm reflecting telescope of the Ritchey-Chretien design, which allows a large field of view although the telescope is very compact (~ 60 cm long). The telescope is evacuated to eliminate the effects of internal seeing. We have established that this telescope forms near diffraction-limited (0.7 arc-second) images and that the custom relay optics for the VMG will convey the solar images to the electronic camera image plane without degrading the resolution.

To map the magnetic fields, we will use a 576 x 384-pixel CCD (charge-coupled device) camera and image collection system made by Photometrics, Inc. in Tucson, Arizona. This system has proven to be the key element in our optics evaluation program. The CCD camera allows rapid quantitative evaluation of diffraction patterns, scattering, image scale, beam deflection, etc. For example, Figure 1, made with an image processing and color hardcopy unit, clearly shows the first diffraction ring and the scattered light pattern around the image of a single point light source. The large dynamic range of the system is evident since the amplitude of the scattered light (green and red areas) is less than one thousandth of the central (white) peak of the diffraction pattern.

The CCD camera readout time will determine the cadence of the observations. Ten readouts of the CCD will be required to collect the electrons needed for a signal-to-noise ratio of unity in a longitudinal field of 10 G (Figure 2). Readout times average 2 s for the whole CCD. Thus, 10 G sensitivity can be obtained in 20 s.

POLARIZATION ANALYSIS

Construction of solar vector magnetic field maps requires precision polarimetry (1:10,000) in narrow (~ 0.15 Ångstrom) bands in the solar spectrum. The CASP magnetograph (Figure 3) is built around an electrically tunable APL-developed Fabry-Perot filter and a polarimeter concept developed at the Space Sciences Laboratory, NASA Marshall Space Flight Center. The polarimeter is especially designed to eliminate crosstalk between the relatively strong line-of-sight magnetic field signal and the much weaker transverse field signal. Crosstalk is caused by unavoidable imperfections in the retardance and positioning of the polarizing elements. The MSFC study suggests that low crosstalk polarization analysis can best be achieved by using a removable achromatic quarter-wave retarder followed by a rotating polarizer.

To minimize instrumental polarization, we use components which are rotationally symmetric about the optical axis. In particular, the magnetograph will be fed by a Cassegrain telescope mounted on a spar rather than one fed by a coelostat or other mirror system.

The polarization of the incident light is expressed in terms of the four Stokes vectors. These are derived from the intensities transmitted by the polarization analyzer (quarter-wave plate plus prism) as it is configured to pass various combinations of linear and circular polarization. A Glan-laser prism is used as the linear polarization analyzer because of its excellent extinction ratio. It is mounted in a programmable precision rotating stage. An HN38 dichroic polarizer is attached to the prism to further increase the contrast ratio between the blocked and transmitted senses of polarization.

A second quarter-wave plate is attached to the rear of the Glan-laser prism to yield circularly polarized light and thereby minimize modulation of the beam intensity by subsequent polarizing components, such as folding mirrors. Provision is also made for mounting a pair of wedge prisms to compensate for beam deviation caused by the polarization analyzer.

All elements of the polarimeter, including a newly developed liquid-crystal polarization rotator, have been procured and shown to conform to our specifications. Tests of the overall polarimeter sensitivity will be started in July, 1988.

FABRY-PEROT FILTER

Our F-P filters are constructed at the National Measurement Laboratory in Australia from a thin wafer of lithium niobate polished to 40 - 50 Å flatness. The acceptance angle of a lithium niobate etalon is five times that for an air-spaced etalon; that is, for the same spatial and spectral resolution, an air-spaced etalon would have to have five times the area of the lithium niobate etalon. The advantage over a birefringent filter is almost as great because of the long path length required by the birefringent filter.

In lithium niobate, application of an electric field induces a change in the refractive index for light propagating along the optic axis. We use this property to tune the filter. The tuning requirements of the solar magnetograph are modest. Typical spectral lines are only 0.2 Å wide, and +/- 500 V will tune the filter through 0.4 Å.

Comparison of the off-axis behavior of a Fabry-Perot etalon with the Doppler shifts due to solar rotation shows that, if the etalon is operated at an appropriate tilt from the suncenter-to-telescope ray, the Doppler shifts from solar rotation can be closely matched (cancelled). Thus, the etalon provides a passband that is at once narrow and correctly positioned on the spectral line everywhere in the field of view.

Last year, we conducted an extensive series of tests of Fabry-Perot filter elements. We tested the filter's ability to withstand voltage cycling equivalent to ten years' operation and to survive the vibration

of a shuttle launch. No deterioration was found. Similarly, the filter withstood bombardment by energetic protons.

We have one 75-mm F-P filter in hand. CSIRO is making another and they now have two ready for coating. At least one should be ready for delivery in August.

In collaboration with investigators from Washington University, we measured the performance of a small-aperture commercial acousto-optic blocker filter and studied a large-aperture device suitable for solar imaging. On the basis of this study, we concluded that such a filter can be built but it requires a developmental effort that is outside the scope of CASP's interests. The acousto-optic filter is now being developed with APL Independent Research and Development funds.

IMAGE MOTION COMPENSATION

The pointing stability required for the relatively long exposures anticipated with the 25-cm telescope will be achieved with an image motion compensation system based on binary correlation. The heart of the system is a sequential binary correlation (SBC) algorithm for computing the solar image offset based on images obtained by the 32 x 32 Reticon photodiode tracking array. A relay mirror position is updated at a 50-Hz rate as the sensed image is compared with a periodically updated reference image. The algorithm can operate well even when only solar granules are in the 10 x 10 arc-sec Reticon field. That is, high contrast features are not required for successful operation.

K. Strohbehn and P. K. Murphy tested the SBC algorithm at APL using solar granulation data obtained by R. B. Dunn at the Sacramento Peak Observatory. Their trials showed that the fast binary registration can give nearly the same results as conventional, slower, grayscale registration. The SBC algorithm introduces rms pointing errors of ~ 0.02 arc-second, which is considered negligible. Strohbehn has implemented the SBC algorithm in custom hardware for the VMG and is scheduled to complete testing of it this summer.

BALLOON-BORNE VECTOR MAGNETOGRAPH

Because of the fine structure of the solar magnetic fields, the full power of a VMG can be realized only when the blurring effect of turbulence in the Earth's atmosphere can be eliminated. This can be accomplished eventually with a space platform or high altitude balloon. Opportunities for a space mission may arise only in the distant future, but because of the Max '91 program, prospects for a balloon flight are much brighter.

Numerous studies have shown that a one-meter class telescope is needed to achieve the short exposure times and high resolution needed to answer the most fundamental questions about solar magnetism. We are now studying how to mate a one-meter telescope to the VMG focal plane instrumentation and fly it on a long-duration balloon mission. First

results are very encouraging since balloons are now able to carry instruments up to six meters in length and up to 2000 pounds weight. We believe that the VMG fed by a one-meter telescope can be ready to participate in the Max '91 programs.

Although a balloon-borne telescope program cannot achieve all the scientific objectives of a long-duration space mission, such as the Optical Solar Laboratory, the contribution of a one-meter instrument to the Max '91 program will be enormous, particularly in vector magnetography where even a flight as short as five or six hours would likely revolutionize our understanding of the structure and evolution of magnetic fields in active regions. A fifteen-day flight would certainly capture many flares and make a major breakthrough in flare research.

ACKNOWLEDGEMENTS

Dr. Kim Strohbehn and Dr. Patricia Murphy of APL designed and implemented the correlation tracker. John Townsend and Benjamin Ballard are developing the computer programs needed to handle solar data. Robert Moore and Harry Zink performed systems analyses and major component evaluation. Gary Starstrom is designing the magnetograph structures on the APL Computer-Aided Design equipment. The 25-cm evacuated telescope was furnished by the High Altitude Observatory of the National Center for Atmospheric Research. Support for the Center for Applied Solar Physics is provided by AFOSR Grant 87-0077.

ORIGINAL PAGE IS
OF POOR QUALITY

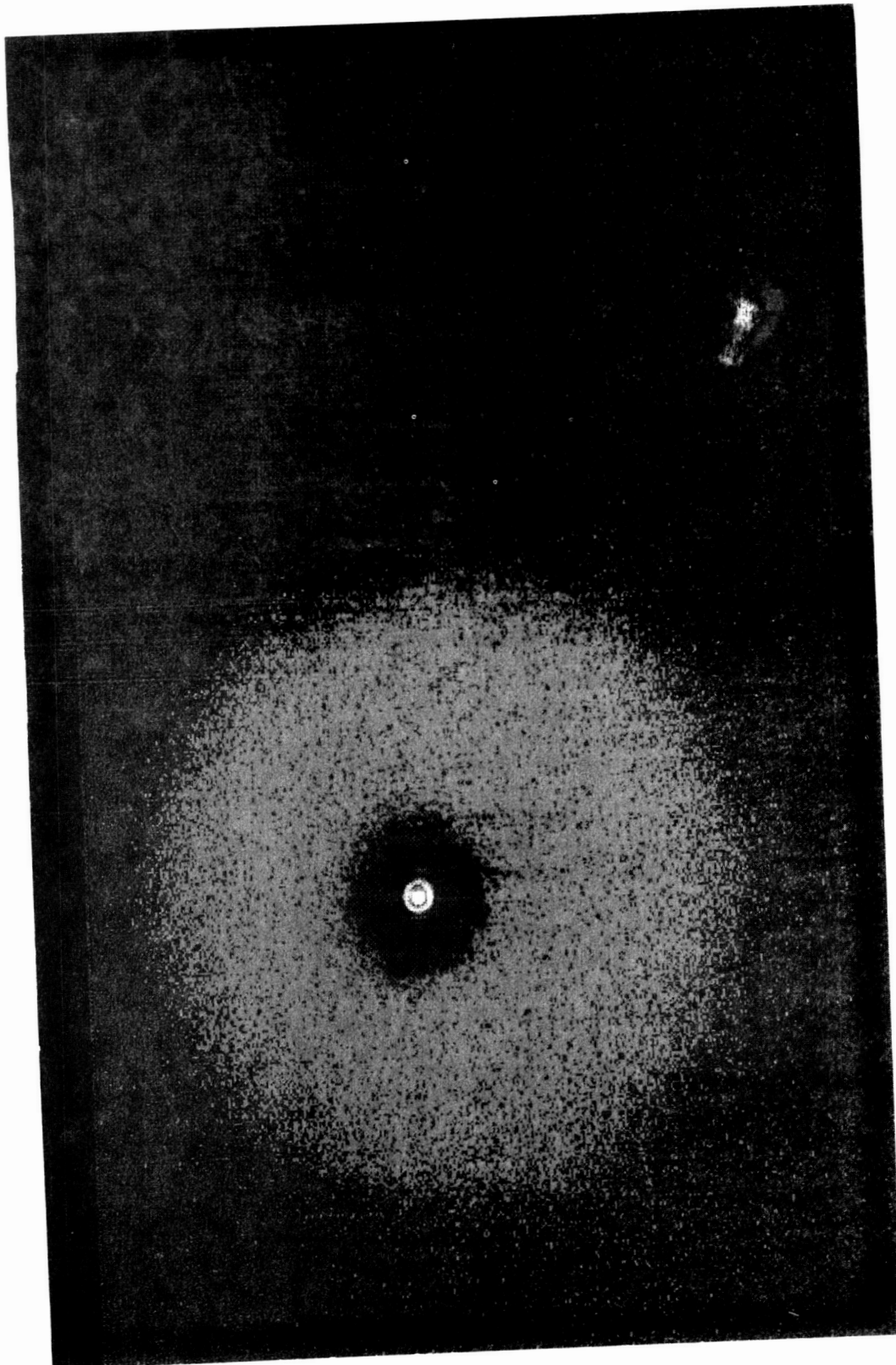


Figure 1. Image of a point light source obtained through the vector magneto graph optics. The peak and the first diffraction ring (white) and scattered light (green and red areas) are clearly shown.

THE JOHNS HOPKINS UNIVERSITY
APPLIED PHYSICS LABORATORY
LAUREL, MARYLAND

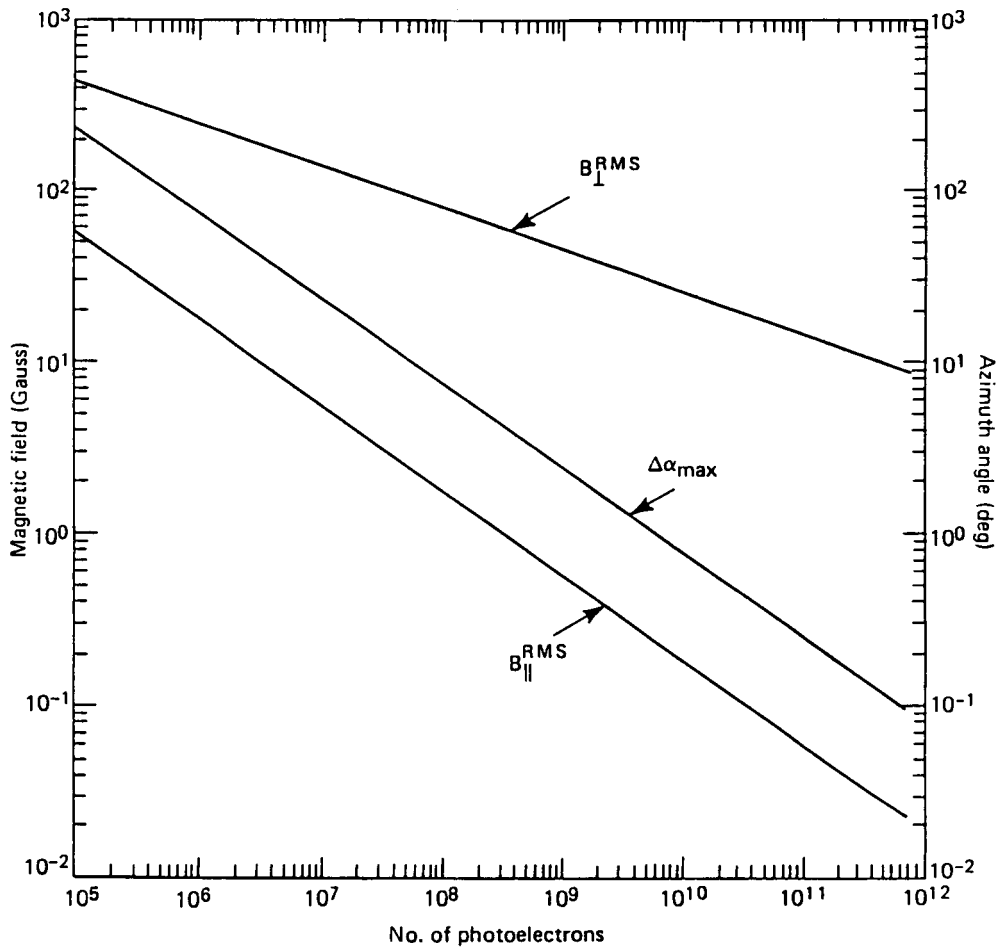


Figure 2 Errors on the measurements of B_{\parallel} , B_{\perp} and α . These curves were computed assuming a line width $\Delta\nu_0 = 0.15\text{Å}$, a depth $P = 0.5$, and a Landé factor $g = 1.5$. The quality factor Q was assumed to be about 2. $\partial^2 p / \partial v^2|_{v=0}$ was assumed to be about 1. The magnetic field taken to compute $\Delta\alpha_{\text{max}}$ is $B_{\perp} = 300$ gauss.

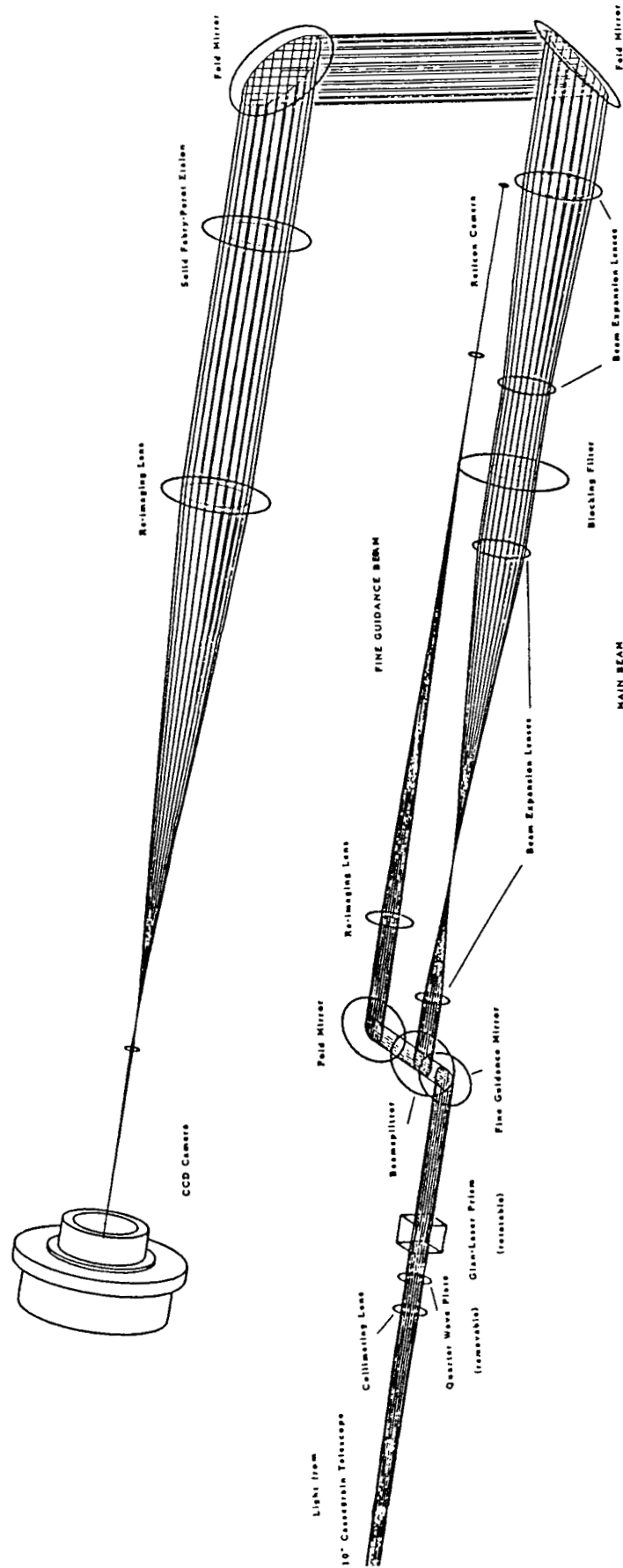


Figure 3. Principal optical components of the CASP vector magnetograph.

ORIGINAL PAGE IS
OF POOR QUALITY

Mechanisms for Fast Flare Reconnection*

G. Van Hoven, D. Deeds and T. Tachi (Dept. of Physics,
Univ. of California, Irvine, CA 92717

Normal collisional-resistivity mechanisms of magnetic reconnection have the drawback that they are too slow to explain the fast rise of solar flares. We will examine two methods proposed for the speed-up of the magnetic tearing instability: the anomalous enhancement of resistivity by the injection of MHD turbulence and the increase of Coulomb resistivity by radiative cooling.² We describe the results of nonlinear numerical simulations of these processes which show that the first does not provide the claimed effects, while the second yields impressive rates of reconnection, but low saturated energy outputs.

*This research was supported, in part, by the Solar-Terrestrial Theory Program of NASA, and by the Atmospheric Sciences Section of NSF; computations were provided by NSF and DOE.

1. D. Biskamp and N. Welter, Phys. Letts 96A, 25 (1983).
2. R. Steinolfson and G. van Hoven, *Astrophys. J.* 276, 391 (1984).

TURBULENT RESISTIVITY: MODEL AND DEFINITIONS

Our two-dimensional force-free model has an initial sheared periodic field

$$\hat{B}_0 = \hat{x} B_0 \sin \pi/a - \hat{z} B_0 \cos \pi/a.$$

We further assume an incompressible inviscid plasma with constant nominal resistivity η_0 . The MHD and energy equations are Fourier-transformed into the wavenumber domain with $\partial/\partial z = 0$, modeled over a finite spectrum, and evolved in time using a predictor-corrector algorithm.

Biskamp & Welter [Phys. Letts. 96A, 25 (1983)] have analytically examined the case where the turbulent spectrum is well separated from the tearing spectrum. They report that in this case the turbulence has the effect of introducing an additional effective resistivity term

$$\eta_t = 1/2 \tau_{corr} \{ \langle v^2 \rangle_{turb} - \langle B^2 \rangle_{turb} \},$$

where τ_{corr} is the correlation or relaxation time of the small-scale spectrum.

Note that η_t is a measure (at least semi-quantitative) of how a given process deviates from being Alfvénic.

TIME-EVOLUTION EQUATIONS

$$\begin{aligned}
 \frac{\partial B_x(0,i)}{\partial t} &= -\frac{\pi n_0 c^2}{4q^2} i^2 B_x(0,i) + \frac{\pi l_i^2}{4q^2} \sum_{m,n=-\infty}^{\infty} \frac{1}{m} B_y(m,n) N_Y(m,i-n) \\
 \frac{\partial B_y(j,i)}{\partial t} &= -\frac{\pi n_0 c^2}{4q^2} (j^2 + i^2 \frac{l_i^2}{q^2}) B_y(j,i) + \frac{\pi j}{4q} \sum_{n=-\infty}^{\infty} B_x(0,i-n) N_Y(j,i-n) \\
 &\quad + \frac{\pi j}{4q} \sum_{m,n=0,j}^{\infty} \left(\frac{n}{m} - \frac{j-n}{j-m} \right) N_Y(m,n) B_Y(j-m,i-n) \\
 \frac{\partial N_Y(j,i)}{\partial t} &= \frac{j}{16\rho q(j^2 + i^2 l_i^2/q^2)} \left\{ \sum_{n=-\infty}^{\infty} \left(j^2 + \frac{i(2n-i)l_i^2}{q^2} \right) B_Y(j,n) B_X(0,i-n) \right. \\
 &\quad \left. + \frac{1}{q} \sum_{m,n=-\infty}^{\infty} (m^2 + n^2 \frac{l_i^2}{q^2}) \frac{n j - m i}{m(j-m)} [B_Y(m,n) B_Y(j-m,i-n) - 4\pi \rho N_Y(m,n) N_Y(j-m,i-n)] \right\}
 \end{aligned}$$

where, for example,

$$B_Y(x,y,t) = \frac{1}{4} \sum_{m,n} B_Y(m,n,t) \sin(m\pi x/\lambda) \cos(n\pi y/\lambda)$$

is the reconnecting field component, and ρ is the mass density.

Because of the assumed periodicities in both x and y (with scale lengths λ and q respectively), the wavenumbers in these directions are multiples of $k_{x0} = \pi/\lambda$ and $k_{y0} = \pi/q$.

TEST CASES

The test cases whose results are illustrated here are designed to realize η_t artificially by continually injecting turbulence into the model (starting at time $t = 0.4$ sec in each case). The chosen parameters include $S = 1000$; $|k_x/k_{x0}| \leq 30$; $|k_y/k_{y0}| \leq 15$; and $k_{x0}a \approx 0.36\pi$, specifying the dimensionless wavelength in the x direction (along the tearing plane) for the most unstable tearing perturbation. (This last means that the scale length in the x direction is about twice that in the y direction.)

The cases illustrated are as follows:

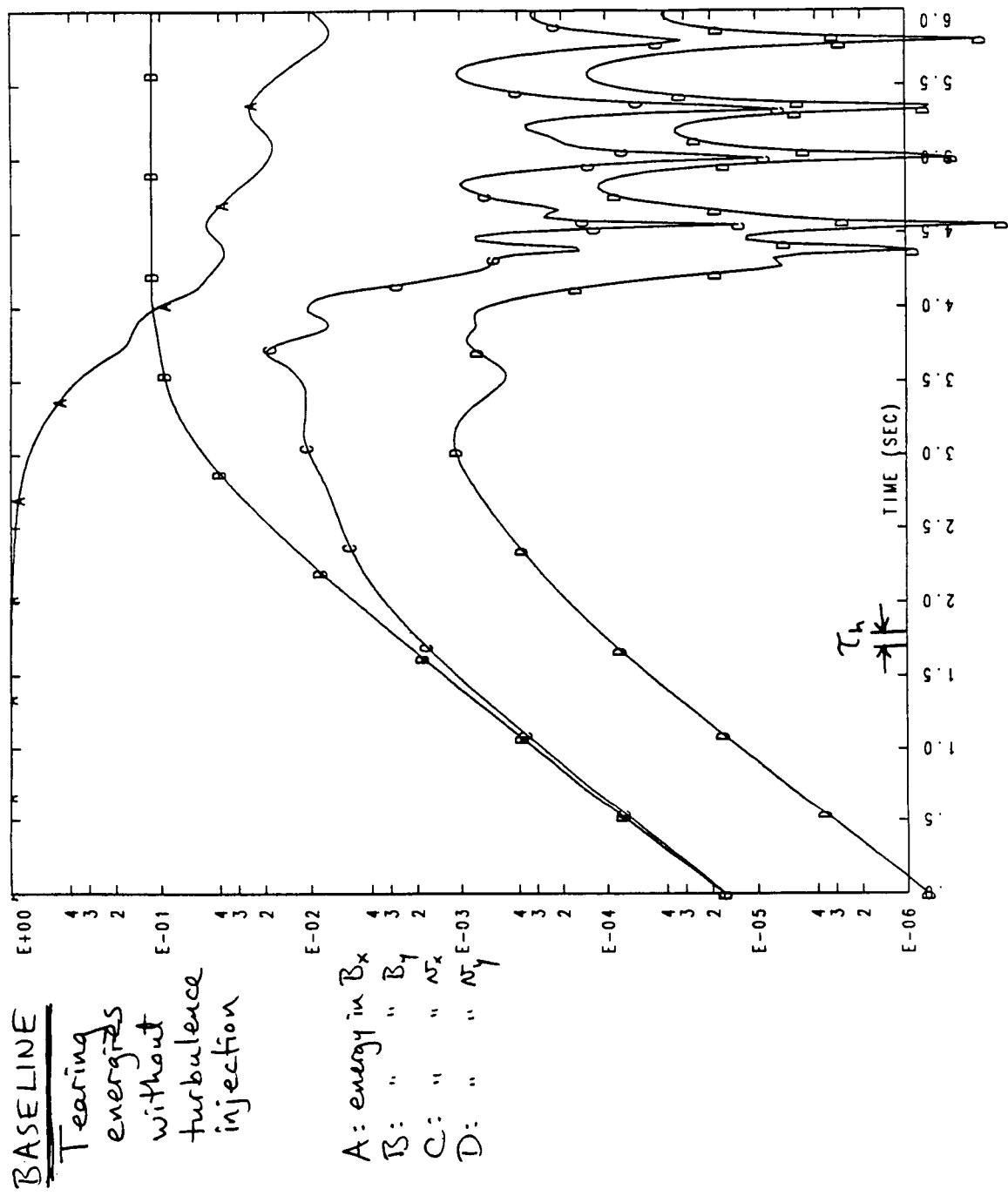
- 1) The baseline - the normal tearing mode is allowed to proceed through linear, nonlinear, and saturation phases; no turbulence is added.
- 2) Turbulence is added to the magnetic induction spectrum at the rate

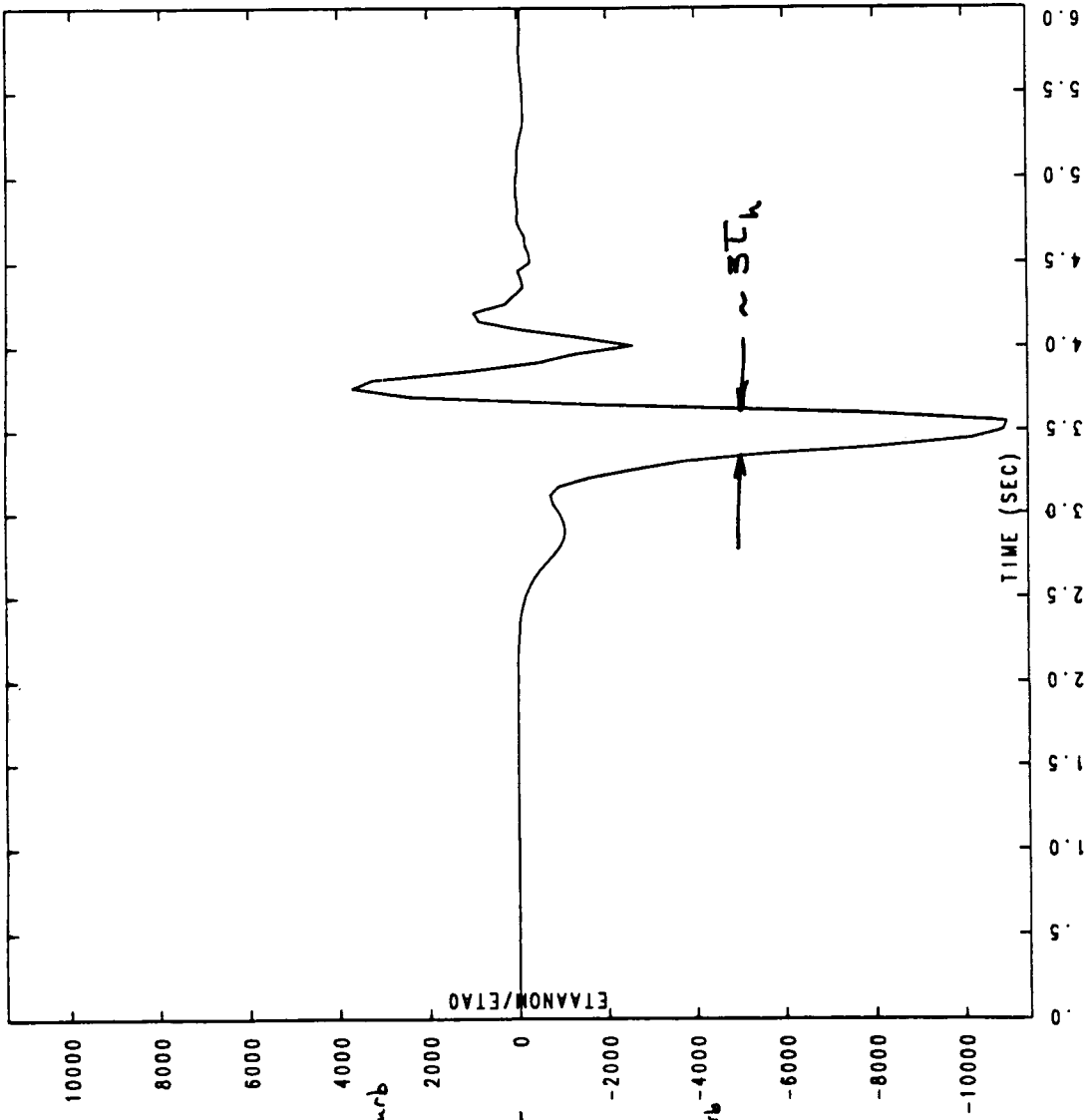
$$\frac{\text{energy injected/unit time}}{\text{background field energy}/\tau_e} \lesssim 10^8$$

(τ_e being the e-folding time of linear tearing growth).

- 3) As for case 2, but turbulent energy is added to the velocity rather than the induction spectrum.

Plotted for each case are the energy in B_x , B_y , v_x , and v_y for the linear tearing portion of the spectrum ($|k_x/k_{x0}| \leq 1$, all k_y), and the quantity η_t normalized to the nominal resistivity η_0 . [n.b.: η_t is calculated according to a prescription given by Montgomery and Hatori, Plasma Phys. and Contr. Fusion 26, 717 (1984)].





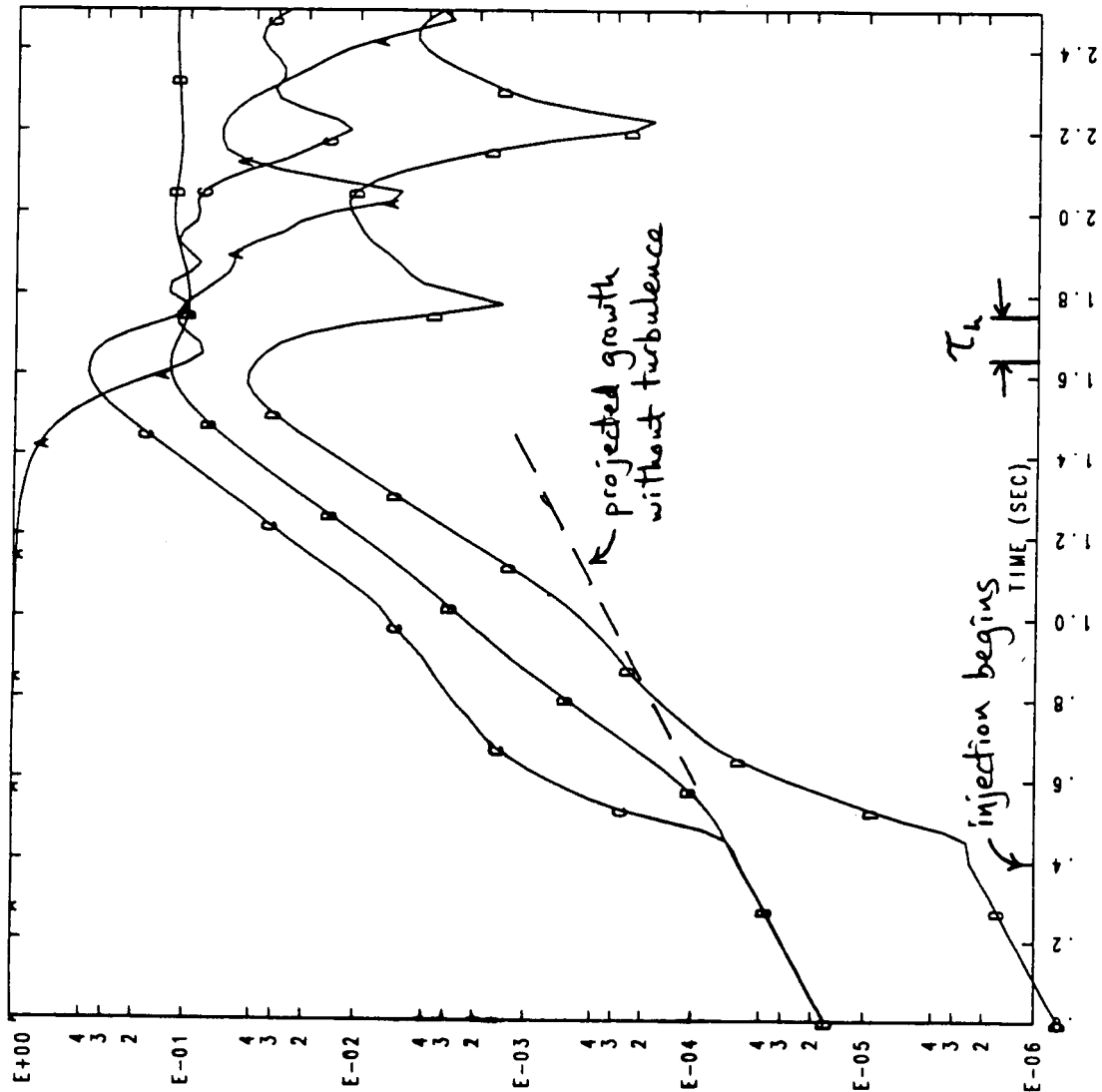
BASELINE

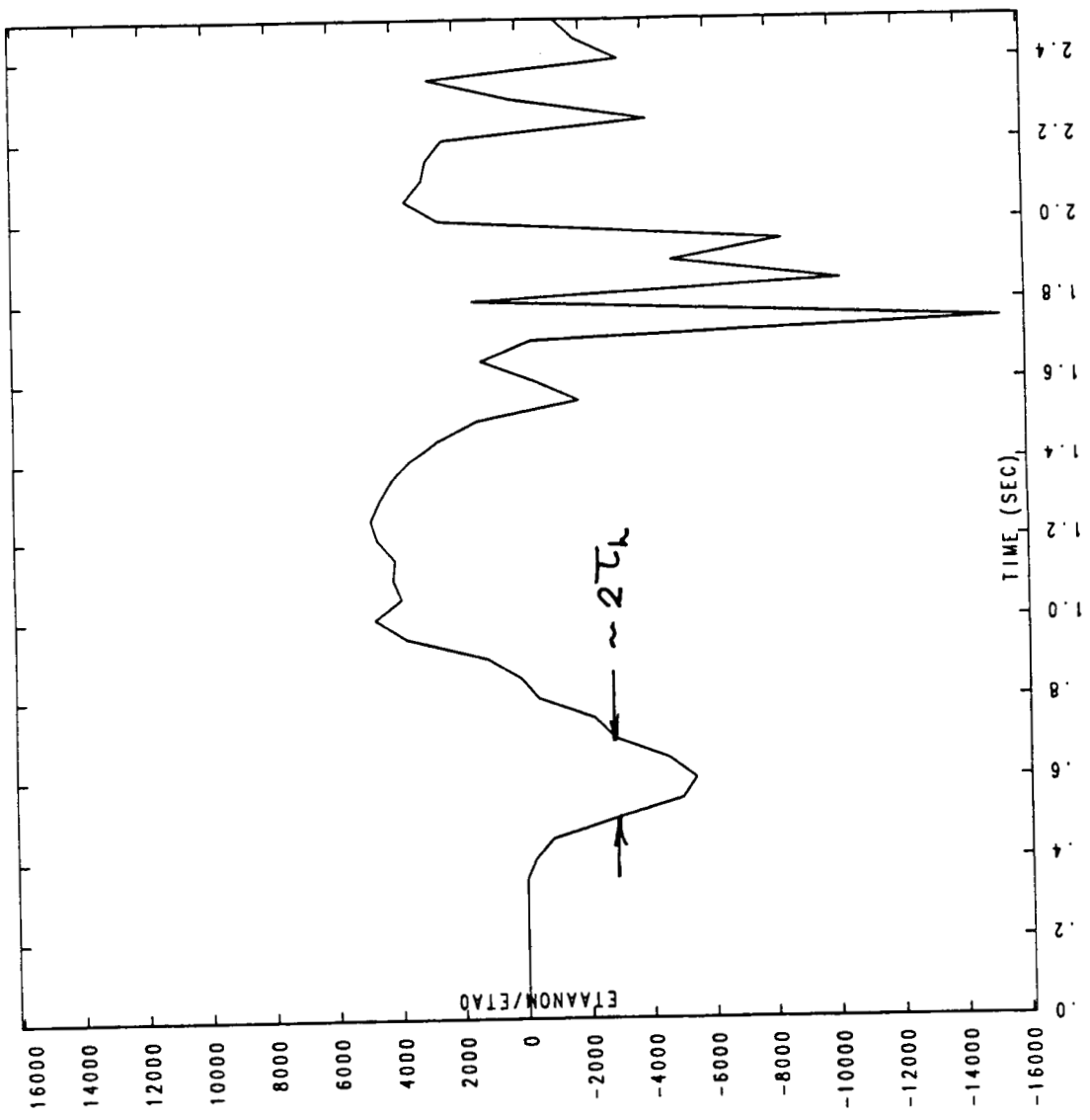
Plot of n_t/n_0

excess $\langle n^2 \rangle_{turb}$

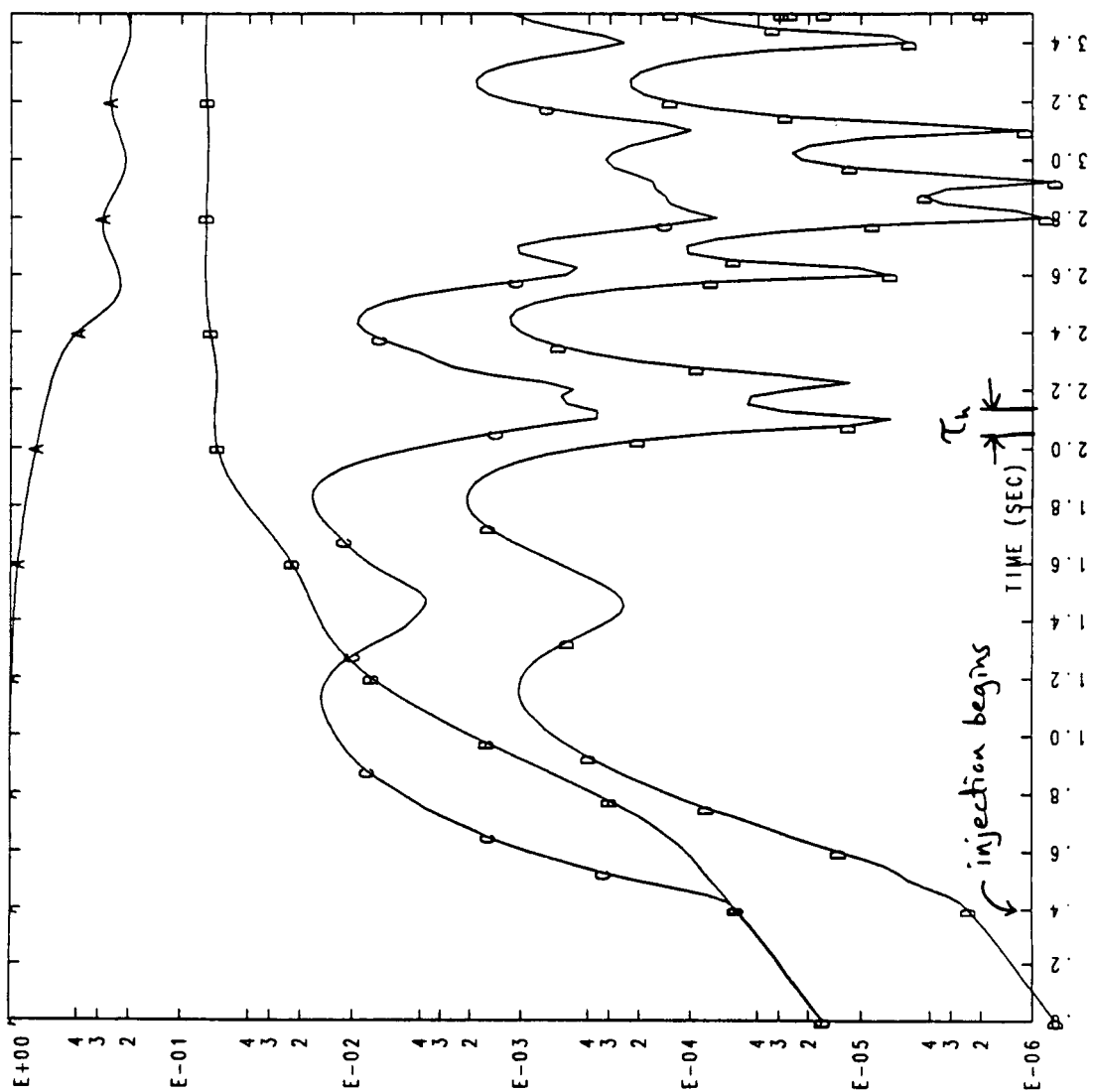
excess $\langle B^2 \rangle_{turb}$

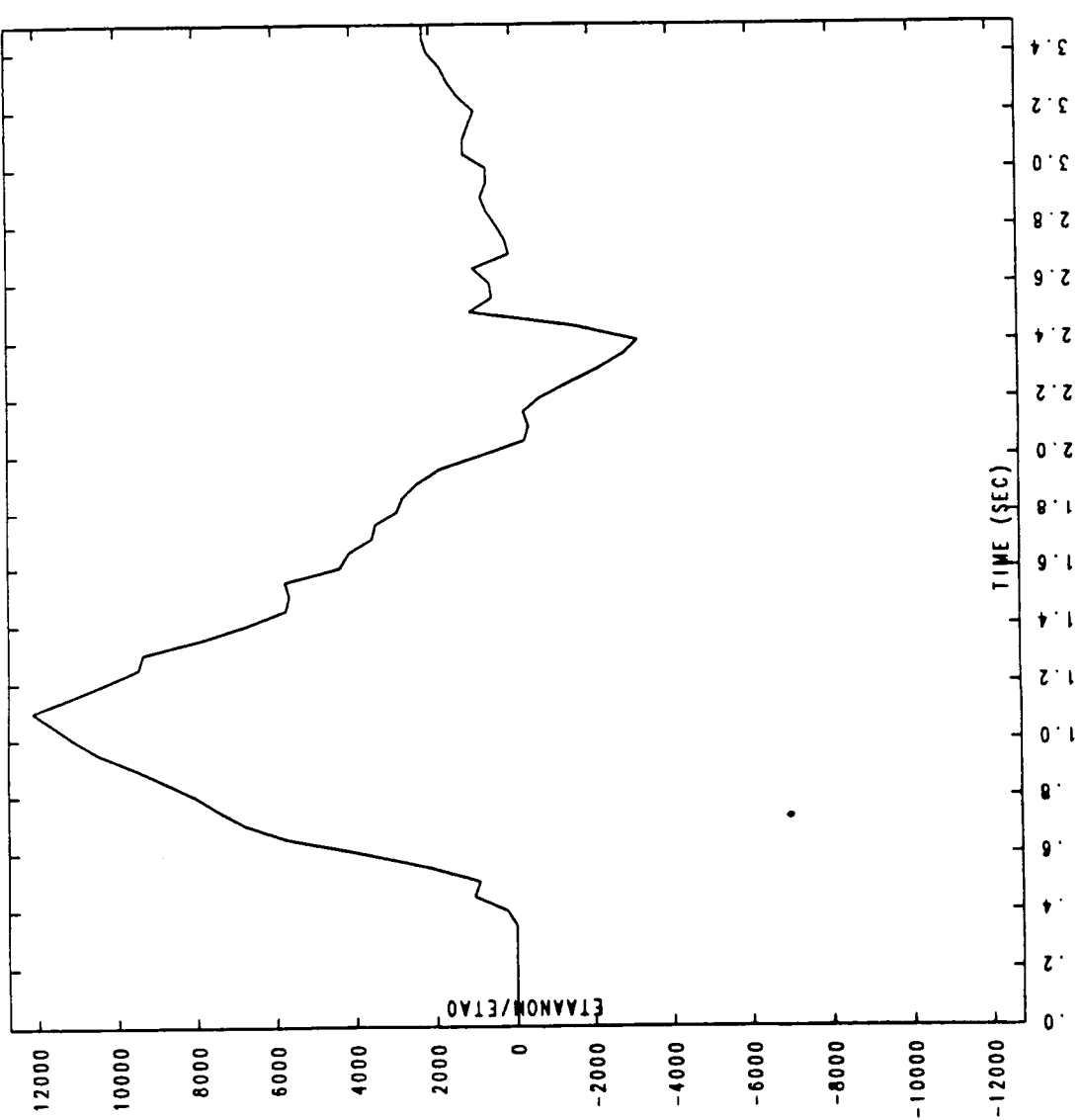
CASE 2
Turbulence
injected
in $\langle \beta^2 \rangle$:
Energies





CASE 3
Turbulence
injected
in $\langle n^2 \rangle$:
Energies





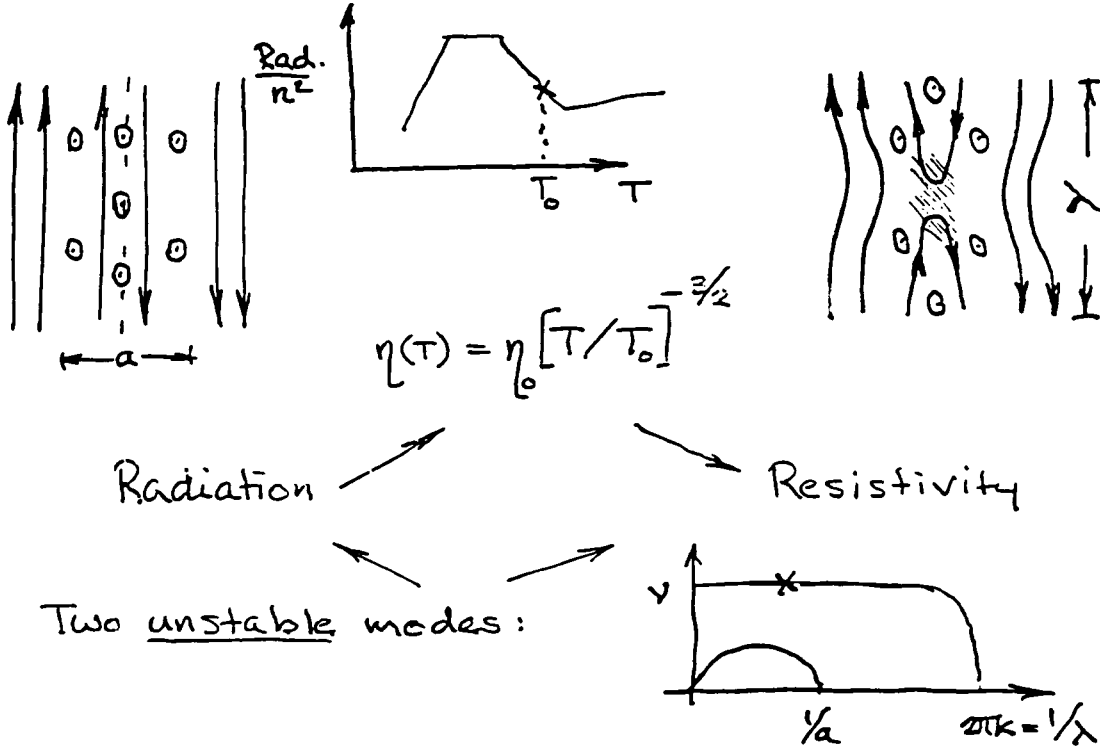
CASE 3
 $\underline{\underline{n_t / n_0}}$

TURBULENT RESISTIVITY: OBSERVATIONS AND CONCLUSIONS

- 1) The quantity η_t is zero for linear growth and after saturation of the unperturbed tearing process; but it deviates markedly from zero during nonlinear growth. Hence it may serve as a measure of what might be called Alfvenicity (or equipartition).
- 2) The presence of turbulence, whether in \mathfrak{B} or in \mathfrak{y} , catalyzes a weak increase in the ~~linear tearing~~ growth rate, with consequent earlier saturation. Saturation levels are not much altered. Other cases (not illustrated) show that this effect is only weakly dependent on the level of turbulence.
- 3) The quantity η_t shows a strong tendency to restore itself to zero (representing equipartition between kinetic and magnetic energies), both in its natural behavior and when it is being artificially driven positive or negative.
- 4) Because η_t takes on large positive and negative values while the enhanced growth rate changes little, its interpretation as a resistivity is questionable.

RADIATIVE RECONNECTION — SUMMARY

G. Van Hoven, T. Tachi & D.D. Schnack



1. Start with fast ($\sim 10^2 \times$) radiative mode

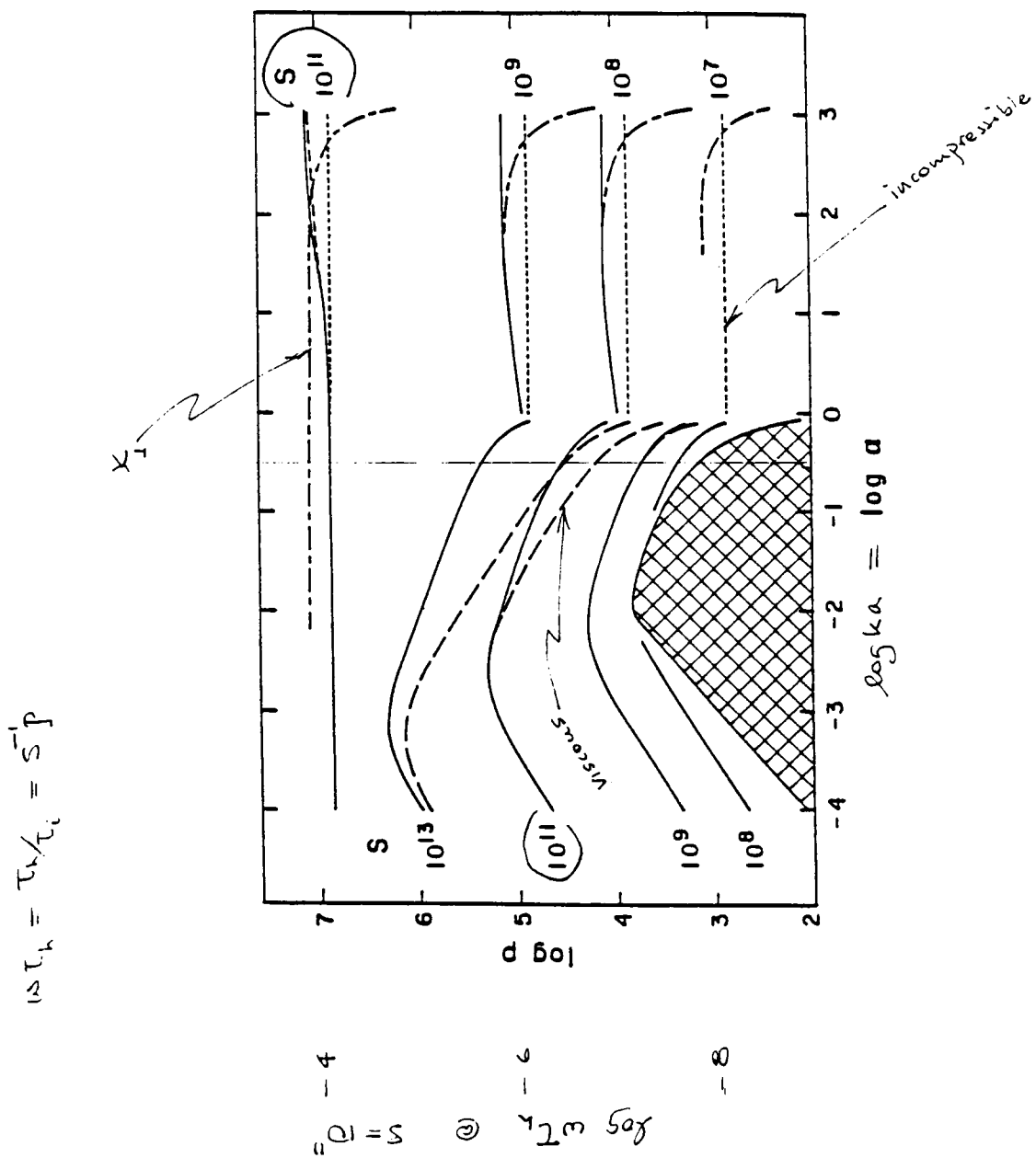
⇒ fast magnetic reconnection
and energy release ;

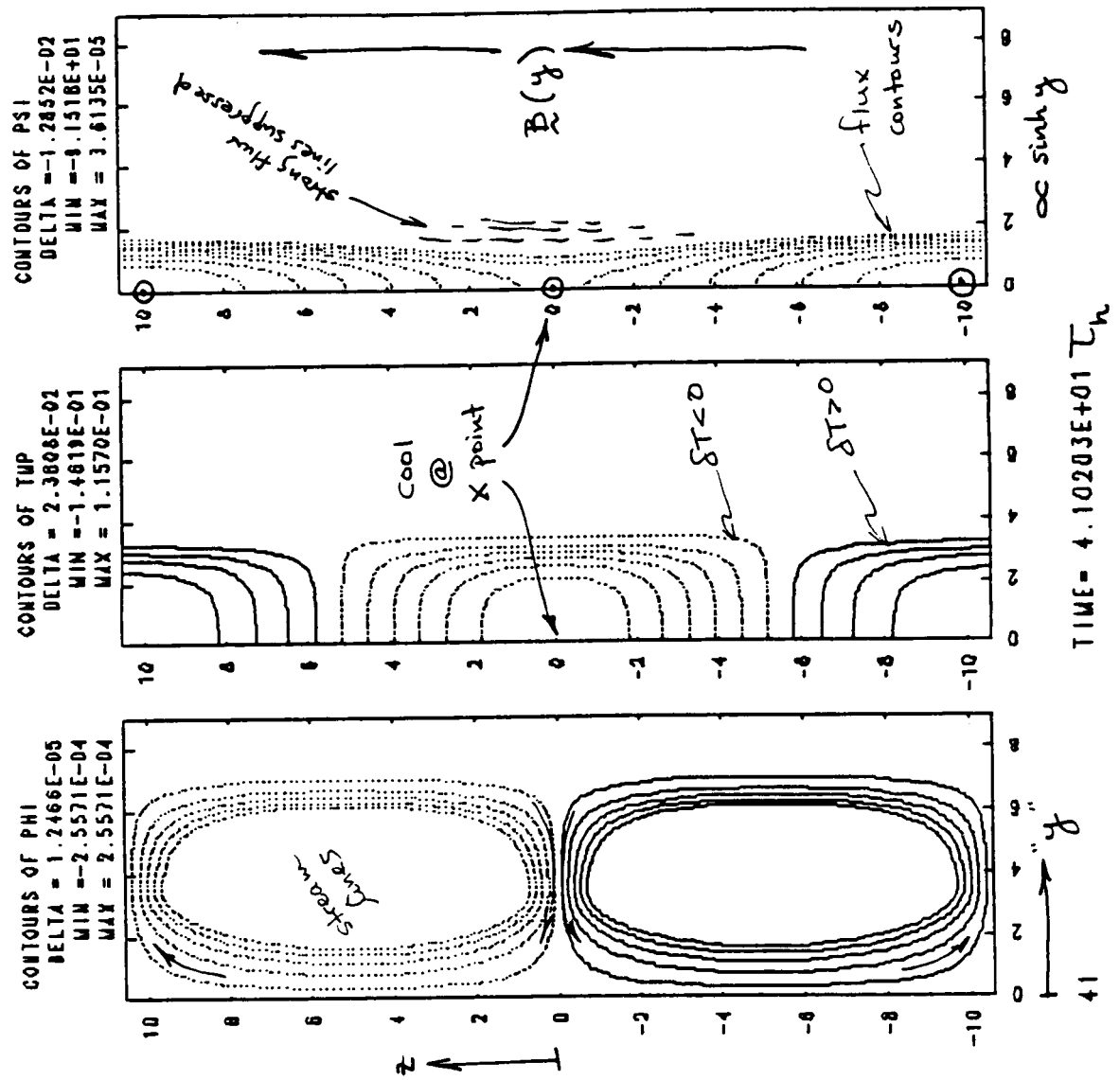
2. Nonlinear limit by computer experiment

⇒ a) sharp reconnection gradients
b) $T/T_0 \rightarrow 10^{-2}$, $\eta/\eta_0 \rightarrow \underline{\underline{10^3}}$

⇒ burst of very fast reconnection

$$\frac{\partial B}{\partial t} \sim \frac{\eta(T)}{\mu_0} \nabla^2 B \rightarrow B/T_h$$

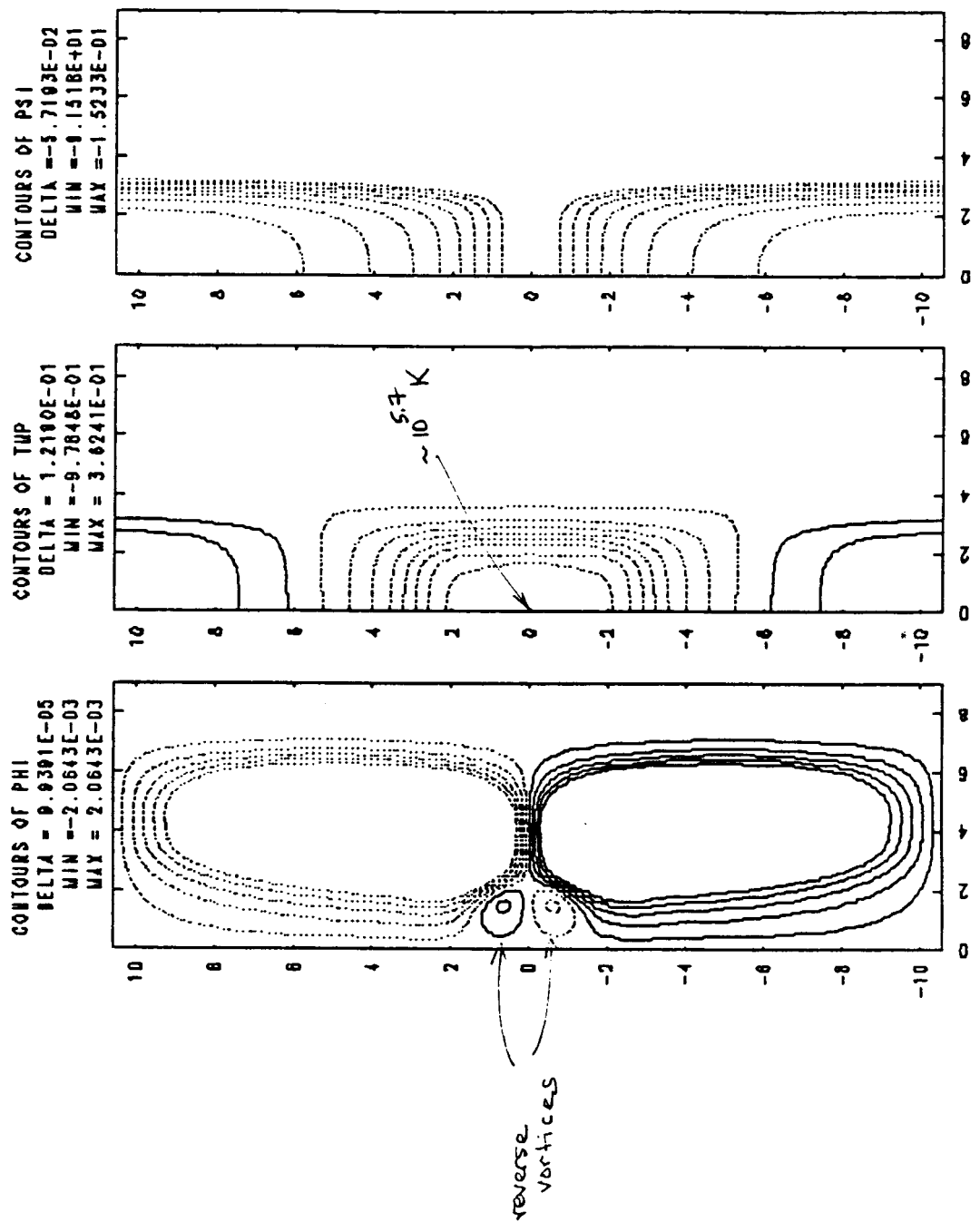


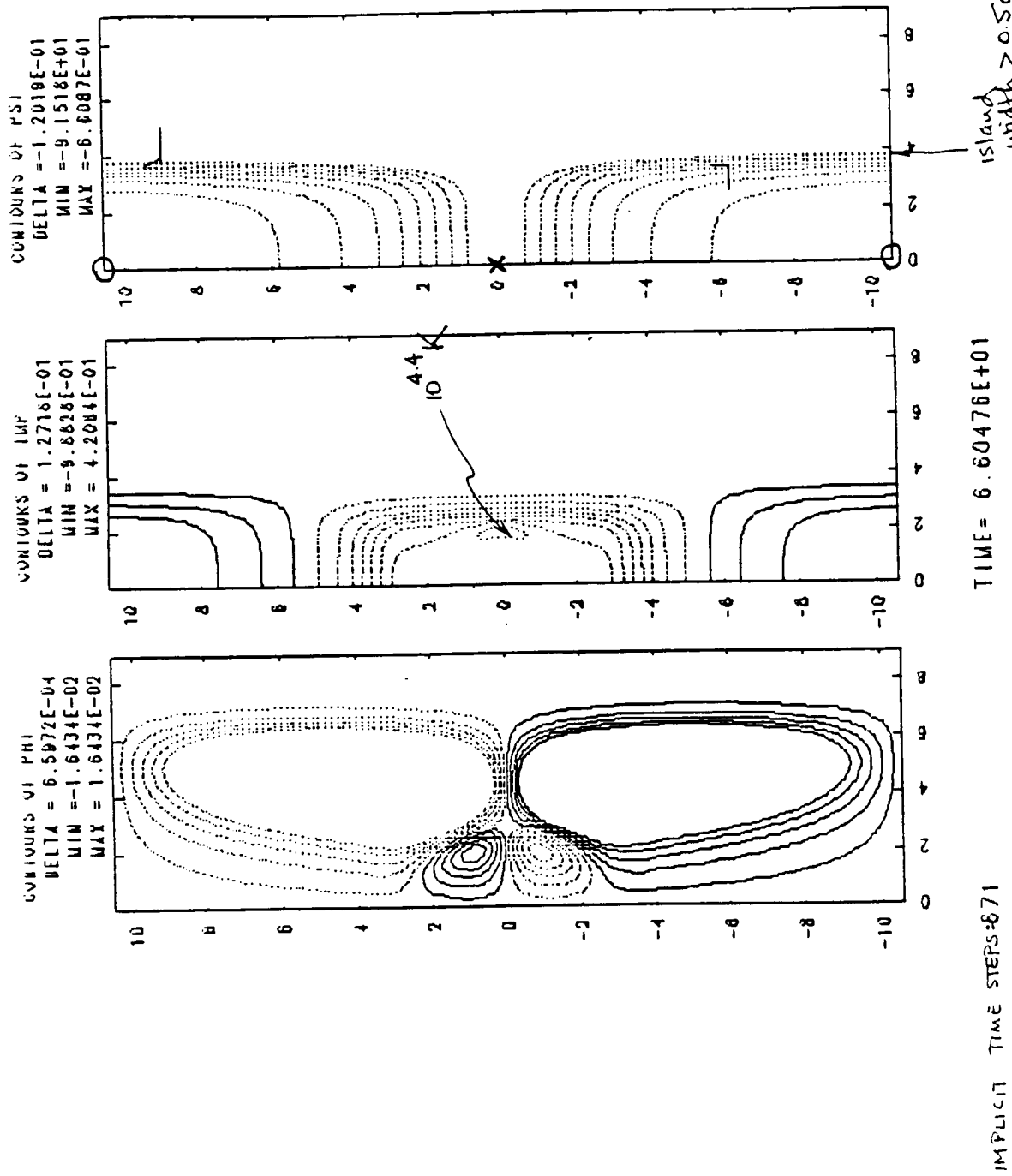


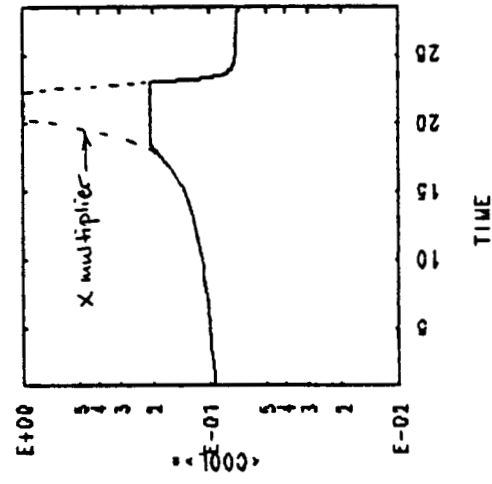
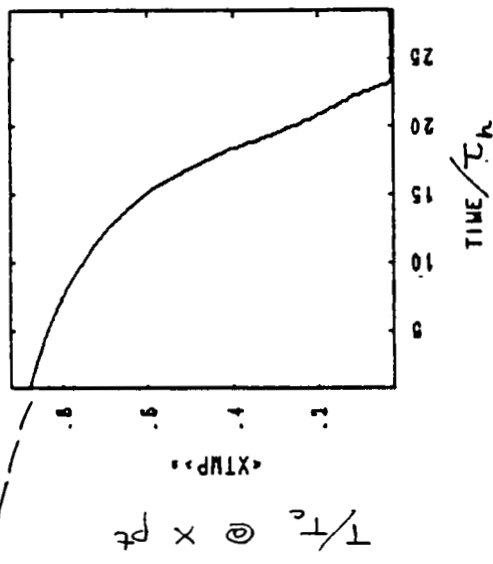
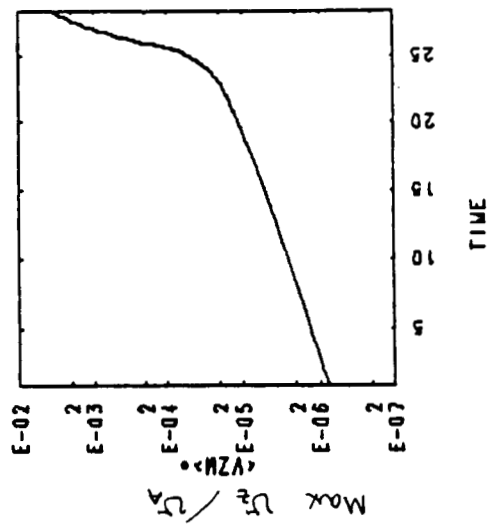
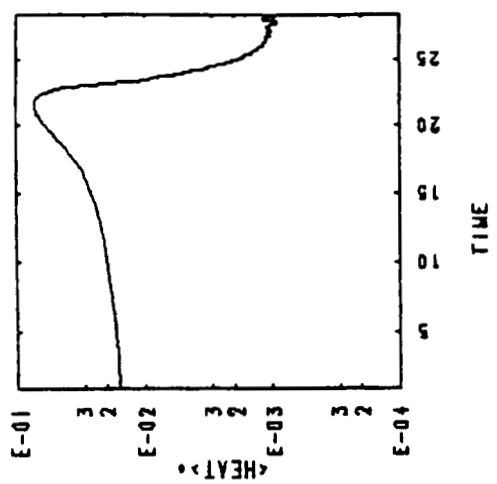
ORIGINAL PAGE IS
OF POOR QUALITY

TIME = 6.27868E+01

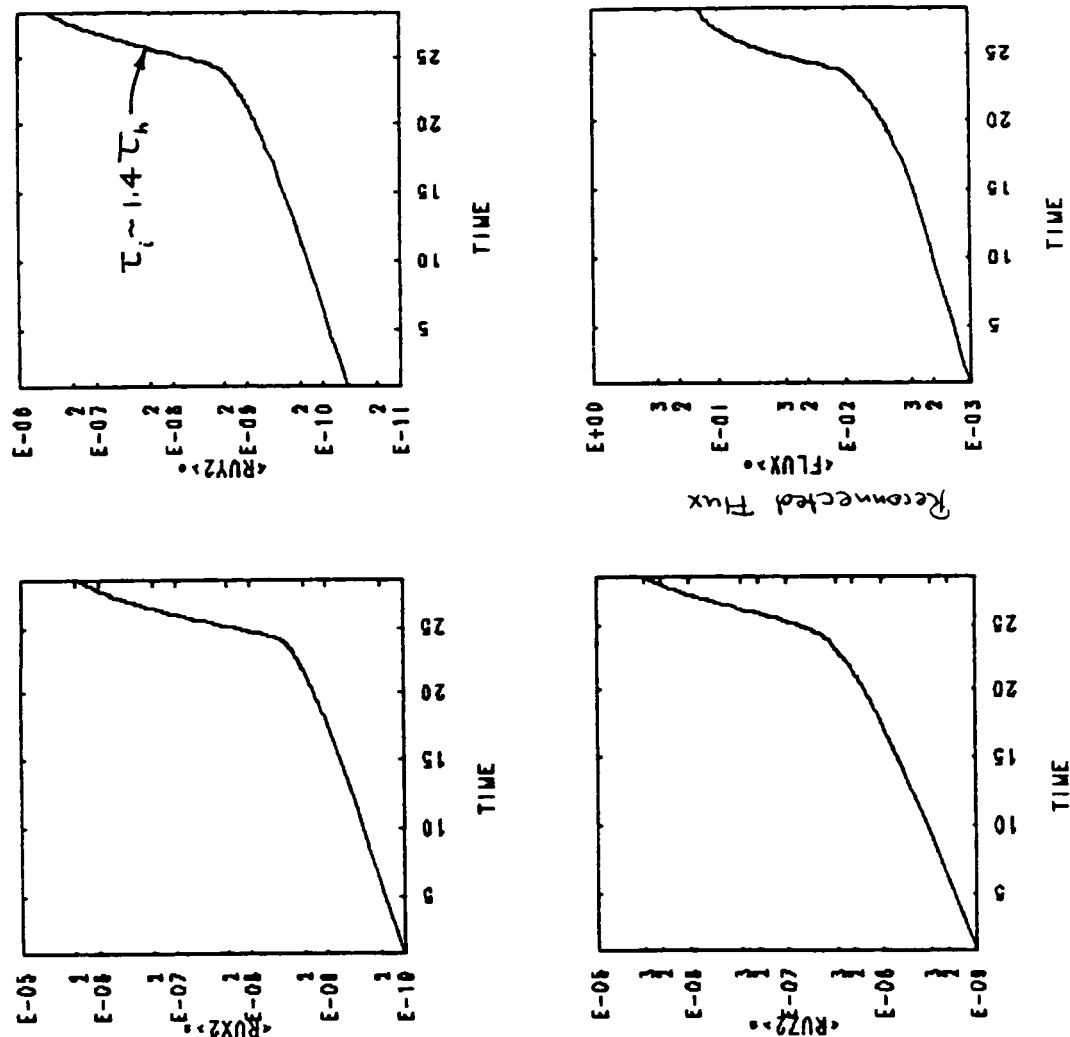
301

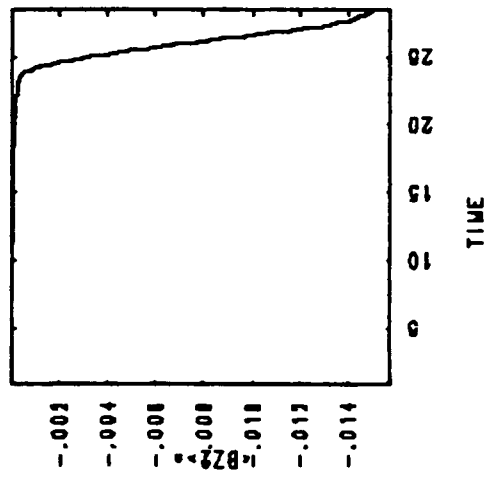
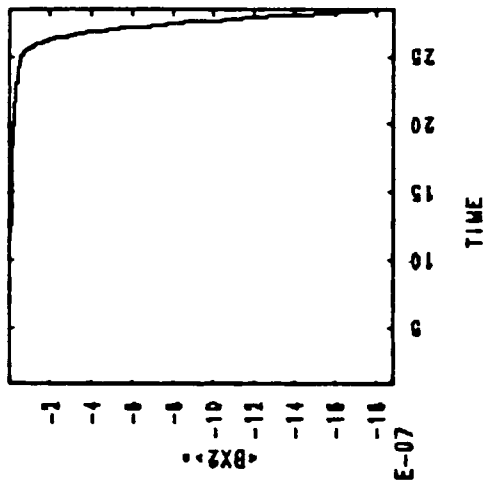
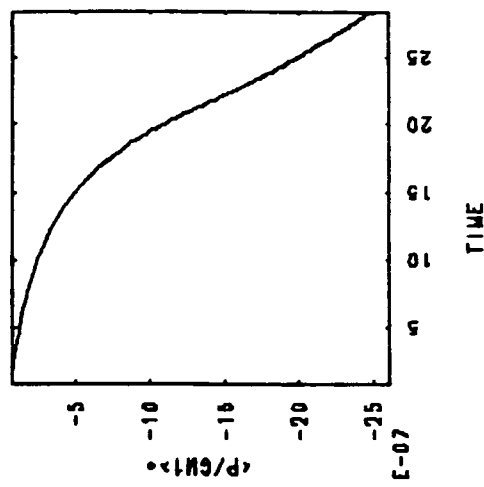
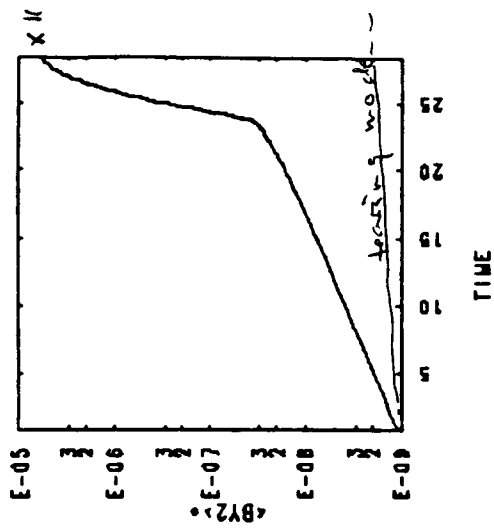






$d\delta n_{310}(\mu_{\mu}, j)$





RESULTS:

1. Magnetic tearing occurs initially at a fast radiative-instability rate,
 $\Omega_{rad} \sim 10^{-0.9} nT^{-2}$
2. Temperature falls from $10^6 K$ to $10^4 K$,
so that the Coulomb resistivity $\eta \sim T^{-3/2}$
increases by $10^3 \times$
3. The high resistivity and sharp gradients
($\delta/a \sim 10^{-1}$) lead to a burst of
very fast* reconnection $\Omega_{rec} \tau_h \sim 1$
4. Saturation appears to occur in the
same way as for the normal
tearing mode.

$$* \quad \tau_{re} \sim \left(\frac{T}{T_0}\right)^{3/2} \left(\frac{\delta}{a}\right)^2 S_0 \tau_{hg}$$

ARCHES SHOWING UV FLARING ACTIVITY

J. M. Fontenla

ES52/Marshall Space Flight Center

Abstract

The UVSP data obtained in the previous maximum activity cycle show the frequent appearance of flaring events in the UV. In many cases these flaring events are characterized by at least two footpoints which show compact impulsive non-simultaneous brightenings and a fainter but clearly observed arch develops between the footpoints. These arches and footpoints are observed in lines corresponding to different temperatures, as Lyman alpha, N V and C IV, and when observed above the limb display large Doppler shifts at some stages. The size of the arches can be larger than 20 arc sec.

Summary

The flaring arches are a rather important constituent of the evolution of active regions in the times between the large flares; also according to Svestka (1988) they constitute a component of the large flares. Their role in the overall energy balance of the active regions is not easy to assess since there is not yet statistics on these events and their distribution and there is no accurate estimate of the released energy in such events.

Since in many aspects the network elements are similar to small active regions, one can expect that these phenomena can also contribute to the energy release in the quiet sun network.

The flaring arches cover a large dynamic range, from rather small events which can be called microflares which are well observed in the transition region lines but at present with no detected counterparts in X-rays and H alpha, up to more energetic events sometimes called compact subflares which display clear X-ray and H alpha signatures.

We believe the less energetic of these events are basically identical to the microflares observed by Porter et al. (1984), and the most energetic are those related with compact flares and can be easily identified in the HXIS X-ray data, like for instance the flaring arches studied by Martin and Svestka (1988).

Some of these UV brightenings are studied by Fontenla et al. (1988) who propose a model of the time development of the brightenings and small UV surges associated with them. The model consists in the sudden release of thermal energy at chromospheric layers where the thermal conduction is not efficiently transmitting the heat to the regions above, nor is able to emit it efficiently in optically thick lines. The resulting overpressure will then accelerate the cold material above along the magnetic field lines and gradually heat it up. This model fits well with the general behavior of the flaring arches we are reporting here, although at that time the X-ray data was unknown to the authors.

The flaring arches are characterized by impulsive brightening of a small area (or primary footpoint) in all transition region lines and (in the cases where we found observations) also in X-rays. Then with extremely short delay, one or more secondary footpoints also display impulsive brightenings. Later, a bridge of fainter emission develops between the footpoints and frequently remains slowly fading after the brightenings of the footpoints disappear. It is also common to observe more than one simple spike in the primary footpoint (probably in a slightly different unresolved location) and several spikes at different

places along the arch. The phenomenon clearly often shows that the arch consists in several magnetic loops with very close primary footpoints but scattered secondary footpoints, and that there is more than one energy release.

There seem to be a continuous range between the small and the large events. However, in the more energetic events, the footpoints in the UV lines are rather intense; in the brighter events the footpoints were so bright that the UVSP instrument shut off at the times the raster reached the primary footpoint. The bridging material does not show such a large increase of intensity in the transition region lines and may even display a decrease in intensity for the more energetic events. In any case, we observe that the contrast in the transition region temperature material between the footpoints and the bridging material increases dramatically with the intensity of the event.

We have observed flaring arches in lines from Lyman alpha up to Fe XXI, which shows the extreme range in temperature of events of this nature, a span from about 10^4 to at least 10^7 K. It is not clear whether the more energetic events reach higher temperatures or just the emitting volume is not large enough so their high temperature emission can be easily observed. Preliminary comparison with X-ray shows that at least in the more energetic events, there is a clear correspondance between the transition region lines brightenings and HXIS localized flaring (courtesy of Z. Svestka).

It is of particular importance to observe in several transition region lines with good spatial and temporal resolution, with coordinatedly imaging X-rays to asses the time evolution of the material there. Such observations promise important findings in the process of magnetical energy release which seem to occur in the flaring arches. Particularly the transition region temperature material is able to produce substantial emission that can be detected easier than H alpha emission. The timing between the colder and hotter emissions would indicate wether the material which is being injected into the arch from the primary footpoint is initially hot and cools down (chromospheric evaporation) or is initially cold

and heats up as proposed by Fontenla et al. (1988). The Doppler velocities of the material should also be observed; their relation to the heating or cooling of the material will clarify if the apparent motion constitutes a real mass motion or the progress of a condensation front.

We consider it of great importance to study in Max91 not only the large flares, but also the smaller ones which are more simple in their structure and are more suitable for theoretical modeling and diagnostics.

THE NEED FOR HARD X-RAY IMAGING OBSERVATIONS
AT THE NEXT SOLAR MAXIMUM

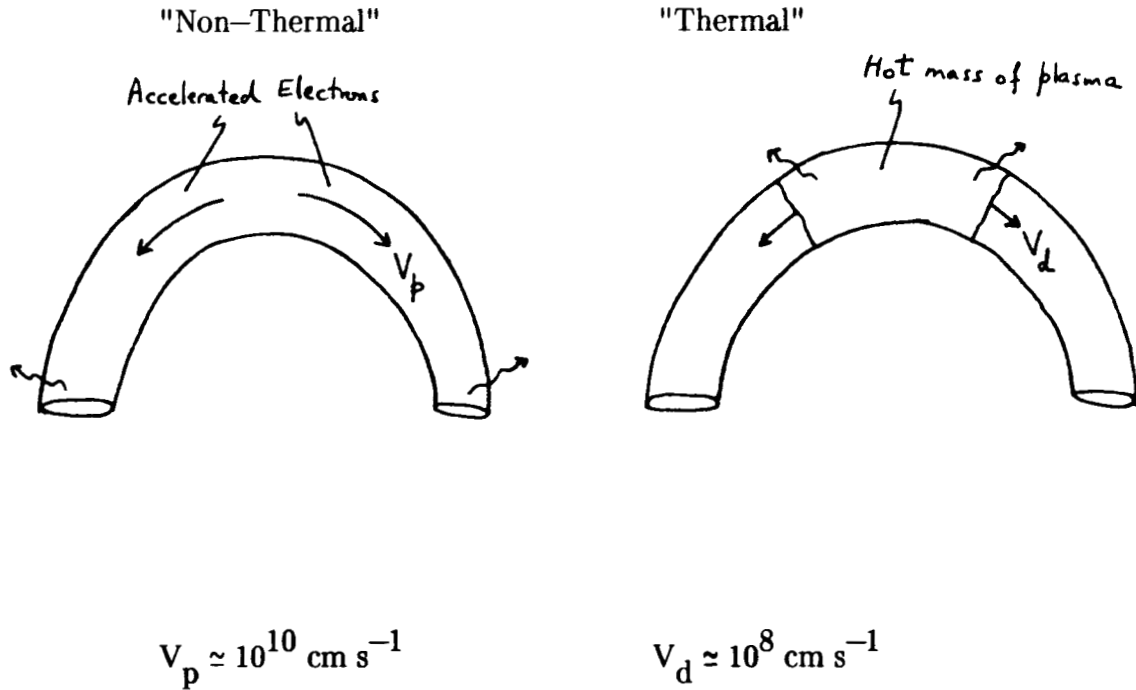
A. Gordon Emslie

Department of Physics, UAH, Huntsville, AL

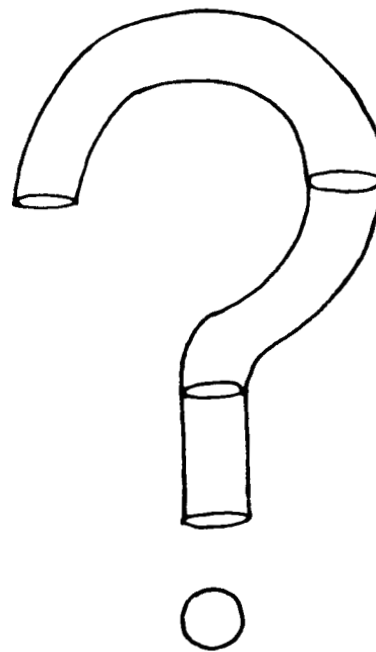
OUTLINE

1. Canonical Models of Solar Hard X-ray Bursts
2. Associated Length and Time Scales
3. Previous Observations – their adequacies and inadequacies
4. Theoretical Modeling – Predictions to be tested
5. What Can be Learned from Arc-second Imaging of Solar Hard X-Rays
 - a. Location of Energy Release Site
 - b. Nature of Acceleration/Heating Mechanism
 - c. Nature of Transport Processes.

CANONICAL (SPELT "GROSSLY OVERSIMPLIFIED") MODELS OF
SOLAR HARD X-RAY BURSTS



REAL MODEL OF SOLAR HARD X-RAY BURSTS



LENGTH AND TIME SCALES

(1) Non-Thermal Model

- Electron travel time $\simeq 0.1$ s (too short for direct imaging time sequence)
- Collision time given by energy loss equation

$$\frac{dE}{dt} = -\frac{K}{E} n v$$
$$E^{3/2} = E_0^{3/2} - \frac{3}{2} \left[\frac{2}{m_e} \right]^{1/2} K n t.$$

For $E_0 = 20$ keV, $E = 15$ keV, $t = \frac{4 \times 10^9}{n(cm^{-3})} \simeq 0.04$ s for $n = 10^{11} cm^{-3}$

- Collisional Length

$$E^2 = E_0^2 - 2 K n z.$$

For $E_0 = 20$ keV, $E = 15$ keV, $z = \frac{3 \times 10^{19}}{n(cm^{-3})} \simeq 3 \times 10^8 cm \simeq 4''$ for $n = 10^{11} cm^{-3}$

- Even in steady-state, the 10 – 20 keV hard X-ray spectrum should evolve significantly on size scales of a few arc seconds

(2) Thermal Model

- Source diffuses into cool corona at $V_d \simeq c_s \simeq 10^8 cm s^{-1} \simeq 2''/sec.$
- With $\simeq 1$ second time resolution, should be able to follow evolution of source

PREVIOUS OBSERVATIONS

(1) SMM HXIS/ Hinotori SXT

Spatial Resolution $\simeq 8''$

Temporal Resolution $\simeq 10$ s

- Adequate to reveal footpoints in early phase, and amorphous source in late phase, but unable to delineate transformation (evolution?) between the two
- Possible low-intensity background present (comparison of HXIS and HXRBS spectra indicates that only about 10% of the emission in the HXIS energy bands was contained in the transmitted pixels)

(2) ISEE-3/PVO

- Occultation of low part of flare by solar disk. Only a fraction of a percent of the emission at high (100keV) energies comes from above 25,000 km.
- Spectra consistent with thin target nonthermal emission ($\gamma = \delta + 1$) in upper part of loop, and thick target nonthermal emission ($\gamma = \delta - 1$) over entire loop.

THEORETICAL MODELING (THICK-TARGET)

- Electron beam creates direct bremsstrahlung (dashed lines), and also heats atmosphere, leading to thermal bremsstrahlung (solid lines).
- Intensity in middle of loop rises due to *two* reasons: (i) evaporation of the target (non-thermal emission), and (ii) heating of coronal plasma (thermal emission).

Low Energies ($\lesssim 15$ keV)

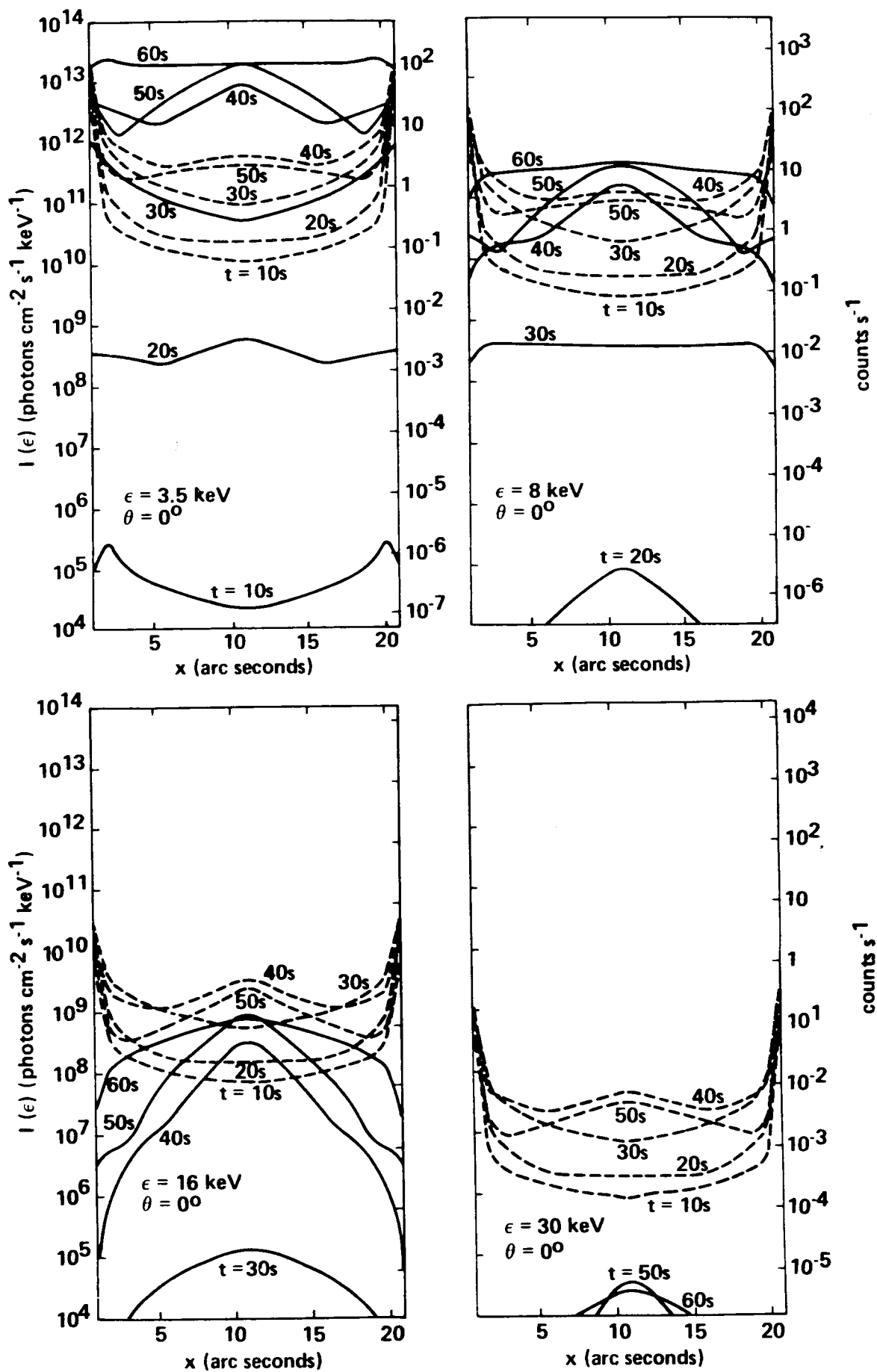
- At first nonthermal emission dominates and shows a strong footpoint signature ($x = 0$ and $x = 21$ arc seconds in the figure).
- Later, nonthermal footpoints are still strong, but the thermal bremsstrahlung from the beam-heated plasma starts to dominate.

High Energies ($\gtrsim 15$ keV)

- Whole event dominated by nonthermal emission. Footpoints less dominant as target evaporates.

Implications of Theoretical Results

- Need to observe at high ($\gtrsim 15$ keV) energies with a few arc second spatial resolution and $\simeq 10$ s temporal resolution to adequately test predicted features.



WHAT CAN BE LEARNED FROM IDEAL DATA?

- If the observed region is sufficiently small, then the emission from the region is thin-target emission, from which it is relatively straightforward to deduce a local electron spectrum.
- We can therefore follow the evolution of this spectrum with space and time, and thereby test the following:
 - Location of Energy Release
 - Nature of Accelerated Particle Spectrum
 - Physics governing Evolution of Particle Spectrum (Transport Processes)
 - (i) Collisions
 - (ii) Reverse Currents
 - (iii) Collective Plasma Processes
 - (iv) Magnetic Mirroring
 - etc., etc.
- It should also be possible, with sensitive enough data, to observe the backscattered albedo patch and so discern the height of the illuminating source.

SUMMARY

With arc-second imaging of solar hard X-rays, with enough sensitivity to provide a few seconds time resolution at energies of order 15 keV and above, we should make major advances in our knowledge of:

- Whether Solar Hard X-Ray Emission is Predominantly Thermal or Non-Thermal
- Whether the Energy Release itself is Predominantly Thermal or Non-Thermal
- The Accelerated Particle Spectrum (Non-Thermal Model)
- The Temperature Distribution of the Source (Thermal Model)
- The Hydrodynamic Response of the Atmosphere to Flare Energy Input

We can also:

- Publish many papers, conference proceedings, etc, and become very famous.

The Fourier Imaging X-Ray Spectrometer (FIXS)

for the

Argentinian, Scout-launched

Satelite de Aplicaciones Cientificas - 1 (SAC - 1)

Brian R. Dennis, Carol Jo Crannell, Upendra D. Desai, Larry E. Orwig - GSFC
Alan L. Kiplinger, Richard A. Schwartz - STX
Gordon J. Hurford - Caltech
A. Gordon Emslie - U. Alabama in Huntsville
Marcos Machado - CNIE Argentina
Kent Wood - NRL

ABSTRACT

The Fourier Imaging X-Ray Spectrometer (FIXS) is one of four instruments on SAC-1, the Argentinian satellite being proposed for launch by NASA on a Scout rocket in 1992/3. FIXS is designed to provide solar flare images at X-ray energies between 5 and 35 keV. Observations will be made on arcsecond size scales and subsecond time scales of the processes that modify the electron spectrum and the thermal distribution in flaring magnetic structures.

FIXS will be capable of imaging X-ray sources that are as large as 3 arcminutes in extent with a resolution as small as 2 - 3 arcseconds. It will have a sensitivity two orders of magnitude greater than that of the Hard X-ray Imaging Spectrometer (HXIS) on SMM. These advanced capabilities are made possible on such a small spin-stabilized spacecraft by using a Fourier-transform imaging technique. Six rotating modulation collimators (RMCs), each with its own xenon proportional counter, are used to measure over 150 spatial Fourier components of the X-ray image. The amplitudes and phases of the Fourier components are determined in real time on board the spacecraft so that ~1000 images per flare can be telemetered. Reconstructed X-ray images can be obtained during a flare in up to 15 energy channels every 2 s; for larger flares, less complete images will be produced on subsecond time scales. This technique of measuring the spatial Fourier components of a source and reconstructing the X-ray image on the ground is mathematically analogous to the imaging technique used in multi-baseline radio interferometry.

The Fourier Imaging X-Ray Spectrometer - FIXS

The FIXS instrument, consisting of six modulation collimators mounted on a rotating spacecraft, is designed to provide images of solar flares at X-ray energies between 5 keV and 35 keV. In this energy range, FIXS will have significantly improved sensitivity, angular resolution, and time resolution compared to any other X-ray imager previously flown or planned for the next solar maximum. The primary objective is to investigate the processes of particle acceleration and plasma heating in solar flares. In particular, FIXS will address the following scientific questions:

- What are the sites of particle acceleration and interactions and how do they evolve spatially and spectrally during flares?
- What role in the overall flare process do energetic electrons play, particularly those with energies below \sim 50 keV, where the bulk of the total energy in electrons must reside?
- What are the sites of plasma heating and how does the thermal energy propagate during flares?
- What is the relationship between the thermal flare plasma and the energetic particles and what role does the "superhot" plasma ($T_e > 3 \times 10^7$ K) play?

To achieve these objectives, FIXS will be capable of imaging X-ray sources that are as large as 3 arcminutes in extent with a resolution as small as 2 - 3 arcseconds. It will have a sensitivity two orders of magnitude greater than that of the Hard X-ray Imaging Spectrometer (HXIS) on SMM and will obtain complete images in up to 15 energy channels every 2 s, with less complete images on subsecond time scales for larger flares. Relative motion of sources from one image to the next will be detectable at the 1 arcsecond level or better. The high sensitivity and fine angular resolution will allow studies to be made on the arcsecond size scales and subsecond time scales which are characteristic of the flaring magnetic structures and of the processes that modify the electron spectrum and the thermal distribution. The high sensitivity and full Sun coverage will allow the spatial study of many flares during the lifetime of SAC-1, thus providing a large sample of flares for statistical analysis.

One aspect of the scientific potential of FIXS can be demonstrated by comparing its capabilities with the expected source dimensions and time scales in two competing solar flare models. For the thick-target model, FIXS can be expected to detect substantial changes in the X-ray spectrum around 20 keV

on size scales of 2 - 3 arcseconds. This is because a 20 keV electron loses 5 keV in a column density of $1.8 \times 10^{19} \text{ cm}^{-2}$, which, for a typical density of 10^{11} cm^{-3} , corresponds to a distance of $1.8 \times 10^8 \text{ cm}$ or 2.4 arcseconds. The time scale of ~ 20 ms is probably beyond the capability of FIXS to resolve. For the thermal model, the high-temperature source expands into the coronal plasma at the ion sound speed of $\sim 10^8 \text{ cm s}^{-1}$ or 1 arcsecond per second. Thus, FIXS should be able to clearly detect the temperature difference across the thermal conduction fronts and trace their movement along the magnetic loop down to the footpoints. The vastly different signatures of the X-ray images in the FIXS data and their evolution during the impulsive phase should allow a clear separation to be made between the two models.

Instrument Characteristics

The FIXS design is based on a Fourier-transform imaging technique. Six rotating modulation collimators (RMCs), one of which is shown in Figure 1, are used to allow up to 144 spatial Fourier components of the X-ray image to be measured during each half rotation of the spacecraft, i. e., every ~ 2 s. The amplitudes and phases of these Fourier components are determined on board the spacecraft in real time so that the information that must be telemetered is reduced to a minimum within the constraints of the available bit rate. The X-ray images are reconstructed on the ground from these Fourier components with the same mathematical techniques used at the VLA and other multi-baseline radio interferometers.

A schematic diagram of a single modulation collimator is shown in Figure 1. The two tungsten grids are separated by 40 cm with identical slit widths and slit spacings. The two grid planes are parallel to each other and the slits are also all parallel and uniformly spaced. The normal to the grid planes, i. e., the axis of the collimator, is parallel to the spacecraft spin axis. The slit widths range from 16 microns for sources with angular sizes as small as 2 - 3 arcseconds to 350 microns for sources that are as large as 3 arcminutes. A xenon proportional counter placed below the bottom grid detects the temporally modulated X-ray signal and provides spectral information with 2 - 3 keV (FWHM) energy resolution between 5 keV and 35 keV. The thickness of xenon at two atmospheres is 5 cm, thus giving $\sim 30\%$ absorption at 30 keV. A graduated aluminum absorber above the counter prevents saturation from the intense flux of soft X-rays during a large flare while transmitting most of the higher energy photons. The sensitive area of the proportional counter and the area of the bottom grid are both circles with a diameter of 6 cm while the top grid has a diameter of 10 cm. In this way the full 6-cm diameter area is always covered by the top grid even when the spin axis of the spacecraft is 3° from the direction to the Sun, the maximum offset angle to be allowed by the spacecraft aspect control system.

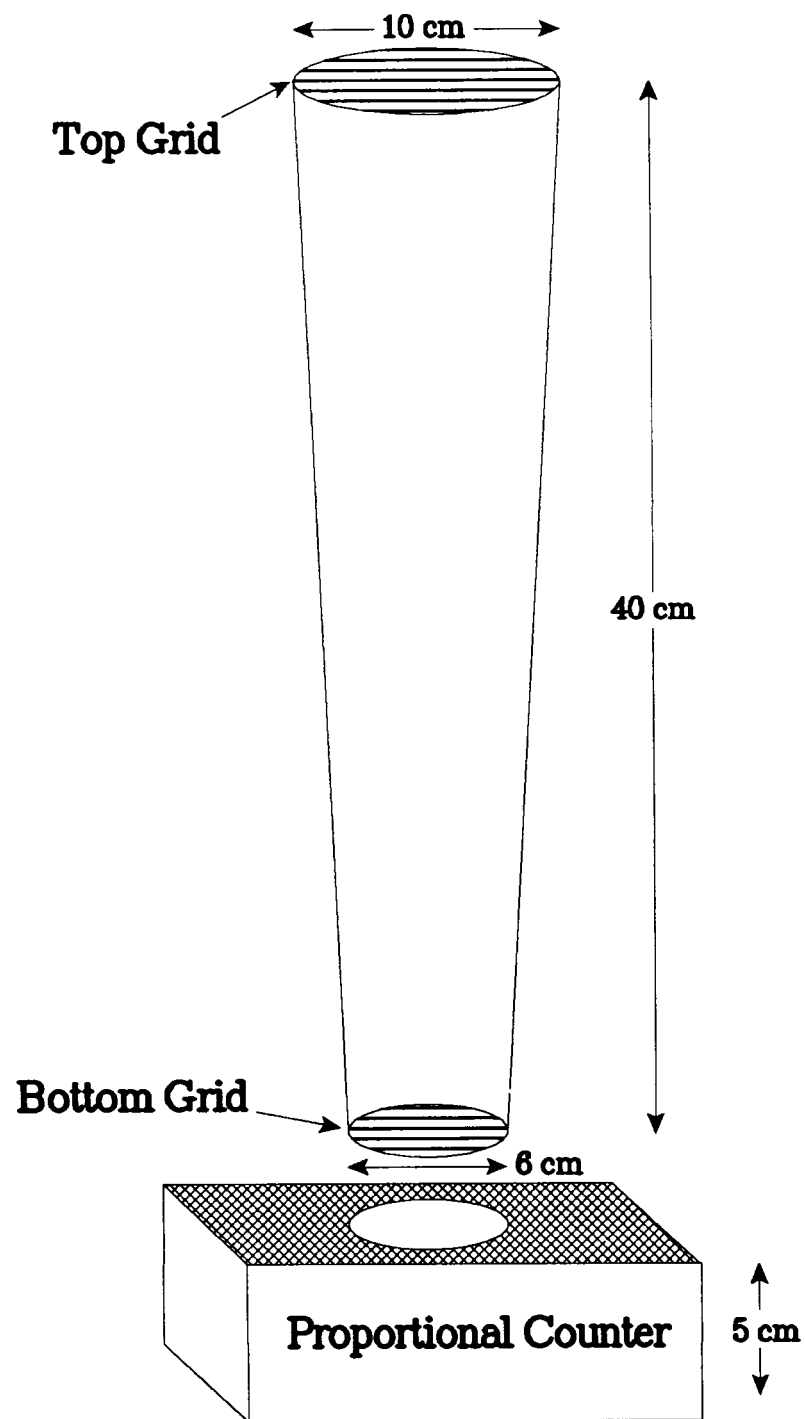


Figure 1. Schematic diagram of one of the six modulation collimator/detector units that make up the FIXS instrument.

The Aspect System

The aspect of the collimators is determined at all times from a solar limb detector that uses a lens mounted on the top grid with a slit and photocell mounted on the bottom grid. This aspect system is shown schematically in Figure 2. The solar image formed by the lens is projected onto the bottom grid plane. As the spacecraft rotates with the spin axis offset from the solar direction by 1 - 3°, the solar image passes over the slit to provide a modulated signal from the photocell. The times of passage of the slit across the solar limbs are marked by rapid increases or decreases in the signal and these times provide a strobe for data collection and also allow the angular distance from the spin axis to sun-center to be determined. Smaller modulations in the photocell output as the slit crosses the solar disc will result from the presence of sunspots. The exact times of these dips will be used on the ground to determine the azimuthal location of the spin axis around the solar direction and hence will allow the flare locations to be determined unambiguously.

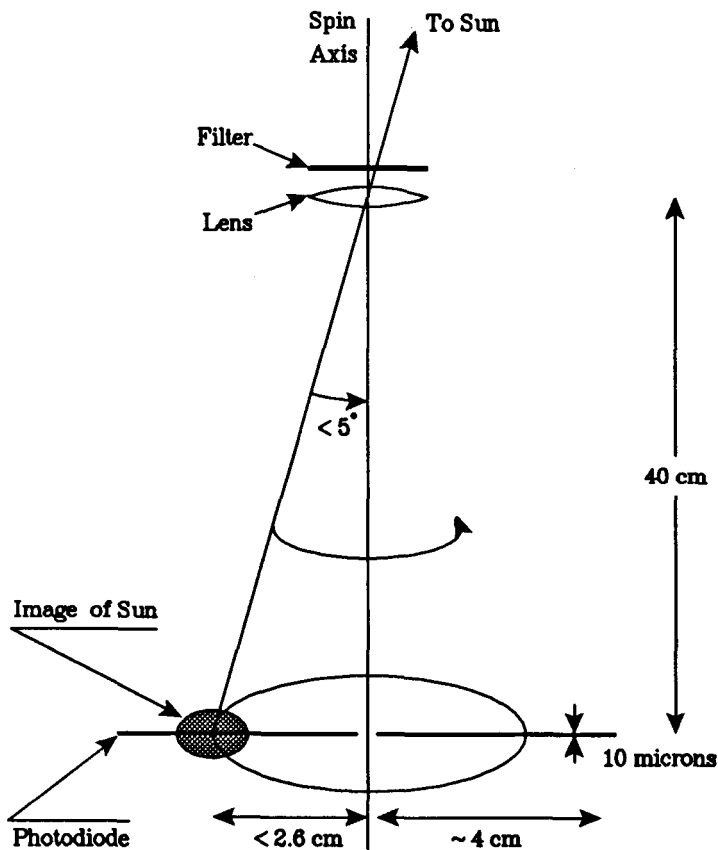


Figure 2. The proposed FIXS aspect system.

On-Board Data Analysis

The on-board determination of the amplitude and phase of the spatial Fourier components from the temporally modulated X-ray signals from the six RMCs is designed to minimize the number of bits to be telemetered. Basically the method involves the use of three microprocessors, one to analyze data from the aspect system and to determine the coarse flare location, one to bin the data for the 144 Fourier components, and one to handle commands and data transmission. Once a flare has begun, its coarse location is determined by comparing the modulated signal from the coarsest RMC with the time profiles expected for sources at different radial distances from the spin axis. These time profiles for half a rotation are stored in the memory of the microprocessor for every arcminute in radial distance from 1° to 5° . By finding the profile that best fits the observed modulation, the flare radial distance from the spin axis and its azimuthal location can be determined and passed on to the second microprocessor.

Once the coarse flare location has been determined, the period of the modulation is known for each 15° of rotation since these are also stored in memory for all radial distances and azimuths. The second microprocessor bins the X-ray data from each RMC and for each energy channel or group of channels modulo these periods for the corresponding rotation angles. The resulting 4-bin distributions contain the information on the amplitudes and phases of all the Fourier components plus the unmodulated background counting rates, and these are stored for later telemetry. In this way, the number of bits that must be telemetered is reduced to a minimum without sacrificing the quality of the images, the time resolution, or the energy resolution of the instrument. Data for over 500 images can be transmitted within the constraints of telemetering 2 Mbits of data every 12 hours imposed by the spacecraft and the single Argentinian ground station. These images can be selected as desired to give high time resolution during the impulsive phase, for example, high energy resolution at less frequent intervals, or poorer time resolution over a longer total time interval for more gradually varying flares. One constraint is that data for images obtained on successive rotations cannot be easily summed together on the spacecraft prior to transmission because of the precession of the spin axis.

Satelite de Aplicaciones Cientificas - 1 (SAC - 1)

Fundamental Parameters

Spacecraft

Mass:	161 kg
Scientific payload:	30 kg
Orbit:	Polar, dawn-dusk, sun-synchronous
Type:	Spin-stabilized
Spin axis:	1 - 3 degrees from direction to Sun
Spin rate:	15 rpm
Origin:	Argentina

FIXS Instrument

Mass:	14 kg
Power:	11 watts
Telemetry:	2 Mbits per dump, one dump per 12 hours
Maximum length:	50 cm

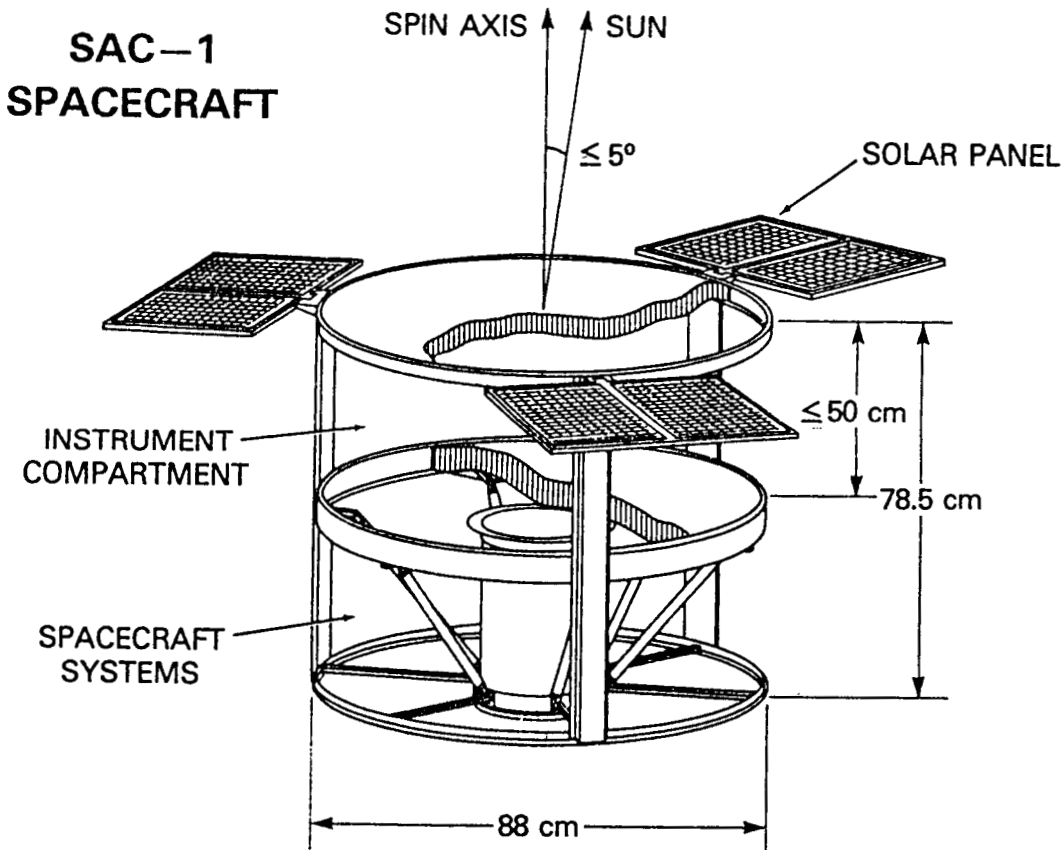


Figure 3. Schematic diagram of the proposed SAC-1 spacecraft

Fourier Imaging X-Ray Spectrometer FIXS

Basic parameters and capabilities.

Design:	Multiple rotating modulation collimators.
Number of subcollimators:	6 tungsten grids, 50 microns thick
Slit widths:	16, 27, 46, 87, 175, 350 microns
Distance between grids:	40 cm
Rotation rate:	15 rpm
Energy range:	5 - 35 keV
Energy resolution:	1 - 2 keV
Number of channels:	15
Efficiency:	10^{-6} at 5 keV, 0.0015 at 6.5 keV, 0.16 at 10 keV, 0.66 at 20 keV, 0.4 at 30 keV
Angular resolution:	3 arcseconds for strongest flares
Field of view:	Whole Sun
Source sizes imaged:	up to 3 arcminutes
Time resolution:	2 s for complete two-dimensional image from ~300 Fourier components, 0.1 s for one-dimensional image from 6 to 8 Fourier components
Effective area:	40 cm ²
Maximum number of images per flare:	>1000

Fourier Imaging X-Ray Spectrometer

FIXS

Collimator Specifications

Collimator type:	Parallel-slit bigrid subcollimators
Number of subcollimators:	6
Top grid diameter:	10 cm
Bottom grid diameter:	6 cm
Separation:	40 cm
Angular resolutions:	8, 14, 24, 45, 90, 180 arcsecond (first harmonic) 2.7, 4.7 and 8 arcsec (third harmonic)
Slit widths:	16, 27, 46.5, 87, 175, 350 microns
Material:	Tungsten
Thickness:	50 microns
Sensitive area:	7 cm ² per subcollimator

Detector Specifications

Type	Xenon proportional counters
Number:	6
Dimensions:	12 cm long, 6.3 cm diameter
Weight:	~0.5 kg
Window:	Beryllium 10 mil (0.025 cm) thick
Window area:	Circular with a diameter of 6 cm
Absorber:	Aluminum, 0.025 cm thick
Fill gas:	97% xenon, 3% CO ₂ , at two atmospheres
Voltage:	<3000 volts
Power:	30 - 40 mW
Energy Range:	5 - 35 keV
Resolution:	1 - 2 keV
Lifetime:	>10 ¹² total counts
Channels:	15
Manufacturer:	R e u t e r S t o k e s o r L N D o r PGT/Outukumpu(Finland)

Comparison with Previous Instruments

HXIS on SMM

Energy range:	3.5 - 30 keV, 6 channels
Angular resolution: (FWHM)	8 arcseconds (fine field of view) 32 arcseconds (coarse field of view)
Field of view:	2.7 arcminutes (fine), 6.4 arcminutes (coarse)
Time resolution:	1.5 s nominal, >10 s actual
Effective area per pixel:	0.077 cm ²

SXT on Hinotori

Energy range:	5 - 40 keV or 17 - 40 keV, 1 channel
Angular resolution:	~10 arcseconds
Field of view:	Full Sun
Time resolution:	~6 s (1/4 of spin period)
Total sensitive area:	~10 cm ²
Effective area:	~1 cm ²

Comparison with Future Instruments

Hard X-Ray Telescope on Solar-A

Energy range:	15 - 100 keV, 4 channels
Angular resolution:	~5 arcseconds
Field of view:	Full Sun
Time resolution:	0.5 s
Total sensitive area:	1.5 cm ² (average) x 64 elements
Effective area:	

GRID on a balloon

Energy range:	20 keV - 1 MeV
Angular resolution:	1.7 arcsecond
Field of view:	Full Sun
Time resolution:	0.1 - 2 s
Total sensitive area:	~600 cm ²
Effective area:	~150 cm ²

Soft X-Ray Telescope on Solar-A

Energy range:	<4 keV
Angular resolution	3 arcseconds
Field of view:	selectable
Time resolution:	n/a
Effective area:	4 cm ²

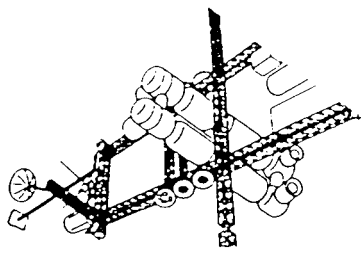
Imaging Solar Flares in Hard X Rays and Gamma Rays
from Balloon-Borne Platforms

Carol Jo Crannell

Laboratory for Astronomy and Solar Physics
NASA-Goddard Space Flight Center

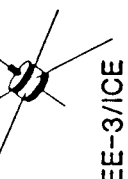
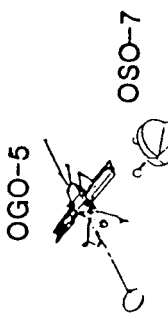
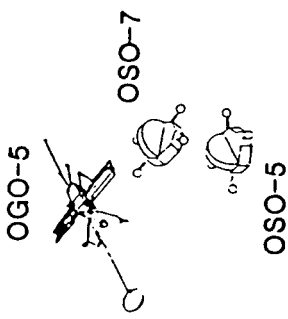
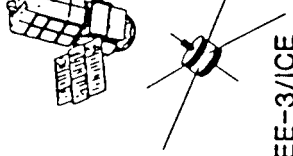
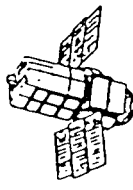
Hard X rays and gamma rays carry the most direct evidence available for the roles of accelerated particles in solar flares. An approach that employs a spatial Fourier-transform technique for imaging the sources of these emissions is described and plans for developing a balloon-borne Gamma Ray Imaging Device based on this instrumental approach is presented. This instrument, GRID on a Balloon, would enable observations with 1.6-arcsecond angular resolution, 10-millisecond time resolution, and whole-Sun field of view on long-duration balloon flights during MAX '91.

NASA SOLAR FLARE MISSIONS



Space Station

SMW

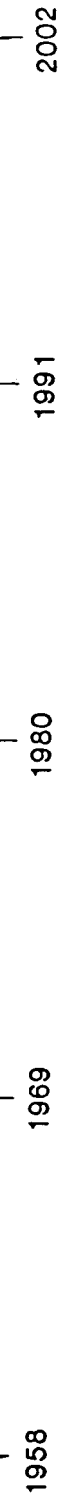


the gap

Peterson & Winckler



SKYLAB



**Proposal for a
GAMMA-RAY IMAGING DEVICE
(GRID)
ON A
BALLOON**

GSFC

Principal Investigator: C. J. Crannell (301) 286-5007

Co-Investigators:

GSFC

B. R. Dennis

W. D. Hibbard

A. L. Kiplinger

E. R. Maier

L. E. Orwig

R. Starr

YALE

S. Sofia

UCSD

H. S. Hudson

LANL

E. E. Fenimore

MSFC

J. M. Davis

J. R. Dabbs

J. Howell

CALTECH

G. J. Hurford

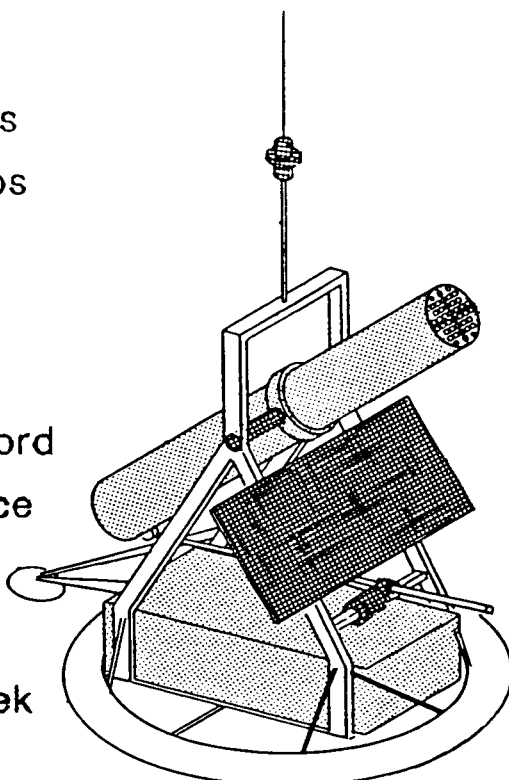
T. A. Prince

DELFT

F. van Beek

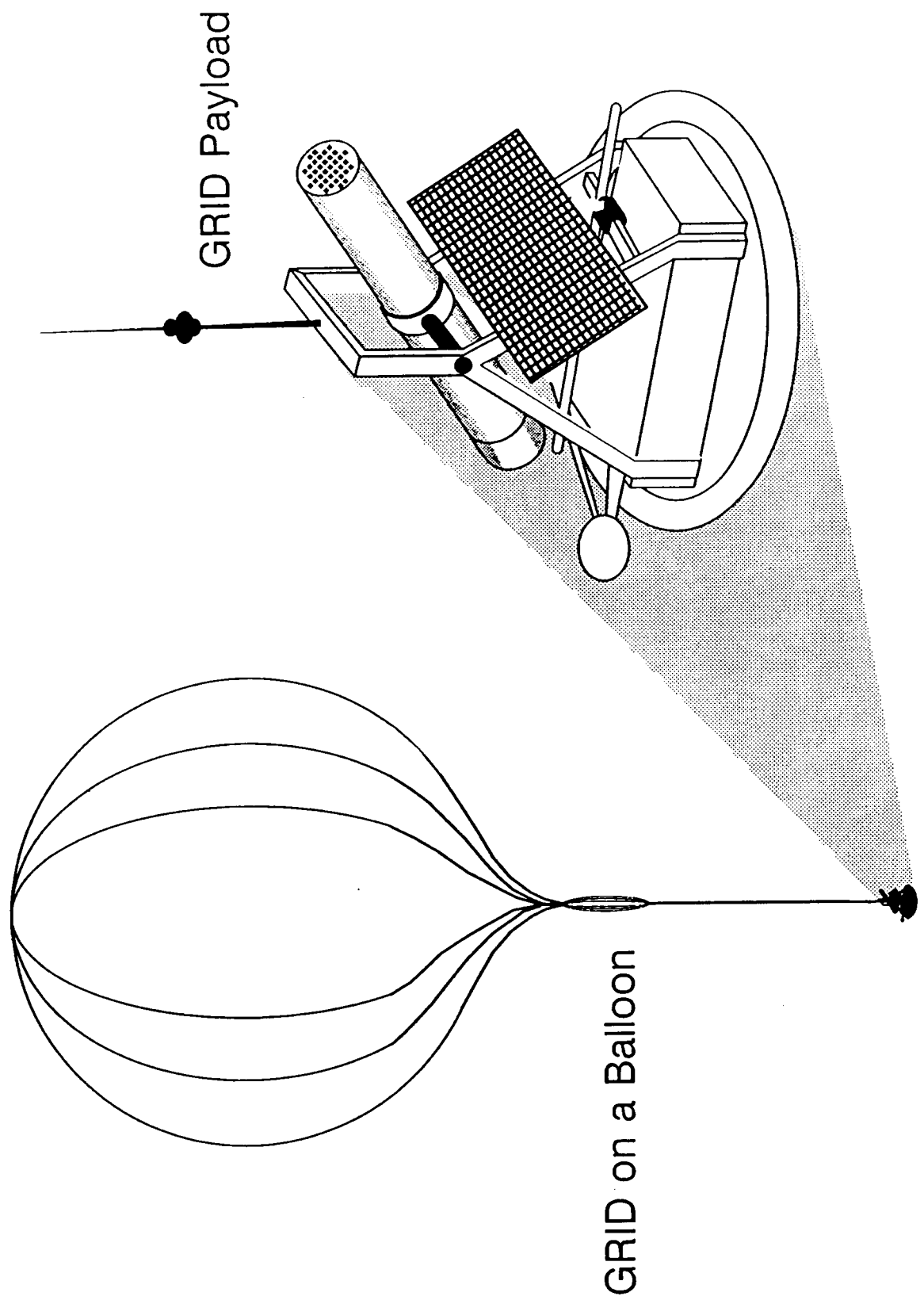
NRL

K. S. Wood

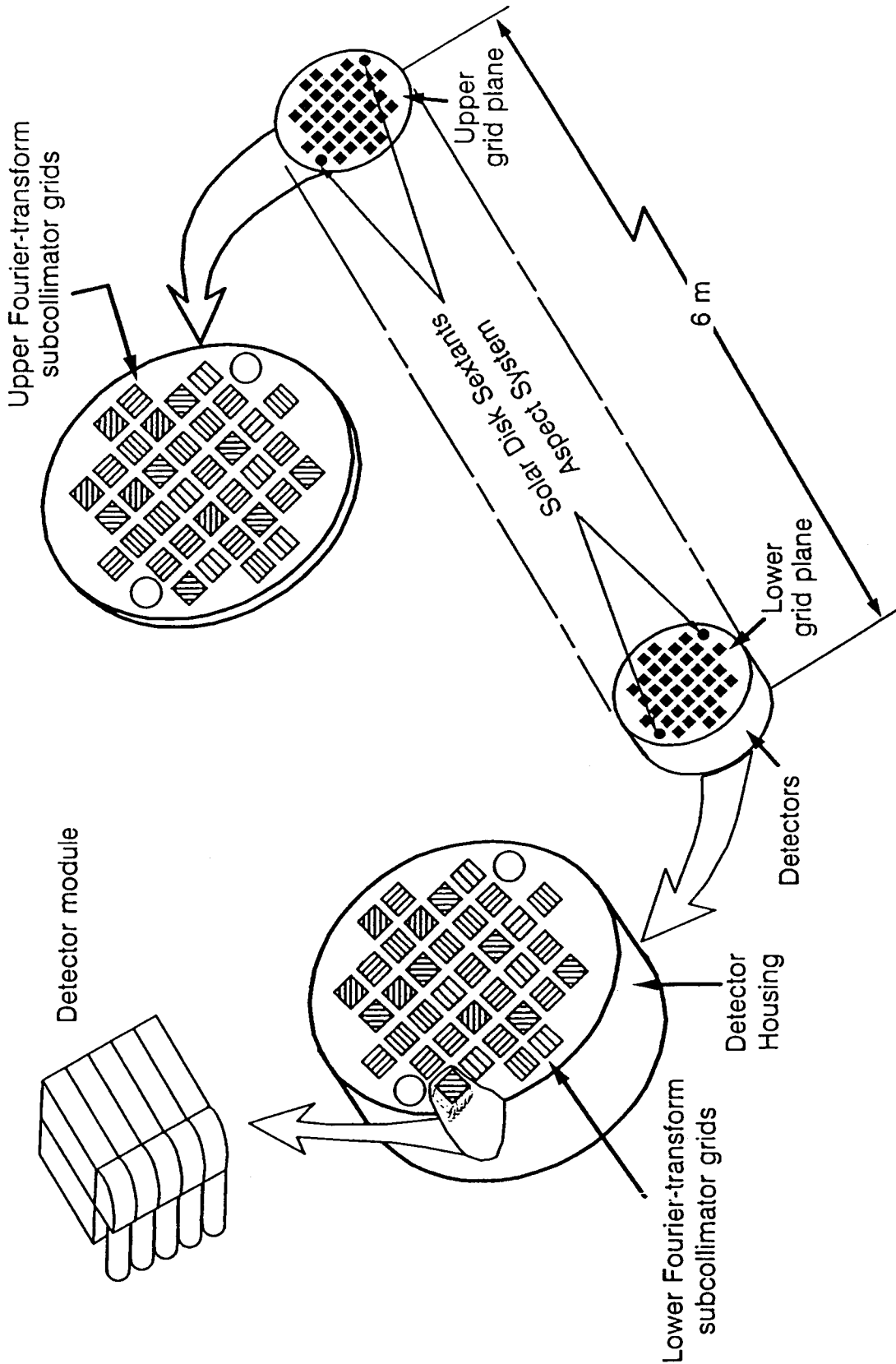


• • • to fill the gap

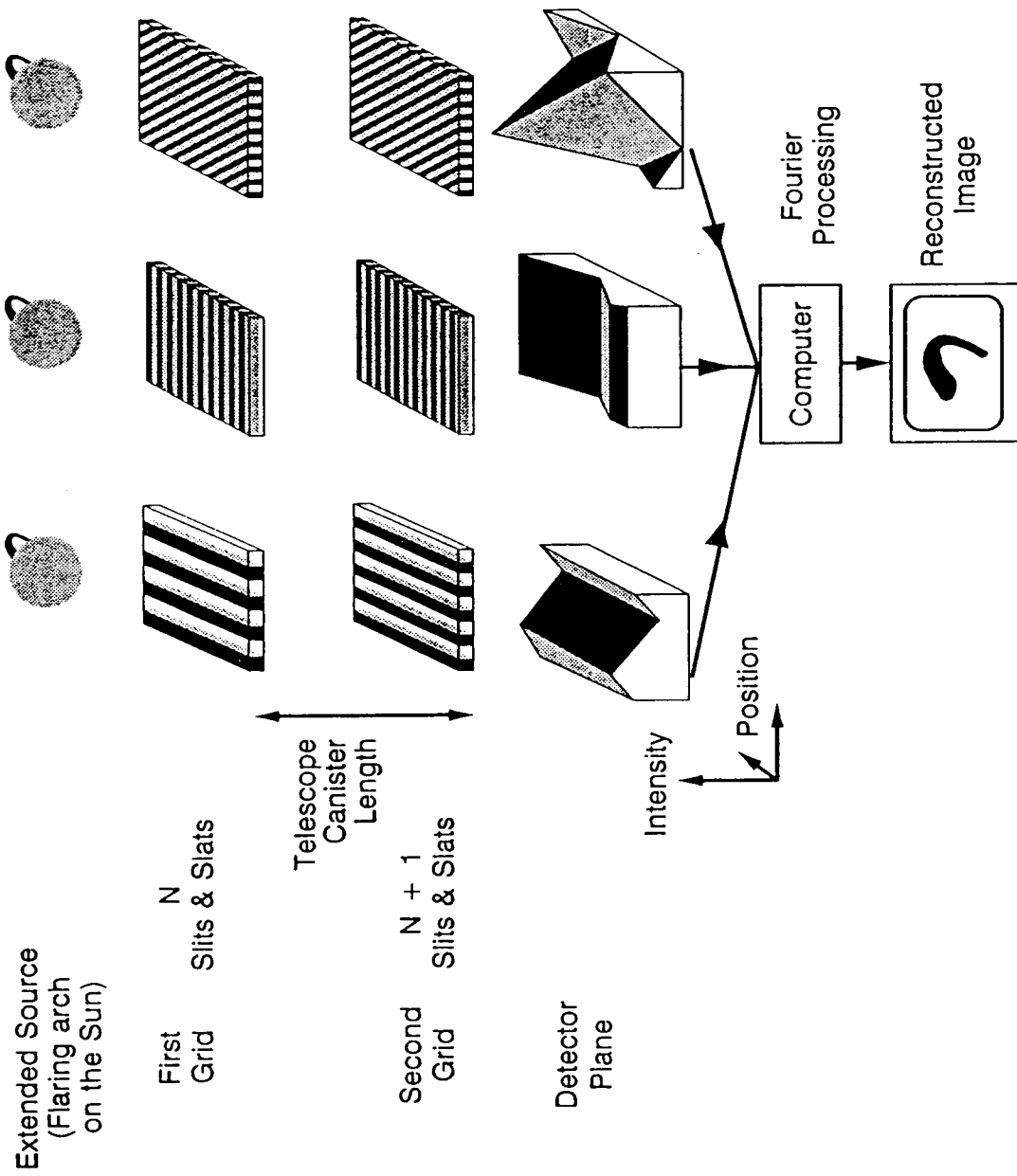
GRID on a Balloon



EXPLODED VIEW OF GRID TELESCOPE



FOURIER TRANSFORM CAMERA



Gamma Ray Imaging Device (GRID) on a Balloon

Objective:

- o Advance solar flare science during the next solar maximum using state-of-the-art balloon-borne instruments

Rationale:

- o Hard X-ray and gamma-ray imaging, together with fine-resolution gamma-ray spectroscopy are identified as the next steps in high-energy solar physics by both MAX '91 study committees
- o No access to space is available on orbital missions during the next solar maximum
- o Balloons offer unique opportunities for repetitive 15-day missions

Gamma Ray Imaging Device (GRID) on a Balloon

Goals:

- Provide a definitive test of solar flare models
- Image the site of high-energy solar flare emissions with spatial resolution corresponding to the fundamental scale length of electron interactions
- Using associated microwave observations, investigate magnetic field structures characterizing the high-energy source site
- Achieve arcsecond spatial resolution and sub-second temporal resolution of hard X-ray and gamma-ray sources in solar flares from 15 to 511 keV
- Develop hard X-ray and gamma-ray imaging technology as a precursor to the Pinhole/Occulter Facility on Space Station

Gamma Ray Imaging Device (GRID) on a Balloon

Approach:

- o Develop GRID as a balloon payload in a cooperative effort between government laboratories, university scientists, and foreign collaborators
- o Use in-house expertise from each participating institution to minimize costs
- o Use heritage of the NASA-sponsored Pinhole/Occulter Facility and MAX '91 studies plus efforts for the SHAPE proposal to define hardware
- o Fly GRID on multiple, long-duration (15-day) balloon missions throughout the next peak in solar activity (1990 - 1994)

Gamma Ray Imaging Device (GRID) on a Balloon

Design Objectives:

obtain hard X-ray and gamma-ray images of solar flares

angular resolution

~ 1.6 arcsecond

temporal resolution

10 milliseconds

energy range

15 to 511 keV

field of view

full Sun

number of Fourier components measured

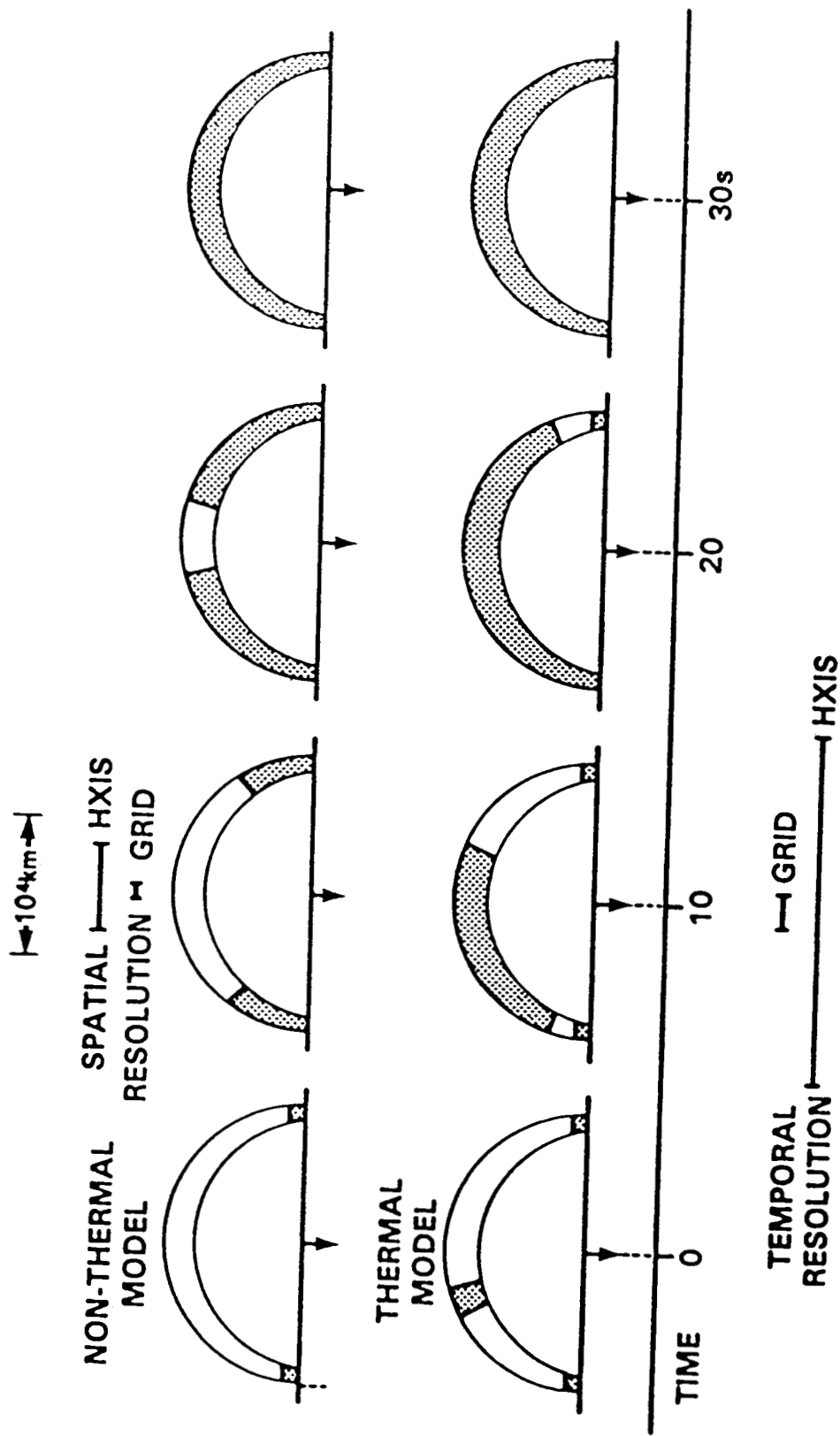
32

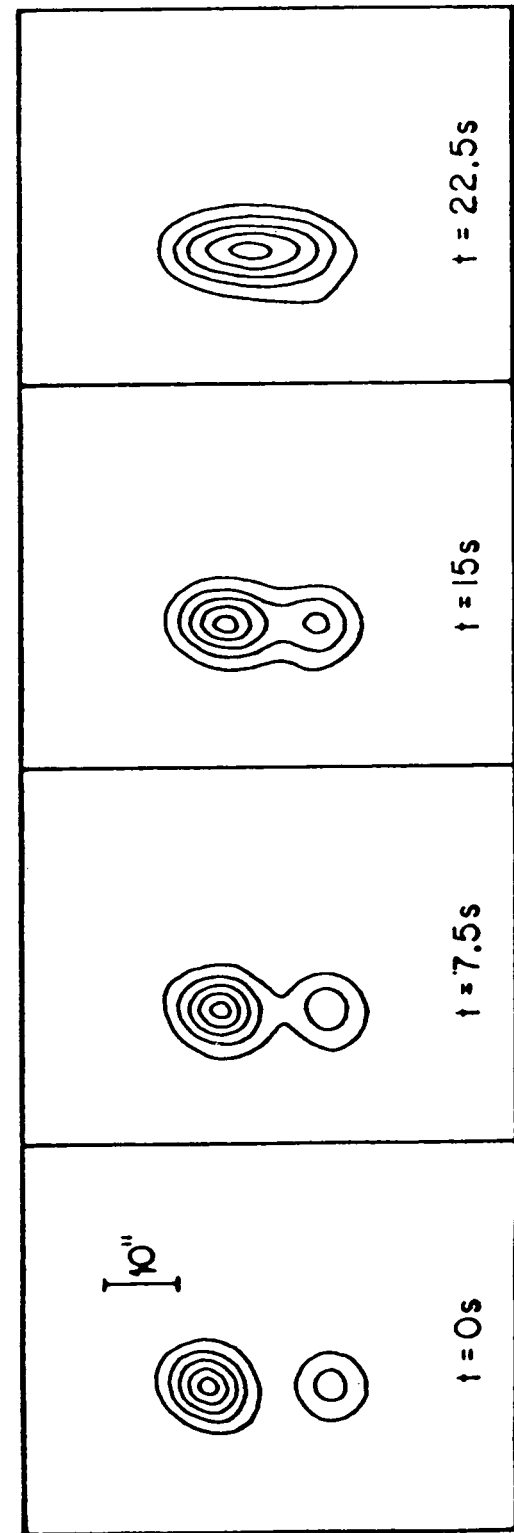
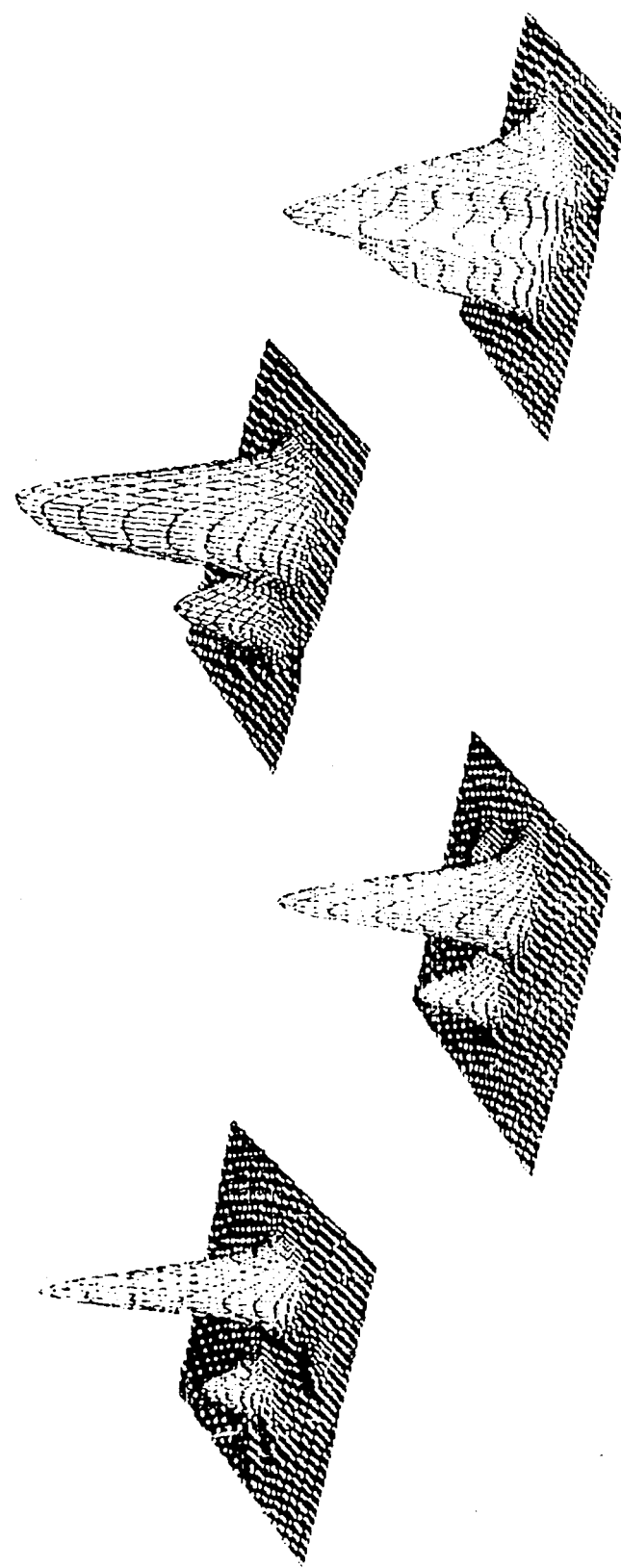
effective detector area

20 cm^2 per component

Instrumental Techniques:

- o spatial Fourier transforms for hard X-ray and gamma-ray flare images
- o aspect determination using the Solar Disk Sextant





N89 - 15870

HIGH-SPATIAL RESOLUTION AND HIGH-SPECTRAL-RESOLUTION DETECTOR
FOR USE IN THE MEASUREMENT OF
SOLAR FLARE HARD X-RAYS

U. D. Desai
L. E. Orwig
Code 682
NASA/Goddard Space Flight Center
Greenbelt, MD

ABSTRACT

In recent years several new technologies have been developed that allow hard X-ray detectors to be made with significantly improved spatial and spectral resolution. These include the development of a new high-density scintillator glass that can be drawn into very fine fibers down to 5 microns in diameter and new semiconductor detectors with keV energy resolution that can be operated at, or significantly closer to, room temperature. It is the purpose of the proposed effort to investigate these new technologies with the objective of developing advanced hard X-ray instruments suitable for use on spacecraft or balloons during the next period of high solar flare activity from 1989 to 1994.

Specifically, in the area of high spatial resolution, we propose to evaluate a new hard X-ray detector with 65-micron spatial resolution for operation in the energy range from 30 keV to 400 keV. The basic detector is a thick large-area scintillator faceplate, composed of a matrix of high-density scintillating glass fibers, attached to a proximity type image intensifier tube with a resistive-anode digital readout system. Since the scintillation glass has excellent optical qualities, provides 15% of NaI(Tl) light output, and has a density of 3.31 g/cm³ (comparable to NaI), such a detector would operate like a NaI or CsI scintillation spectrometer, but with high spatial resolution. Such a detector, combined with a coded-aperture mask, would be ideal for use as a modest-sized hard X-ray imaging instrument up to X-ray energies as high as several hundred keV. As an integral part of this study we also propose to critically evaluate several techniques for X-ray image coding which could be used with this detector.

In the area of high spectral resolution, we propose to evaluate two different types of detectors for use as X-ray spectrometers for solar flare observations. (1) Planar silicon detectors operating at room temperature that have 1-2 keV FWHM energy resolution and can be used from ~5 keV to ~30 keV. These semiconductor detectors not only offer high spectral resolution, but can also be fabricated for use as high-spatial-resolution detectors. This can be achieved by using either electro-etching or charge-sharing techniques. (2) High-purity germanium detectors (HPGe) can now be made to operate with keV energy resolution at much warmer than liquid-nitrogen temperatures (~90 K). Such detectors would require significantly lower-capacity coolers than those required for normal HPGe detectors and could be used to significantly higher X-ray energies than the silicon detectors.

Instruments utilizing these high-spatial-resolution detectors for hard X-ray imaging measurements from 30 to 400 keV and high-spectral-resolution detectors for measurements over a similar energy range would be ideally suited for making crucial solar flare observations during the upcoming maximum in the solar cycle.

INTRODUCTION

Observations made with instruments aboard the Solar Maximum Mission, Hinotori, ISEE-3, PVO, and Venera spacecrafts, as well as observations carried out with balloon-borne and ground-based instrumentation during the last solar maximum have greatly advanced our knowledge and understanding of solar flare phenomena. This is particularly true for solar flare X-ray emissions, where key observations have been made in three areas: 1) the rapid temporal structure observed in hard X-ray flare emission alone and simultaneous with other flare emissions, 2) the first-ever imaging of flares in hard X-rays, and 3) the first and only high-spectral-resolution observations of flare hard X-ray emissions. For example, despite limitations on the instrumental spatial and time resolution, the HXIS instrument on SMM and SXT on Hinotori have shown the existence of spatially separated hard X-ray footpoints in the impulsive phase of some flares, as well as more spatially extended sources in other flares. High-spectral-resolution observations do exist, but for only one flare observed with a balloon-borne spectrometer (Lin, et al. 1981).

While these results have demonstrated how important hard X-ray imaging measurements and high-spectral-resolution measurements are to understanding the complex solar flare processes, they also clearly show the need for hard X-ray measurements with improved spatial resolution and with high spectral resolution, obtained simultaneously and with high time resolution. The need for such measurements is clearly expressed in the The Solar Maximum Mission Flare Workshop Proceedings (Chapter 5, p. 5-18) and is strongly supported by the Report of the MAX '91 Science Study Committee (Dennis, et al. 1988).

We propose to continue a research program initiated in FY'88, whose goals have been to investigate two types of detectors which take advantage of recent advances in technology. The first is a high-spatial-resolution detector which utilizes a faceplate fabricated from newly-developed glass scintillator fibers coupled to an image intensifier tube with a resistive-anode readout system. The high-spectral-resolution effort involves two separate devices, one an ion-implanted planar silicon detector operated at room temperature, and the second, an HPGe detector tailored for operation at temperatures significantly higher than the normal liquid-nitrogen range. These detectors will be studied with a view toward developing hard X-ray imaging and spectrometer instruments which are compatible with small-payload concepts, as opposed to developing larger facility-class instruments. For example we propose to develop a simple, light-weight, low-power spectrometer suitable for Scout-launched payloads or piggy-back flights, opportunities which may be available during the next solar maximum (~1990-1993). A small spectrometer can still produce significant scientific results if it is optimized to operate in the range from 5-200 keV where the photoelectric cross-section is large and there are many observable flares. We feel that such detectors offer great promise in providing the required instrumentation for measurements during the next solar maximum.

Also for the imager, we plan to continue our investigation into various techniques for aperture coding which can best take advantage of the detector's capability for detecting hard X-rays with very high spatial resolution. This effort will ultimately lead to the development of a hard X-ray imaging instrument which will utilize a high-spatial-resolution detector coupled to the appropriate aperture coding device and electronic readout system.

A. High-Spatial-Resolution Detectors

Hard X-rays cannot be imaged by either reflection or refraction techniques. Total absorption - shadow casting - is the only modulation imaging technique available. Various ideas have been proposed for imaging hard X-rays and gamma-rays (Mertz and Young 1961; Oda 1965; Dicke 1968; Brandt, et. al. 1968; Makashima 1982; Fenimore and Cannon 1978; Hudson 1978; McConnell, et. al. 1981). Of these techniques, there are basically two methods for achieving high angular resolution. Variations on the pinhole technique require detectors with very high spatial resolution and/or long distances between the mask and the detector plane, as the angular resolution is given by d/D , where d is the detector resolution and D is the distance between the mask and detector. Instead of making direct images, or their convolution through multiple holes, the requirement of high spatial resolution in the detector plane can be relaxed by using a Fourier-transform technique. However this approach requires extreme precision in the fabrication and alignment of the mask elements. Currently, the Fourier-transform technique is receiving more attention due to the relatively poor spatial resolution, 2-5 mm, of the best crystal scintillator detectors. A detector with greatly superior position resolution would allow the development of competitive instruments which use direct pinhole imaging techniques.

A recently developed high-density (3.3 gm/cm^3), optical-quality scintillating glass which can be drawn into thin fibers (diameters down to 5 microns) offers the opportunity of making a position-sensitive scintillating face-plate. This material has a scintillating efficiency equivalent to 15% of NaI. The superior spatial resolution is achieved by the inherent property of the fibers to pipe the scintillating light output and confine it to a single fiber. We will evaluate this material for its spectral light output characteristics, as well as its hard X-ray detection

However, our primary effort will be the evaluation of a 25-mm dia., five-stage image intensifier tube which has a digital resistive-anode readout system. This tube has already been ordered with FY '88 GSFC Director's Discretionary Funds. We anticipate delivery of the tube soon and will begin evaluation of the tube under the present proposal. This tube is expected to have a spatial resolution of 65 microns. An evaluation of the photocathode noise and the contribution to noise from the channeltron will be carried out.

The ultimate goal is to investigate this faceplate/tube combination as an image sensor in a coded-aperture imaging system for hard X-ray measurements. To this end we intend to investigate various methods of aperture coding for use with this detector system. In particular, we are extremely interested in evaluating both the Fresnel zone plate coded-imaging technique and the "Fresnel Sandwich" coder (Mertz 1965). These techniques have not enjoyed popularity because of the relatively poor spatial resolution of existing detectors. However, the high spatial resolution of the proposed detector allows us to take much better advantage of these image-coding techniques.

B. High-Spectral-Resolution Detectors

The purpose of this investigation is to explore the operation of planar germanium and silicon detectors at temperatures well above the normal liquid nitrogen range and within a charged-particle environment for use as instruments designed to measure solar flare X-ray spectra. High-purity germanium detectors have been in routine laboratory use for at least 15 years for X-ray and gamma-ray spectroscopy. They offer superior energy resolution of ~300-700 eV FWHM, may be cycled from room temperature to liquid-nitrogen temperatures repeatedly with no degradation, can accurately measure spectra without distortion at count rates exceeding 20,000 events/sec, and enjoy excellent linearity and gain stability.

Recently developed room-temperature, ion-implanted silicon detectors are commercially available for 3igh-resolution spectroscopy from 2-30 keV. Such room-temperature ion-implanted silicon detectors developed by Enertec, Inc. have achieved 1-keV energy resolution. This is made possible by reducing the leakage current to the nanoampere range by proper surface passivation techniques, a process which reduces the internal background noise to a very low level. The use of low-noise FET preamplifiers aids in the achievement of keV spectral resolution. Silicon detectors do offer excellent spectral resolution, but with a Z of 14, their photoelectric stopping power limits their usefulness to X-ray energies below 40 keV. We propose to evaluate several of these units, one of which has already been ordered with current FY'88 funds.

Other semiconductor detectors may be operated at room temperature but suffer from severe problems. CdTe detectors have poor energy resolution because of incomplete charge collection. HgI_2 detectors are small, unstable, and have poor charge transport characteristics. $CdTe$ and HgI_2 may someday be ready for space applications, but at the present time silicon and germanium detectors are the only ones which offer the necessary combination of resolution, stopping power, and reliability for the proposed application.

BASIC REQUIREMENTS FOR X-RAY IMAGING IN ASTROPHYSICS

	NON-SOLAR	SOLAR
O	WIDE F.O.V.	~ 1° F.O.V.
O	ARCMIN RES.	ARCSEC RES.
O	HI SENSITIVITY VERY LOW NOISE BACKGROUND	SOLAR FLARE EVENTS ARE INTENSE; SMALL AREA O.K.
O	MOD. TIME RES. γ-RAY BURSTS X-RAY BURSTS COSMIC BKGND	HI TIME RES. (~5msec) SOFT (2 - 20 keV) & HARD (20 - 200 keV) EVENTS

X-RAY IMAGING

- O COLLIMATION - SCANNING
- O CODED-APERTURE IMAGING

RECENT DEVELOPMENTS:
ASTROPHYSICAL
MEDICAL

CODED APERTURE IMAGING

FILLED APERTURES
TRANSMISSION > 50%

- ZONE PLATE
- UNIFORMLY REDUNDANT ARRAY
- STOCHASTIC
- BIGRID & MULTIGRID

DILUTE APERTURES
OPAQUENESS > 50%

- ANNULUS
- ROTATING SLITS
- NON REDUNDANT HOLES

THICKNESSES REQUIRED FOR 90% ATTENUATION FOR TWO ENERGIES AND VARIOUS MATERIALS:

	Cu	Al	Pb (cm)	NaI'	W
50 keV	0.11	2.6	0.04	.06	--
100 keV	1.26	6.3	0.11	1.09	0.1

X-RAY IMAGING DETECTORS

- O LARGE AREA MULTI-ANODE P.C.
- O ELECTRON OPTICS: X-RAY IMAGE INTENSIFIERS
- O PROXIMITY TYPE: X-RAY IMAGE INTENSIFIERS
WITH MULTIPLE DIODE TYPE OF AMPLIFICATION
WITH MULTIPLE MICROCHANNELTRON AMPLIFICATION

HIGH DENSITY SCINTILLATING GLASS

- O OHARA OPTICAL SCG-1 CERIUM-DOPED
(SiO_2 + LiO_2 + Al_2O_3 + MgO + Ce_2O_3)
- O NE902a (12% NaI)
- O "SES" CONSULTANTS – SC56, SC61
BaO ADDED TO INCREASE DENSITY
AS WELL AS FIBER DRAWING CAPABILITY

SPECIFICATIONS

DENSITY 3.31 gm/cm³ (NaI = 3.65 gm/cm³)

REFRACTIVE INDEX n_D (5893Å) = 1.591
 n_A (4047Å) = 1.607

λ OF EMISSION: BROADBAND CENTERED @ 4000Å

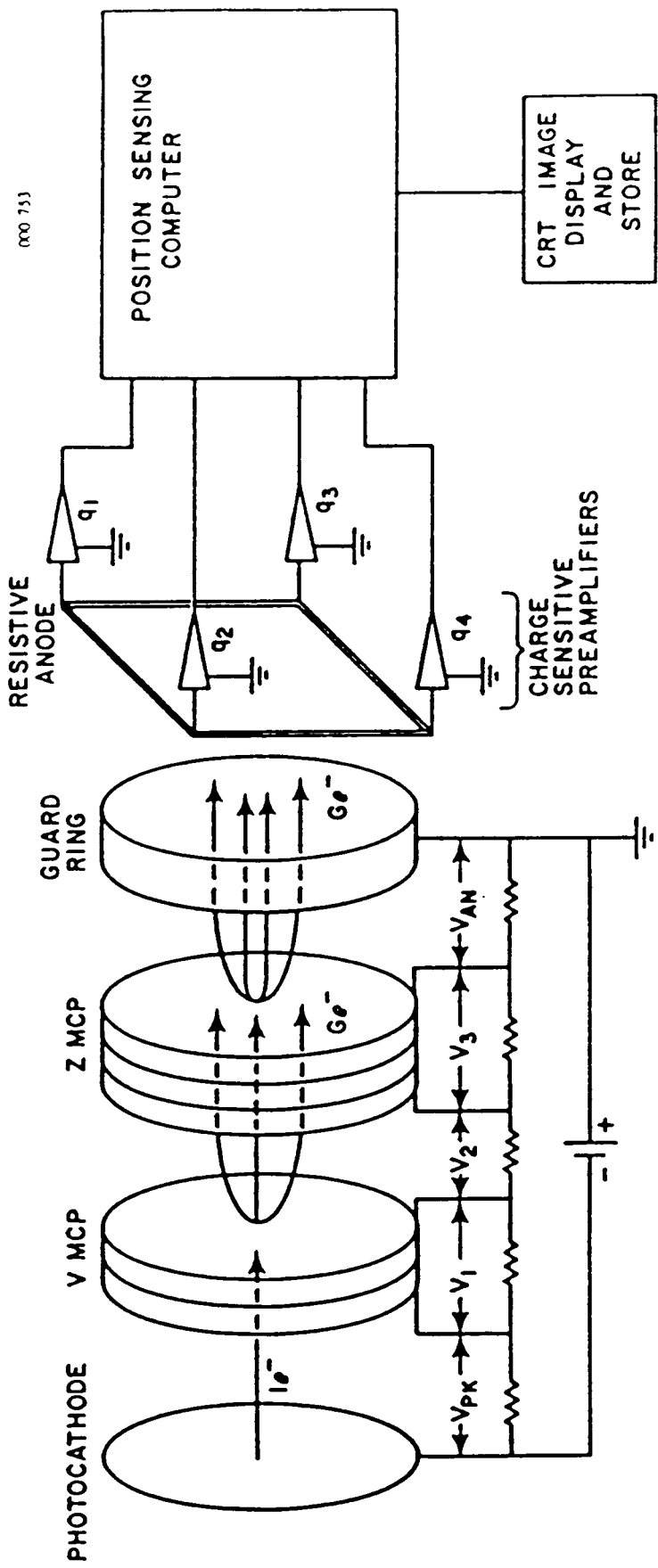
DECAY TIME 56 nsecs

LIGHT OUTPUT ≈ 15% OF NaI

RADIATION LENGTH 4.8 cm

CLEAR TRANSPARENT GLASS, STABLE UP TO 500° C,
NON-HYDROSCOPIC

THEORY OF OPERATION



A COSMIC and SOLAR
X-RAY and GAMMA-RAY INSTRUMENT
for a SCOUT LAUNCH

D.J. Forrest, W.T. Vestrand and EL Chupp
Space Science Center and Physics Dept.
University of New Hampshire
Durham, NH 03824

Presented as a Poster Paper at the
Max '91 Workshop

American Astronomical Society Meeting
Kansas City
June 5-9, 1988

Abstract

We present an overview for a set of simple and robust X-Ray and Gamma-Ray instruments which have both cosmic and solar objectives. The primary solar scientific objective is the study of the beaming of energetic electrons and ions in solar flares. The instrument will measure spectra and polarization of flare emissions up to 10 MeV. At X-Ray energies both the directly emitted flux and the reflected albedo flux will be measured with a complement of six X-Ray sensors. Each of these detectors will have a different high Z filter selected to optimize both the energy resolution and high rate capabilities in the energy band 10-300 keV. At energies >100 keV seven 7.6x7.6 cm NaI and a set of 30 concentric plastic scattering detectors will record the spectra and polarization of electron bremsstrahlung and nuclear gamma-rays. All of the components of the instrument are in existence and have passed flight tests for earlier space missions. The instrument will use a spinning solar orientated Scout spacecraft. The NaI detectors will act as a self-modulating gamma-ray detector for cosmic sources in a broad angular band which lies at 90° to the sun-earth vector and hence will scan the entire sky in 6 months.

Solar Objectives

There is growing evidence that particle streams, both electrons and ions, exist in solar flares. Vestrand et al. (1987) showed that solar flares detected on GRS/SMM at energies >300 keV had a strong excess near the solar limb. The spectral shape of the electron bremsstrahlung in these flares also had a clear dependence on the flare position. More recently Bai (1988) used both HXRBS and GRS data to show that the brightness ratio of X-rays at >300 keV to 25 keV was more than 10 time larger for limb flares as compared to disk center flares. This anisotropic X-ray emission can only be explained by electron beams (Dermer and Ramaty, 1986). One of the objectives of the MAX'91 program should be observations which can quantify particle beams in solar flares (Dennis et al., 1988).

Observable Predictions of Particle Beams

Electron Bremsstrahlung Emission

Albedo X-ray Component

Early statistical tests of the positional brightness of solar flares at energies near 25 keV failed to detect evidence for electron beams (Datlowe et al., 1977). One of the reasons for this is due to the fact the reflected or albedo x-rays from the photosphere almost exactly compensates for the changing brightness of the directly emitted x-ray emission (Bai and

Ramaty, 1978; Langer and Petrosian, 1977, Vestrand et al., 1987). It is important to note, however, that the spectral shape of these two components are quite different in the energy band 10 - 150 keV (Santangelo et al., 1973). Instrumentation which can spectroscopically separate these two components will be sensitive to electron beaming.

Polarization

Numerous calculations have shown that x-rays produced by electron beams will be polarized (Bai and Ramaty, 1978; Langer and Petrosian, 1977; Emslie and Brown, 1980). The current experimental status and prospects for polarization measurements of solar flares at energies up to 150 keV have been recently reviewed (Chanan et Al., 1988). This study points out the desirability of extending the measurements to much higher energies. Earlier polarimeters were only designed to cover the energy band up to 150 keV.

Nuclear Line Emission

Doppler Shifts and Line Shapes

The measurement of the Doppler energy shift of gamma-ray lines is a historical way of measuring ion beams. The application of this technique to solar flares has been reviewed (Ramaty and Crannel, 1976). More recently Werntz and Lang (1988) have extended this type of observation to show that line structure and line splitting from nuclear de-excitation of ^{12}C and ^{16}O can also be used to determine ion beaming.

Polarization of Nuclear Lines

Sawa (1987) recently pointed out that nuclear line emission is also polarized if it is produced by ion beams. He showed that the degree of polarization for the ^{12}C and ^{16}O lines can be much larger than 50%. He also pointed out that unlike Doppler Shift measurements, polarization observations can reveal the full particle geometry rather than just the line-of-sight component.

The above shows that polarization observations, particularly if made in conjunction with other observations, has the potential of addressing beaming of both electrons and ions.

INSTRUMENT

This Scout Gamma-Ray Instrument is based on a design first presented by Morfill and Pieper (1973). They showed that a self-modulating or "active anti-collimator" detection system, based on a rotating detector array, can have a 20-50 times higher sensitivity per unit mass than a conventional well-shaped detector-shield system at energies greater than a few hundred keV.

Their basic design has been modified by the addition of plastic scintillator scattering detectors. This gives the instrument good polarization sensitivities for solar emission without compromising its self-modulating cosmic capabilities. The NaI portion of the instrument will operate as a gamma-ray spectrometer with the same basic spectral capabilities as the GRS on SMM.

Six NaI X-ray detectors, each with a different high-Z filter, will provide good energy resolution and high rate capabilities in the solar X-ray albedo energy band.

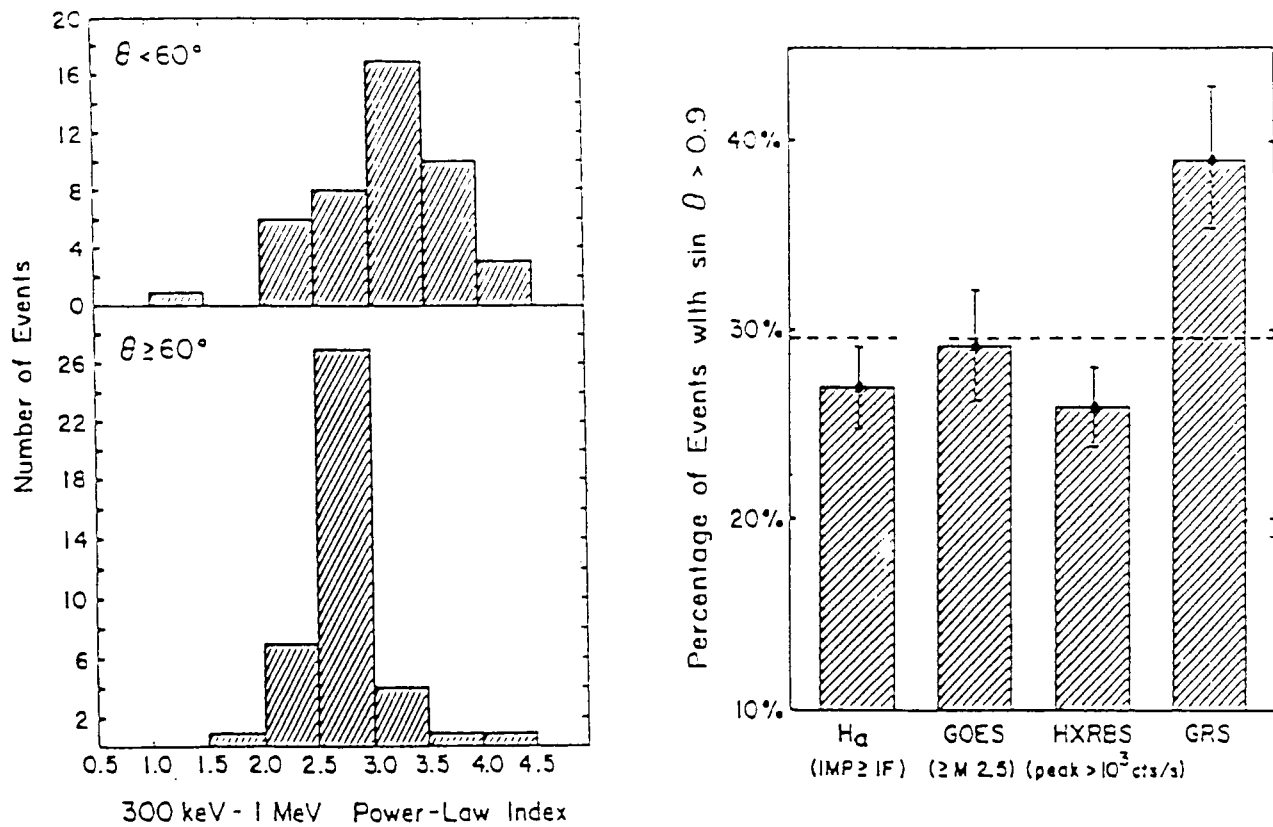
References

Morfill, G. and Pieper, G.F., A Directional Low Energy Gamma-Ray Detector, (1973), in the proceedings of the conference on "Transient Cosmic Gamma- and X-Ray Sources" (Sept. 20-21, 1973, Los Alamos Sci. Labs.), LA-5505-C.

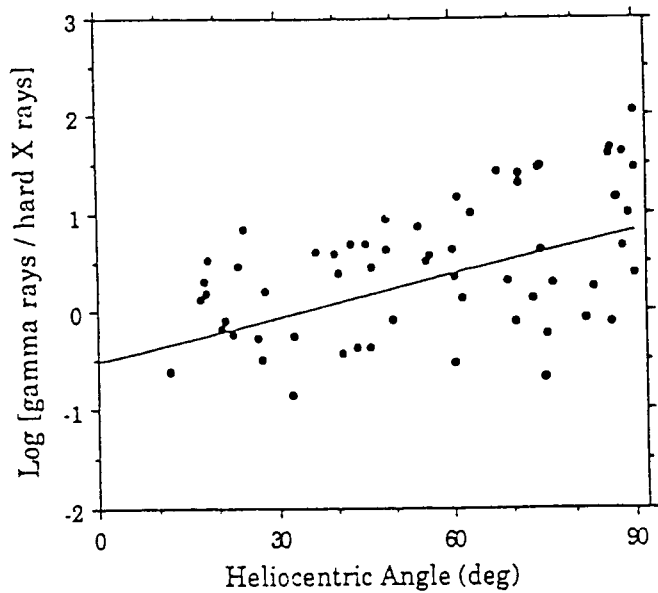
Bai, T., Directionality of Continuum Gamma Rays from Solar Flares, 1988, Ap. J., In Press.

Bai, T. and Ramaty, R., Backscatter, Anisotropy, and Polarization of Solar Hard X-Rays, 1978, Ap. J., 219, 705.

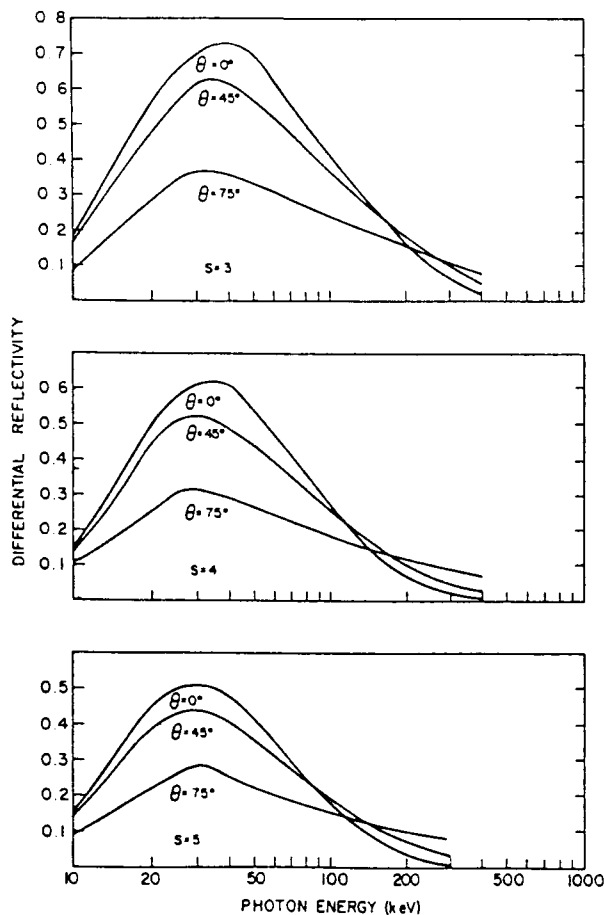
- Chanan, G. A., Emslie, A. G. and Novick, R., Prospects for solar flare X-Ray Polarimetry, 1988, *Solar Phys.*, In Press.
- Datlowe, D. W., O'Dell, S. L., Peterson, L. E. and Elcan, M. J., An Upper Limit to the Anisotropy of Solar Hard X-Ray Emission, 1977, *Ap. J.*, 212, 561.
- Dennis, B., Canfield, R., Bruner, M., Emslie, G., Hildner, E., Hudson, H., Hurford, G. and Lin, R., Novic,R, Tarbell,T ; MAX '91: Flare Research at the Next Solar Maximum, 1988, Greenbelt, MD: NASA-GSFC.
- Dermer, C. D. and Ramaty, R., Directionality of Bremsstrahlung from Relativistic Electrons in Solar Flares, 1986, *Ap. J.*, 301, 962.
- Evans, R. D., The Atomic Nucleus, 1955, New York: McGraw-Hill Book Co.
- Langer, S. H. and Petrosian, V., Impulsive Solar X-Ray Bursts. III. Polarization, Directivity, and Spectrum of the Reflected and Total Bremsstrahlung Radiation From a Beam of Electrons Directed Toward the Photosphere, 1977, *Ap. J.*, 215, 666.
- Petrosian, V., Directivity of Bremsstrahlung from Relativistic Beams and the Gamma Rays from Solar Flares, 1985, *Ap. J.*, 299, 987.
- Ramaty, R. and Crannell, C. J., Solar Gamma-Ray Lines as Probes of Accelerated Particle Directionalities in Flares, 1976, *Ap. J.*, 203, 766-768.
- Ramaty, R., Miller, J. A., Hua, X. M. and Lingefelter, R. E., Models of Gamma- Ray Production in Solar Flares, 1988, In: Nuclear Spectroscopy of Astrophysical Sources edited by G. H. Share and N. Gehrels. New York: AIP.
- Santangelo, N., Horstman, H. and Horstman-Moretti, E., The Solar Albedo of Hard X-Ray Flares, 1973, *Solar Phys.*, 29, 143-148.
- Sawa, Z. P., Linear Polarization of 4.43 MeV $^{12}\text{C}^*$ and 6.13 MeV $^{16}\text{O}^*$ Gamma Rays as Indicators of Directions of Particles in Solar Flares, 1987, *Solar Phys.*, 107, 167-171.
- Vestrand, W. T., Forrest, D. J., Chupp, E. L., Rieger, E. and Share, G., The Directivity of High Energy Emission from Solar Flares: Solar Maximum Mission Observations, 1987, *Ap. J.*, 322, 1010-1027.
- Wertz, C. W. and Lang, F. L., Solar Flare Gamma-Ray Line Shapes, 1988, In: Nuclear Spectroscopy of Astrophysical Sources edited by G. H. Share and N. Gehrels. New York: AIP, In Press.



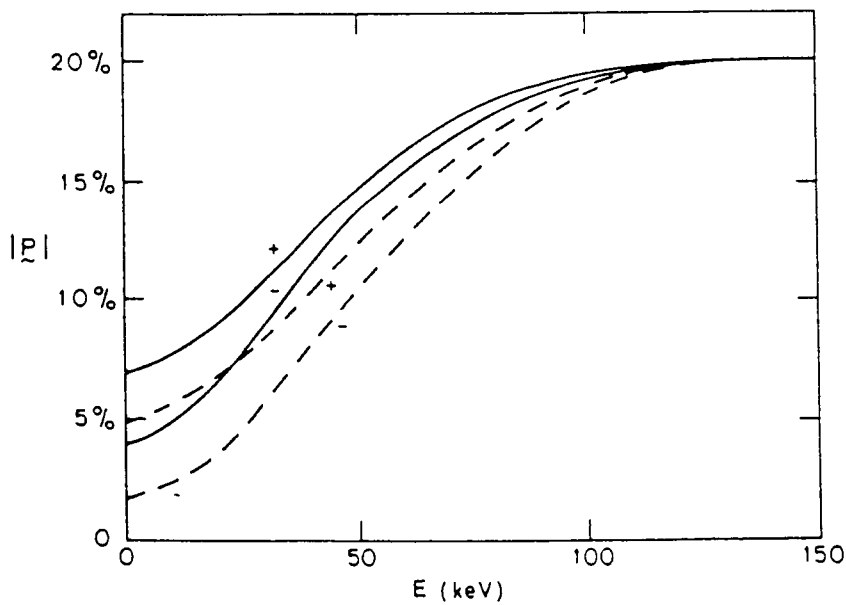
Display 1. These two figures show a) the distribution of the fitted power law index within the energy band 0.3-1.0 MeV for flares with heliocentric angles $< 60^\circ$ and $> 60^\circ$; and b) the fraction of detected events > 300 keV near the solar limb as compared to three other flare emissions which are expected to be isotropic (Vestrand et al., 1987).



Display 2. The distribution of SMM flares showing the relative gamma-ray to x-ray brightness as a function of the flare heliocentric angle (Bai, 1988).



Display 3. The calculated X-ray albedo from solar flares given as a fraction of the "direct" X-ray emission for three different "direct" emission power laws and three different flare positions. These calculations assume the "direct" emission is isotropic (Bai and Ramaty, 1978).



Display 4. A model dependent calculation of the polarization fraction as a function of energy. Some of the decrease at low energies is caused by thermal emission and some by the unpolarized albedo flux (Emslie and Brown, 1980).

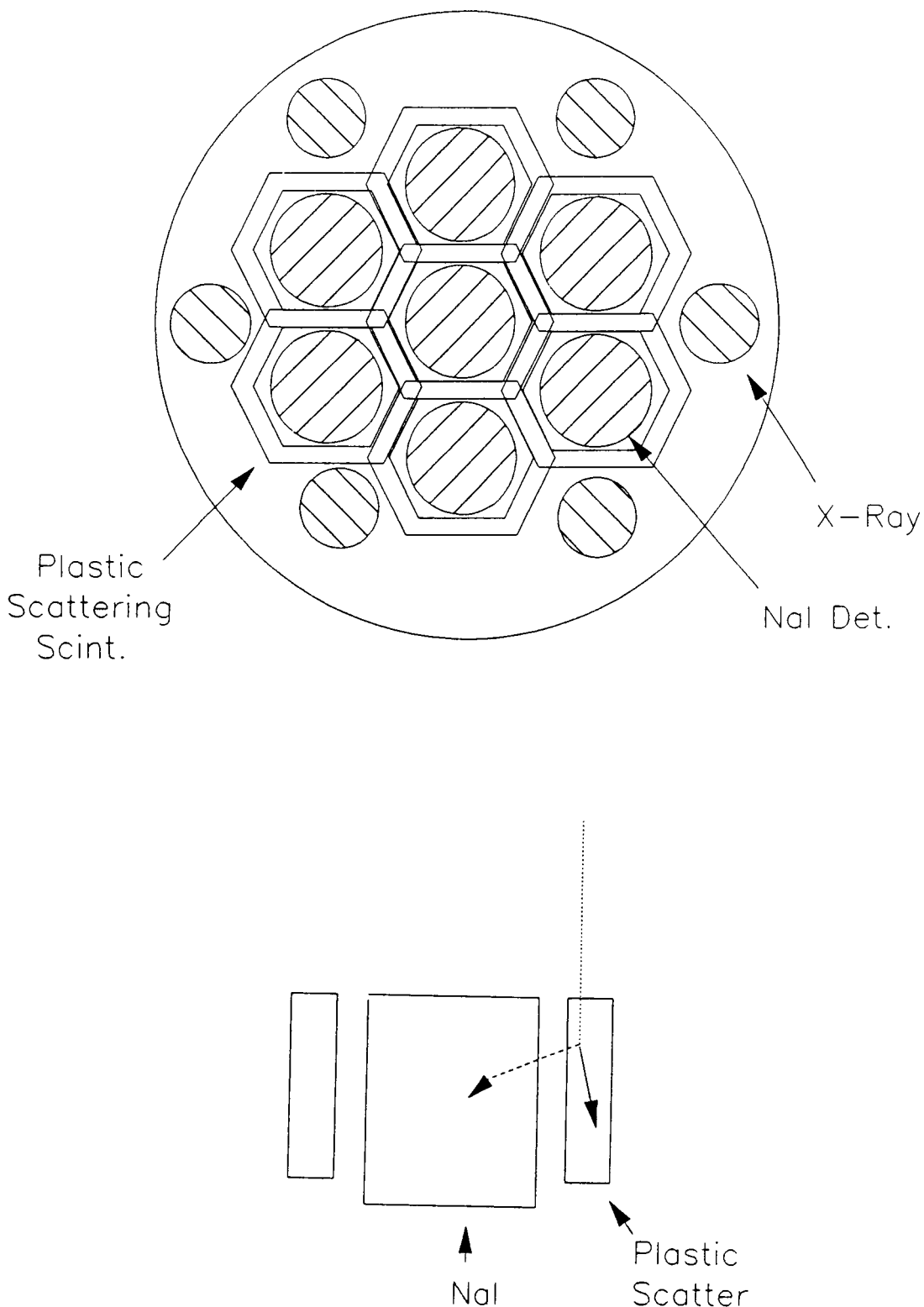
TABLE I

Projected linear polarization amplitudes $P(\theta)$ of 4.43 MeV $^{12}\text{C}^*$ and 6.13 MeV $^{16}\text{O}^*$ gamma-rays assuming gaussian substates distributions $P(j, m)$ of width σ

θ (°)	4.43 MeV $^{12}\text{C}^*$		6.13 MeV $^{16}\text{O}^*$	
	$\sigma = 0.95$		$\sigma = 1.5$	
	$\sigma = 0.95$	$\sigma = 1.5$	$\sigma = 1.0$	$\sigma = 1.5$
0	0	0	0	0
10	0.06	0.02	0.07	0.03
20	0.11	0.07	0.20	0.09
30	0.21	0.14	0.36	0.17
40	0.32	0.22	0.52	0.27
50	0.43	0.31	0.65	0.37
60	0.53	0.39	0.75	0.46
70	0.62	0.45	0.81	0.51
80	0.69	0.50	0.82	0.53
90	0.72	0.52	0.82	0.54

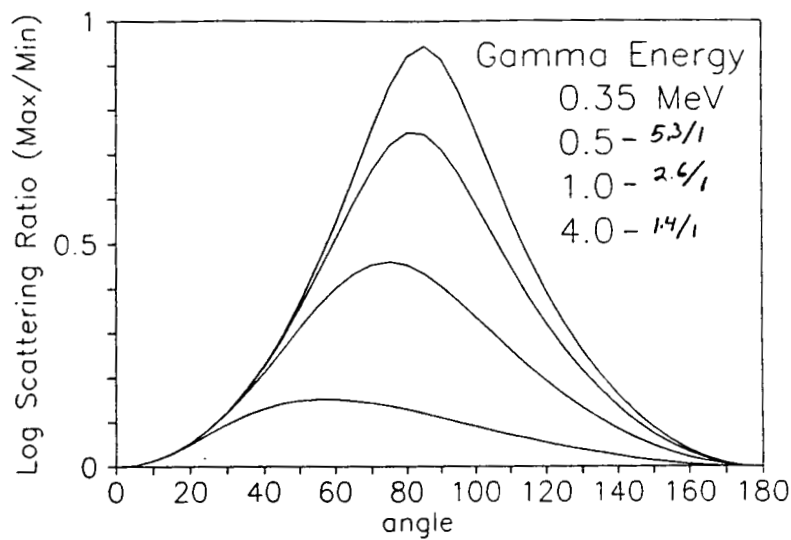
Display 5. A Table of calculated nuclear polarization amplitudes from flare emissions of ^{12}C and ^{16}O (Sawa, 1987).

Scout Solar X- and Gamma-Ray Instrument



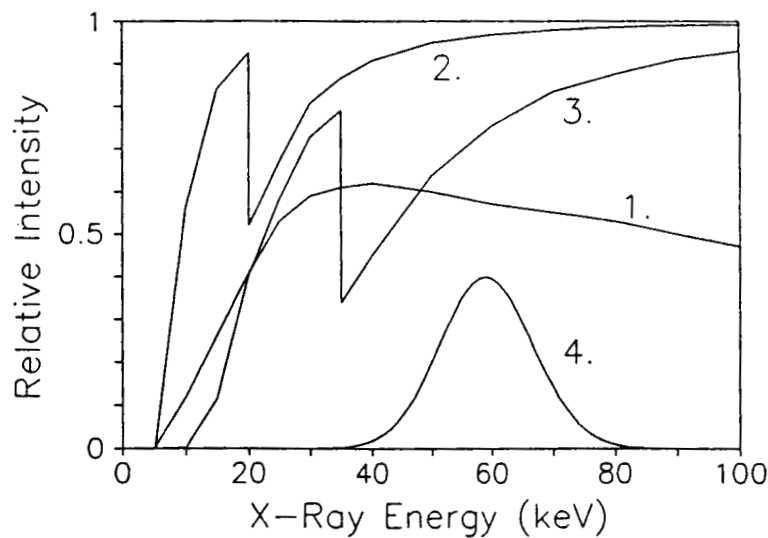
Display 6. A top view of the detector array showing the NaI detectors, the 30 plastic scattering detectors and the 6 x-ray detectors. The lower panel shows the scattering geometry between the plastic and NaI detectors for the polarization measurements.

Compton Scattering
Polarization Scattering Ratio



Display 7. A plot of the intrinsic maximum to minimum Compton cross-section polarization scattering ration for 4 energies between 0.35 to 4.0 MeV as a function of the scattering angle (Evans, 1955).

Albedo X-Ray Filter Example



1. Albedo X-rays relative to Primary Spectrum
2. Attenuation from 42Mo (K edge = 20 keV)
3. Attenuation from 55Cs (K edgr = 36 keV)
4. GRS NaI X-ray Energy Resolution Response

Display 8. This composite figure shows the energy dependent attenuation of two different filter elements. It also shows the characteristic albedo spectrum and a Gaussian peak representing a NaI x-ray detector resolution. High spectral resolution flux measurements are obtained by making spectral observations of the same flare with six different detectors, each having a different energy response because of the different filters.

Flare Observation During Max'91 Balloon Campaigns

David J. Forrest
Space Science Center
University of New Hampshire
July 1988

Abstract

I present a brief overview of some of the large flare properties as observed during the prime SMM flare observation interval, 1980 - 1984. Two of these properties, namely their tendency to occur in groups and the strong effects of the 154 day periodicity, can be used to increase the probability of detecting large flares during the limited observing duration of Max'91 balloon campaigns provided the solar flaring characteristics of the 1991 Solar Cycle follows that observed in 1980-1984.

Observations

One of the major objectives of NASA's Max'91 Program will be to observe solar flares with a new generation of instrumentation to be flown on high altitude balloons. These observations will be greatly enhanced if they can be made in coordination with those from improved ground based observations. It is an unfortunate fact that balloon flight experiments are limited both in the times that they can be launched and their total flight duration once they are launched. In the following I present the characteristics of flares observed in 1980-1984, having GOES soft X-Ray emission $>M2.5$, as a surrogate for the reasonably large flares which we hope to observe in 1981-1985.

In order to extrapolate to other flare sizes I note the following properties of flares having GOES emission $>M2.5$. Vestrand et al. (1987) showed that the solar positions of these events are consistent with isotropic emission. He also stated that 70% of the ~150 GRS flares detected at energies >300 keV (detection limit of $F(>300 \text{ keV}) >\sim 4 \text{ photons/cm}^2$) had a GOES size $>M2.5$. There were 233 GOES $>M2.5$ events within the times that the SMM was in daylight and able to observe the sun. Bai (1987) has stated the relationship between GOES sizes and HXRBS events and Dennis (1985) has given a size-frequency relationship for HXRBS events.

During the 1500 days between March 1980 and the end of May 1984, the NOAA Solar-Geophysical Data reported 577 solar flares having a GOES size $>M2.5$. Figure 1 shows these events binned up into 15.4 day intervals. It is clear that these flares are not randomly distributed in time. It is this non-random distribution which can be used to increase the probability of flare observation during the Max'91 balloon campaigns.

There are two explanations for this observed non-random behavior. First is the presence of a relatively small number of Super-Active Regions which produce large numbers of flares during a single solar disk transient (Bai, 1987). The second is the well observed 154 day periodicity observed in the detection of solar flares (Rieger et al., 1984; Dennis, 1985; Bai and Sturrock, 1987). It is important to note that these two phenomena are not the same. Many Super-Active Regions occur outside of the 154 day preferred interval (Bai, 1987) and Bai and Sturrock (1987) have shown that the 154 day periodicity is not associated with increased flare production in a single active region but is a global effect.

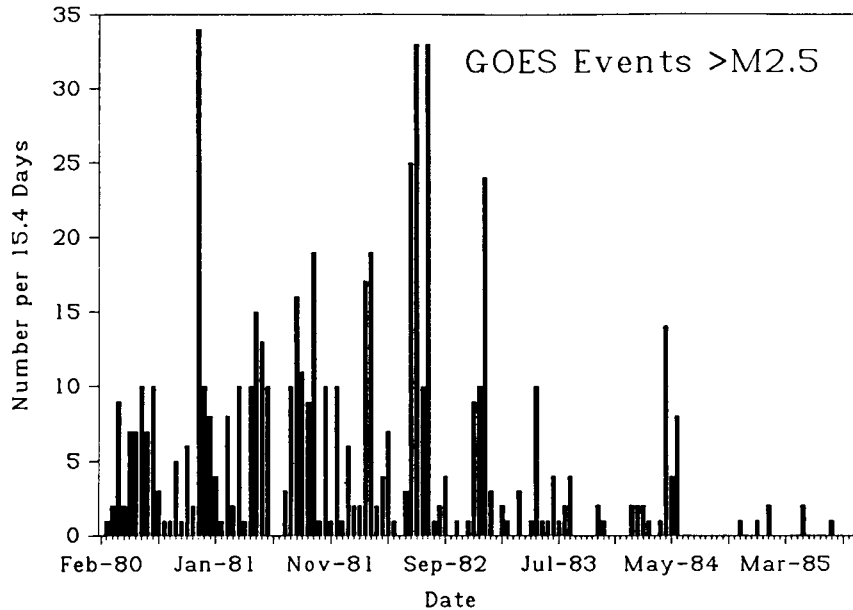


Figure 1. The time distribution of GOES >M2.5 flares reported in the Solar-Geophysical Data Reports from March 1980 to January 1986.

We illustrate the potential use of these phenomena as a flare predictor in the following two figures. Figure 2 shows the distribution of time intervals between successive flares. This data was obtained from the 577 flares shown in Fig. 1 between March 1980 and May 1984. It is clear that the detection of a >M2.5 event greatly increases the probability of another event over at least a 24 hour interval. Figure 3 shows the number of >M2.5 events binned up with the 154 day periodicity. Again this data shows the the flare detection probability can be increased by scheduling balloon campaigns within a given time.

- Bai, T., Distribution of Flares on the Sun: Superactive Regions and Active Zones of 1980-1985, Ap. J., 314, 795, 1987.
- Bai, T. and Sturrock, P.A., The 152-day Periodicity of the Solar Flare Occurrence Rate, Nature, 327, 601, 1987.
- Dennis, B.R., Solar Hard X-Ray Bursts, Solar Phy., 100, 465, 1985.
- Rieger, E. et al., Evidence for a 154 Day Periodicity in the Occurrence of Hard Solar Flares (Time Period 1980-1983), Nature, 312, 623, 1984.
- Vestrand, W.T. et al., The Directivity of High-Energy Emission from Solar flares: Solar Maximum Mission Observations, Ap. J., 322, 1010, 1987.

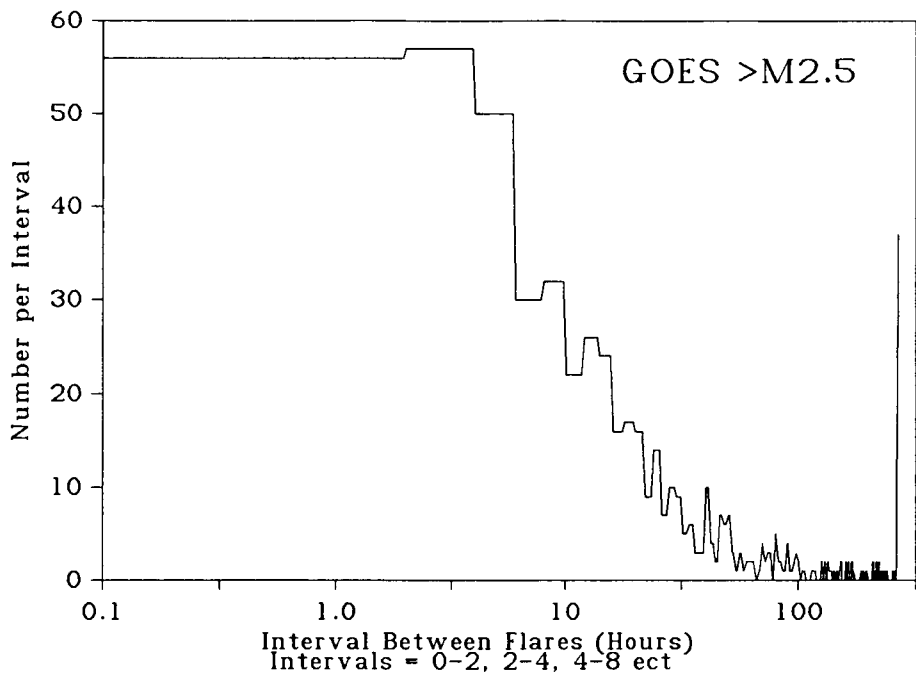


Figure 2. The distribution of time intervals between successive GOES >M2.5 flares measured in hours. The 1st interval is 0-2 hours, the 2nd 2-4, the third 4-8, ect. The high point at the end of the trace shows that there were 37 intervals larger than 256 hours.

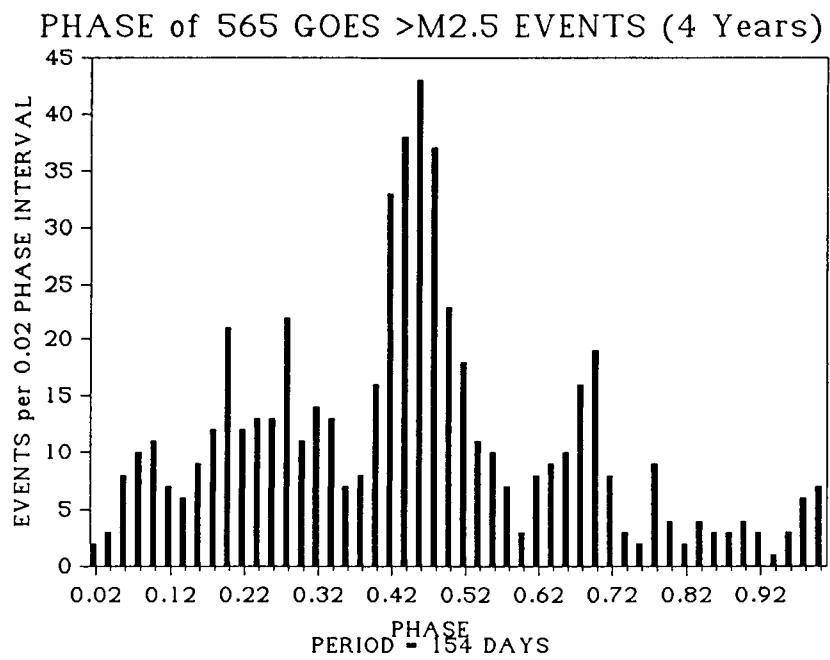


Figure 3. The epoch folded distribution of GOES >M2.5 flares within the 154 day period. These events occurred over a 4 year interval representing about 10 periods. The flares have been binned up in intervals, each 3.08 days long, so that each data point represents about 31 days of observation.

SOLAR RESPONSE OF THE BATSE INSTRUMENT ON THE GAMMA-RAY OBSERVATORY

G.J. Fishman, C.A. Meegan, T.A. Parnell, and R.B. Wilson
Space Science Laboratory
NASA/Marshall Space Flight Center
Huntsville, Alabama 35812

W. Paciesas
Physics Department
University of Alabama in Huntsville
Huntsville, Alabama 35899

T. Cline, B. Teegarden, and B. Schaefer
Laboratory for High Energy Astrophysics
NASA/Goddard Space Flight Center
Greenbelt, Maryland 20771

Hugh Hudson and J.L. Matteson
Center for Astrophysics and Space Sciences
University of California, San Diego
La Jolla, California 92093

Abstract: The Burst and Transient Source Experiment (BATSE) on board the Gamma-ray Observatory (GRO) aims at comprehensive observations of time profiles, spectra, and locations of high-energy transient sources. The mysterious cosmic γ -ray bursts provided the main motivation for the observations, but BATSE will make excellent observations of many classes of sources, and in particular solar flares. This paper analyzes the solar response of BATSE, as inferred from its design parameters, for two purposes: the optimization of the solar observations themselves, and the characterization of the solar effects on ordinary non-solar observations.

1. Introduction

The Gamma-Ray Observatory, the second of NASA's "Great Observatories" after the Hubble Space Telescope, contains four major instruments for γ -ray

astronomy. Each of these is much more capable than predecessors in its category. The delay of the GRO launching caused by the Challenger accident has moved its observation period squarely into the maximum phase of solar flare activity: the presently-scheduled launch date of March, 1990, is approximately a year before the expected peak of flare activity. Understanding the solar response of these instruments is therefore important not only scientifically but also from the point of view of non-solar observations, since the sun frequently becomes an extremely bright "nuisance" source of hard radiations under these conditions.

These notes describe the BATSE experiment in particular, beginning with a heliocentric view of its design, followed by comments on the detector responses to model solar input spectra, and concluding with an assessment of the operating modes of the instrument electronics. For the solar community and for the GRO experimenters, it would be desirable for the other GRO instruments to be subject to solar analyses of this type in preparation for launch.

2. BATSE: Description from a Solar Point of View

2.1 Detectors

The BATSE instrument consists of eight pairs of detectors, each pair oriented along the outward normal to one face of a regular octahedron. This approximates an isotropic coverage of the sky and also allows approximate determination of the origin on the sky of a given high-energy transient via detector response ratios. The main detector of each pair is a NaI(Tl) scintillation counter (50.8 cm diameter \times 1.27 cm thick); the primary purpose of this detector is to provide high counting rates for time-profile measurements and burst locations. These large-area detectors have rather poor energy resolution, about 30% (FWHM) at 100 keV. The second detector of each pair is also a NaI(Tl) detector (12.7 cm diameter \times 7.62 cm thick), but optimized for γ -ray and hard X-ray spectroscopy in a wide energy band (ranging from 7 keV to > 50 MeV, and with energy resolution of 7% (FWHM) at 662 keV).

Both types of detector offer significant capabilities for solar observation. Of course the source-location capability is of little interest, since the precision will probably not be good enough to contribute to physical interpretations of solar sources. However the large area (~ 5730 cm 2) and fast electronics (up to 200,000 cps without spectral distortion) make the large-area detectors attractive for the detection of weak bursts or of fine time structure in strong bursts. The great sensitivity of the large-area detectors

places their dynamic range of effective response in a domain unaccustomed to attention by solar physicists. This is both a strength and a weakness for solar observations, since there is a tendency in flare research to study preferentially the most dramatic and spectacular "big flare" events.

The spectroscopy detectors are probably of more intrinsic interest for solar physicists, offering a new and powerful look at the rich physics mostly defined now by the γ -ray observations of the Solar Maximum Mission (1980—present). These observations (e.g. Chupp, 1984) showed powerful acceleration of energetic (few MeV) ions to occur commonly in flares, rather than in a rare sub-class of "proton flares." Given the ubiquity of this particle acceleration, the γ -ray emission lines – chiefly prompt inelastic-scattering lines – have many diagnostic uses, not least of which is the energetics of solar flares, which appears to be dominated by the acceleration of energetic particles.

2.2 Electronics

The BATSE digital electronics unit possesses a great deal of flexibility in its operating modes, in order to maximize the return of information about the different high-energy sources in the face of on-board memory and telemetry limitations. The design of this electronics and its software has many implications for the utility of the solar data that will be returned by the BATSE instrument. Many performance features can also be altered during the mission with new software, if desirable.

The GRO telemetry is packetized, with an individual instrument such as BATSE creating and labeling its own packet types for entry into the telemetry. One BATSE packet contains 455 16-bit words, and a new packet is transmitted every 2.048 seconds. Each packet contains some routine scientific data independent of the current observational mode, plus the specialized data corresponding to that particular mode; these routine data generally consist of integral counting rates with relatively low spectral and temporal resolution. For solar purposes, of course, such routine data will mainly be useful as a means of defining the statistics of burst occurrence under well-determined conditions, and as basic synoptic support data for simultaneous observations carried out by other observatories. Each different observing mode produces a different packet type, optimized for one or another specialized observation. Section 4 below discusses some of the mode structure as relevant to the purposes of solar observing.

2.3 Routine Data

The routine science data in each packet contains the following items of interest:

- Discriminator rates for each of the eight large-area detectors at time resolution of 1.024 sec:

Channel 1	$25 \text{ keV} < E < 50 \text{ keV}$ (adjustable)
Channel 2	$50 \text{ keV} < E < 100 \text{ keV}$
Channel 3	$100 \text{ keV} < E < 300 \text{ keV}$
Channel 4	$E > 300 \text{ keV}$

- Discriminator rates for each of the eight spectroscopy detectors, at a time resolution of 2.048 sec:

Channel 1	$E > 7 \text{ keV}$
Channel 2	$E > 14 \text{ keV}$ (adjustable)
Channel 3	$E > 25 \text{ MeV}$
Channel 4	$E > 50 \text{ MeV}$

- Continuous data from each of the eight large-area detectors, at 16-channel energy resolution and 2.048-second time resolution. The sixteen channels are narrow at low energies and broad at high energies, adequately resolving the detector resolution below 100 keV.

The spectroscopy detectors cover large spectral ranges, and to optimize their coverages the plan is to have different units operating at different gain settings. Four will run at the nominal gain setting described in the User's Manual and shown above; two will run at reduced ($0.4\times$) gain; and two at expanded ($4\times$) gain. For the spectroscopy detectors, channel 1 is also adjustable in the sense that it is always a factor of two lower than channel 2.

These routine data may not appear to hold very much interest for solar physics, given the long history of simple photometric hard X-ray and γ -ray observations (e.g. Dennis, 1986), but in fact their continuity and large dynamic range should make them useful in statistical studies. Note that some of the eight detectors will be shadowed from solar radiation by the body of the spacecraft and other instruments; this suggests that we can observe more intense flares with those detectors facing away from the Sun, for which the bulk of the spacecraft will reduce the powerful low-energy radiation. The projected area of the large-area detectors is $\sim 5730 \text{ cm}^2$, far exceeding that of any previous solar experiment, so that BATSE will make significant observations of "microflares" (Lin et al., 1981).

The spectroscopy detectors exceed in total photopeak efficiency the γ -ray spectrometer experiment on board the **Solar Maximum Mission** (e.g. Chupp, 1984), so that routine data may also be interesting from the statistical point of view and for “microflare” observations. Unfortunately, the BATSE routine data do not give much emphasis to the spectroscopy detectors, which were added to BATSE relatively late in the program.

3. Detector Responses to Solar Input

Solar fluxes of γ -rays, hard X-rays, and especially soft X-rays can be enormous by comparison with the fluxes from cosmic sources (e.g. Seyfert galaxies). Furthermore these solar fluxes are extremely time-variable, leading to the classical problem of solar high-energy photometry in obtaining sufficient dynamic range. The solar high-energy spectrum is relatively well understood, however, with some uncertainty in detail regarding the “superhot” spectrum in the 20–40 keV range, so that the BATSE detector response should be amenable to numerical modeling. We have developed a model of the spectroscopy detector and its entrance-window geometry, as shown in Figure 1, suitable for Monte Carlo calculations of response. These calculations need to be made in enough generality so that the dynamic range can be understood precisely; then we will be able to optimize trigger and data modes for either solar or non-solar observational objectives. One should note that complete generality in these calculations will require including the Earth and the spacecraft mass-distribution model as well as the simple detector model.

4. BATSE Observing Modes

4.1. General Overview

The BATSE electronics provide a powerful variety of different observing modes, to be used for different properties of bursts; pulsar observations are also possible via on-board phasing of data. These observational modes fill the remainder of each of the data packets (after housekeeping and routine science data have been accommodated) at 128 16-bit words per packet. The choice of packet type and the readout schedule of packets depends upon what observations are desired. Table 1 (From Table 2.3-2 of the User’s Manual) lists some of the individual packet types.

The on-board burst memories offer still more flexibility in BATSE data transmission. For burst observations a burst-recognition trigger logic allows

a portion of memory to be filled according to the requirements of the observing mode and its parameters. Because the sun is bursty, the triggered data will be most important for solar purposes,¹ and we must pay proper attention to the trigger criteria. One should note that the solar flare trigger in BATSE consists of a set of restrictions on a set of data that have already satisfied the basic burst trigger. This implies that obtaining solar burst observations will require the generation of burst-memory-overwrite criteria and/or shortened "solar" burst-memory readout modes; otherwise the primary burst trigger criteria are likely to be defined in such a way as to minimize the number of solar triggers – given that GRO will fly during solar maximum!

Table 1. BATSE Data Types

Mnemonic	Number in Sequence	Description
PSRx		Pulsar modes, not applicable
HER	8	Large-area detector
SHER	16	Spectroscopy HER
DHER	24	Both detector sets HER
DISC	1	Selected detector rates
PREB	8	Preburst buffer readout
HERB	128	Large-area HER burst
TTE	128	Time-tagged event data
TTS	128	Time-to-spill
MER	32	Medium resolution data
SHERB	128	HERB for spectroscopy
STTE	128	TTE for spectroscopy

The three sections of Table 1 contain pulsar packets (PSRx), high-energy-resolution packets (xHER), and burst packets. The priority scheduling of packet transmission can be chosen by program, typically to have packets with burst data (up to about five minutes' worth) interleaved with packets of other types. The burst memory can be read out in one GRO orbit (about 96 minutes period). The time binning and energy resolution of the data differ from packet type to type. Further description of individual types follows:

¹BATSE also generates a solar trigger to alert the other experiments on board GRO.

- HER data for the large-area detectors consist of 128-channel spectra for each detector, one per packet. Spectroscopy detectors (SHER) have 256-channel resolution and therefore need 16 packets. DHER packets have both types of detector. If nothing else were being transmitted, therefore, DHER packets would provide high resolution at 24×2.048 sec = 49 sec time resolution. Either SHER or DHER would provide excellent solar γ -ray observations, albeit with rather coarse time resolution, if these packet types dominated the telemetry allocation.
- DISC data follow the large-area detector rates in the four most brightly illuminated detectors that trigger the burst mode, in four energy channels at 64 msec resolution. For solar purposes, DISC packets can provide high-time-resolution data for intercomparison with radio or other observations.
- Time-tagged event data (TTE for large-area, STTE for spectroscopy detectors) consist of memory data in four channels for large-area, or 16 bits per photon for spectroscopy. For the spectroscopy detectors the energy resolution is 128 channels; for both types of detector the (short-term) time resolution is 2 μ sec. These data are stored in memories with capacities of 32,000 words for large-area, and 64,000 words for spectroscopy. Nominally the burst trigger will happen as time-tagged events are being stored in a ring-buffer arrangement in these memory boards, so that some of the first quarter of the memory will have pre-burst data; the remaining 3/4 will follow the trigger time and proceed until the capacity is used up. There is flexibility in the choice of detectors from which to store events.
- Time-to-spill data (TTS) applies to large-area data only, and is a mechanism for obtaining high time resolution in four-channel spectra by measuring the time intervals needed to obtain a specified number of counts.
- Medium-energy-resolution (MER) data are 16-channel spectra from the large-area detectors selected at a burst trigger.
- High-resolution burst data from spectroscopy detectors are in SHERB packets, a sequence of 128 giving 64 spectra from one of three memory units as filled by the four brightest detectors at burst trigger. Spectra are accumulated in multiples of 64 msec, determined by an on-board

program, with the possibility of increasing the integration time as the burst proceeds.

4.2 Solar Possibilities

Many of the data types listed above have some possible utility for solar observations, although it is clear that some would be preferred over others. Probably the most important direct solar scientific contributions from BATSE (i.e., not considering for the moment the important supporting role that BATSE high-energy monitoring will perform) will come from the spectroscopy detectors, which will add greatly to our knowledge of γ -ray lines and continuum. To obtain high time resolution in these observations, burst data storage in memory mode will be necessary. This means SHERB or STTE data types.

The choice of observing mode and its parameters will be subject to a great deal of pressure as the BATSE experimenters optimize the primary science programs of the experiment. It is likely that the great flexibility of the BATSE data system will allow a considerable amount of experimentation before optimal modes can be found. Because solar flares will occur so frequently during the GRO mission, they may in fact provide a good basis for program optimization.

5. Conclusions and Recommendations

- The BATSE investigators should carry out a thorough modeling effort to understand the detector responses to solar inputs.
- There should be solar participation in discussions of spacecraft mass distribution and simulated response, including atmospheric albedo effects.
- It may be appropriate to recommend a minimal use of the instrument flexibility at the beginning of the GRO observations – several months of data under the same observing conditions would be conducive to good statistics.
- We should consider the possibility of using the solar trigger to enable a BATSE mode selection for solar data. Could this be done in a low-priority configuration, so that a stored solar burst could be overwritten?

- There should be a solar working group, possibly with help from guest investigators, to assess the data starting at time of launch. This group should form earlier than launch, if possible, so that it can get sufficiently along on the learning curve to be useful.
- The possibility of solar “campaigns” over restricted time periods (e.g. VLA availability) for coordinated observations should be explored.

Acknowledgements. NASA supported this work at UCSD under grants NAS 8-36081 and NSG-7161.

References

- BATSE team 1986, *Flight Software User's Manual*, NASA/MSFC Technical Report.
- Chupp, E., 1984: *Ann. Revs. Astron. Astrophys.* **22**, 359.
- Dennis, B., 1986: *Solar Phys.* **100**, 465.
- Fishman, G.J., Meegan, C.A., Parnell, T.A., Wilson, R.S., and Paciesas, W., 1984: Santa Cruz proceedings.
- Lin, R.P., Schwartz, R.A., Pelling, R.M., and Hurley, K.C., 1981: *Astrophys. J.* **283**, 421.

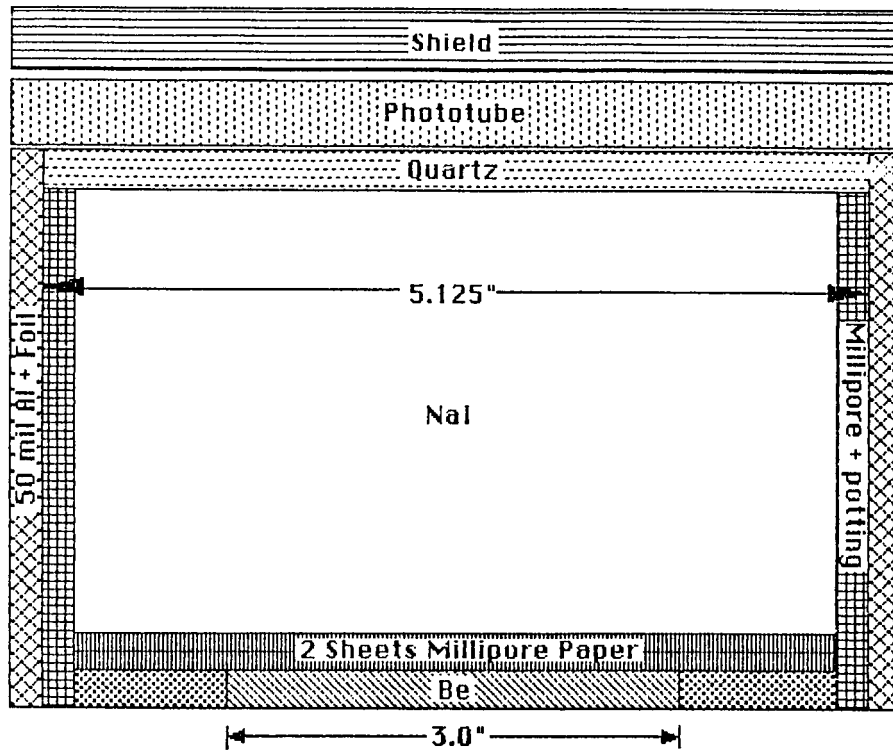


Figure 1. Model for Monte Carlo simulation of the BATSE spectroscopy detector, showing some of the materials and geometry. Flux may be incident from any direction, since the BATSE experiment contains eight of these modules oriented in the directions normal to the faces of a regular octahedron. The nominal view direction is downwards on this sketch.

DEVELOPMENT OF A HIGH-SPEED H-ALPHA
CAMERA SYSTEM FOR THE OBSERVATION OF
RAPID FLUCTUATIONS IN SOLAR FLARES

INVESTIGATORS:

Dr. Alan L. Kiplinger
NASA/GSFC and STX Corporation
Code 602.6

Dr. Brian R. Dennis
&
Dr. Larry E. Orwig
NASA/GSFC
Code 682

Dr. P. C. Chen
NASA/GSFC and C.S.C.
Code 684

Laboratory for Astronomy and Solar Physics
Goddard Space Flight Center
Greenbelt, MD 20771

This development is currently being supported by:

NASA RTOP 682-170-38-51-76

ABSTRACT

We have developed a solid-state digital camera system for obtaining H α images of solar flares with 0.1 s time resolution. Beginning in the Summer of 1988, this system will be operated in conjunction with SMM's Hard X-Ray Burst Spectrometer (HXRBS). Important electron time-of-flight effects that are crucial for determining the flare energy release processes should be detectable with these combined H α and hard X-ray observations.

Charge-injection device (CID) cameras provide 128x128 pixel images (0.8 arc-sec/pixel) simultaneously in the H α blue wing, line center, and red wing, or other wavelength of interest. The data recording system employs a microprocessor-controlled, electronic interface between each camera and a digital processor board that encodes the data into a serial bitstream for continuous recording by a standard video cassette recorder. With a combined data rate of 4 Megabaud for a three camera system, a typical one week observing run is expected to produce approximately 100 gigabytes of data at a storage cost of approximately \$1/Gigabyte. Only a small fraction of the data (i.e. data containing flares) will be permanently archived through utilization of a direct memory access interface (a DRE-11CC) onto a VAX-750 computer.

In addition to correlations with hard X-ray data, observations from the High Speed H α Camera will also be correlated and optical and microwave data and data from future MAX '91 campaigns. Whether the recorded optical flashes are simultaneous with X-ray peaks to within 0.1 s, are delayed by tenths of seconds or are even undetectable, the results will have implications on the validity of both non-thermal and thermal models of hard X-ray production.

I. INTRODUCTION AND SCIENTIFIC BASIS

i. Introduction

A significant fraction of the science effort during the last solar cycle has been directed toward observations of solar flares with high time resolution. Correlations of subsecond x-ray variations with UV and microwave variations have placed important constraints on models of solar flares. Microwave images obtained with the VLA have good spatial resolution but relatively poor time resolution (~ 3 s). Ultraviolet images obtained with the Solar Maximum Mission (SMM) can have good time resolution, but at the expense of observing at only one or a few pixels. Clearly, there is a great need for new correlative studies of solar flares to achieve high time resolution and high spatial resolution simultaneously in order to resolve effects such as those resulting from electron time-of-flight. These effects are crucial for determining causal relationships among emitting components and in identifying the flare energy release process or processes.

ii. Hard X-Ray Emission

In the non-thermal electron beam model for hard X-ray emission, electrons accelerated near the top of a flaring coronal loop stream along magnetic field lines until they reach the relatively dense layers of the lower corona and upper chromosphere. Here they produce hard X-ray bremsstrahlung at energies ranging from tens of keV to several MeV (cf. Brown, 1971; Emslie, 1980). Electrons with energies of ~ 35 keV produce many of the X-rays seen by the Hard X-ray Burst Spectrometer (HXRBS) on SMM. For typical flare loop dimensions of $1\text{-}5 \times 10^4$ km, electrons of this energy should traverse the loop in 0.1-0.5 s or longer depending upon their pitch angle with respect to the loop's magnetic field. Observations on timescales of ~ 0.1 s or less are required to resolve electron time-of-flight effects.

With the high-time resolution of HXRBS on SMM, hundreds of fast X-ray spikes with durations of less than 1 s and rise and decay times of some tens of milliseconds have been detected (Kiplinger *et al.*, 1983). The existence of such variations in hard X-rays offers the opportunity to correlate variations at differing energies on timescales that are considerably less than one second. Note for non-thermal models, the observed hard X-ray time profile is the convolution of the temporal evolution of the electron acceleration process with propagation effects associated with the beam of electrons interacting in the target (cf. Emslie, 1983). Alternatively, the relevant timescales in thermal models stem from the bulk heating and the cooling of the source through, for example, conduction, convection, expansion and radiation (cf. Smith and Auer, 1980). Thus, the observation of hard X-ray variations on timescales as short as, or shorter than, the anticipated timescales can place constraints on some or all of the above processes.

iii. Expected Response in H α

The H α emission line ($\lambda 6563\text{\AA}$) can provide spatial information very accurately if it can be shown that there is a good temporal correlation

between the H α and hard X-ray time profiles. In a CCD study of H α fluctuations, Kampher and Magun (1983) have shown that there is a component of the H α emission that shows impulsive variations that are coincident with microwave spikes. However, with a time resolution of only 1.4 s, coincidence could only be established to within 2 s. In a photographic study by Kurokawa (1986) with 1 s time resolution, coincidence of hard x-ray spikes with H α fluxes, as measured in the blue wing, was established to within one second. This study also concludes that the impulsive phase of an H α flare is characterized by fast and successive brightenings of many flare points with point sizes of 1 arc-sec or less. However, there may be some ambiguity in interpreting H α results since the line is produced from plasmas with low effective temperatures, $T_{\text{eff}} \sim 10^4$ K, which are generally associated with cooler thermal components that develop during a flare. Indeed, both of the the H α studies described above did identify both impulsively varying bright points and bright points or patches which vary on much slower timescales.

Detailed observations in H α can provide a wealth of diagnostic information on differing physical processes. Calculations of the sensitivity of H α profiles to electron beam fluctuations by Canfield and Gayley (1985) describe the temporal response of the spectral line. An instantaneous injection of an electron beam into the chromosphere is expected to produce an impulsive rise in H α intensity over the entire line profile on a chromospheric heating timescale, $t_h \approx 10$ ms. In addition to this major impulsive rise, the blue wing of the line is expected to show a secondary response on the hydrogen ionization timescale, $t_i \approx 0.3$ s. A third effect of the rapid injection of energy into the chromosphere is the creation of a high pressure region and its resultant compression wave. This wave, in turn, forms a chromospheric condensation whose emission begins to dominate the red wing of the line, and to some extent the line center, approximately 1 second after the impulsive rise. For this reason, and the fact that H α intensities generally increase from thermal plasmas that build up during the flare, observations in the blue wing of H α may provide the greatest contrast for observing impulsive brightenings resulting from subsequent electron beam injections later in the flare.

In summary, the expected response of H α to a rapid onset of an electron beam would be for the intensity in the entire profile to rise within 10 ms of the rise in hard X-ray fluxes, with a smaller, secondary rise in the blue wing following by about 0.3 s. Finally (after 1.0-1.5 s) the red wing and, to a lesser degree, the line center should show a secondary rise due to hydrodynamic effects. Few of these effects have been detected or even studied observationally. This is due to the lack of the proper instrumentation and to the vast quantities of data that must be collected to insure sufficient temporal and spatial sampling of the flare.

II. EXPERIMENTAL DESIGN AND OPERATION

i. The Digital H α System consists of the following components:

Detectors: The detectors are solid-state charge-injection device (CID) cameras which feature a high signal-to-noise ratio and which provide 128x128 pixel images at the rate of 10 frames/s. A CID camera has been chosen since it allows shutterless operation; furthermore, the ultra-low noise

levels of CCDs are unnecessary in this high-light-level/short exposure-time environment. The system is initially a two camera system with one camera operating at center-line H α and the second camera operating 1.1 Å in the blue wing.

Recording System: Each data recording system (one for each camera) consists of a computerized interface and controller which connects the camera to a commercially available digital processor board. This board encodes the data for recording onto standard video cassette recorder (VCR) tapes. The interface serializes the digital camera data and adds absolute timing information (accurate to 1 ms) to the data stream. The VCR is a means of temporarily storing the large quantities of data obtained. With each camera yielding ~5 gigabytes of data each observing day, a seven day observing run would produce ~100 gigabytes of information that can be stored on ~25 reusable VCR tapes. (One hundred gigabytes is equal to the total amount of data returned by SMM in 19 months.) Computer archiving of data recorded during flares is only necessary for the small fraction of data that will be studied. Archiving of the digital data utilizes a direct memory access interface board (known as a DRE11-CC) in a VAX computer which copies the data onto a hard disk and ultimately onto magnetic tape.

Optical System: The telescope to be employed initially is a 40-cm Cassegrain telescope at Goddard stopped down to 15 cm by a heat rejection filter. The off-axis beam enters a 0.5 Å (FWHM) dual-passband H α filter. As shown in Figure 2, one passband is situated at line center with the other situated 1.1 Å in the blue wing. The passbands are separated by a polarizing beamsplitter and directed to two of the cameras. Although it is initially configured to be a two camera system, a third camera can be added which will observe at the wavelength of H α *300Å. The third camera utilizes a beam from a standard beamsplitter that is situated in front of the dual-passband H α filter system. With an effective focal length of 7.3 meters, the 128x128 pixels of the CID cameras correspond to a projected field of view of 1.7'x1.7' field of view at 0.85" per pixel.

ii) Observing Program:

With a startup time of two hours or less (instead of two days for Sacramento Peak), we can respond within the early growth stages of an active region when the most impulsive flares tend to occur. However, since only 10% of flares exhibit subsecond time variability (Kiplinger *et al.*, 1983) and since only a fraction of active regions display a propensity to produce such flares, we do not intend to observe on a routine daily basis. Rather, we will decide to observe in a fashion analogous to the "bumping" decisions we currently make for our Sacramento Peak observations. We anticipate observing for five- to seven-day intervals perhaps ~4 times per year under conditions of moderate solar activity (i.e. initial stages of the solar cycle).

One of us, Alan Kiplinger, has proposed to NASA and NSF to assume the role of MAX '91 coordinator and to carry out research at the University of Colorado in Boulder. Operation of this camera is part of his proposed research; therefore, after the high-speed system becomes operational at Goddard

(and assuming that Kiplinger does move to Colorado) we anticipate moving the camera system to a 45-cm cassegrain telescope at the University of Colorado. The Colorado location will continue to provide a 100% availability of telescope time (during daytime hours) and a short startup time. Moreover, relocation to Boulder will provide far better seeing and transparency conditions than are typically present at Goddard. Moving the instrument westward will also provide two more hours of overlap in observing time with any collaborative programs that may be operating from New Mexico to Hawaii. Observations from Boulder will also mark the curtailment of the Sacramento Peak program, thus providing a significant increase in observing time on the Vacuum Tower Telescope for other important Max '91 programs.

iii) Data Analysis

As a principal investigator in an ongoing CCD program with the National Solar Observatory, Kiplinger has developed the necessary software to analyze data produced by the new high-speed system. Interactive routines that perform field flattening corrections and also generate time profiles from any selected part of an image are maintained on the SMM Data Analysis Center (DAC) VAX. Both the SMM DAC and the APAS Vaxlab Computer at the University of Colorado have Grinnell image processing systems that can utilize this software. Thus, the analyses will be carried out in Boulder once the camera system is relocated.

A major part of the analysis is to study temporal correlations of hard X-ray fluxes measured with HXRBS with optical fluxes from various parts of the images at all of the observed wavelengths. The data would also be compared with the high-spectral, low-temporal resolution data to be obtained by Richard Canfield in Hawaii when simultaneous observations are available. Although comparisons with HXRBS data will be an initial focus, data from other instruments such as the Gamma Ray Imaging Device (GRID) to be proposed within the MAX '91 balloon program and BATSE of the Gamma Ray Observatory would be of great interest.

iv) Current Program Status and Schedule

Current Status:

As of June, 1988, the development of the high speed $H\alpha$ system stands as follows:

- Construction of the optical/mechanical system has been completed.
- Major components of the electronic interface of the first camera have been constructed and we are awaiting arrival of the microprocessor that directs the data flow.
- Single camera operation at Goddard is expected by the summer of 1988 with two camera operation beginning by late 1988.

Schedule:

An approximate schedule for development of the high-speed system is as follows:

1988

Fabrication of the second interface should begin by the summer of 1988 with two camera operation beginning by the fall.

Construction of the third interface and procurement of the additional camera and recorder should begin by late 1988.

1989

Move of the two camera system to Boulder. Due to the similarities of telescopes at the two locations, it is expected that operation at Boulder could begin within a few days of the arrival of the instrument.

The H α filter previously purchased by Goddard in 1971 will be refurbished in order to remove serious internal reflections. This filter will utilize light from the third beam for H α red-wing observations.

Development of the mechanical and optical system for the third camera should be completed, along with the interface for the third camera.

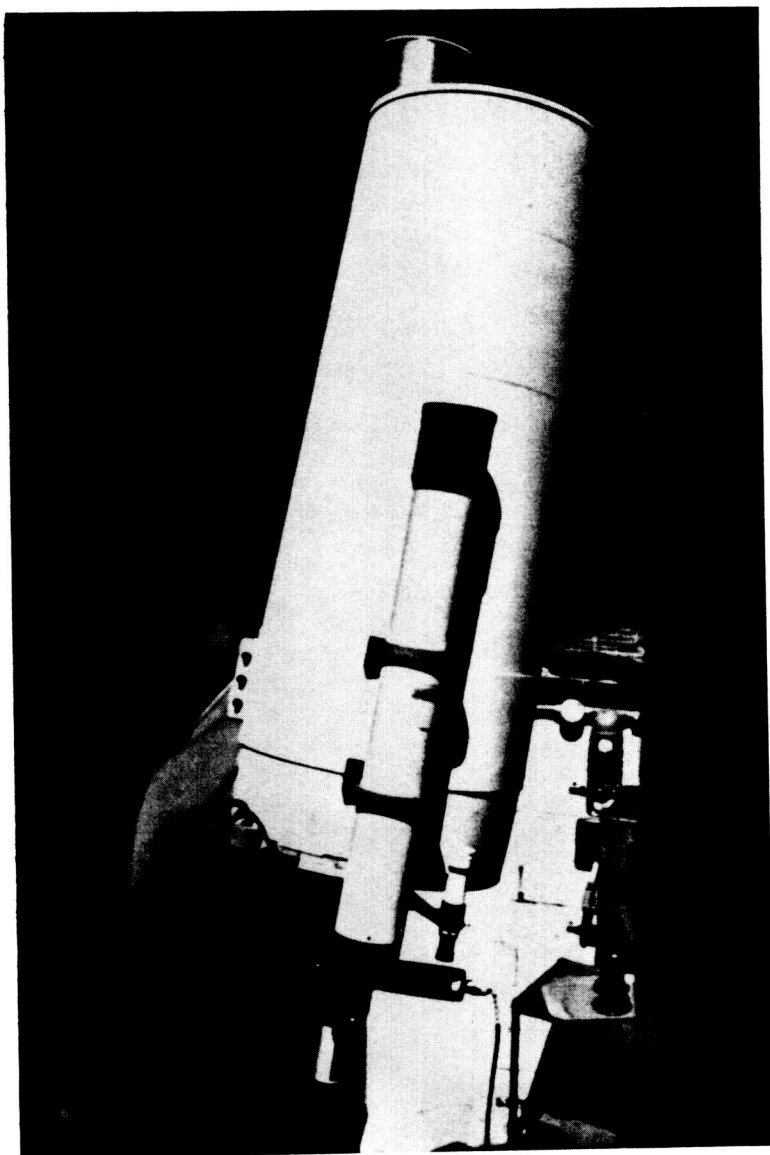
1990

Three camera operation is expected by early 1990.

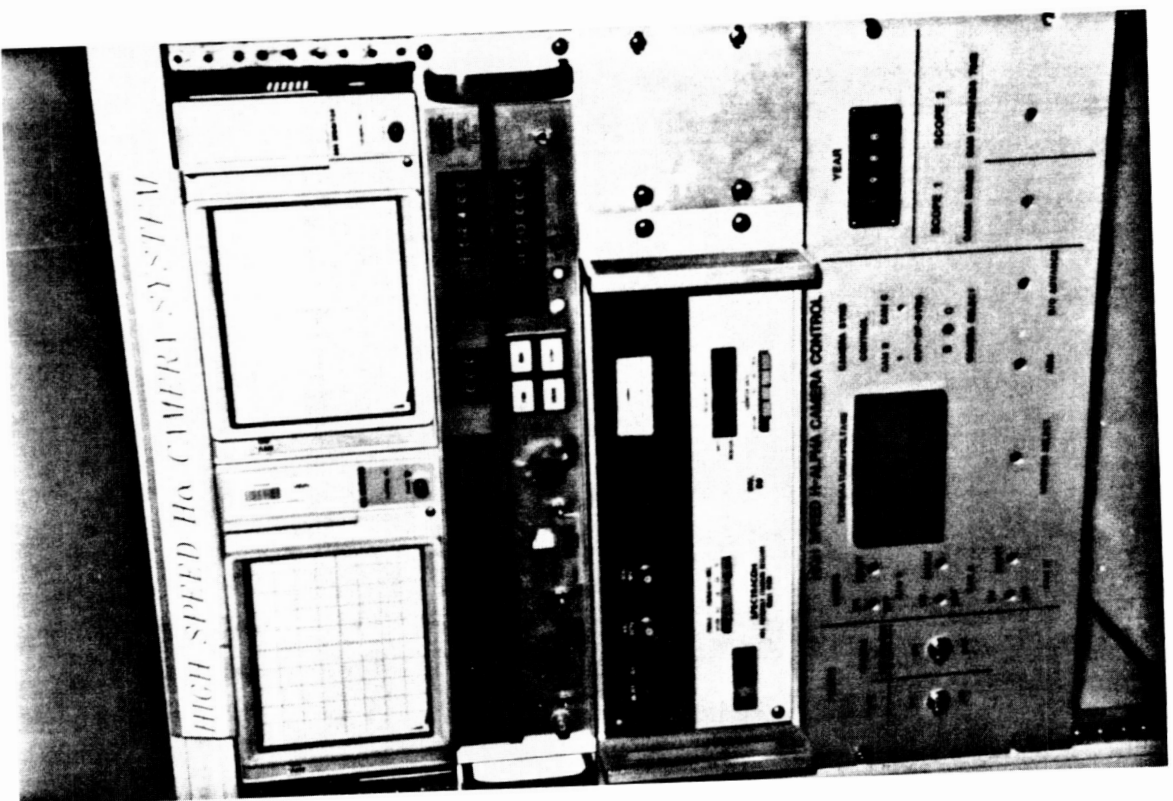
III. REFERENCES

- Brown, J. C. 1971, Solar Phys., 18, 489.
Canfield, R. C., and Gayley, K. 1985, in Rapid Fluctuations in Solar Flares, NASA CP 2449, p249.
Emslie, A. G. 1980, Ap. J., 235, 1055.
Emslie A. G. 1983, Ap. J., 271, 367.
Kamphur, N., and Magun, A. 1983, Ap. J., 274, 910.
Kiplinger, A. L., Dennis, B. R., Emslie, A. G., Frost, K. J., and Orwig, L. E. 1983, Ap.J. Letters, 265, L99.
Kurokawa, H. 1986, Proc. of the National Solar Observatory/Solar Maximum Mission Symp. 20-24 August 1985, The Lower Atmosphere of Solar Flares, ed. D. Neidig, p51.
Smith, D. F. and Auer, L. H. 1980, Ap. J., 238, 1126.

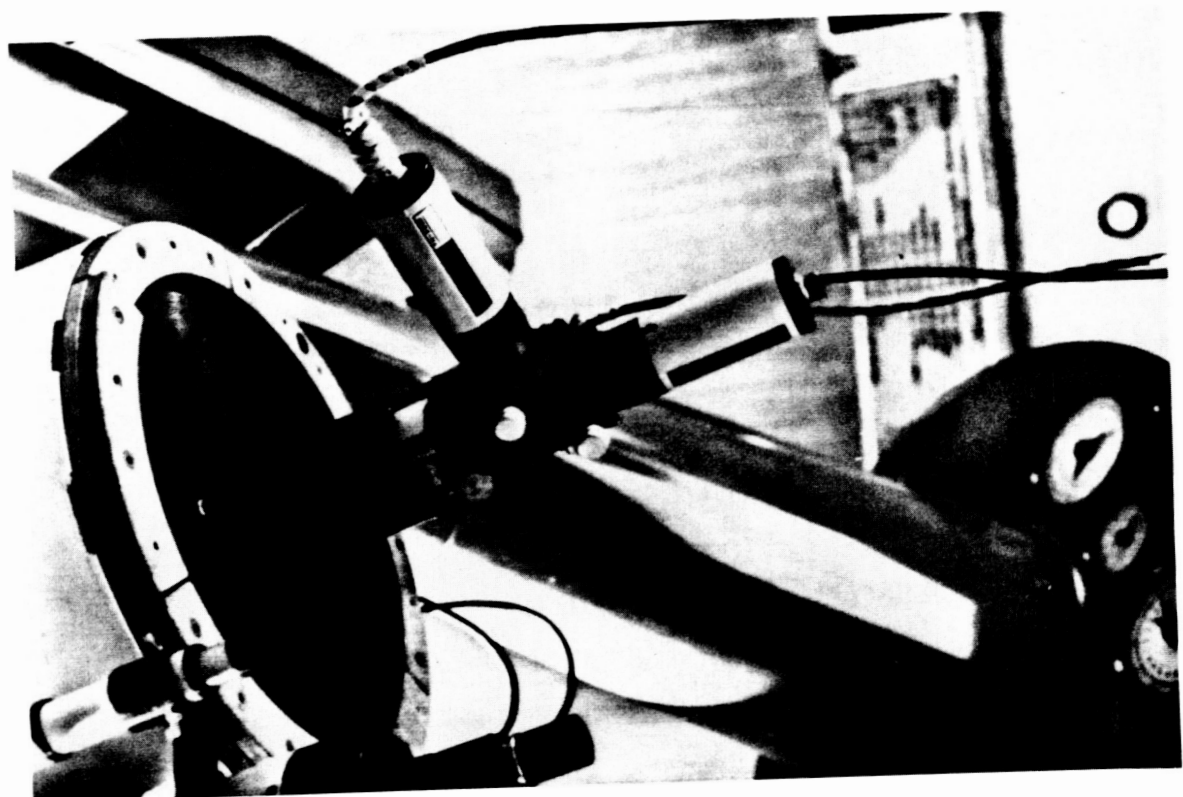
ORIGINAL PAGE IS
OF POOR QUALITY



NASA/Goddard 0.4 m (16-inch) Cassegrain Telescope
with 6-inch heat rejection filter (top) and
Dual Camera Assembly (bottom).



Camera Displays, Time Encoder
and Camera Control Panel



H- α Filter and Dual
Camera Head Assembly

ORIGINAL PAGE IS
OF POOR QUALITY

ORIGINAL PAGE IS
OF POOR QUALITY



Six-inch aperture stop on 0.4 m telescope.
The aperture stop houses the heat rejection filter.

Does the Resistive Tearing Instability Nonlinearly Evolve to a Fast Reconnection Mode?*

R.S. Steinolfson (U. Texas, Austin)

A fundamental problem in applying linear tearing instability theory to the rapid processes (particle acceleration, heating) in flares has been the characteristically slow rate of reconnection. This problem can be at least partially overcome if the tearing mode nonlinearly evolves to a regime in which the reconnection rate is substantially enhanced, such as that for the Petschek configuration. This possibility has often been suggested, and some numerical simulations appear to provide support for such a view. We use numerical simulations to study the nonlinear evolution of the tearing instability and show that a fast Petschek-like regime may not be achieved. This conclusion follows when there are sufficient grid points within the diffusion region to completely resolve the nonlinear dynamical interactions in the diffusion layer. When the numerical resolution is not adequate, the solution does appear to approach a Petschek configuration. The resolved solution contains reverse flow vortices and current sheets, terminated with a current reversal, similar to those obtained by Syrovatsky (JETP, 33, 933, 1971).

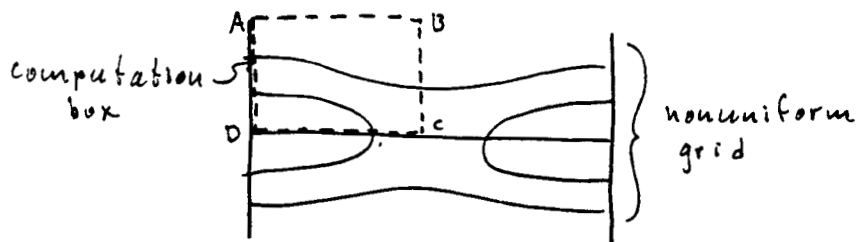
*Research supported by NASA and NSF. Computations performed at SDSC.

Does the Resistive Tearing Instability
Nonlinearly Evolve to a Fast Reconnection Mode?

R. S. Steinolfson
Institute for Fusion Studies
University of Texas, Austin

Results from two studies concerning the rate of reconnection of magnetic field lines are reported on. Both illustrate the need to numerically resolve the physical processes inside the diffusion layer in order to simulate the correct evolution.

The model assumes incompressible MHD with constant resistivity in a slab geometry. The time-dependent equations are solved numerically using a fully implicit method. A linearly growing mode provides the initial disturbance. Only one quadrant of the complete mode is simulated as shown in the sketch below:



The boundary conditions are -

B-C, C-D; symmetry

D-A; symmetry for the first study, outflow for the second

A-B; linear extrapolation although it is so far

removed from the tearing layer by the nonuniform grid that it has virtually no influence.

The results from the individual studies are as follows:

A. Nonlinear evolution of a linearly growing mode

The first set of plots below (indicated by ①) are for an unresolved diffusion layer while for the second ② sufficient resolution was used to correctly simulate the nonlinear effects of the resistive terms. The two solutions were started with the same linear mode and are compared after evolving for the same time period. The solution in set ① is simply an amplified linear mode, while that in set ② shows the development of reverse flow vortices.

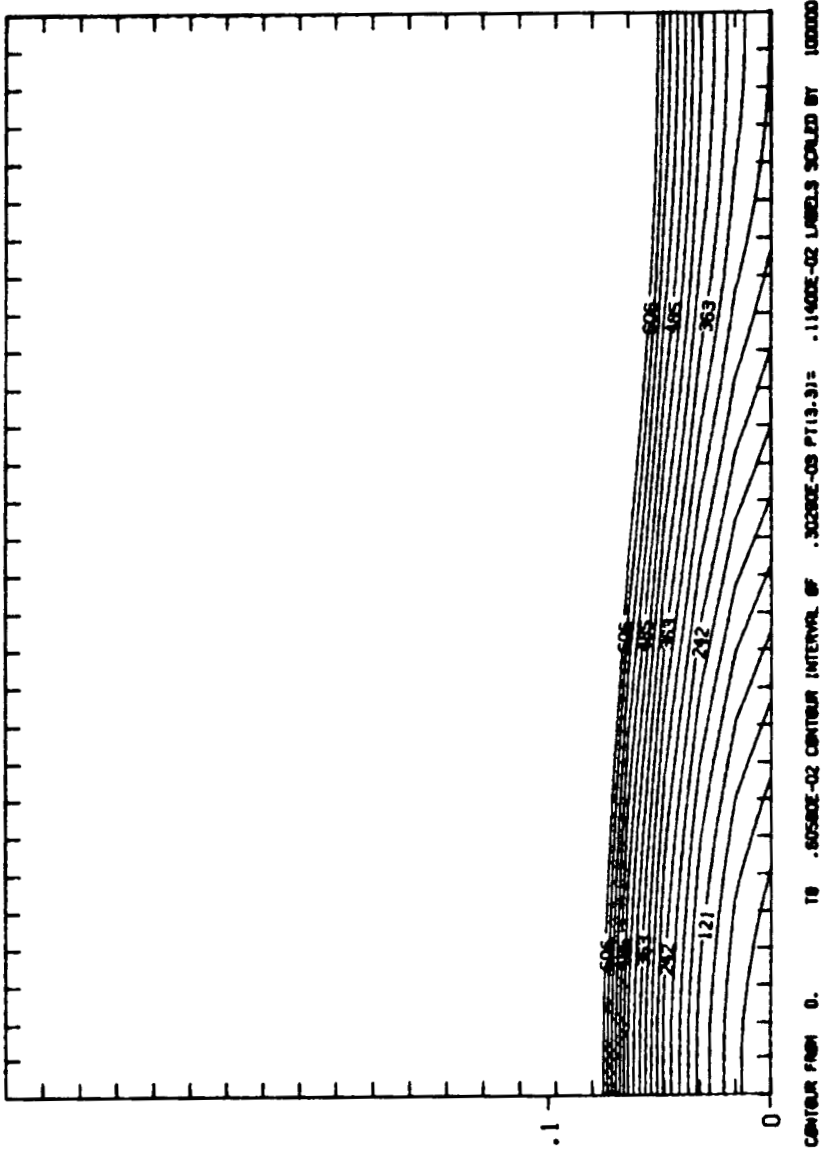
ORIGINAL PAGE IS
OF POOR QUALITY

ORIGINAL PAGE IS
OF POOR QUALITY

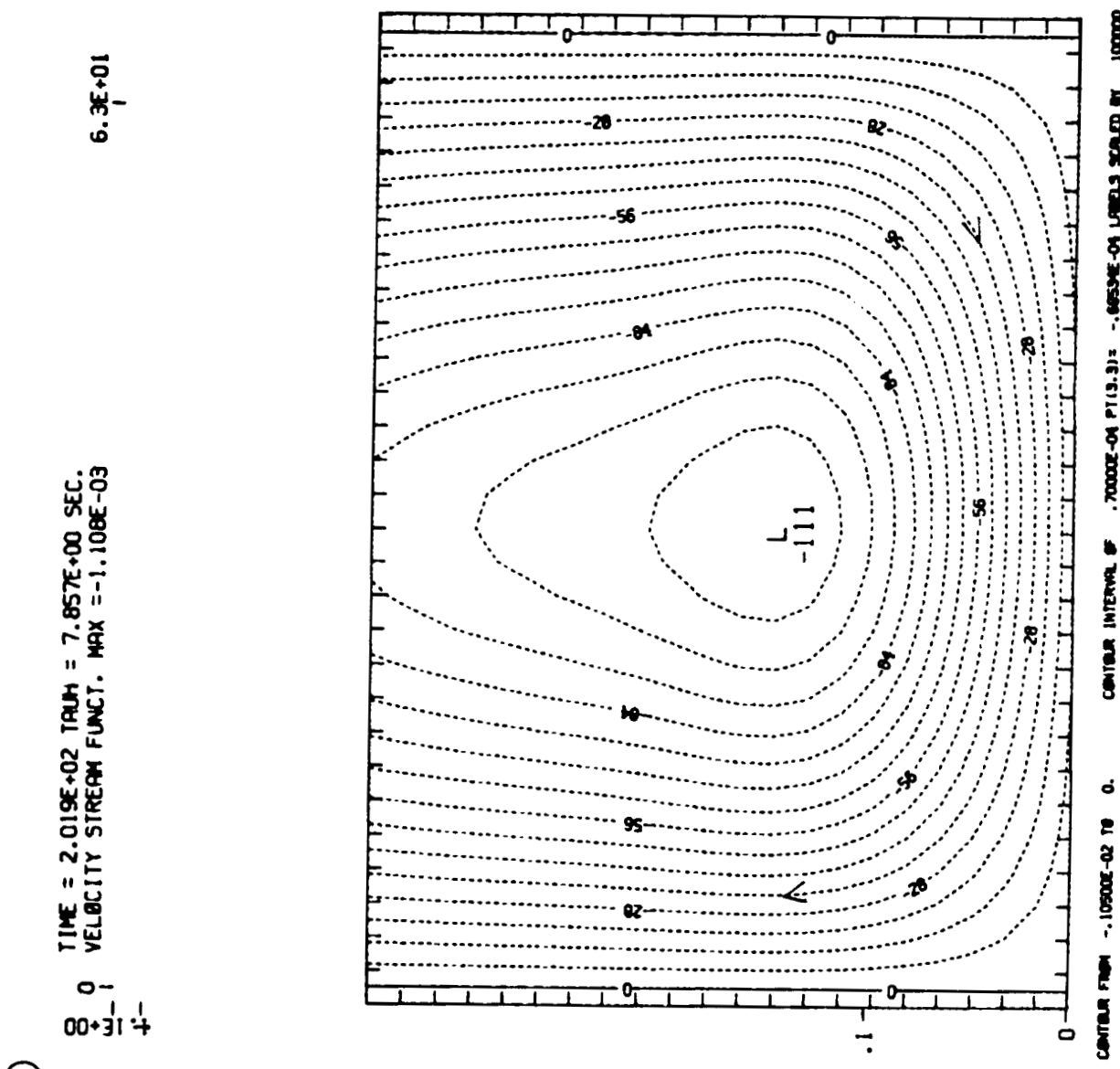
① Unresolved diffusion layer

8.0 TIME = 2.019E+02 TAUH = 7.857E+00 SEC.
CONSTANT FLUX CURVES

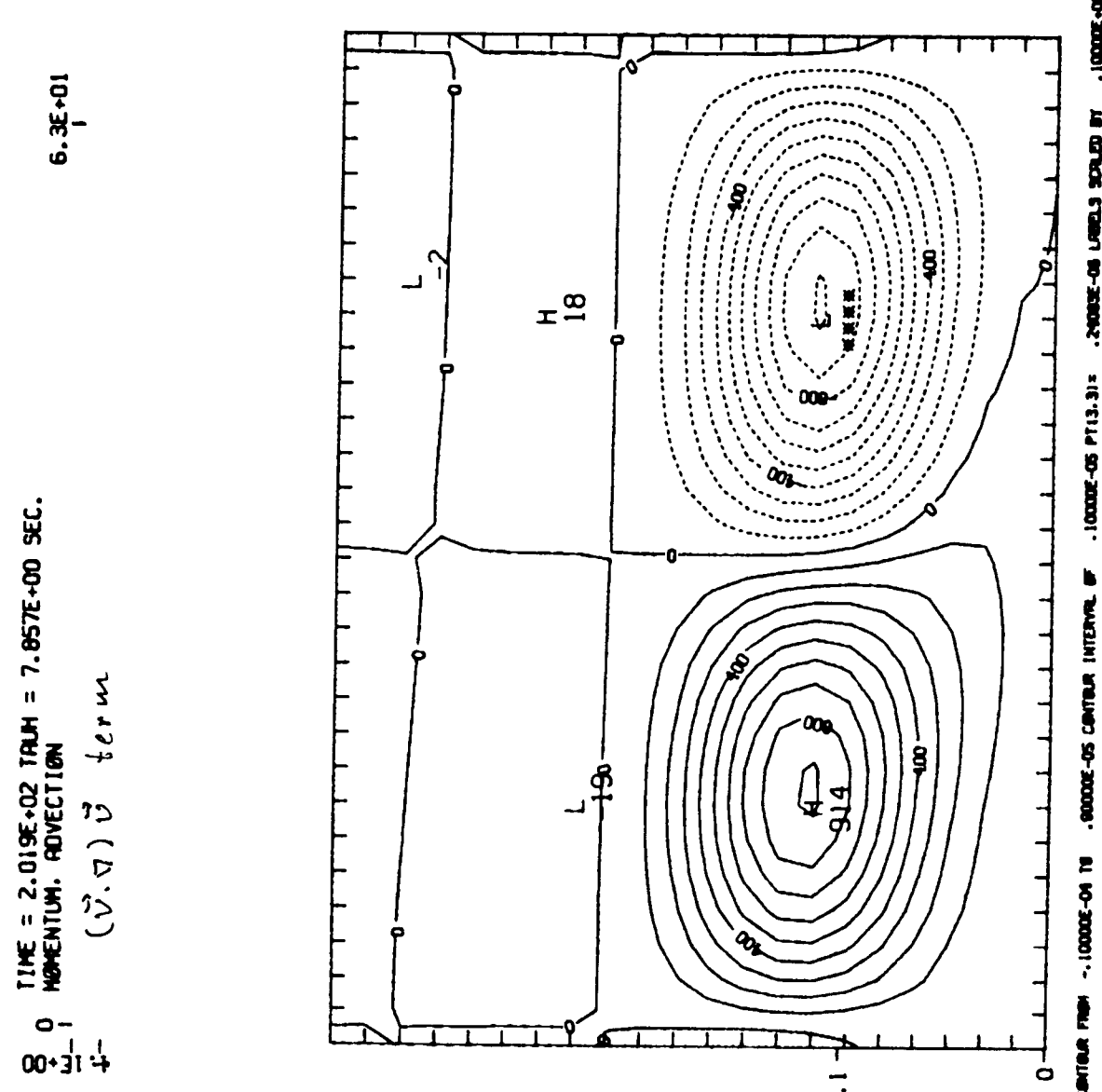
6.3E+01



ORIGINAL PAGE IS
OF POOR QUALITY



ORIGINAL PAGE IS
OF POOR QUALITY



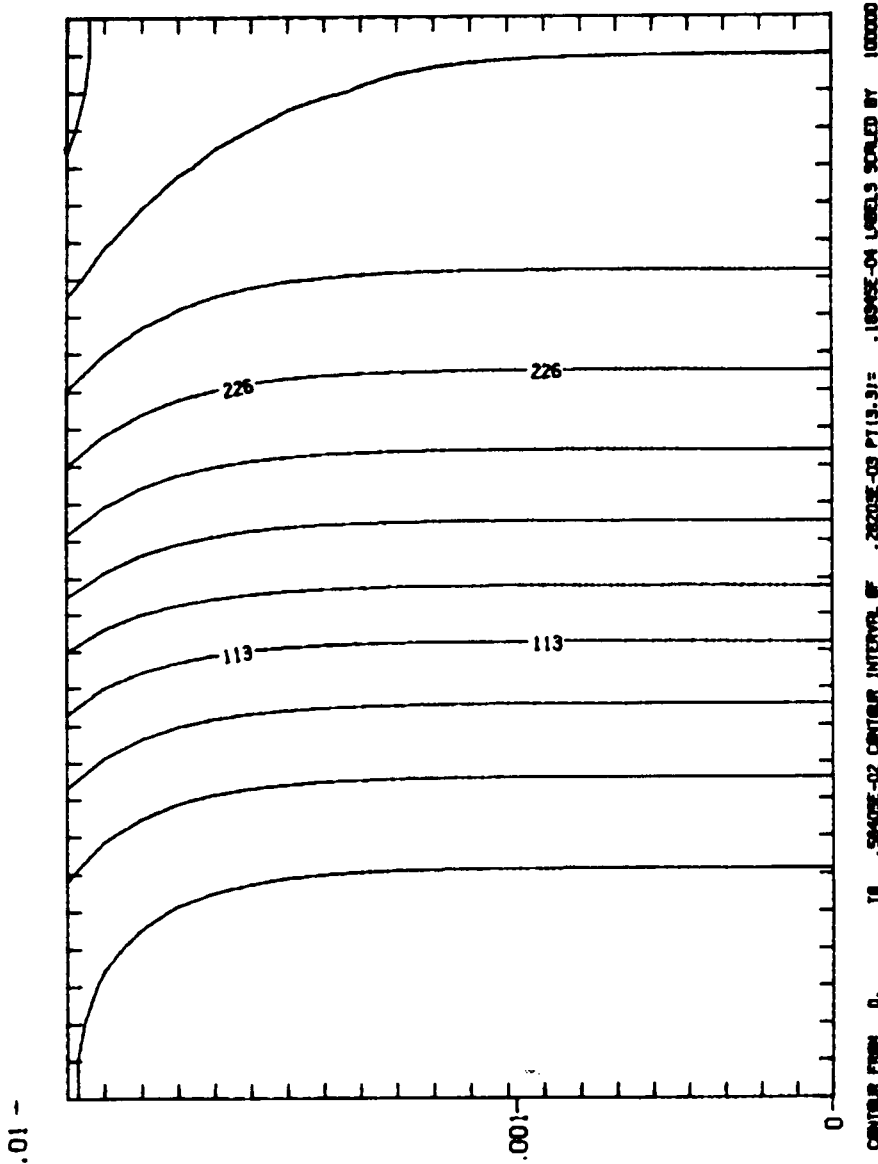
-

(2)

Resolved

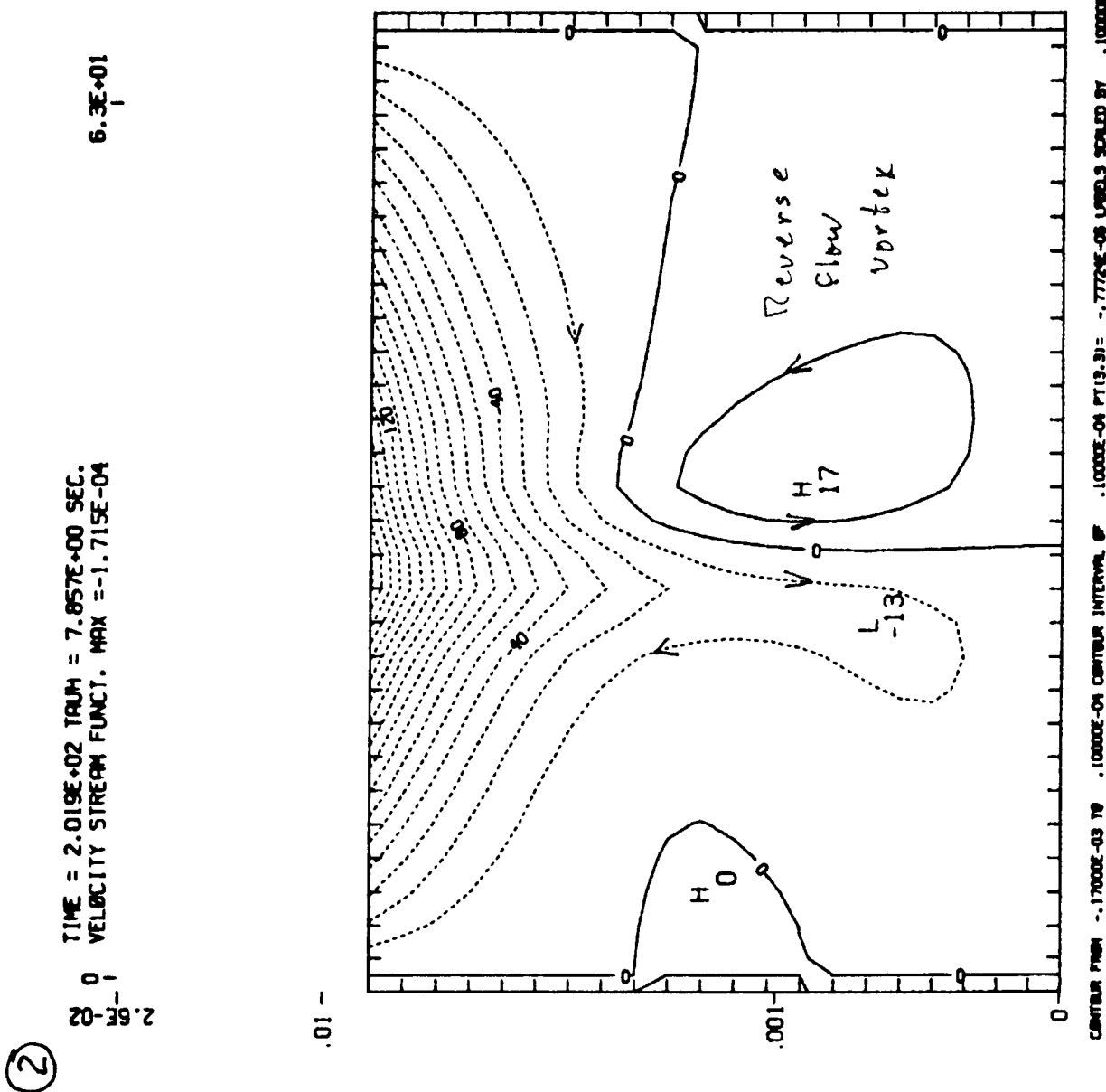
TIME = 2.019E+02 TRIM = 7.857E+00 SEC.
CONSTANT FLUX CURVES

6.3E+01



ORIGINAL PAGE IS
OF POOR QUALITY

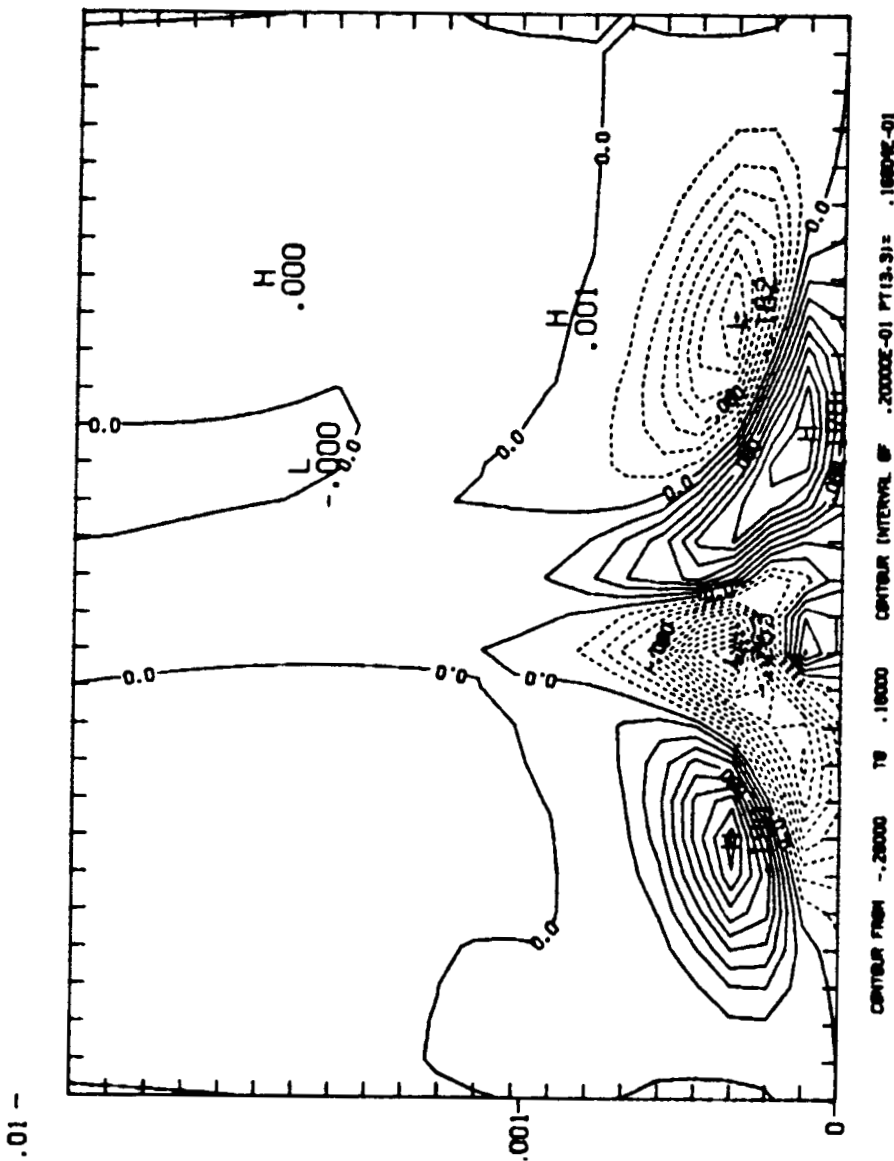
ORIGINAL PAGE IS
OF POOR QUALITY



(2)

TIME = 2.019E+02 TRIM = 7.857E+00 SEC.
MOMENTUM, PROJECTION

6.3E+01



ORIGINAL PAGE IS
OF POOR QUALITY

B. Development of the Petschek regime

The solutions are again initiated with the same linear mode, but the boundary conditions along boundary D-A in the above figure are modified to permit an outflow. As shown in set ③, a continuous outflow develops when the resistive layer is not resolved. However, when sufficient grid points are located within the layer, as shown in set ④, ~~then~~ an outflow initially develops but eventually the nonlinear terms prevent the formation of a regime with outflow along D-A

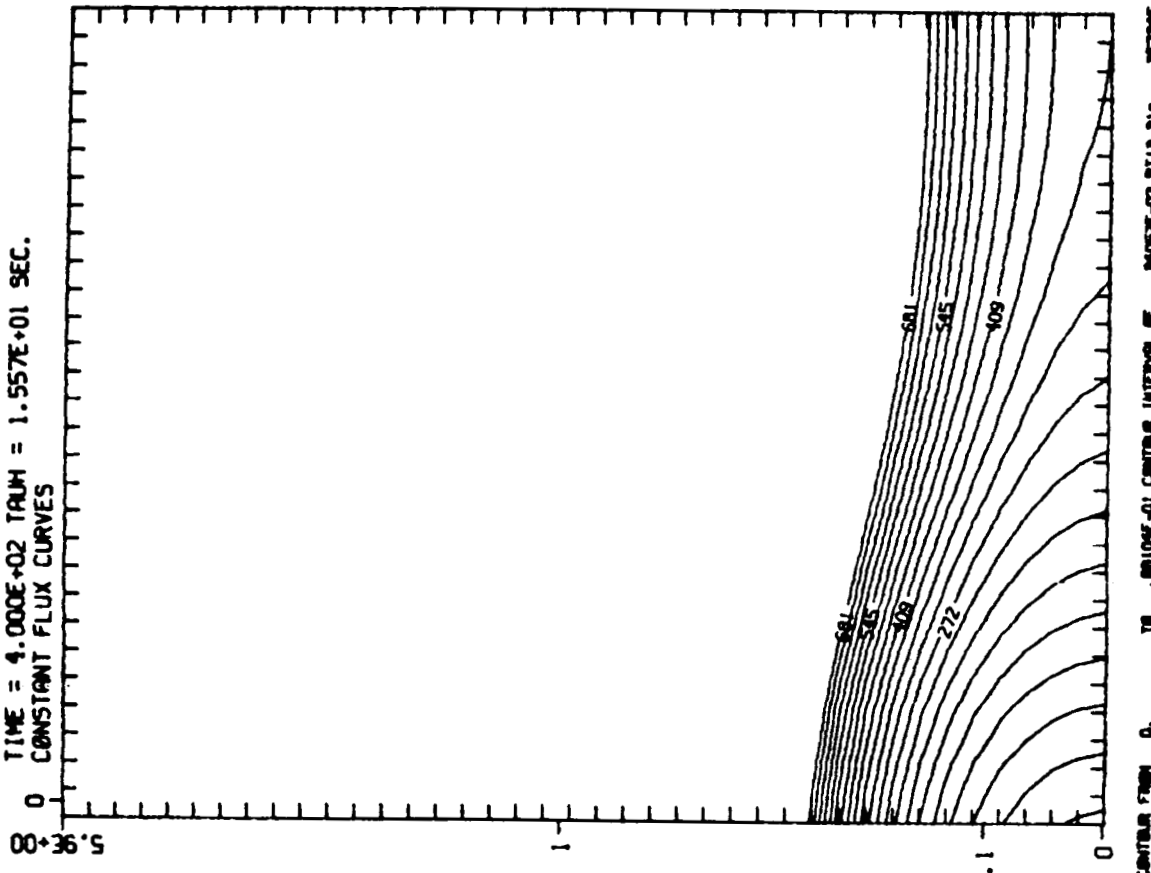
ORIGINAL PAGE IS
OF POOR QUALITY

Insufficient resolution

(3)

TIME = 4.000E+02 TMAX = 1.557E+01 SEC.
CONSTANT FLUX CURVES

6.3E+01

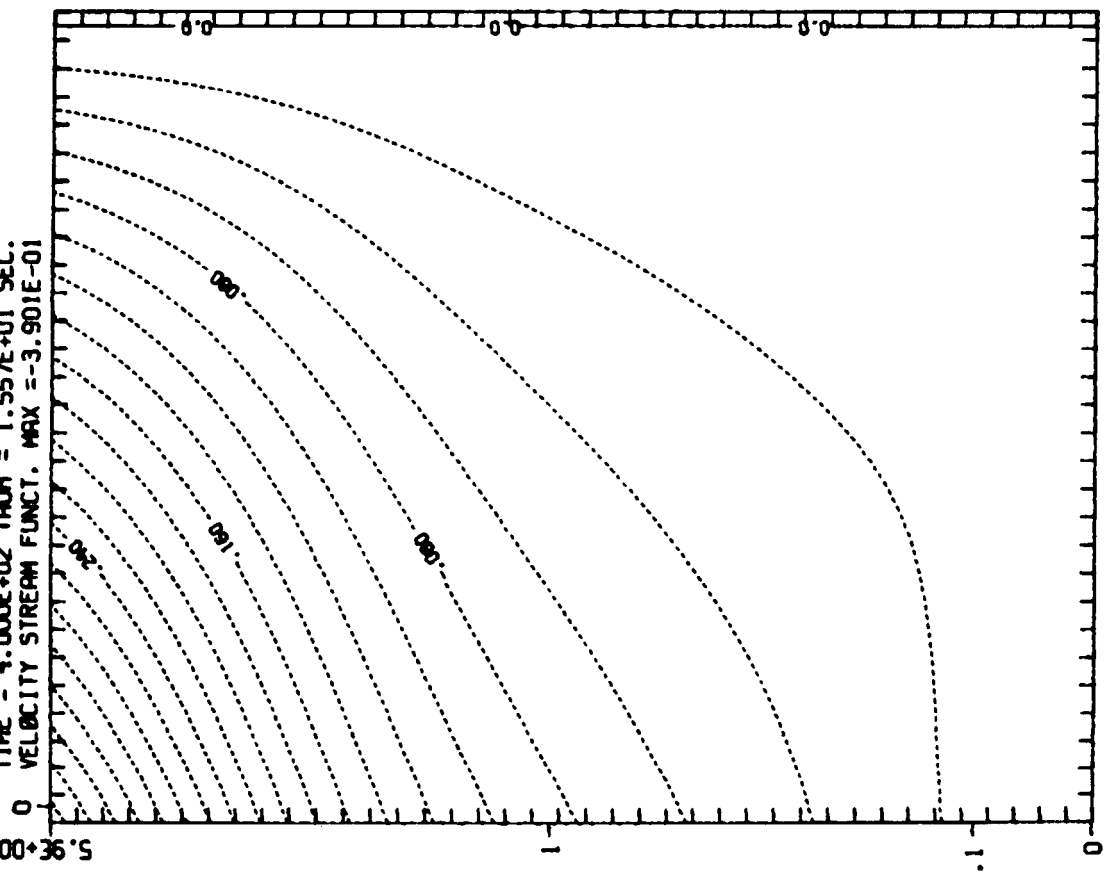


17

ORIGINAL PAGE IS
OF POOR QUALITY

6.36E-01
TIME = 4.000E+02 TAUH = 1.557E-01 SEC.
VELOCITY STREAM FUNCT. MAX = -3.901E-01

CONTINUATION - 36000 79 0 CENTER INTERVAL 87 .20000E-01 7713.302 -71122E-02



(3)

147.00
VECTORS

TIME = 4.000E+02 TRIM = 1.557E+01 SEC.
VELOCITY VECTORS. VMAX = 1.471E-01

00+36°S

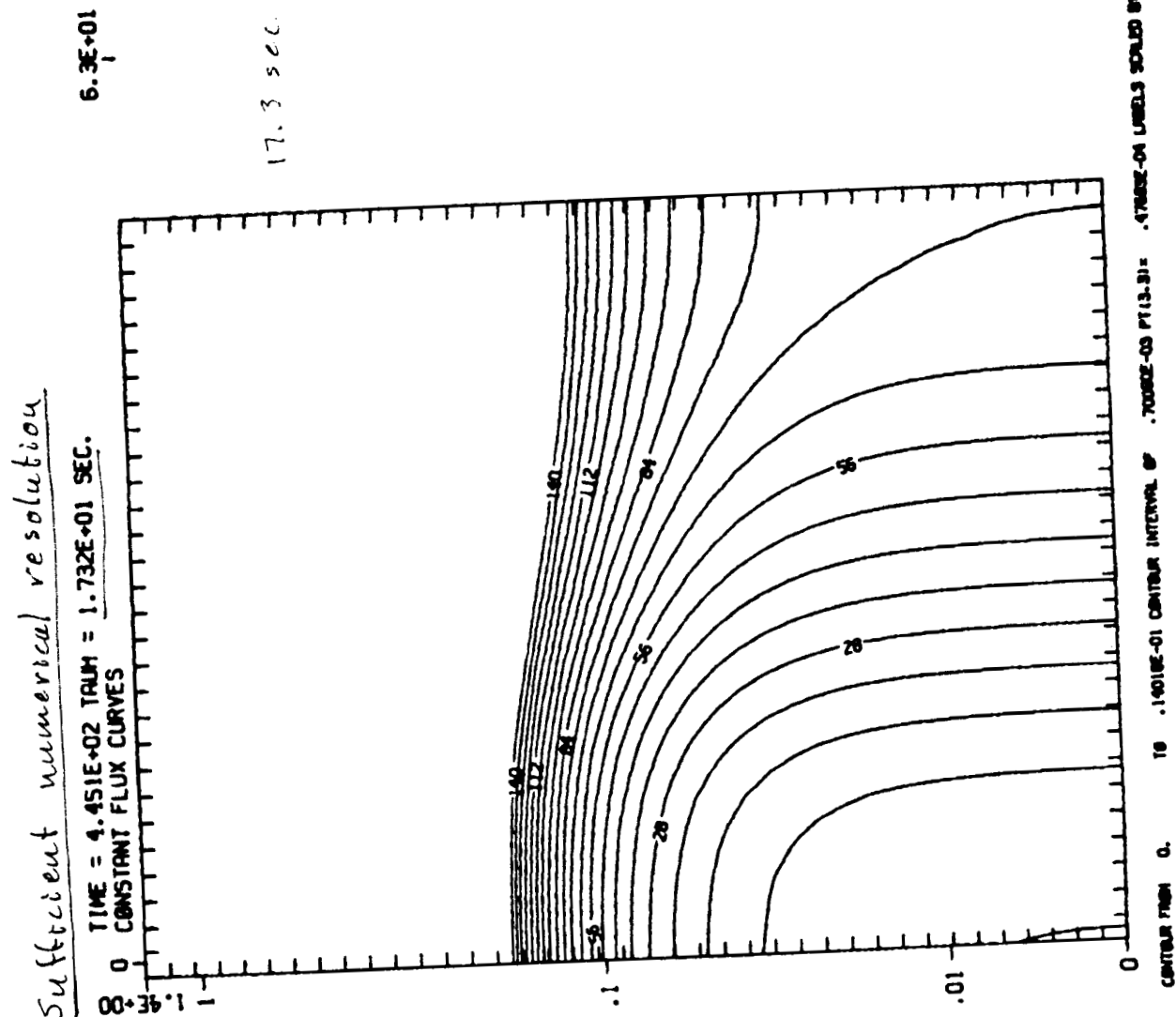
0 10 20 30 40 50 60 70 80 90 100 110 120 130 140 150 160 170 180 190 200 210 220 230 240 250 260 270 280 290 300 310 320 330 340 350 360 370 380 390 400 410 420 430 440 450 460 470 480 490 500 510 520 530 540 550 560 570 580 590 600 610 620 630 640 650 660 670 680 690 700 710 720 730 740 750 760 770 780 790 800 810 820 830 840 850 860 870 880 890 900 910 920 930 940 950 960 970 980 990 1000

(3)

ORIGINAL PAGE IS
OF POOR QUALITY

17

ORIGINAL PAGE IS
OF POOR QUALITY



1000.

0.000E+00 PT(3,3)= - .0000E+00 LAYER SOLVED BY

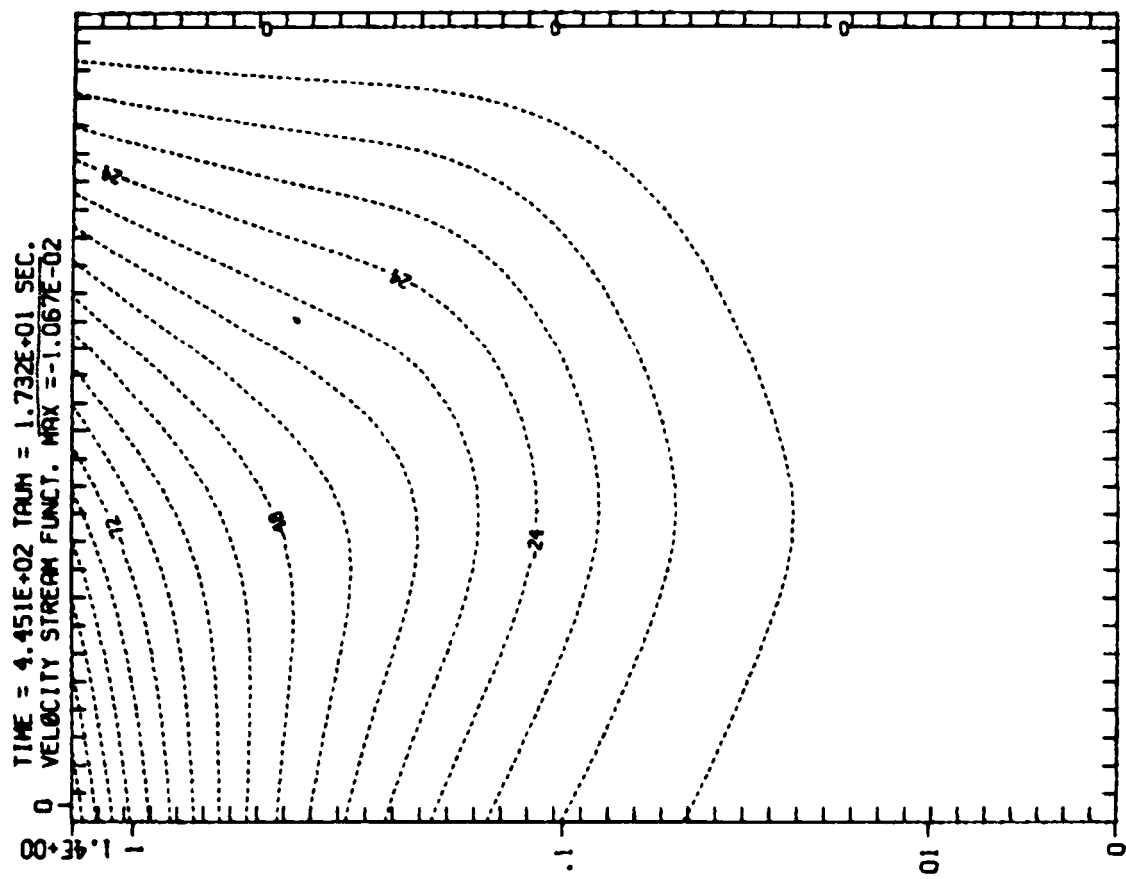
center row = 10000E-01 0. center interval = .0000E+00

ORIGINAL PAGE IS
OF POOR QUALITY

6.3E+01

17.3 sec

TIME = 4.451E+02 TAUH = 1.732E+01 SEC.
VELOCITY STREAM FUNCT. MAX = -1.067E-02

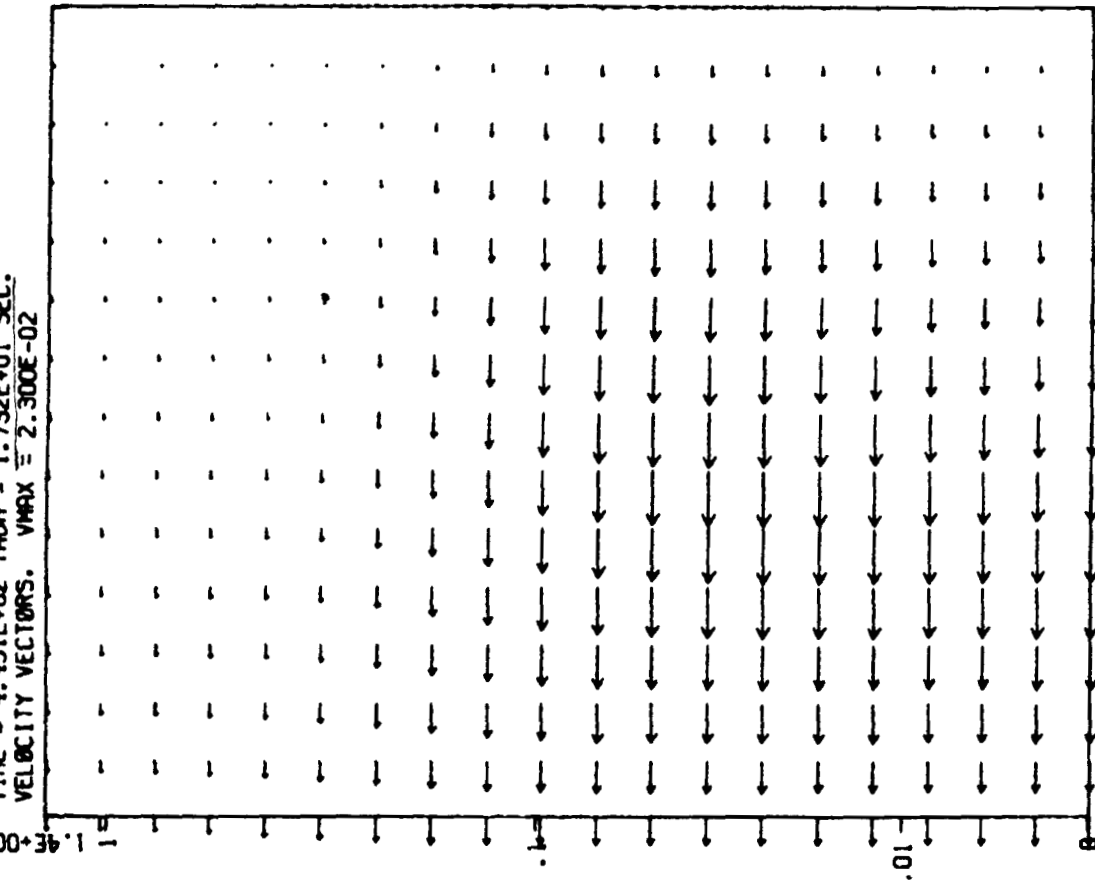


ORIGINAL PAGE IS
OF POOR QUALITY

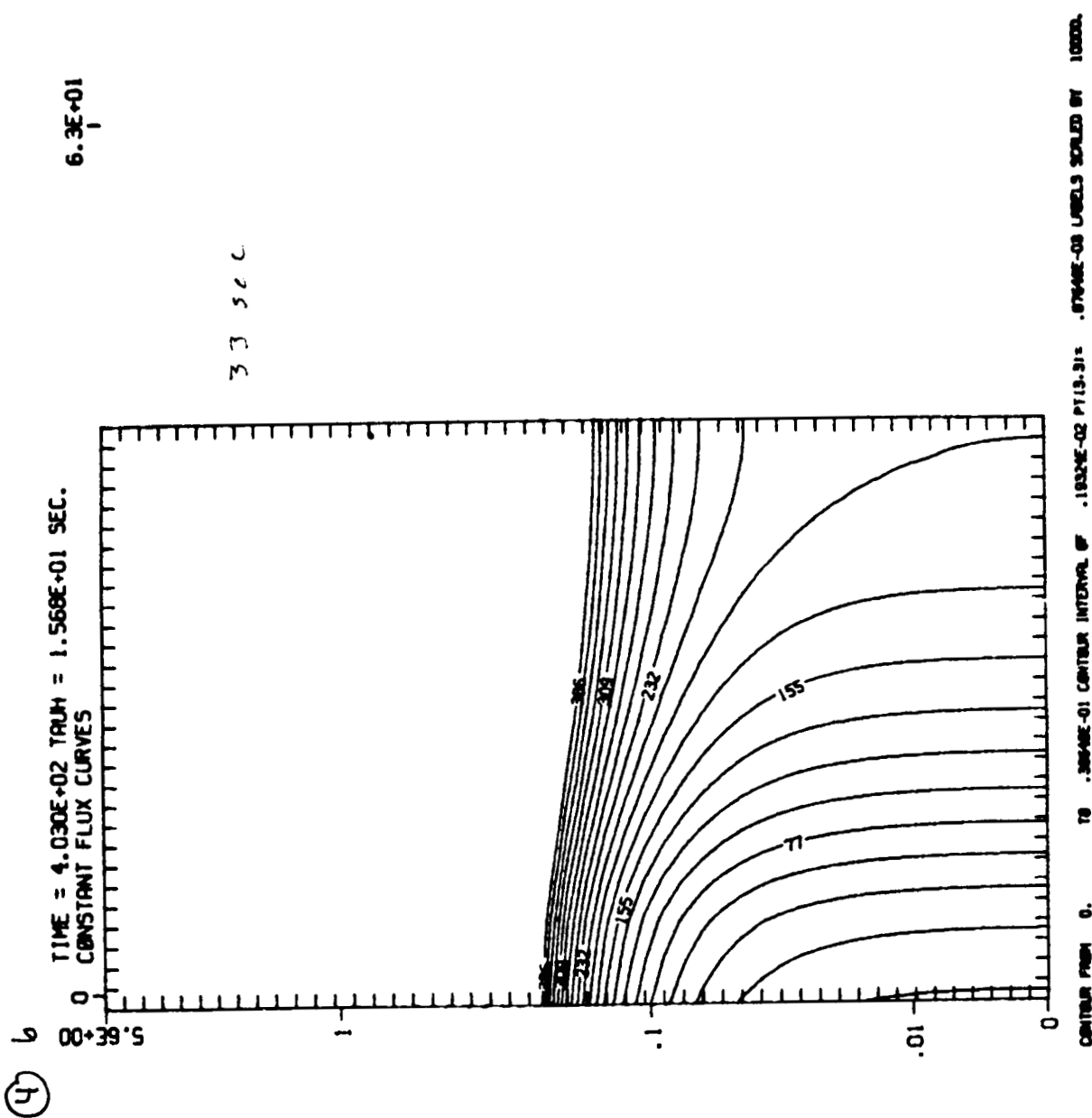
520E-01
RECEIVED REC'D BY

17. J sec

TIME = 4.451E+02 TAUH = 1.732E+01 SEC.
VELOCITY VECTORS. VMX = 2.300E-02

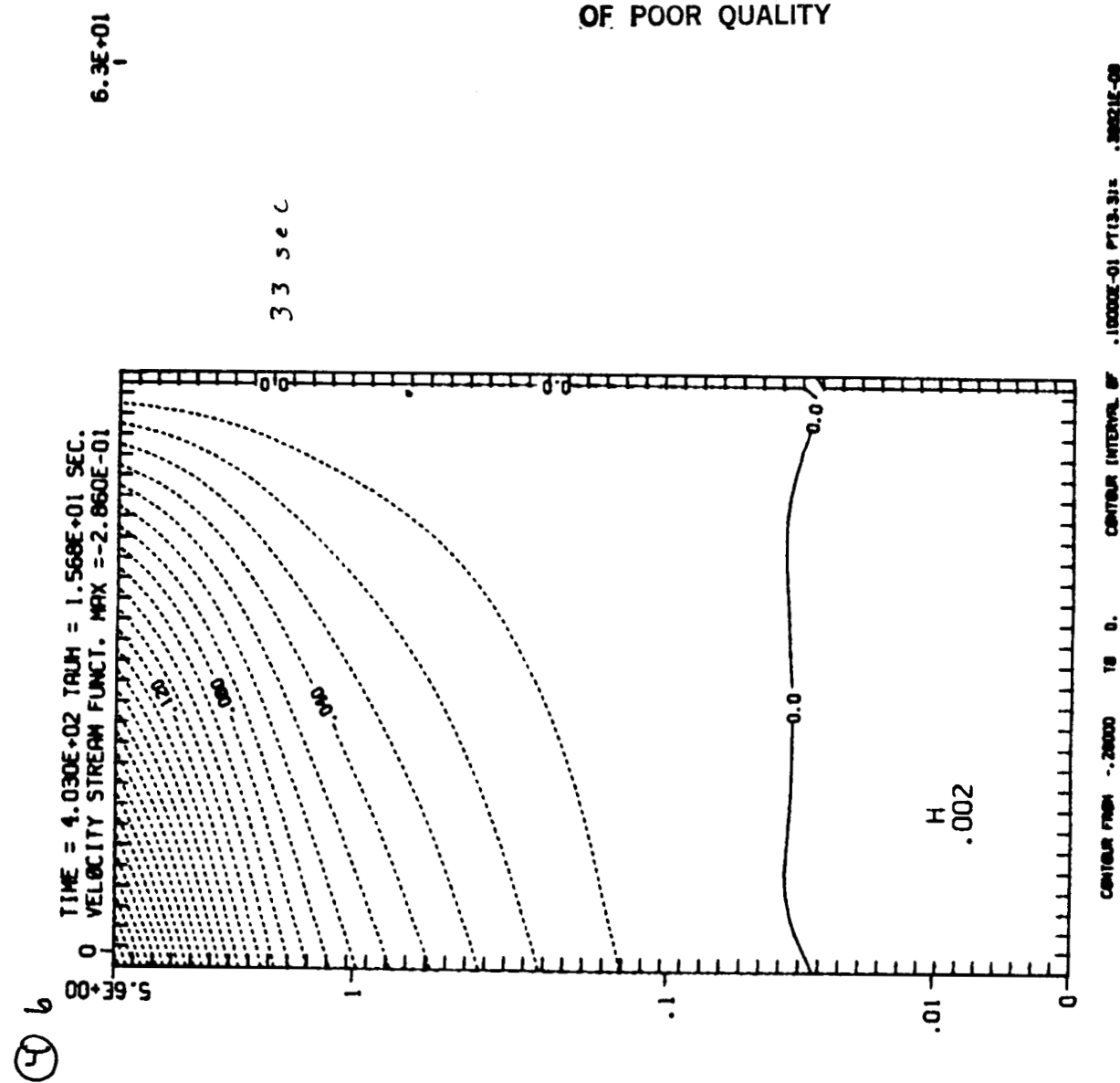


(4)



**ORIGINAL PAGE IS
OF POOR QUALITY**

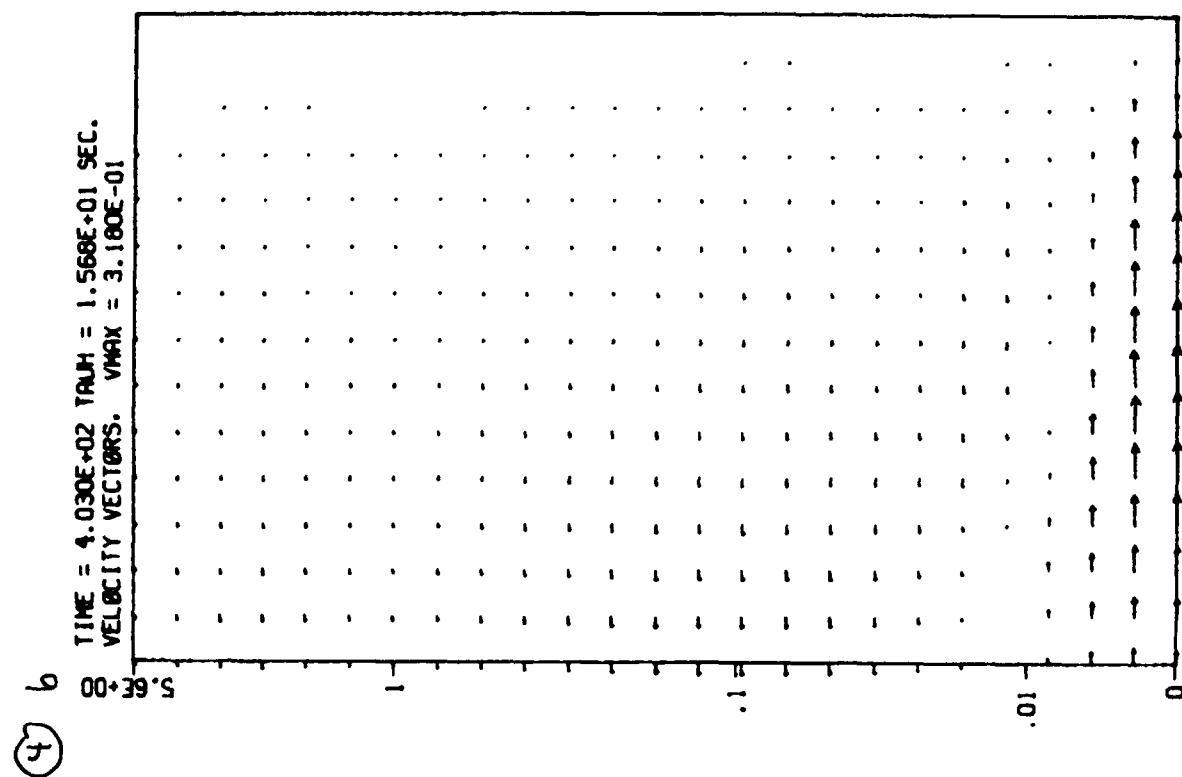
ORIGINAL PAGE IS
OF POOR QUALITY



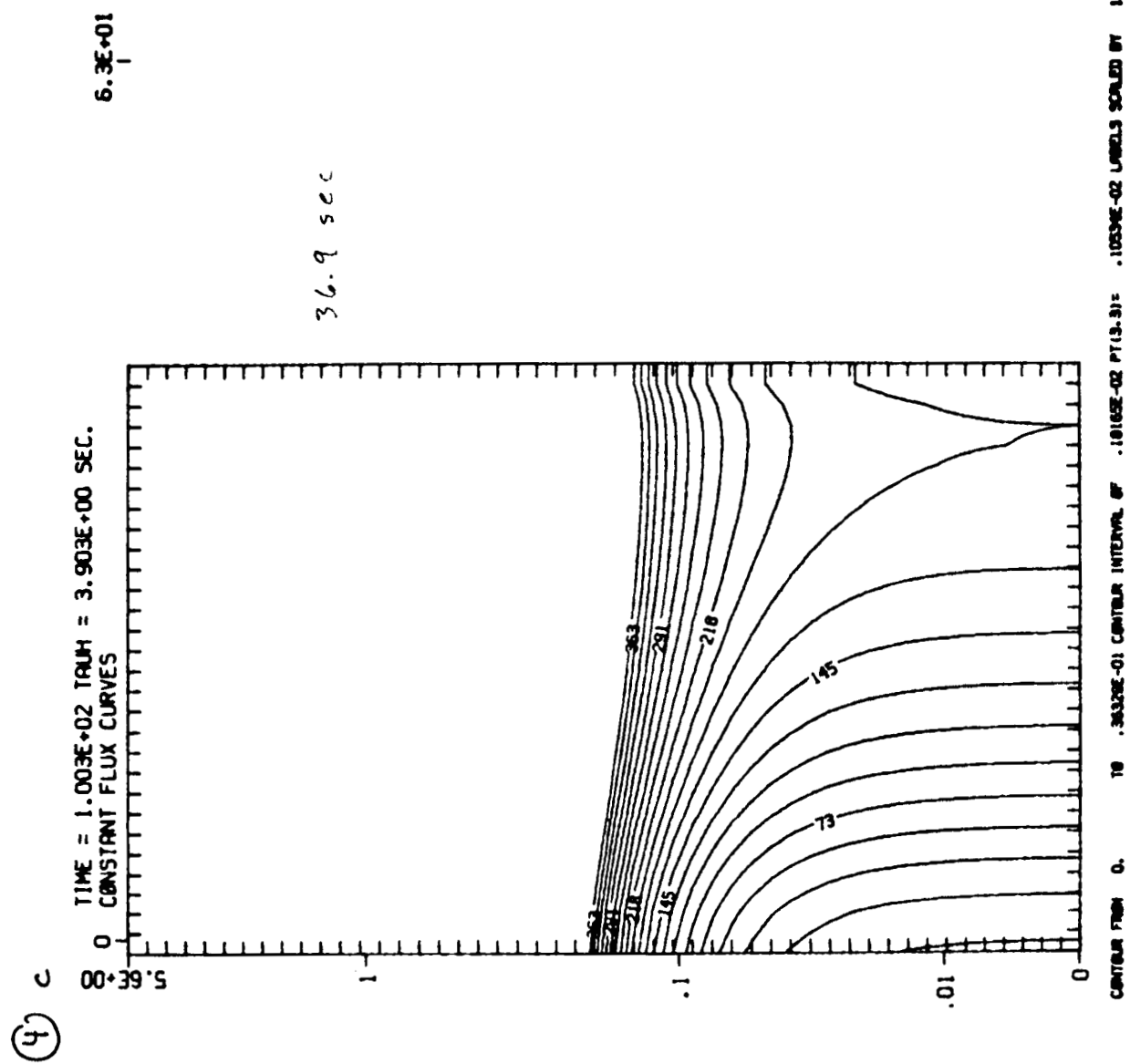
315-40
REED READER

ORIGINAL PAGE IS
OF POOR QUALITY

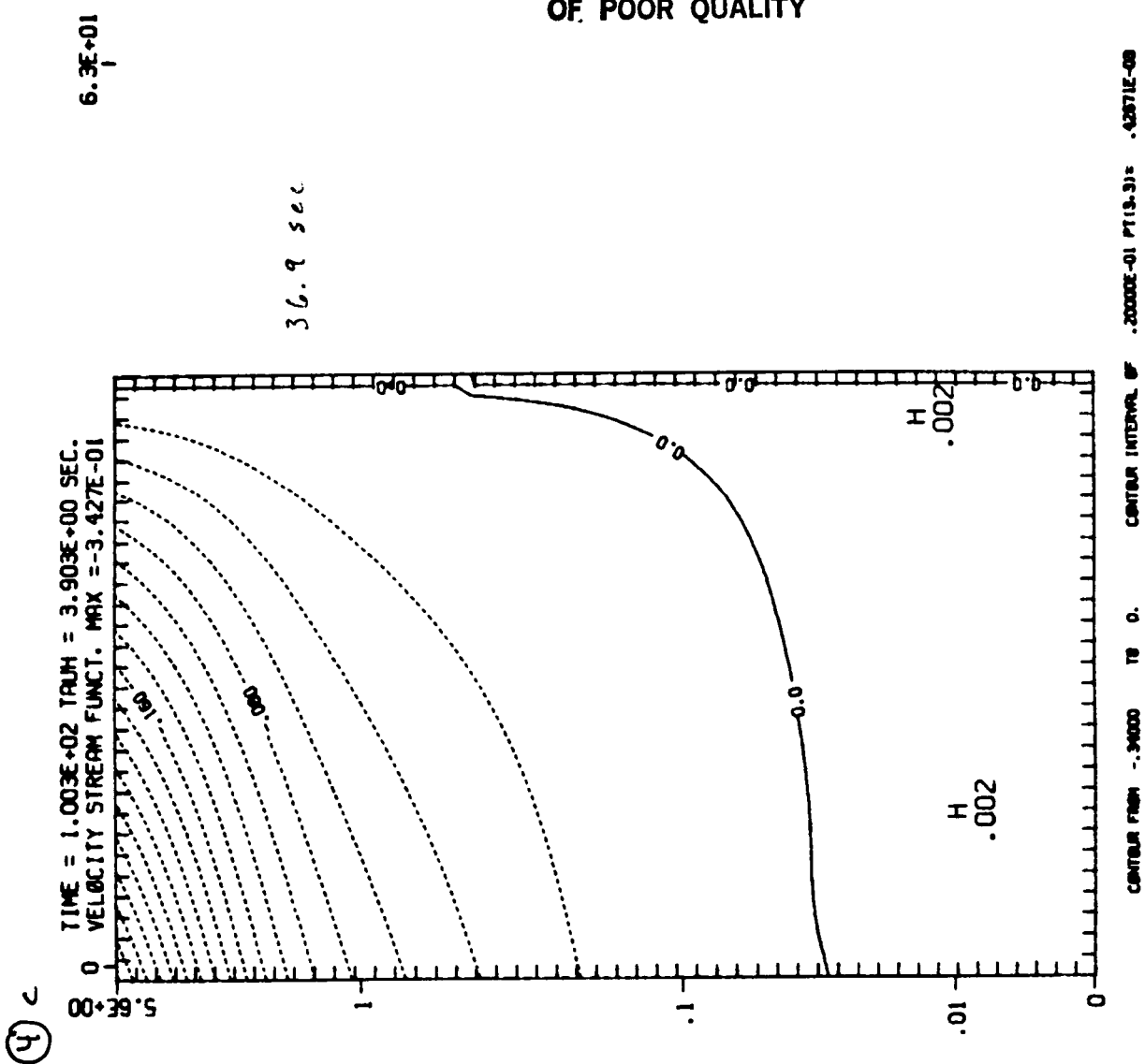
33 sec



**ORIGINAL PAGE IS
OF POOR QUALITY**



ORIGINAL PAGE IS
OF POOR QUALITY

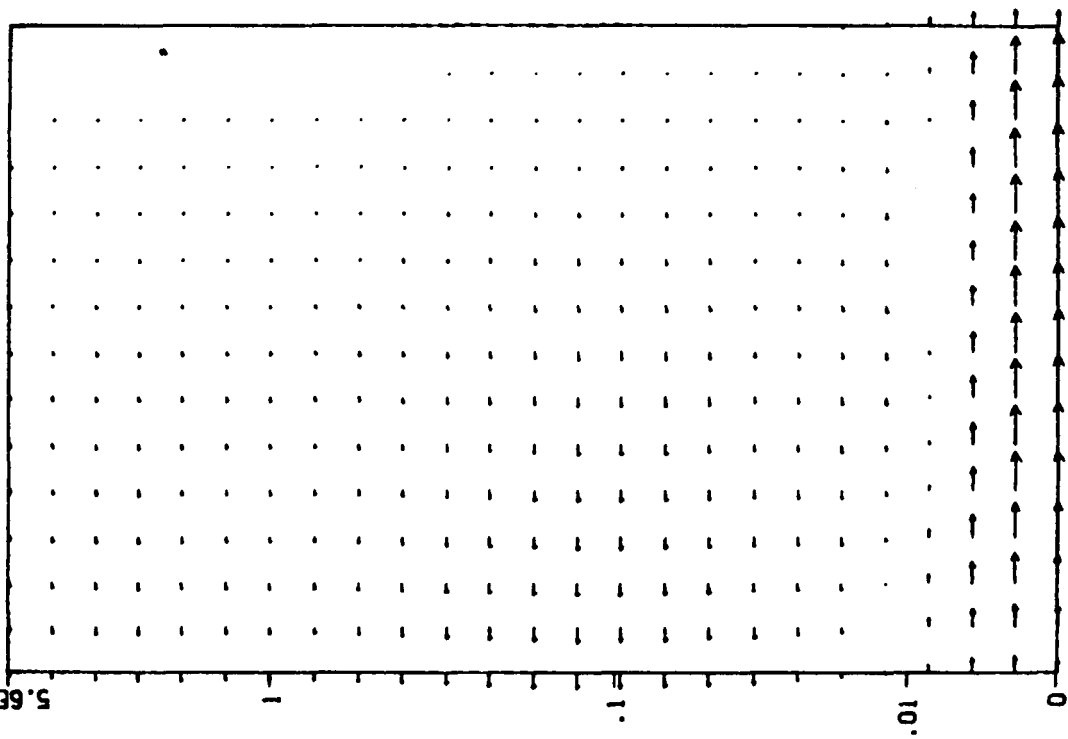


ORIGINAL PAGE IS
OF POOR QUALITY

TIME = 3.903E+00 SEC.
MAX VECTORS = 3.260E-01

36.9 sec

(4) C
TIME = 1.003E+02 TRUTH = 3.903E+00 SEC.
VELOCITY VECTORS. MAX = 3.260E-01



N89 - 15876

Modelling a C-type Flare Observed in Microwaves and Hard X-rays

E.J. Schmahl and M.R. Kundu

University of Maryland

Astronomy Program

and

B.R. Dennis

Laboratory for Astronomy and Solar Physics

GSFC

To be submitted to the Proceedings of the

Max '91 Workshop

June 1988

Abstract

Modelling a C-type Flare Observed in Microwaves and Hard X-rays

Using the Very Large Array at 6 and 20 cm wavelength and the Hard X-ray Burst Spectrometer on the Solar Maximum Mission, we have observed a two-ribbon flare from the onset phase through the maximum and decline on November 14, 1981. Because of the extensive size of the microwave source and the gradual variations in hard x-rays whose spectrum becomes progressively flatter with time, the flare is classified as a C-type flare. Considering the hardening of the x-ray spectrum and its non-impulsive nature, we invoke a coronal trap model for the energetic electrons. The microwave emission is easily accounted for by gyrosynchrotron radiation from mildly relativistic electrons. We have found that the source must be optically thick at 20 cm during the maximum phase, but as the source evolved toward an optically thin regime, the intensity decreased while the degree of circular polarization increased. In an initial homogenous model, we found that the computed microwave spectrum was too narrow to match the patrol spectrum from 606 to 15400 MHz. Because of this fact and the observed limbward displacement of the 20 cm emission from the H α emission, we were led to an inhomogeneous model of the magnetic field which traps the electrons. In our new model, the magnetic field consists of a dipolar arcade bridging the H α ribbons, and extending to heights of order 4 to 5×10^4 km. The variation of the magnetic field strength from footpoints to apex causes the gyrosynchrotron spectrum to be broader.

Since the height of the arcade, its width and footpoint field strengths are known from the H α , 20 cm, and magnetograph observations, there are relatively few free parameters in the model.

We present and discuss preliminary conclusions regarding the electron distributions producing the hard x-rays and the microwaves, and the suitability of this model for C-type flares.

Modelling a C-type Flare Observed in Microwaves and Hard X-rays

The two-ribbon, class 2B flare of 1981 November 14 was observed by HXRBS in x-rays with energies from 31 to 539 keV and in microwaves at the VLA and the patrol telescopes at Palehua. Fig. 1 shows the time profiles of x-rays and the microwave flux. By combining the microwaves with the hard x-rays we shall attempt to distinguish between the thin and thick target models, estimate the range of coronal magnetic fields in the trapping loops, and estimate the degree of pitch angle anisotropy in the trapped electrons.

The HXRBS channels were fitted to a power law and the index γ plotted as a function of time. The time profile (Fig. 2) shows that the spectrum hardened from $\gamma=4.0$ to about $\gamma=3.3$ starting from just before the x-ray maximum and continuing until at least 15 minutes afterwards. Because of the spectral hardening, and also because of the large area of the flare, this flare is classified as a type C, following the characterization of Tanaka, (IAU Symp. No. 71, 1983) and Tsuneta et al., (Ap. J. 280, 887, 1984).

The microwave patrol data were fitted to a double power law function, and the upper index α plotted as a function of time. Although this index is not strictly equal to the high frequency index of the microwaves, the profile shows that the spectrum hardened significantly and monotonically through the flare.

To show the evolution of the microwave spectral index, we have plotted the 8800 MHz flux against the 15400 MHz flux (Fig. 3). This shows that, from shortly before the main hard x-ray peak to well after, the spectrum hardens steadily with the logarithmic slope α decreasing from -1.3 (at 22:02) to -0.5 (at 22:20). This index differs somewhat from that derived by the double power law fit (Fig. 2), but shows the same qualitative behavior. In general, the microwave indices imply electron energy indices δ which are around 2.2-2.7, which argues for thin target emission.

We have made numerous snapshot maps of the flare at both 6 and 20 cm, but focus on the period after the hard peak at 22:03 UT. Fig. 4 shows the 6 cm I and V VLA maps at 22:05 and 22:11 UT. Note the two oppositely polarized peaks in the 6 cm map; these appear to straddle the H α filament in the flaring region. Figure 5 shows the 20 cm I and V VLA maps at the same times as the previous 6 cm maps. The 20 cm intensity source is single, with its location centered between the two 6 cm peaks (Fig. 4). The polarization map shows that the edges of the source are polarized in the same sense as the two 6 cm sources. From the VLA maps alone, it is apparent that the burst source must be a large loop overlying the neutral line, and this is borne out by comparison with H α photographs from Big Bear (courtesy of H. Zirin).

When the 20 cm map for 22:40 UT is overlain on the H α photograph, the similarity is striking (Fig. 6). We have made a 33" shift in position (away from the limb) of the 20 cm map (see dashed arrow) to align the H α ribbons and the maxima of the microwave map. The shift corresponds to a projection effect with the height of the 20 cm sources 4-5 $\times 10^4$ km above the H α ribbons.

One of the most important features of the microwave spectrum is its large width (Fig. 7). Note the extreme breadth of the spectrum throughout the flare. For comparison, compare the overlay of a gyrosynchrotron spectrum of a homogeneous source. The breadth indicates that the source contains a wide range of magnetic field strengths, presumably in a system of loops trapping the electrons.

To account for the observed spectrum, we have computed gyrosynchrotron emission as a function of frequency from a model dipole loop with parameters esimated from the observations (Fig. 8). The magnetic field is that due to a buried linear dipole. The magnetic field strength at the footpoint is specified as a free parameter, but may be estimated from magnetograph observations.

We have computed gyrosynchrotron spectra from the model loop

system for a wide range of parameters, keeping the observable constraints in mind. The crosses in Fig. 9 show the Palehua flux at 22:08:00 UT. The highest curve is the flux integrated over the entire loop, while the lower curves are the flux at selected points from the center outward toward the footpoints. We allowed the pitch angle distribution to depart from anisotropy, using the form:

$N(\phi) = (\sin(\phi))^p$, where $p=0$ corresponds to the isotropic case. For this kind of distribution, Parker (Phys. Rev. 107, 924, 1957) showed that the density of electrons in the loop is inversely proportional to the p th power of the magnetic field at that point.

Conclusions:

1. The hard x-ray spectrum hardens with time, and when modeled in terms of thin and thick target bremsstrahlung, gives energy indices of 3.1-2.7 and 4.6-4.3 (respectively). The microwave spectrum also hardens with time. The microwave spectral index (which depends somewhat on the method used to define it) corresponds more closely to the thin target model than the thick.
2. As evidenced by the broad microwave spectrum, the microwaves are generated in a set of regions with widely ranging magnetic field strengths.
3. The VLA maps show that these regions are a continuous, smooth system, rather than isolated sources: the 6 cm source is double, spanning the neutral line, and the 20 cm source is single with polarized edges, also spanning the neutral line. The simplest good representation of the source is a dipolar potential field bridging the neutral line between the H-alpha ribbons.
4. Pitch angle distributions for a trapped population ($p>0$) fit the ob-

served flux spectrum better than an isotropic distribution. The best fit appears to be with $p=2$, corresponding to a moderately anisotropic distribution with $N(\phi)=(\sin(\phi))^2$,

5. The flux spectrum can be fit reasonably well by the model, although the flat peak is not exactly reproduced. The model successfully predicts that at higher frequencies ($f>5$ GHz) the source appears double, and at lower frequencies ($f<2$ GHz) the source appears single.

Acknowledgements

Dr. M. Melozzi made the VLA maps of this flare and performed some of the early analysis of the data. We thank Dr. H. Zirin for providing us with Big Bear photographs. The VLA is operated by the National Radio Astronomy Observatory under contract with the National Science Foundation.

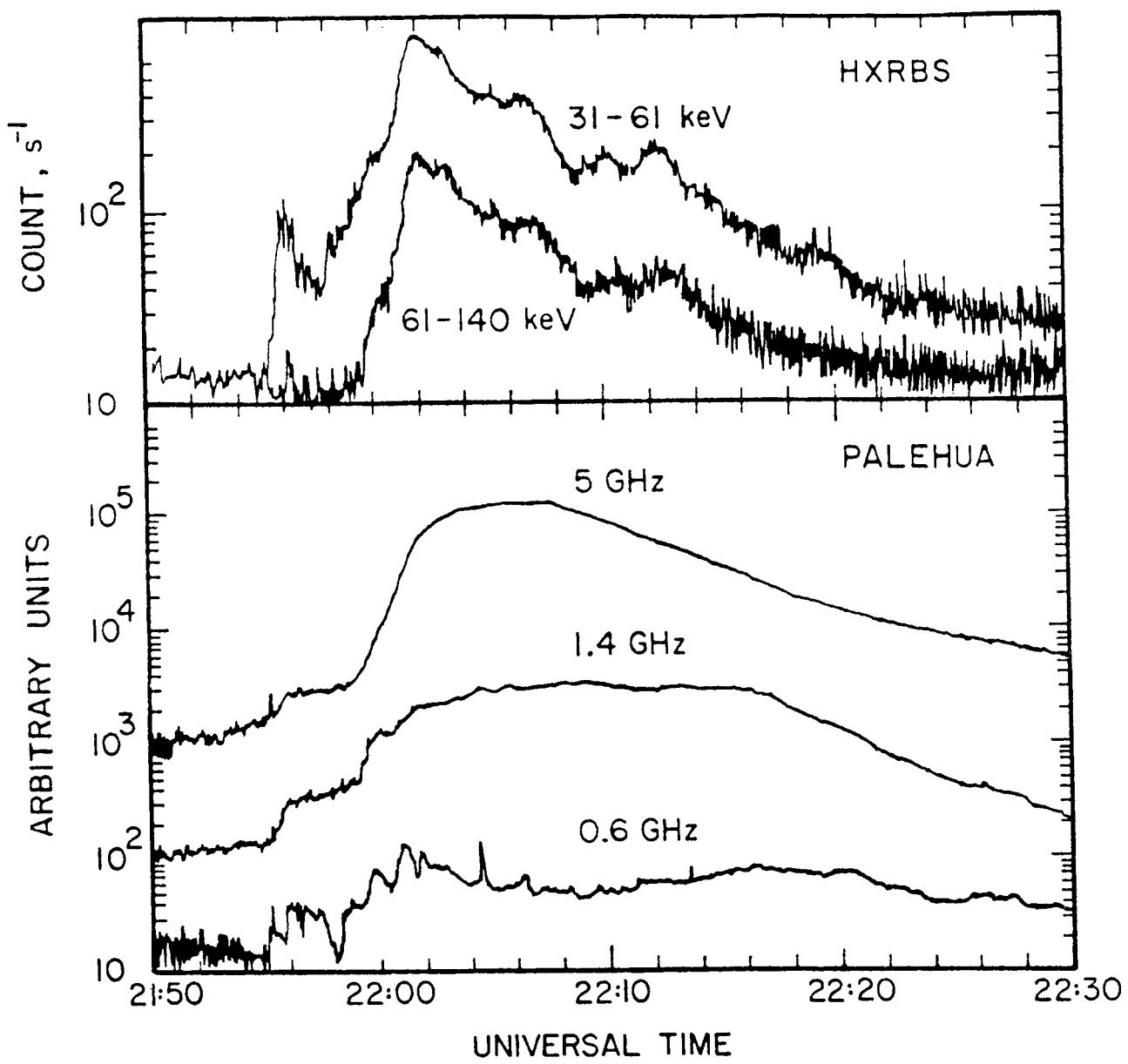


Fig. 1.

The two-ribbon, class 2B flare of 1981 November 14 was observed by HXRBS in x-rays with energies from 31 to 539 keV and in microwaves at the VLA and the patrol telescopes at Palehua.

- a. HXRBS count-rate time profiles for the 31-61 keV and 61-140 keV channels and the corresponding spectral index.
- b. Palehua single-dish observations at 4.995, 1.415 and 0.602 GHz. The first two frequencies (6 and 20 cm) are those used at the VLA for mapping this flare.

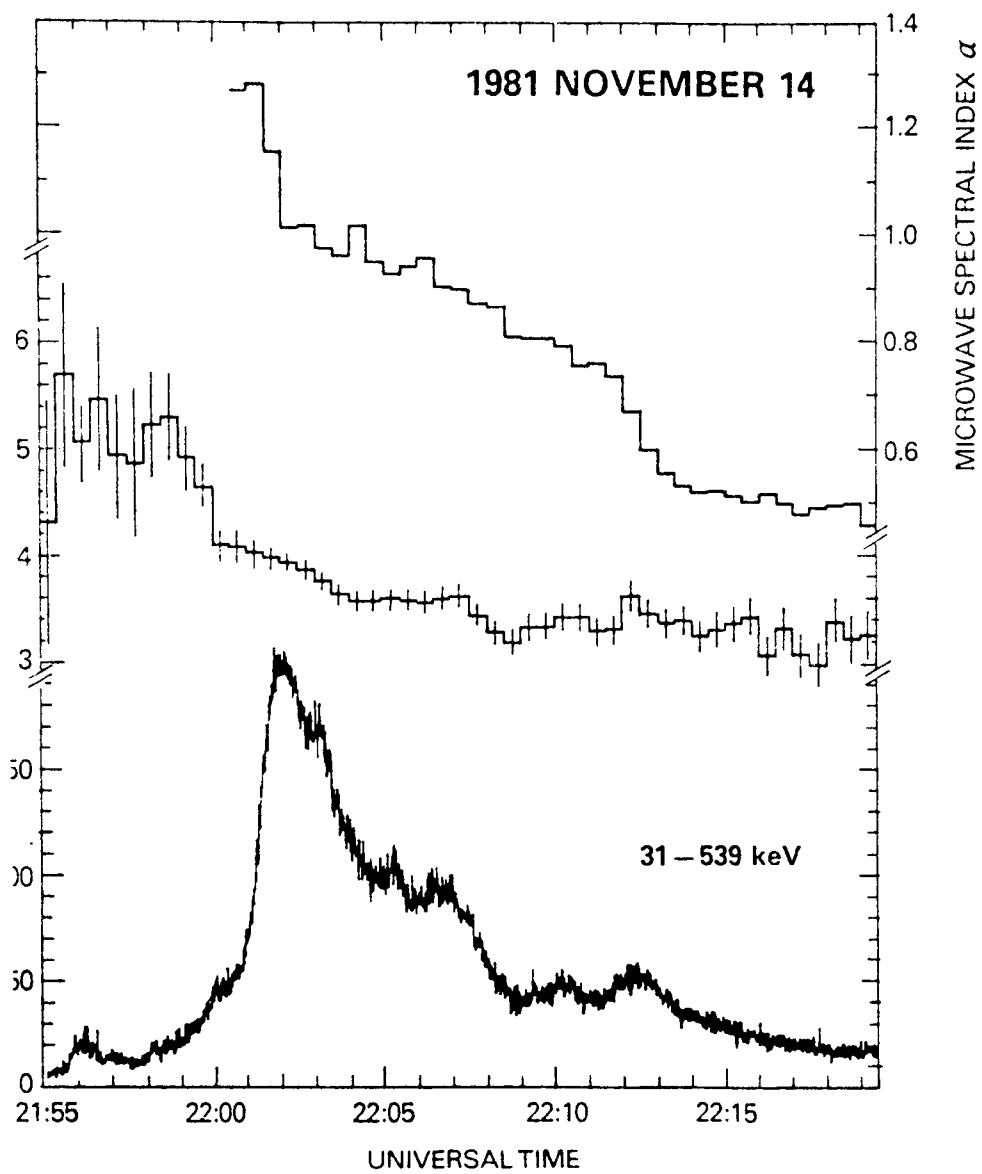


Fig. 2.

The HXRBS channels were fitted to a power law and the index γ plotted as a function of time. The time profile shows that the spectrum hardened from $\gamma=4.0$ to about $\gamma=3.3$ starting from just before the x-ray maximum and continuing until at least 15 minutes afterwards.

The microwave patrol data were fitted to a double power law function, and the upper index α plotted as a function of time. Although this index is not strictly equal to the high frequency index of the microwaves, the profile shows that the spectrum hardened significantly and monotonically through the flare.

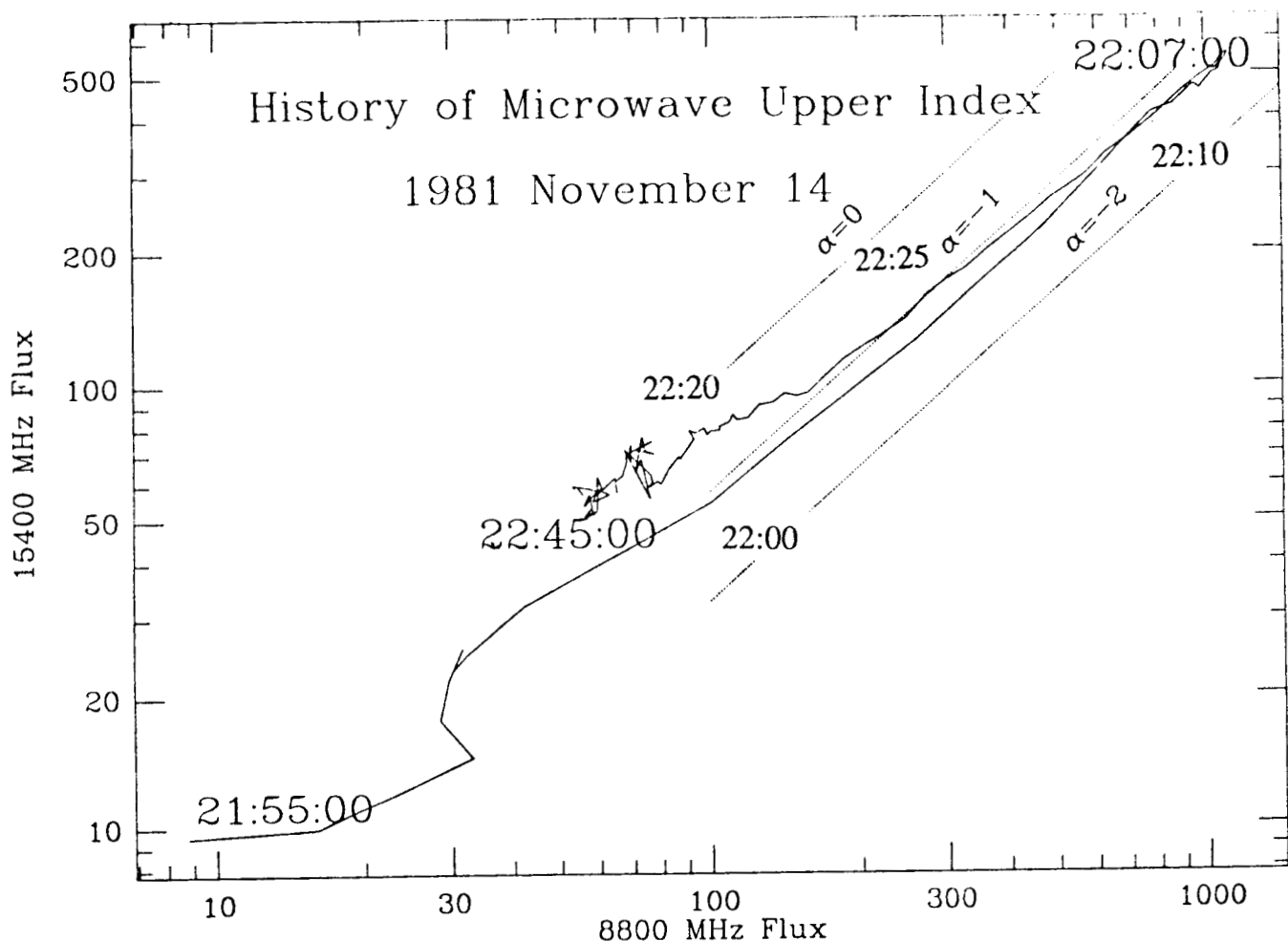


Fig. 3.

To show the evolution of the microwave spectral index, we have plotted the 8800 MHz flux against the 15400 MHz flux. This shows that, from shortly before the main hard x-ray peak to well after, the spectrum hardens steadily with the logarithmic slope α decreasing from -1.3 (at 22:02) to -0.5 (at 22:20). This index differs somewhat from that derived by the double power law fit (Fig. 2), but shows the same qualitative behavior.

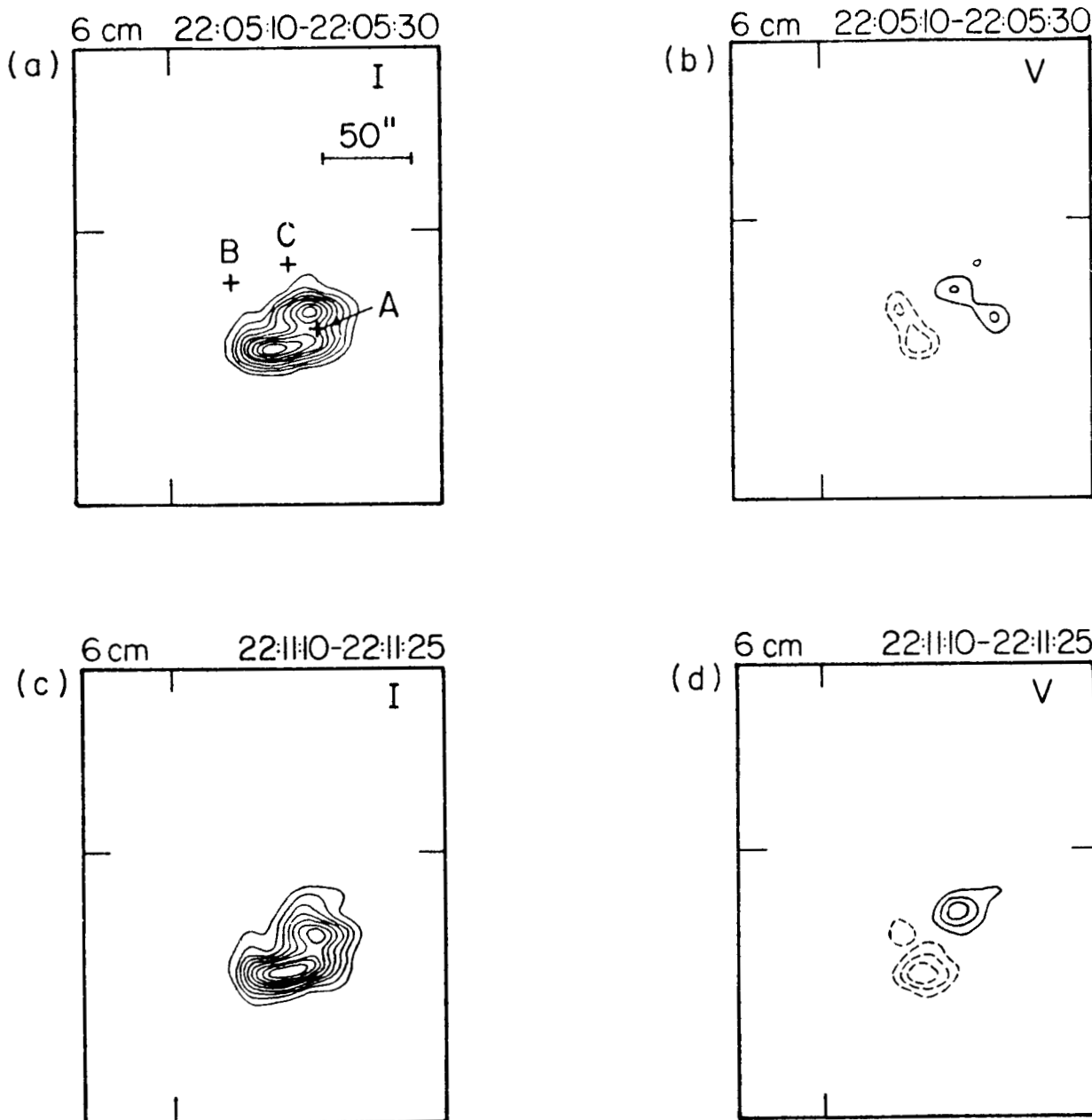


Fig. 4.

6 cm I and V VLA maps just after the main peak in hard x-rays. Note the two oppositely polarized peaks in the 6 cm map; these appear to straddle the H α filament in the flaring region. The lowest contour in (a) and (c) is 8.1×10^6 K, and in (b) and (d) it is 4×10^6 and 6×10^6 K respectively. The contour intervals are the same as the base contour.

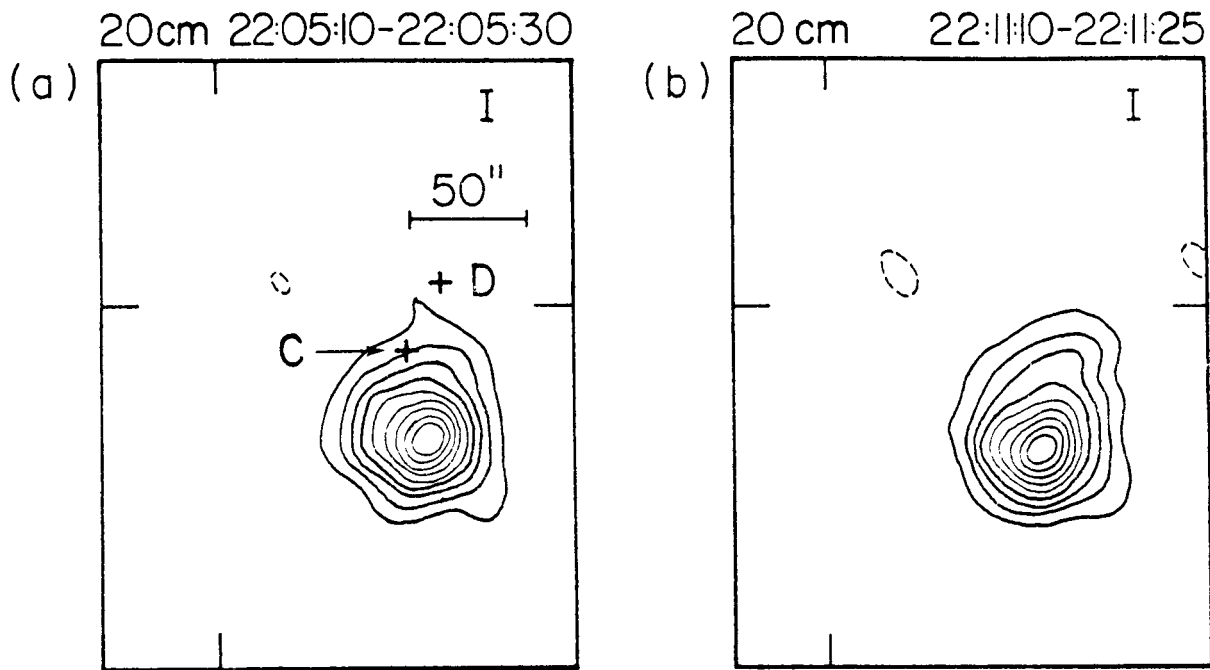
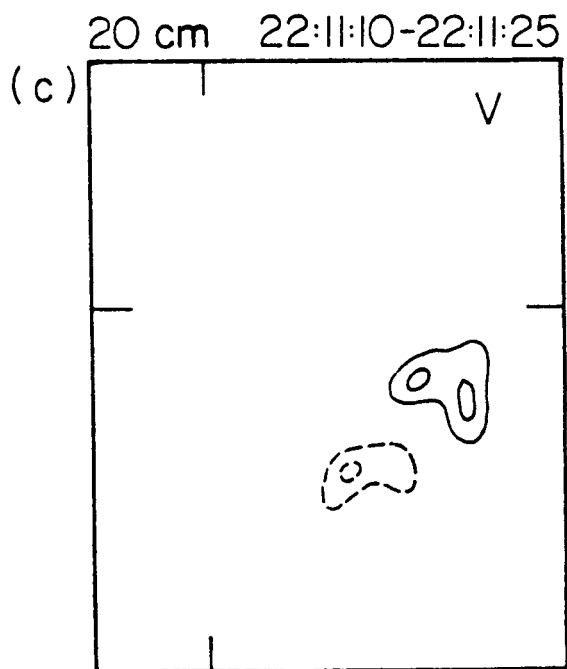


Fig. 5.

20 cm I and V VLA maps just after the main peak in hard x-rays. The 20 cm intensity source is single, with its location centered between the two 6 cm peaks (Fig. 4). The polarization map shows that the edges of the source are polarized in the same sense as the two 6 cm sources. The lowest contours are 1.7×10^7 K, 1.9×10^7 K, and 7.4×10^6 K in maps (a), (b) and (c), respectively. The contour intervals are the same as the base contour.



ORIGINAL PAGE IS
OF POOR QUALITY

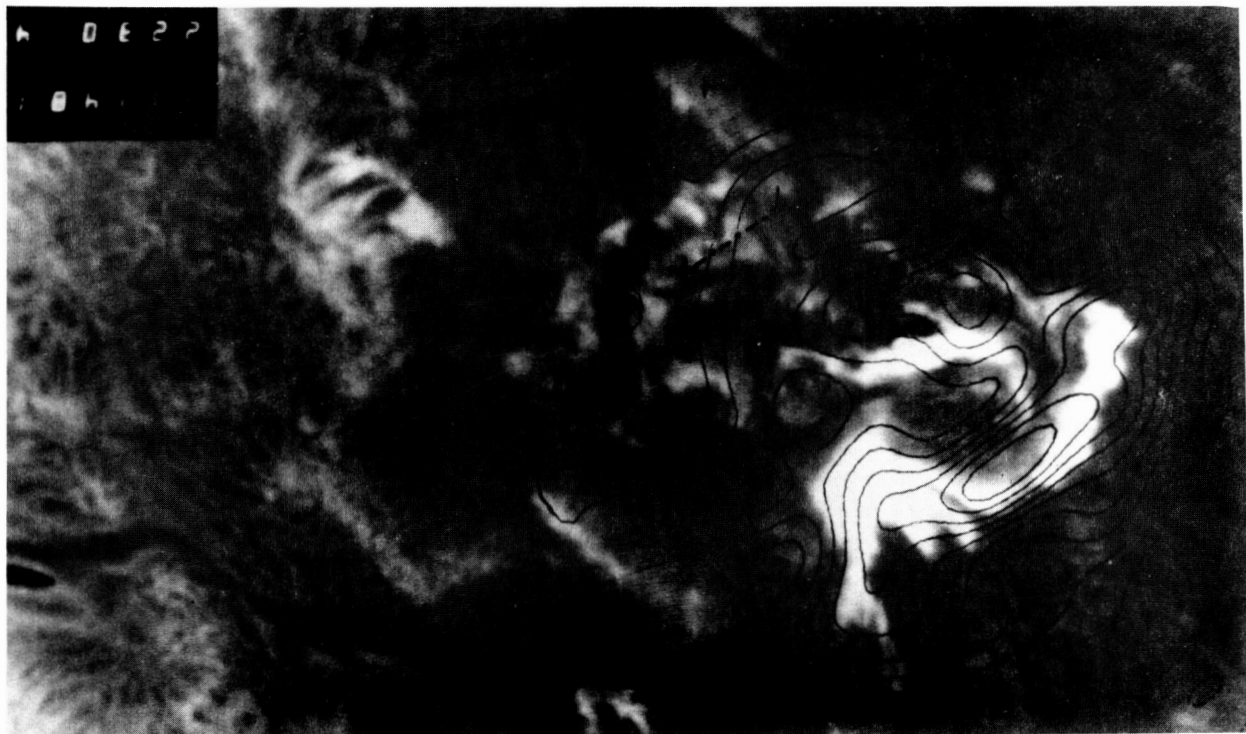


Fig. 6.

When the 20 cm map for 22:40 UT is overlain on the H α photograph, the similarity is striking. We have made a 33" shift in position (away from the limb) of the 20 cm map (see dashed arrow) to align the H α ribbons and the maxima of the microwave map. The shift corresponds to a projection effect with the height of the 20 cm sources $4-5 \times 10^4$ km above the H α ribbons.

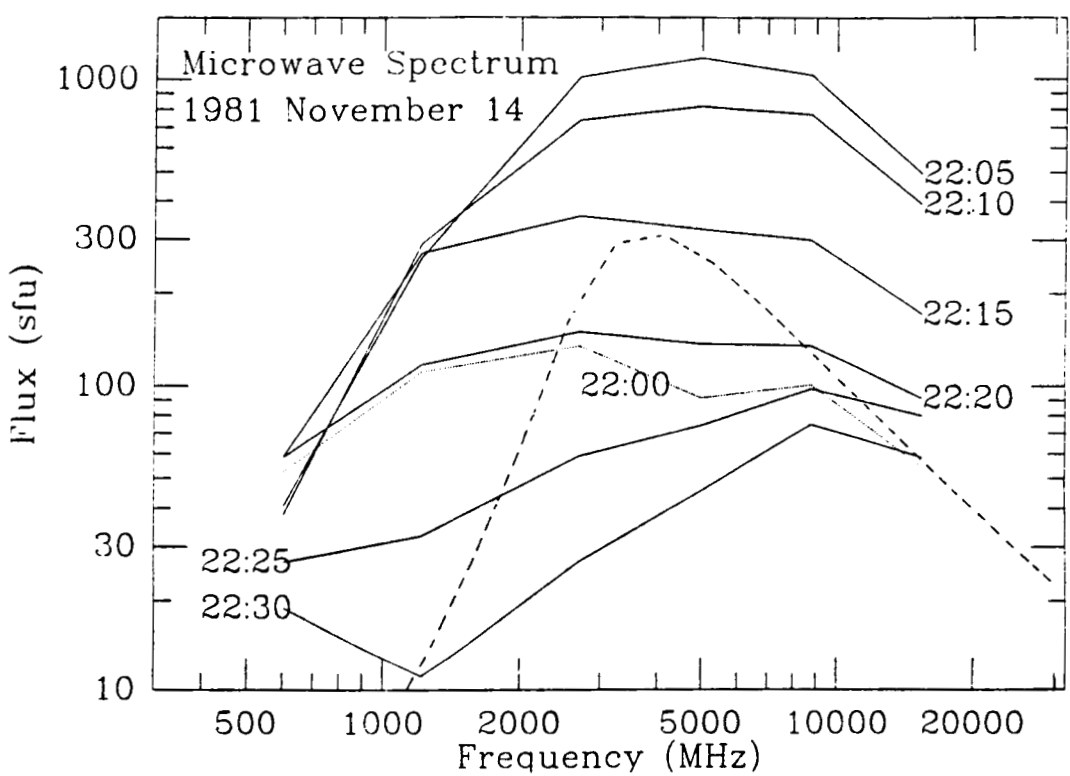


Fig. 7.

Microwave spectrum at selected times during the flare. Note the extreme breadth of the spectrum throughout the flare. For comparison, compare the overlay of a gyrosynchrotron spectrum of a homogeneous source. The breadth indicates that the source contains a wide range of magnetic field strengths, presumably in a system of loops trapping the electrons.

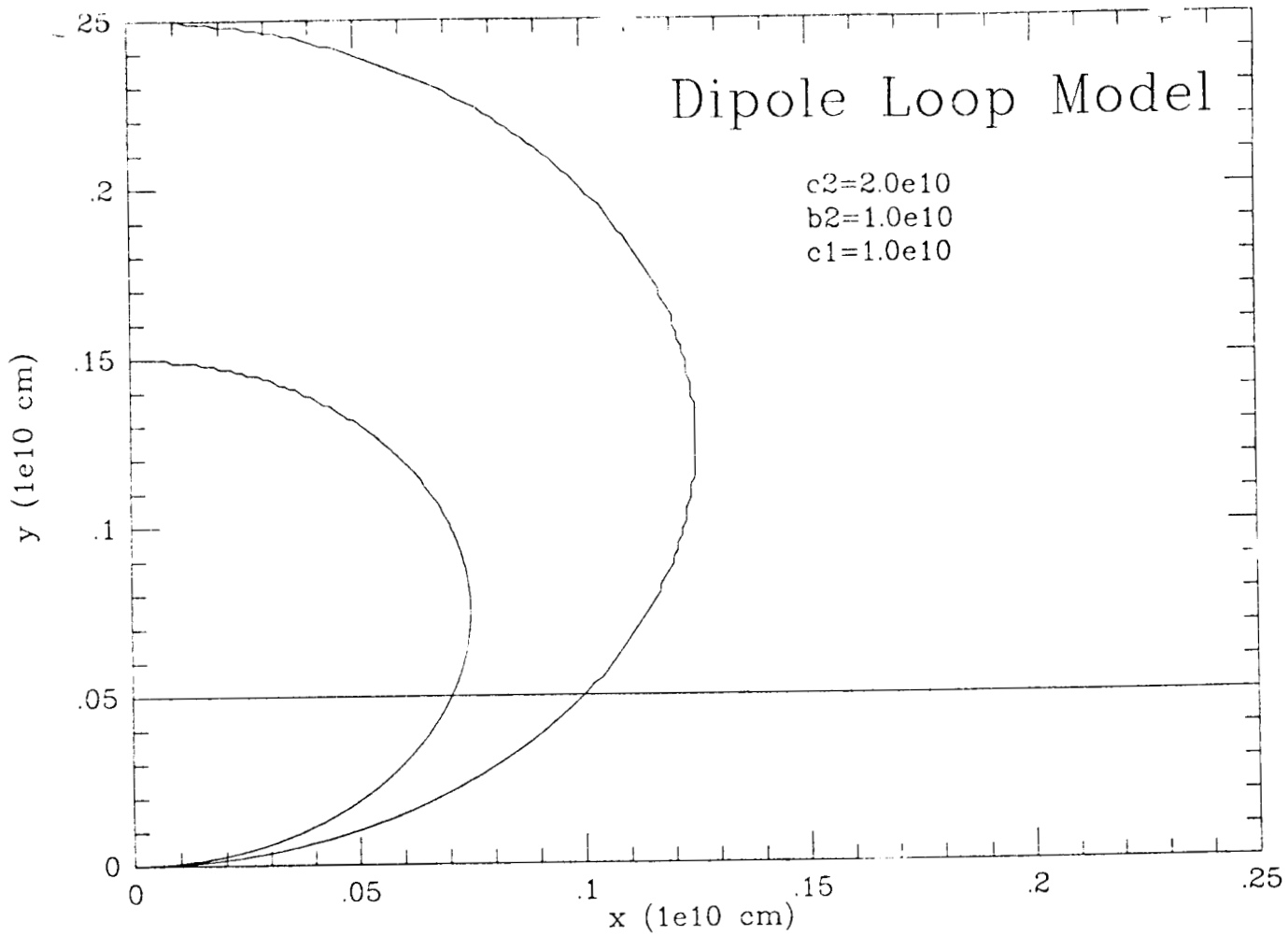


Fig. 5.

To account for the observed spectrum, we have computed gyrosynchrotron emission as a function of frequency from a model dipole loop with parameters estimated from the observations. The magnetic field is that due to a buried linear dipole. Typical values of the parameters are:

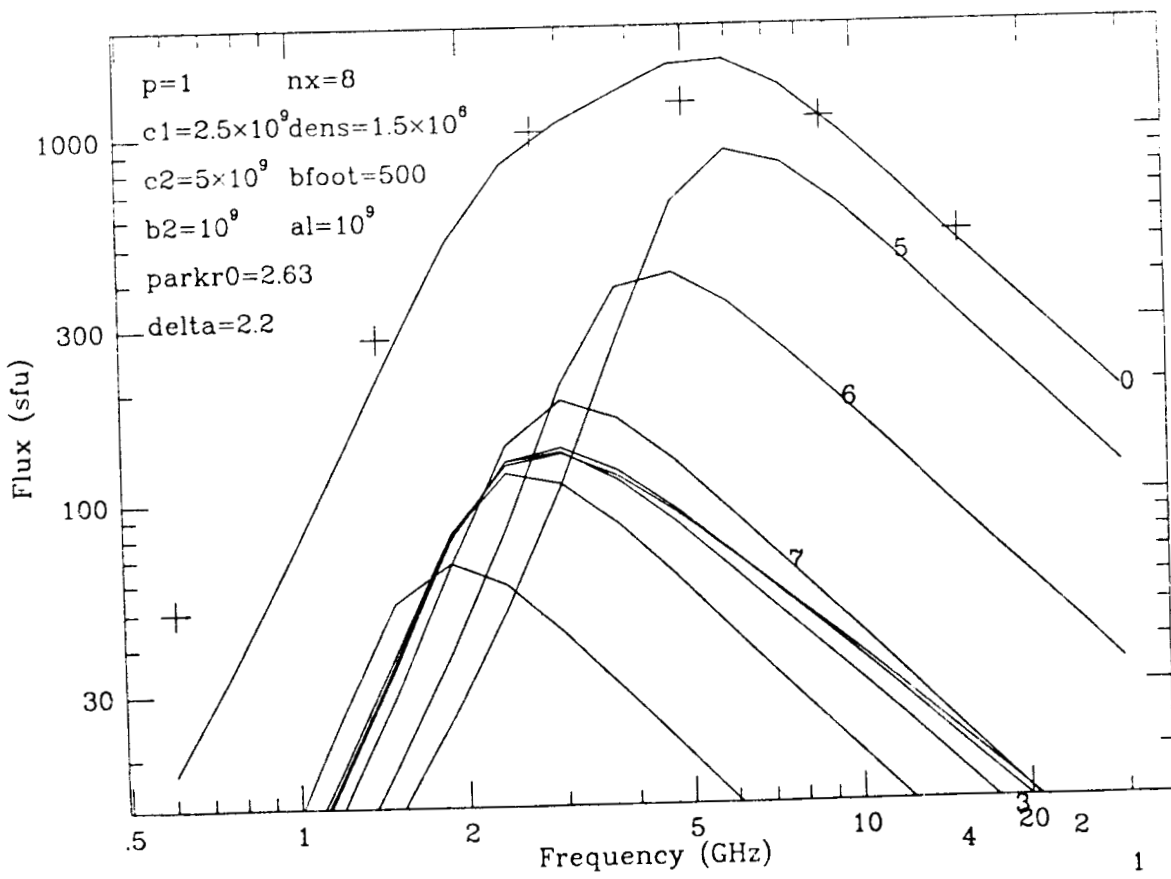
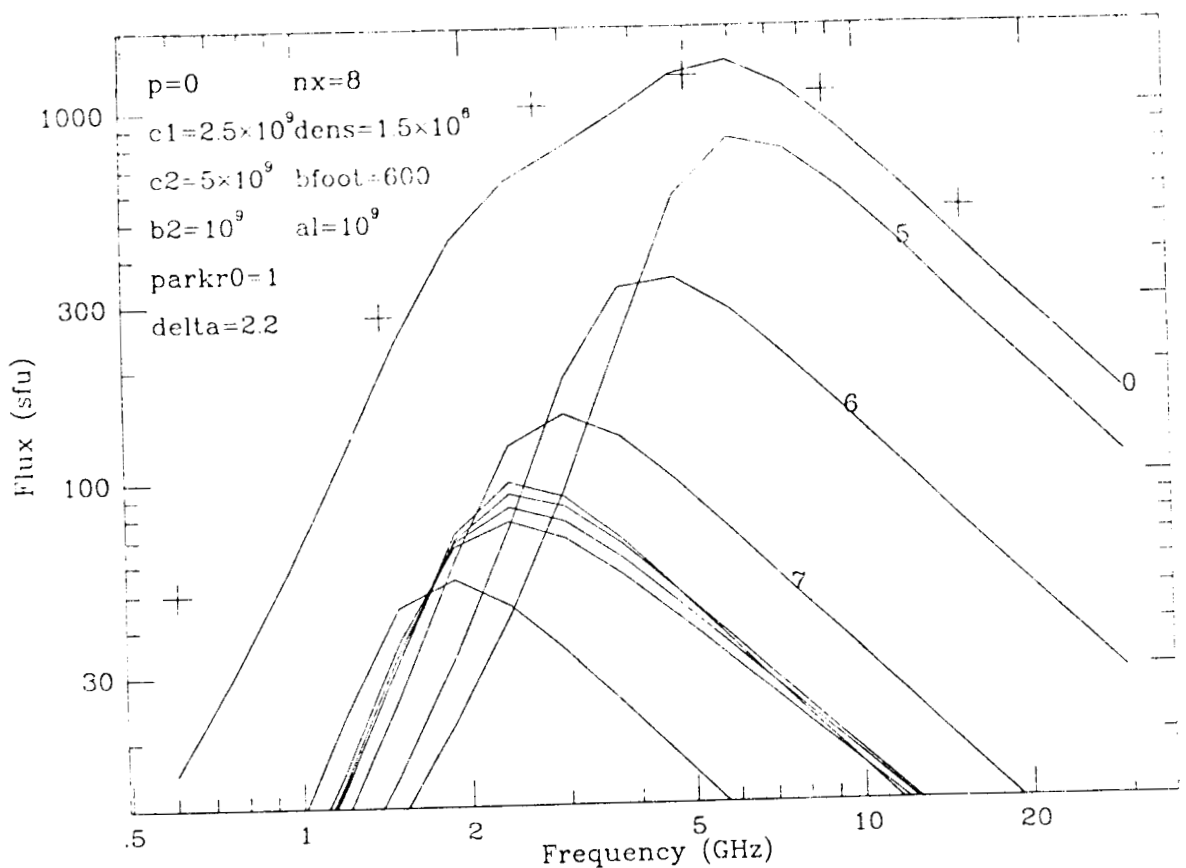
Apex height: $c_2 = 2.0 \times 10^{10} \text{ cm}$

Inner height: $c_1 = 1.0 \times 10^{10} \text{ cm}$

Footpoint separation: $b_2 = 1.0 \times 10^{10} \text{ cm}$

Loop z-thickness: $a_l = 1.0 \times 10^{10} \text{ cm}$

The magnetic field strength at the footpoint is specified as a free parameter, but may be estimated from magnetograph observations.



ORIGINAL PAGE IS
OF POOR QUALITY

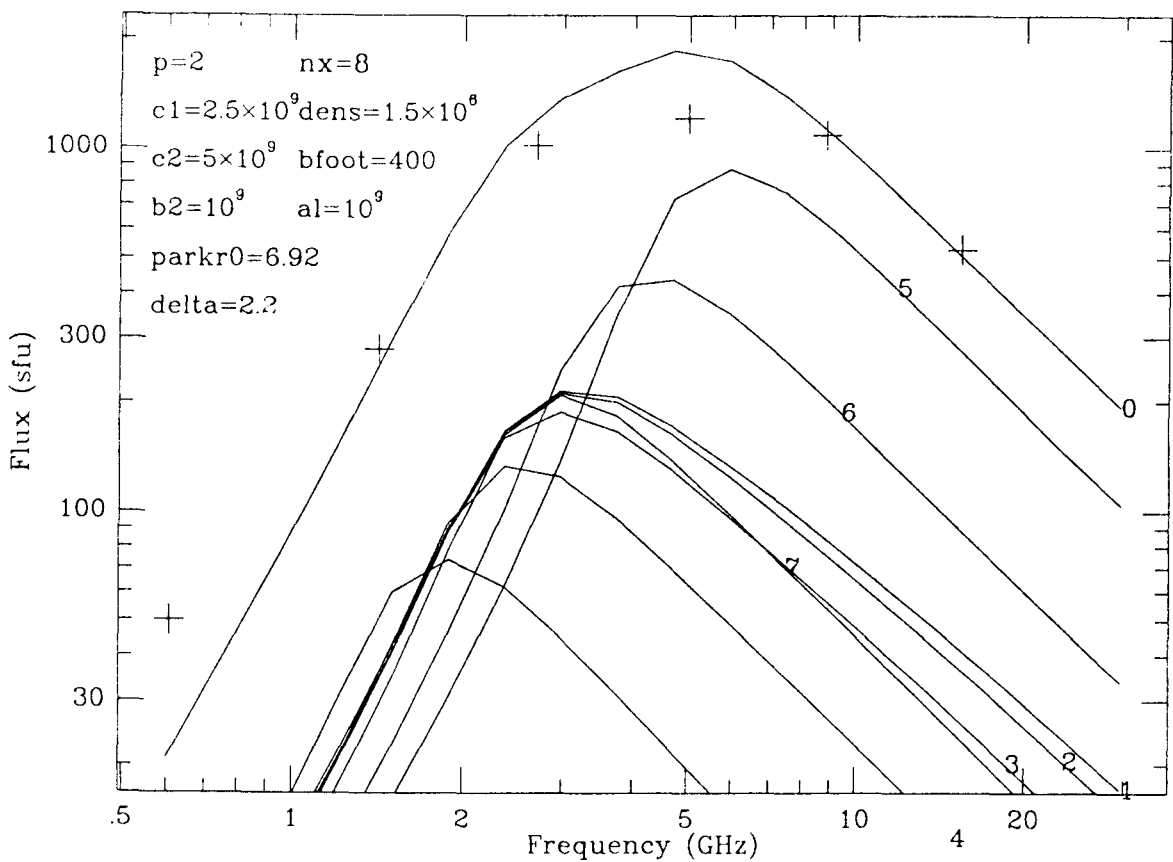


Fig. 9.

We have computed gyrosynchrotron spectra from the model loop system for a wide range of parameters, keeping the observable constraints in mind. The crosses show the Palehua flux at the flare maximum, 22:08:00 UT. The highest curve is the flux integrated over the entire loop, while the lower curves are the flux at selected points from the center outward toward the footpoints (1~center, 5~inner cusp of loop, 8~outer cusp of loop). In addition, we allowed the pitch angle distribution to depart from anisotropy, using the form:

$N(\phi)=(\sin(\phi))^p$, where $p=0$ corresponds to the isotropic case. For this kind of distribution, Parker (Phys. Rev. 107, 924, 1957) showed that the density of electrons in the loop is inversely proportional to the p th power of the magnetic field at that point.

a. $p=0$: Note how the top of the spectrum tilts to the left. This is due to the greater contribution from the inner cusp where B is large. In this case of isotropy, the electron density is constant along the lines of force.

b. $p=1$: In this case, as in c and d, the apex has a higher density than the legs of the loop. ($\text{parkr}_0=\text{apex/foot density ratio.}$)

c. $p=2$: As p increases, the radiation becomes more highly beamed, and the contribution from the legs (curves 5,6) is relatively smaller.

C - 4

ORIGINAL PAGE IS
OF POOR QUALITY

**A High-Resolution Gamma-ray and Hard X-ray Spectrometer
for Solar Flare Observations in Max-91**

R. P. Lin, D. W. Curtis, P. Harvey, K. Hurley, J. H. Primbsch, D. M. Smith
Space Sciences Laboratory, University of California at Berkeley

R. M. Pelling, F. Duttweiler
CASS, University of California at San Diego

ABSTRACT

We describe a long duration balloon flight instrument for Max-91 designed to study the acceleration of >10 MeV ions and >15 keV electrons in solar flares through high resolution spectroscopy of the gamma-ray lines and hard X-ray and gamma-ray continuum. The instrument, HIREGS, consists of an array of high-purity, n-type coaxial germanium detectors (HPGe) cooled to $<90^{\circ}\text{K}$ and surrounded by a bismuth germanate (BGO) anticoincidence shield. It will cover the energy range 15 keV to 20 MeV with keV spectral resolution, sufficient for accurate measurement of all parameters of the expected gamma-ray lines with the exception of the neutron capture deuterium line. Electrical segmentation of the HPGe detector into a thin front segment and a thick rear segment, together with pulse-shape discrimination, provides optimal dynamic range and signal-to-background characteristics for flare measurements. Neutrons and gamma-rays up to $\sim 0.1\text{--}1$ GeV can be detected and identified with the combination of the HPGe detectors and rear BGO shield.

HIREGS is planned for long duration balloon flights (LDBF) for solar flare studies during Max-91. We describe the two exploratory LDBFs carried out at mid-latitudes in 1987-88, and discuss LDBFs in Antarctica, which could in principle provide 24 hour/day solar coverage and very long flight durations (20–30 days) because of minimal ballast requirements.

Introduction

High resolution spectroscopy of flare gamma-ray line and hard X-ray and gamma-ray continuum emission can provide a qualitatively new window on flare particle acceleration processes. This is because essentially all the nuclear gamma-ray lines produced by the energetic ions, and many of the important features of the hard X-ray continuum produced by the energetic electrons, are unresolved by present spacecraft detectors (Figure 1). High resolution measurements from ~ 10 keV to $\gtrsim 20$ MeV are required for:

- 1) Nuclear line spectroscopy, including determination of line shapes and asymmetries, to provide detailed information on the shape of the energy spectrum and angular distribution of the accelerated ions.¹
- 2) Flare hard X-ray continuum spectroscopy to provide the detailed shape of the energy spectrum of the accelerated electrons which very likely carry a large fraction of the total flare energy.² High resolution is required to resolve the steep spectrum of the emission from the high temperature "superhot" plasmas³ in the flare and to identify and resolve the sharp breaks⁴ in the accelerated electron spectrum. These features appear to be critical clues to the acceleration mechanism.
- 3) Very high sensitivity measurements of the narrow neutron capture deuterium line at 2.223 MeV to determine whether even small flares can accelerate ions to > 10 MeV energy.⁵
- 4) Resolution of the many expected nuclear gamma-ray lines to provide a powerful new method of obtaining solar elemental abundances.⁶
- 5) Determination of the shape and temporal evolution of the positron annihilation line at 511 keV to give information on the temperature and density of the annihilation region.⁷

With high sensitivity measurements the temporal evolution of the accelerated ions and electrons can be closely followed, and the role of electron acceleration in very small transient releases of energy, i.e., microflares,⁸ and their relationship to coronal heating,

can be explored.

Below we describe the design for a High Resolution Gamma-Ray and Hard X-ray Spectrometer (HIREGS). HIREGS cleanly separates the ≤ 200 keV hard X-ray region from the gamma-ray line region (0.4–20 MeV) so the high spectral resolution needed for line measurements can be maintained even in the presence of the very intense [$\geq 10^4$ ($\text{cm}^2 \text{ sec}^{-1}$) above 10 keV] flare hard X-ray fluxes.

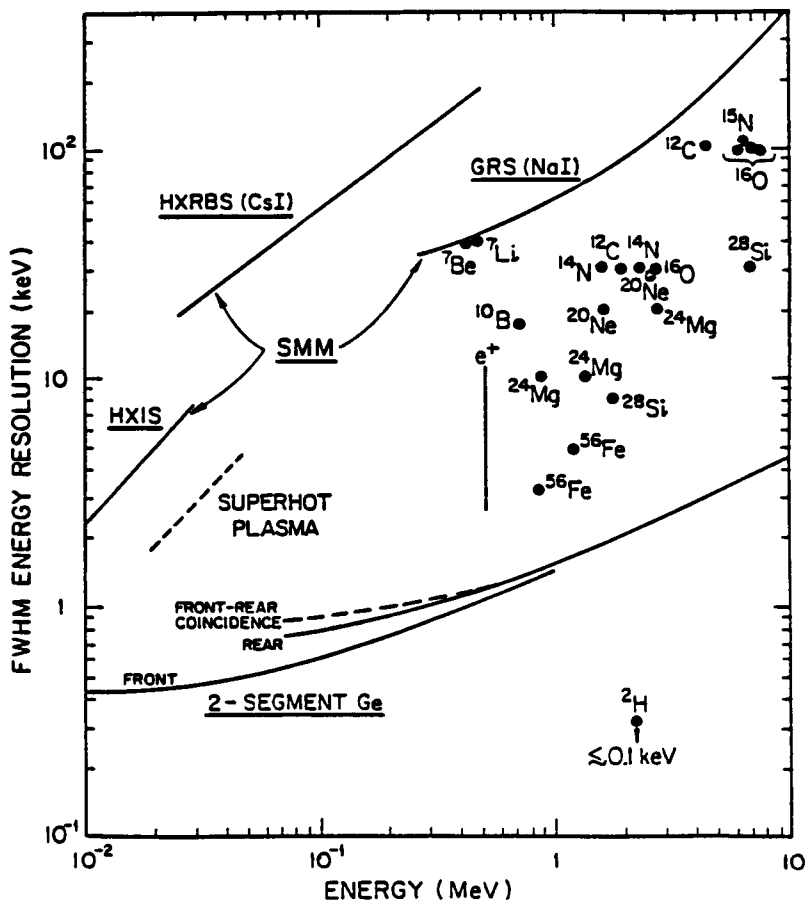


Fig. 1. The spectral resolution of the HIREGS 2-segment HPGe detectors is compared with that of the hard X-ray and gamma-ray instruments on SMM. The typical line widths expected for gamma-rays in solar flares are shown, as well as the resolution required to resolve the steep super-hot thermal component (dashed line).

Instrument Description

HIREGS consists of an array of 12 dual-segment, high-purity germanium (HPGe) detectors in a BGO scintillator annulus and back shield/detector assembly (Figure 2). The HPGe detectors are contained in a cryostat and cooled to an operating temperature of 90°K with liquid nitrogen. Table I gives the instrument parameters.

Segmented HPGe Detectors

The closed-end HPGe detectors are fabricated from n-type material, 6.5 cm in diameter and 6.5 cm thick, and are operated in the reverse bias mode, i.e., the holes are collected by the outside electrode.

Each detector has multiple collecting electrodes which divide it into two distinct volumes, or segments, according to the electric field pattern (Figure 3). In the central 1.0 cm diameter hole which extends to within ~6 mm of the top, two separate contacts are provided.¹⁰ The top contact collects charge from the upper 1 cm segment of the detector, and the long lower contact collects charge from the bottom ~5.5 cm coaxial segment. The curved outer surface and top surfaces are implanted with boron to make a very thin (~0.3 micron) window for X-rays.

The top segment alone is used at low energies (\leq 200 keV) where photoelectric absorption dominates (Figure 4). Photons are absorbed in the top ~1 cm segment, while Compton scattered photons and detector background are rejected by anticoincidence with the adjacent bottom segment of the detector. Therefore, this mode has the excellent background rejection properties of a phoswich type scintillation counter.¹¹

Higher energy (\geq 200 keV) photons are detected primarily in the thick bottom segment alone mode, with a smaller fraction also detected via top-bottom coincidences (Figure 4). The bottom segment is shielded by the top segment from low energy, \leq 10² keV protons. Even in the largest flares the peak count rates of the bottom segment is \leq 2 \times 10⁴ c/s per detector. Each detector has independent signal paths for the front and rear segments as indicated in Figure 3. Each signal path includes a cooled FET wide bandwidth charge sensitive preamplifier, followed by dual shaping amplifiers.¹² A slow shaper-amplifier (~10 μ s time constant) is used for pulse height analysis, and a fast shaper-amplifier-discriminator (~100 ns) supplies fast pulses for coincidence, pileup

rejection, timing, and rate accumulations. The pile-up rejection system allows operation at rates up to 5×10^4 s⁻¹ per detector without resolution degradation.

Table II shows that in a flare the size of the 27 April 1981 gamma-ray flare,¹³ several hundred to a couple thousand counts would be obtained by HIREGS in each of a dozen major lines (including four lines of Fe). Flare bremsstrahlung continuum will usually dominate the detector background, leading to line-to-continuum ratios of $l/c \approx 1$ to 10, except for the broad Li-Be combined lines where $l/c \approx 0.2$. These lines will be detected at ~ 10 –60 σ 's significance, permitting line shapes, asymmetries, etc. to be accurately determined. Even for a flare with line fluences more than 30 times smaller, most of these lines could be detected at the 3σ level if the l/c remained the same. For detection of narrow lines HIREGS is ~ 5 –10 times as sensitive as the SMM GRS instrument.

The most sensitive indicator of ion acceleration is the narrow nuclear line of neutron capture deuterium at 2.223 MeV, which is delayed from the impulsive phase by the thermalization time for the neutrons. HIREGS can detect at 3σ significance a 2.223 MeV line fluence $\gtrsim 10^3$ times smaller than the 4 August 72 event. If all flares accelerate ions to tens of MeV energy and the gamma-ray emission scales as the microwave burst intensity, then ~ 10 –15 flares should be detected per month in the 2.223 MeV line near solar maximum.

Good background rejection is important for the 511 keV positron annihilation and the 2.223 MeV neutron capture deuterium line, which usually lasts well past the impulsive phase. Also SMM observations show that following the impulsive phase there is a delayed phase in some (perhaps many) flares which is dominated by nuclear emissions.¹⁴ The segmented HPGe detector provides the basic configuration for powerful background rejection techniques in the gamma-ray line region from a few hundred keV to several MeV (see ^{15,16} for details).

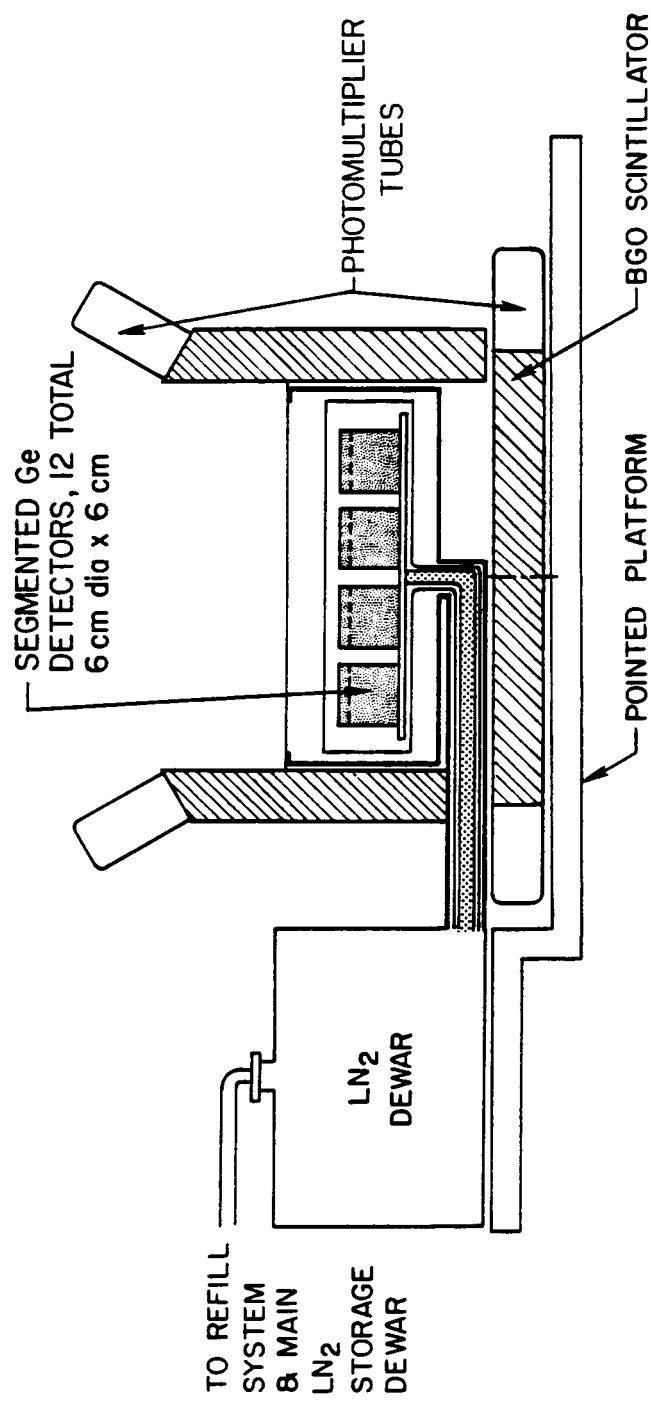


Fig. 2. Schematic of HIREGS instrument.

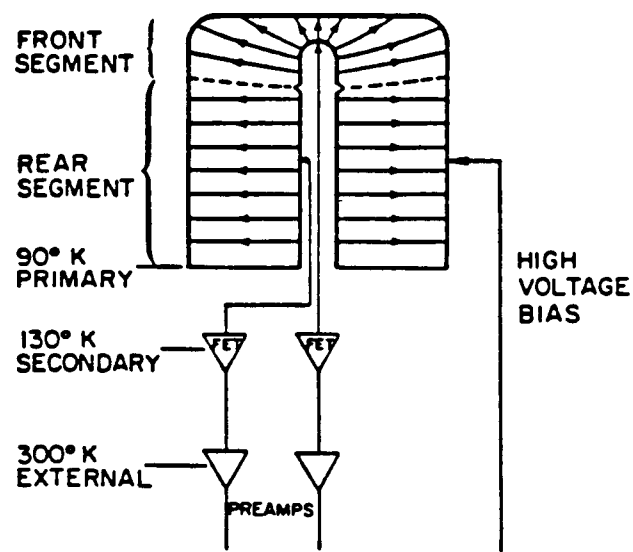


Fig. 3. Schematic of a dual-segment HPGe detector.

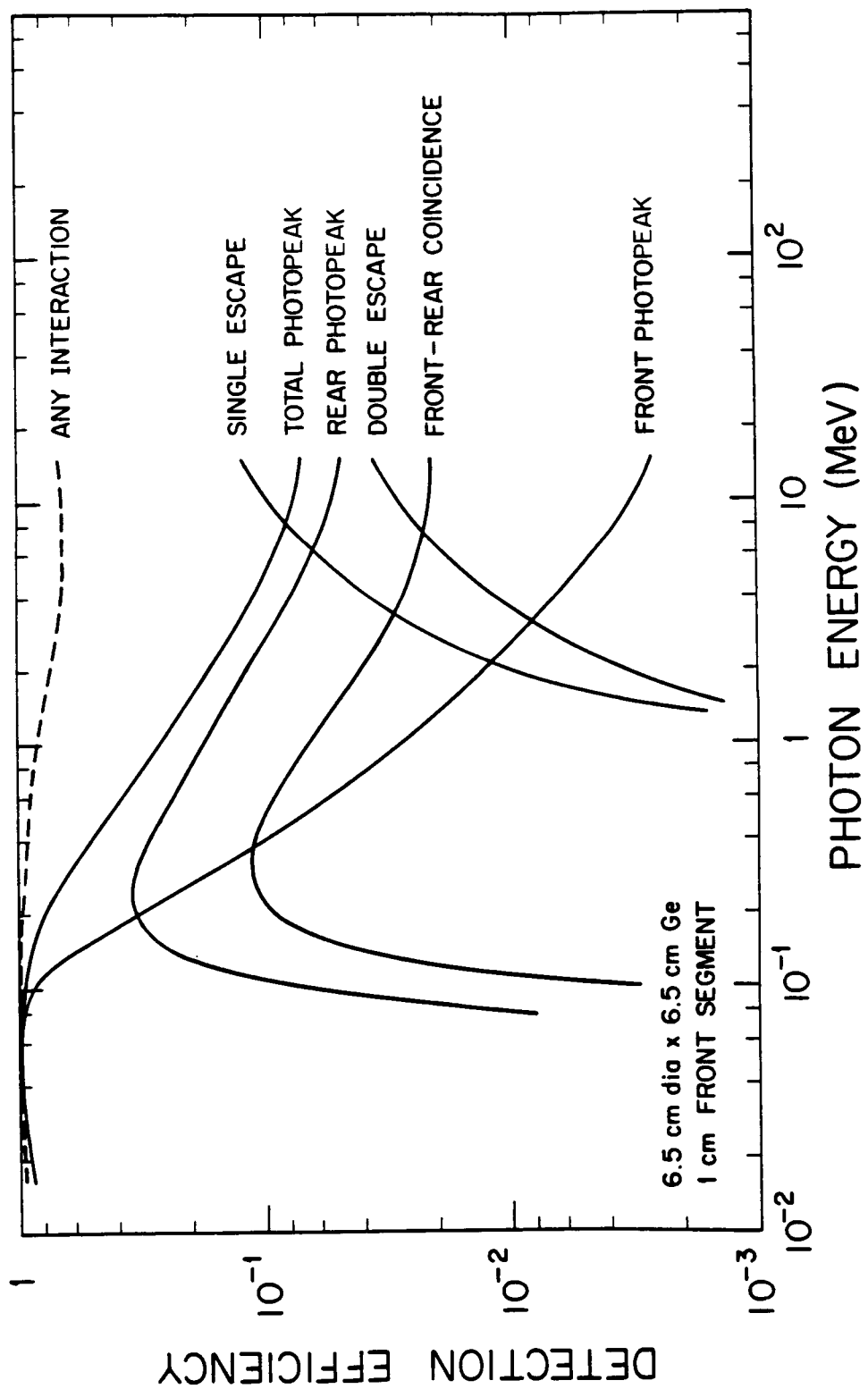


Fig. 4. The photopeak efficiency for the top segment and bottom segment of the HPGe detector is shown here for different modes.

Table I. HIREGS Instrument Parameters

Energy range	10 keV to 20 MeV (high-resolution HPGe)
Gamma-rays and hard X-rays	10 keV to 20 MeV (high-resolution HPGe)
Energy resolution	0.6 to 5 keV FWHM (high-resolution HPGe)
Total detector area	400 cm ² HPGe
Field of view	120° FWHM
Shields	5-cm-thick BGO on sides and rear
Germanium detector cooling	~90°K for 20 days with liquid nitrogen

Table II. Solar Flare Gamma-Ray Lines

Line Energy (MeV)	Excited Nucleus	FWHM (keV)	Fluences at Earth in FWHM		Counts in HIREGS (1000 s)			HIREGS 3 σ line sensitivity fluence ph/cm ² (10 ⁻⁴ /10 ⁻³ s)
			Lines	Flare Continuum (ph/cm ²)	Line	Flare Continuum	Detector Background	
Prompt Lines								
-0.45	⁷ Li, ⁷ Be	62	20	105	3.7x10 ³	1.1x10 ⁴	1.7x10 ³	0.67/0.2
0.847	⁵⁶ Fe	4.5	5	2	630	250	40	0.15/0.05
0.931	⁵⁶ Fe	5	2	2	230	230	35	0.15/0.05
1.238	⁵⁶ Fe	9	2.5	2	250	200	35	0.2/0.06
1.317	⁵⁶ Fe	13	2.5	2	240	190	45	0.2/0.06
1.369	²⁴ Mg	18	7.5	3	690	280	55	0.25/0.08
1.634	²⁰ Ne	23	13	2.5	1.1x10 ³	200	45	0.25/0.08
1.779	²⁸ Si	25	8	2	630	180	45	0.25/0.08
2.313	¹⁴ N	54	6	3	410	205	50	0.3/0.1
4.438	¹² C	115	10	1.5	510	80	20	0.25/0.08
6.129	¹⁶ O	120	10	1	440	44	10	0.2/0.06
Delayed Lines								
0.511	e ⁺	2-10	25	—	4.3x10 ³	—	44-220	~0.25/~0.12
2.223	² H	3(0.1)*	60(4.3)*	—	4x10 ³	—	3	0.1/0.05

* This line has an intrinsic width of ~0.1 keV, so the HIREGS instrument FWHM resolution (3 keV) is substituted. The 2.223 MeV fluence observed for the 27 April 1981 flare is highly attenuated because the flare is located near the limb; the value of 60 is for a comparable flare within ~70° of disk center.

Long Duration Balloon Flights

Long duration balloon flights (LDBF) offer an attractive way to obtain high energy measurements during the next solar maximum, since energetic photons and neutrons are able to penetrate the upper layers of the earth's atmosphere. Large, powerful instruments, up to ~3000 lbs. total payload weight, can be carried by the present standard 28.4 million cu. ft. balloons to altitudes of ~130,000 ft. (40 km). At that altitude there is less than 3 g/cm² of overlying atmosphere, so high quality hard X-ray and gamma-ray measurements down to ~15 keV are possible.

For standard zero-pressure balloons the temperature of the gas, and therefore the balloon altitude, is controlled by the radiation received from the Sun and the Earth. Thus the balloon is at high altitude during sunlight hours but drops during nighttime. If the balloon initially reaches a high daytime float altitude it will remain above the tropopause in its day-night excursions under normal conditions without ballast drops. Then, in this simple **R**Adiation **C**Ontrolled ballo**ON** (RACOON) mode,¹⁷ flight durations are limited only by balloon lifetime and gas losses (which can be offset by ballast drops). During the three-month summer season at mid-latitudes, strong stable zonal winds flow with high velocity approximately along latitudinal lines, so circumglobal LDBFs are feasible.

In 1983 a 15 million cubic ft. balloon with an ~1200 lb. payload, designed to search for solar flare neutrons, made a circumnavigation of the globe in the southern hemisphere in ~18 days.¹⁸ In 1987, two exploratory RACOON balloon flights were launched from Alice Springs, Australia. One payload carried a complement of hard X-ray and gamma-ray detectors, including both liquid-nitrogen cooled germanium detectors for high spectral resolution and large-area phoswich scintillation detectors for high sensitivity, for observations of microflares and flares from the sun.¹⁹ The standard, 28.4 million cubic ft., 0.8 mil polyethylene, zero-pressure balloon developed for normal short-duration flights was used. The payload was designed for automated continuous 24 hours/day operation with a solar cell power system, a pointing and navigation system, data and telemetry systems, etc.

The payload was launched at ~2100 UT February 9, 1987, from Alice Springs, Australia. Due to a malfunction of the ballast control system all 900 lbs of ballast were dropped at launch. The balloon thus flew as an unballasted RACOON for the entire flight. With the loss of ballast the ascent was extremely rapid (~1500 ft./min), and the balloon reached a float altitude of ~132,000 ft.—i.e., ~2000 ft. higher than normal. Some of the helium was vented, and perhaps some leaks developed from the stress of the rapid ascent.

Figure 5 shows the balloon altitude versus time. The daytime float altitude generally decreased throughout the flight. Preliminary analysis indicates that balloon lift decreased at a rate of ~2–3% per day, possibly from a small leak. The gas temperature, and therefore the float altitude, are determined primarily by the radiation the balloon receives from the sun and the earth. Cold storm clouds below the balloon are responsible for the sharp drops in altitude superimposed on the general long-term decrease. Ballast drops totaling ~15% (900 lbs) of the total balloon plus payload weight would have kept the daytime balloon float altitude near 130,000 ft. for the entire trip from Australia to Brazil.

The trajectory of the balloon is shown in Figure 6. The balloon started westward at an average rate of ~30° longitude per day (~130 km/hour), but slowed down as the balloon altitude decreased. The payload was commanded to cut down over Brazil after 12 days, and was recovered with relatively minor damage.

All the detectors, the experiment data system, and electronics appeared to have functioned perfectly. The data transmission to the GOES spacecraft appears to have been intermittent. Only ~10% of those data have been recovered. All of the data, however, were stored in the on-board VCR tape. Analysis of those data is underway.

In January–February 1988 two more 28.4 million cu. ft. balloons were flown from Alice Springs, Australia to Brazil. One payload contained germanium and scintillation detectors to search for gamma-ray lines and hard X-ray continuum from the new supernova 1987A. Again, the ballast system malfunctioned, but the balloon made it to Brazil after ~9 days.

Also in January, 1988, a 11.8 million cu. ft. balloon carrying a coaxial germanium detector system was launched from near McMurdo in Antarctica (latitude \sim 78°S), again to search for gamma-ray lines from the new supernova 1987A. The balloon drifted very slowly along the 78° latitude line and the payload was cut down 65 hours later near Vostok, about 80° west of McMurdo, where the payload was recovered. Because of the 24-hour sunlight, the balloon lost less than 0.5% of its lift per day. Thus, in addition to the possibility of 24-hour observation per day, versus \sim 12 at mid-latitudes, much longer flights (perhaps 20–30 days) are feasible because much less ballast is needed.

In the Antarctic during the summer the sun will be at angles to the zenith of \sim 67°. Thus, solar photons must traverse \sim 7.7 g/cm² of atmosphere to reach a balloon instrument at a height of \sim 130,000 ft. (3 g/cm² overlying atmosphere). At mid-latitudes the overlying atmosphere (at the same altitude) is \sim 3 g/cm² near noon but averaged over the full 12 hours/day of observing provides only \sim 10–20% better transmission of gamma-ray line energies than Antarctica (Figure 7). The difference rises to about a factor of two at hard X-ray energies, but of course photons are plentiful in that range.

The much longer flight durations and 24 hours/day observation times available for Antarctica very significantly increase the probabilities for detecting solar gamma-ray events. Clearly Antarctic balloon flight capabilities need to be developed for Max-01.

Table III summarizes the expected number of gamma-ray line and hard X-ray flare events for a typical mid-latitude, Australia to Brazil flight, and for a \sim 12 day circumnavigation flight around the south pole. Because of the low ballast requirements, two circumnavigations should be possible in a single flight, so that numbers in Table III for Australia could be doubled.

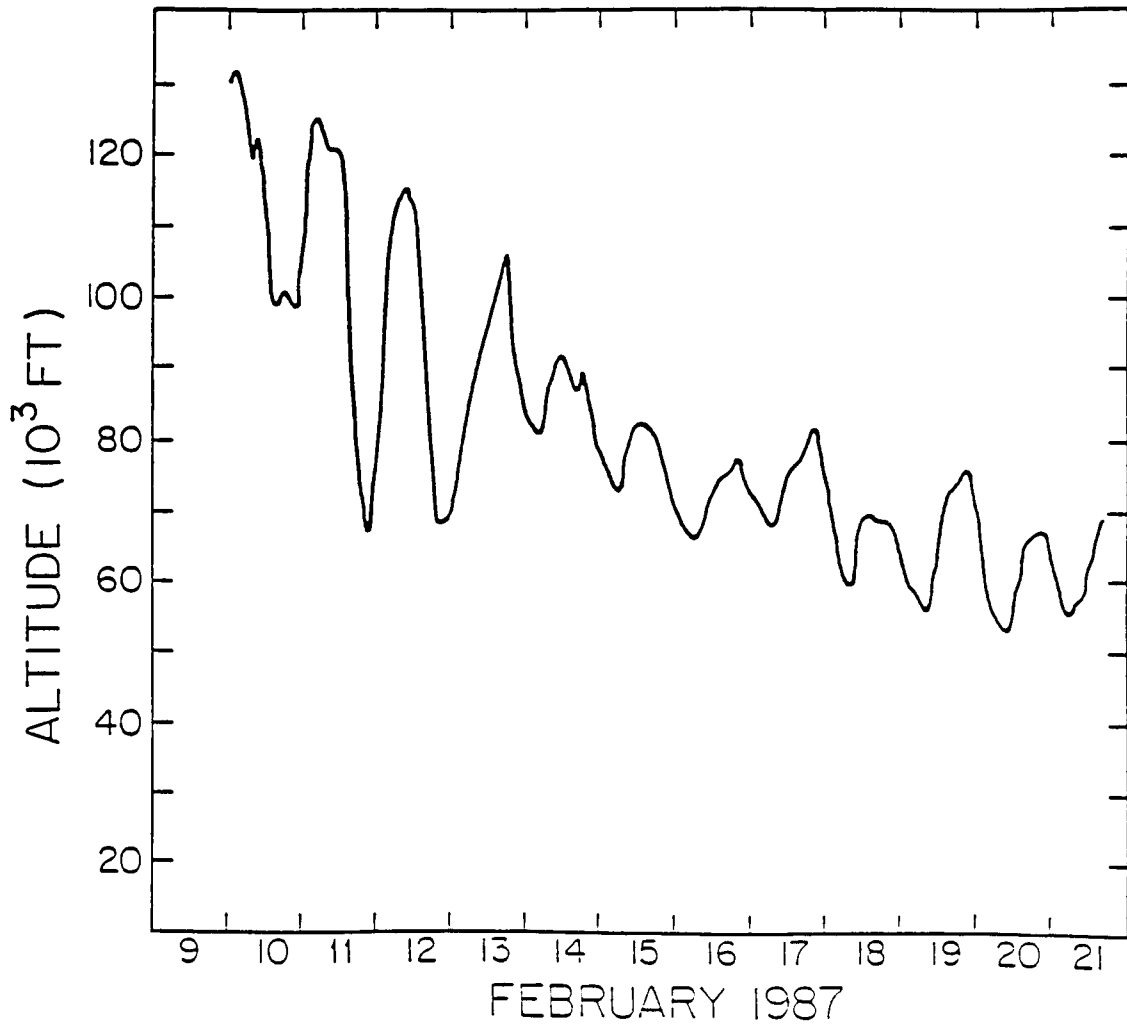


Fig. 5. Balloon altitude versus time (unballasted).

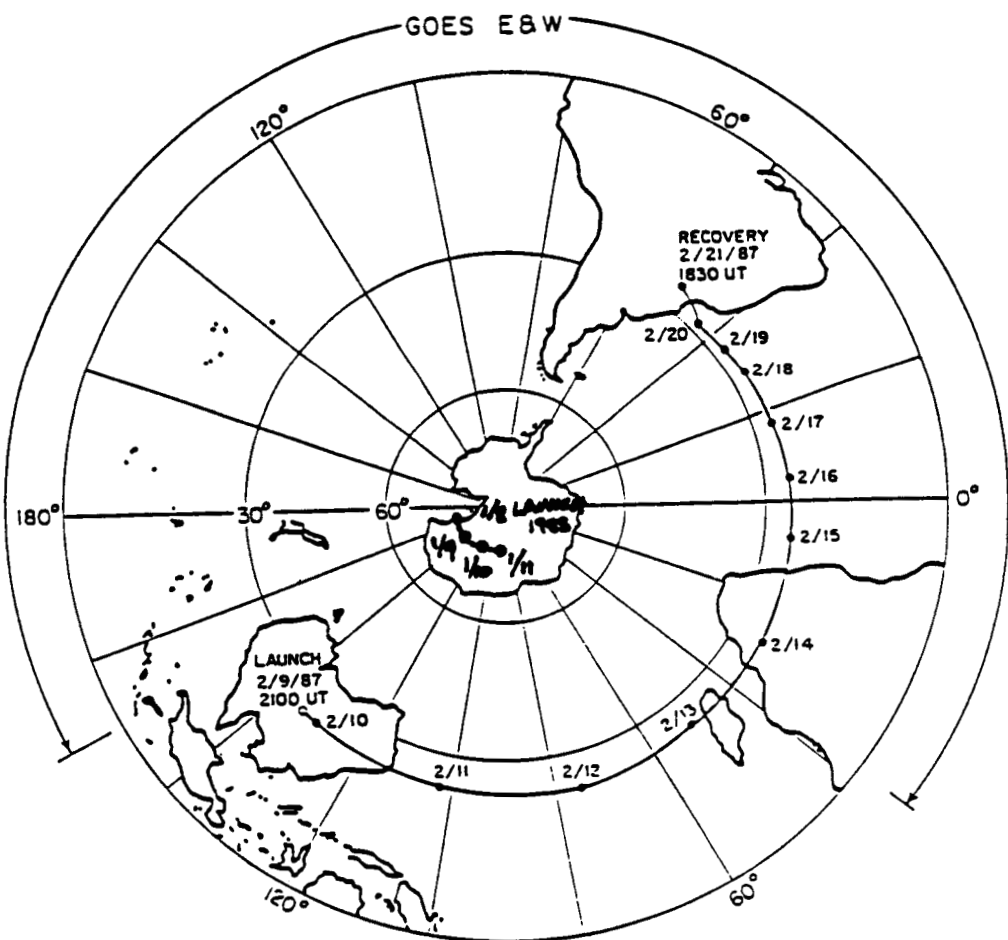


Fig. 6. Balloon trajectory from Australia to Brazil.

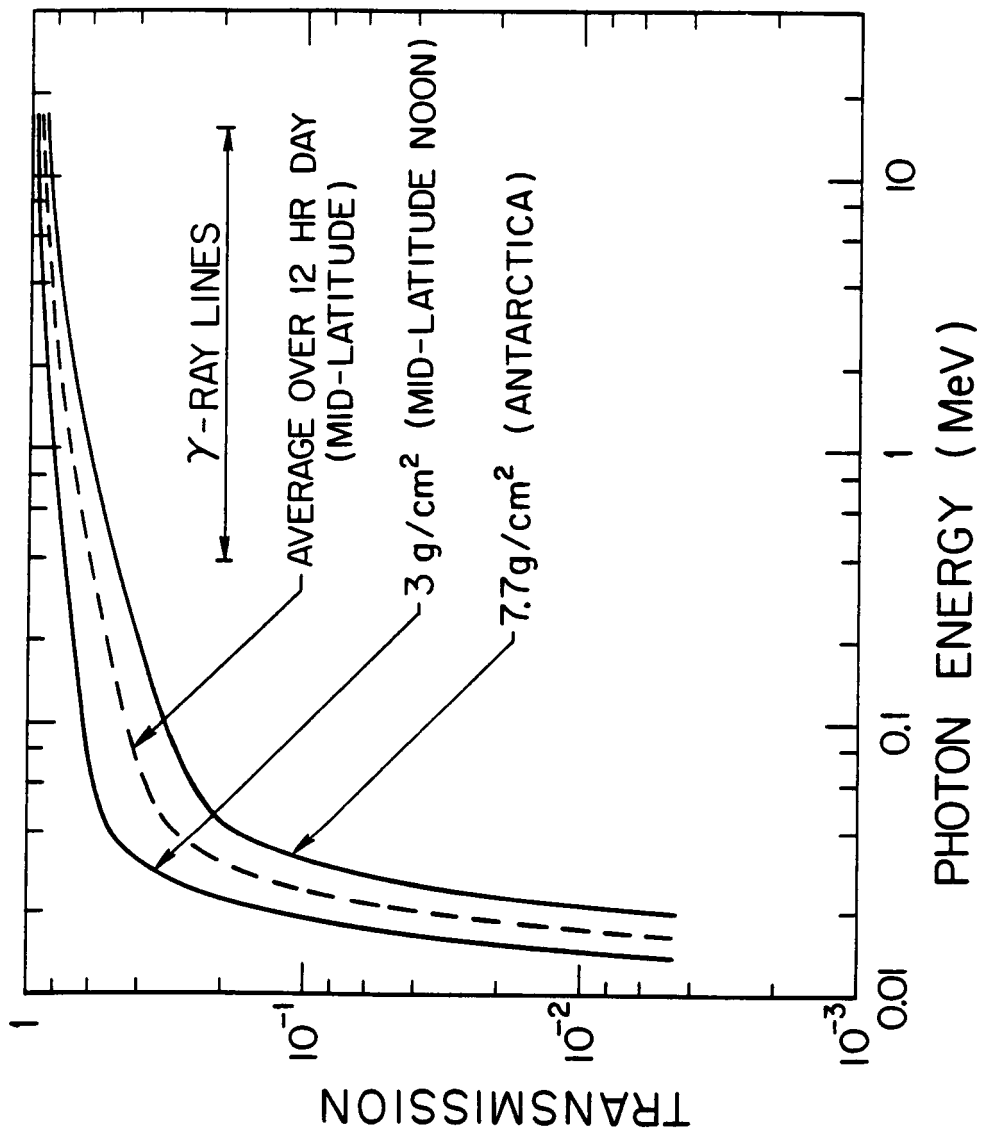


Fig. 7. Photon transmission for mid-latitudes (dashed line gives average over 12 hour day) as compared with Antarctica (24 hours/day).

Table III. HIREGS Event Probabilities*

	Mid-latitude	Antarctica
	7 days (12 hrs/day)	12 days (24 hrs/day)
High resolution spectroscopy flare event ($>10\sigma$ in several lines)	~0.35	~1
Detection of several gamma-ray lines in a flare	1.4	~4
Detection of narrow 2.223 MeV neutron-capture line, if every flare accelerates >10 MeV ions	3.5	~10
Hard X-ray continuum fast spectroscopy flare (~1 sec detailed spectra)	14	~24
Hard X-ray microflares	≥ 700	~1200

* Assumes scaling with hard X-ray peak flux distribution measured by SMM.

Acknowledgments

This research was funded in part by NASA grants NAGW-516 and NAGW-449.

REFERENCES

- R. Ramaty and R. E. Lingensfelter, *Ann. Rev. Nucl. Sci.* **32**, 235 (1982).
- R. P. Lin and H. S. Hudson, *Solar Phys.* **50**, 153 (1978).
- R. P. Lin, R. A. Schwartz, R. M. Pelling, and K. C. Hurley, *Astrophys. J. Lett.* **251**, L109 (1981).
- R. P. Lin and R. A. Schwartz, *Astrophys. J.* **312**, 462 (1987).
- E. L. Chupp, *Ann. Rev. Astron. Astrophys.* **22**, 359 (1984).
- R. J. Murphy, R. Ramaty, D. J. Forrest, and B. Kozlovsky, *Proc. 19th Intern. Cosmic Ray Conf., La Jolla*, **4**, 240 and 253 (1985).
- C. J. Crannell, G. Joyce, R. Ramaty, and C. Werntz, *Astrophys. J.* **210**, 582 (1978).
- R. P. Lin, R. A. Schwartz, S. R. Kane, R. M. Pelling, and K. C. Hurley, *Astrophys. J.* **283**, 4211 (1984).
- D. J. Forrest, W. T. Vestrand, E. L. Chupp, E. Rieger, J. Cooper, and G. Share, *19th Intern. Cosmic Ray Conf. Papers*, NASA Conf. Publ. 2376, Vol. 4 (NASA, Washington, D.C., 1985), p. 146.
- P. N. Luke, *IEEE Trans. Nucl. Sci.* **NS-31**, 312 (1984).
- J. L. Matteson, P. L. Nolan, W. D. Paciesas, and R. M. Pelling, *Space Sci. Instr.* **3**, 491 (1977).
- D. A. Landis, F. S. Goulding, and R. M. Pehl, *IEEE Trans. Nucl. Sci.* **NS-18**, 115 (1970).
- D. J. Forrest, *Positron-Electron Pairs in Astrophysics*, M. L. Burns, A. K. Harding, and R. Ramaty, eds. (AIP, New York, 1983), p. 3.
- D. J. Forrest, W. T. Vestrand, E. Rieger, and G. H. Share, *Bulletin American Astr. So.* **18**, 697 (1986).
- J. Roth, J. H. Primsch, and R. P. Lin, *IEEE Trans. Nucl. Sci.* **NS-31**, 367, 1984.
- D. M. Smith, M. Shapshak, R. Campbell, J. H. Primsch, and R. P. Lin, *this volume* (1988).
- V. Lally, *Proc. XXIV COSPAR Conf., Ottawa, I*, 1.4 (1982).
- R. Koga, F. M. Frye, Jr., A. Owen, B. V. Denehy, D. Mace, and J. Thomas, *19th Intern. Cosmic Ray Conf. Papers*, NASA Conf. Publ. 2376, Vol. 4 (NASA, Washington, D.C., 1985), p. 142.
- R. P. Lin, D. W. Curtis, J. H. Primsch, P. Harvey, W. K. Levedahl, D. M. Smith, R. M. Pelling, F. Duttweiler, and K. C. Hurley, *Solar Physics*, accepted for publication (1988).

**Coordinated Videomagnetograph Observations by
the Big Bear and Huairou Observatories**

Haimin Wang, Alan Patterson and Harold Zirin
Big Bear Solar Observatory, Caltech

and

Guoxiang Ai and Hongqi Zhang
Huairou Station, Beijing Observatory

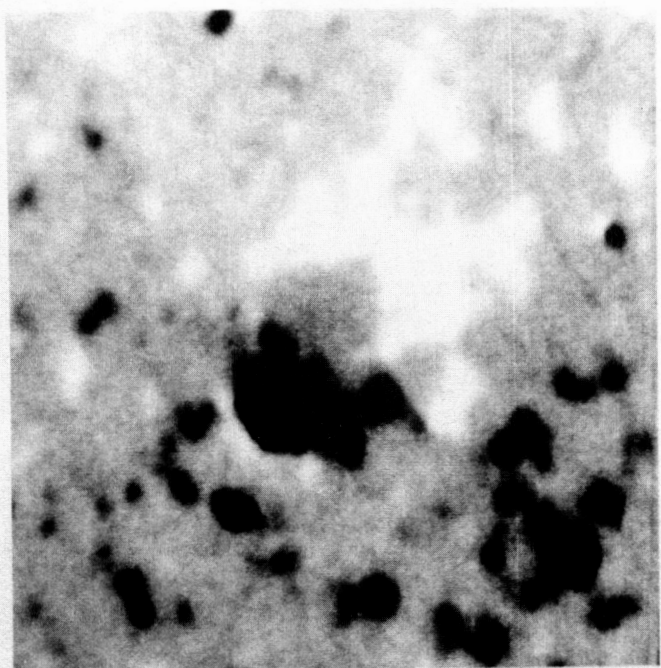
A new videomagnetograph patterned after the BBSO system was installed at Huairou in 1987, and five days of coordinated observing were carried out from Sept 24 to 29, 1987. The data have been combined to make a continuous movie of the fields around a stable spot. A 57-hour magnetograph run with two seven-hour gaps were achieved from 2330 UT, Sept 24 to 0830 UT, Sept 27. The frames have been reregistered and justified to eliminate the change of scale with meridian distance. The intensities were corrected for cosine effect. Preliminary examination of the data shows continuous decrease of the total magnetic field during this period by more than 50%. The principal loss of flux appears to be due to "cancellation" at the main neutral line. Some flux disappears due to fragmentation, which makes the elements fall below our threshold, while only a tiny loss due to diffusion can be detected.

Figs 1 and 2 display 8 frames taken 8 hrs apart. The white rim at the left of

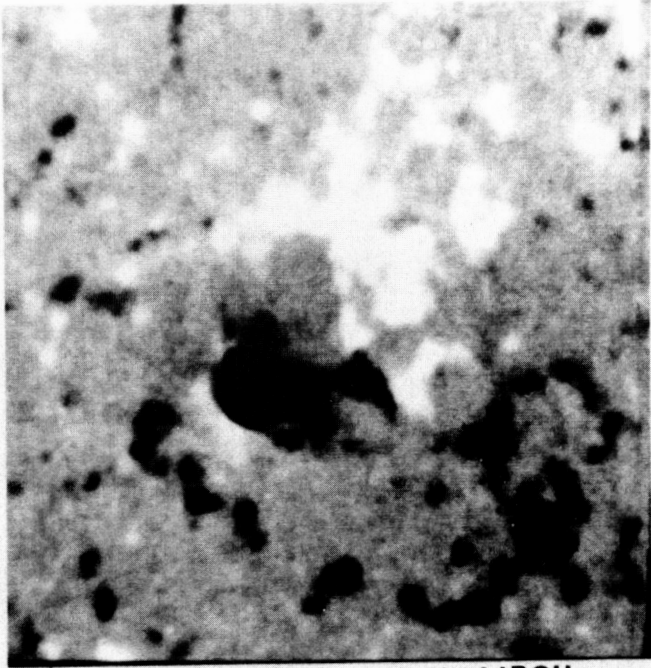
the umbra is a continuous outflow of flux from the spot, which is the same polarity but tilted away from us. These elements collect in dark clumps of vertical fields around the spot. The larger elements of the magnetic network are largely unchanged during the period except for a general decrease of the stronger plages. The network cells last much longer than 20 hours. There is continual merging and small-scale motion, and we find several centers toward which flow is directed. The longest lasting elements appear to be those toward which flow is directed. Intranetwork elements often show sharp changes in trajectory during their lifetimes. A VCR tape of the run was shown at the meeting.

It is planned to continue this program during Max91, including transverse field measurements as well. Several long runs have already been obtained in 1988.

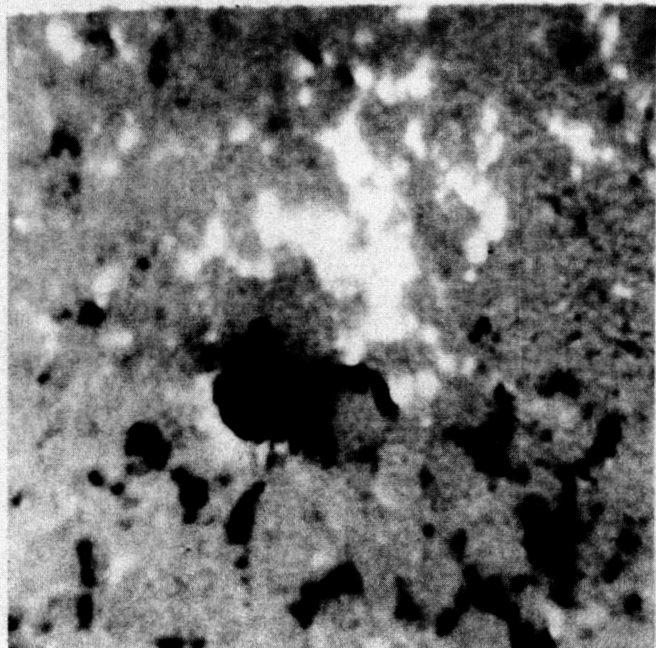
ORIGINAL PAGE IS
OF POOR QUALITY



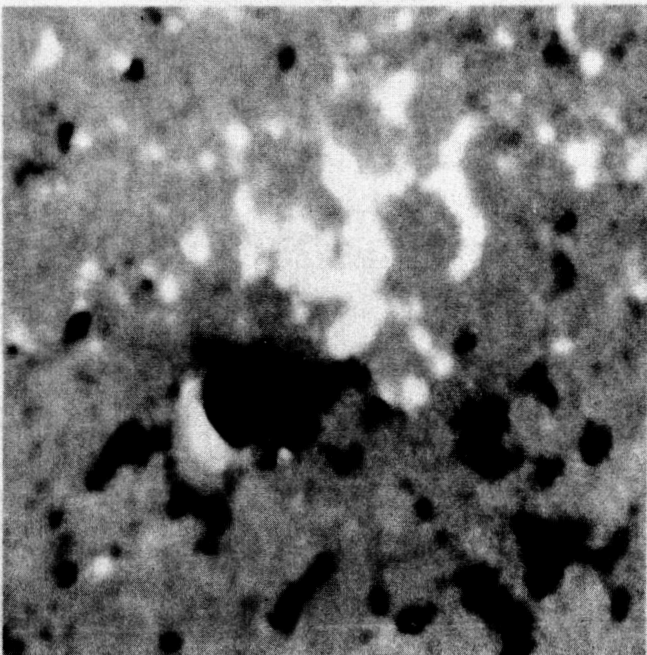
SEP 24 2345UT HUAIROU



SEP 25 0817 HUAIROU



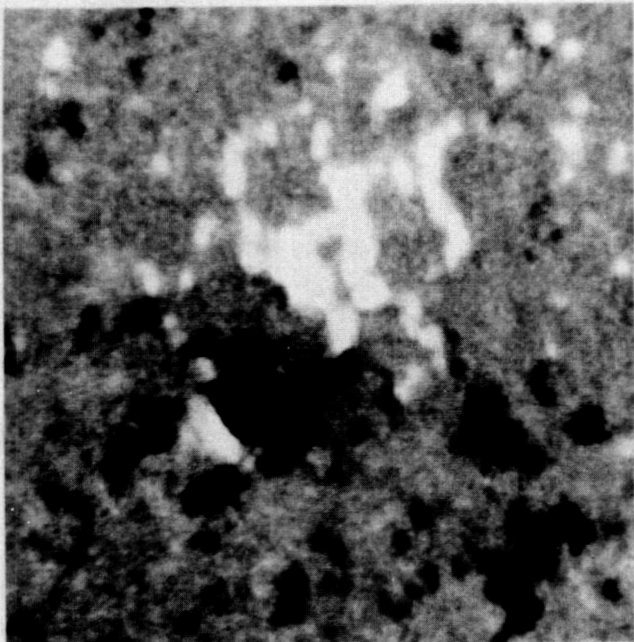
SEP 25 1614 BBSO



SEP 26 0027 HUAIROU

50"

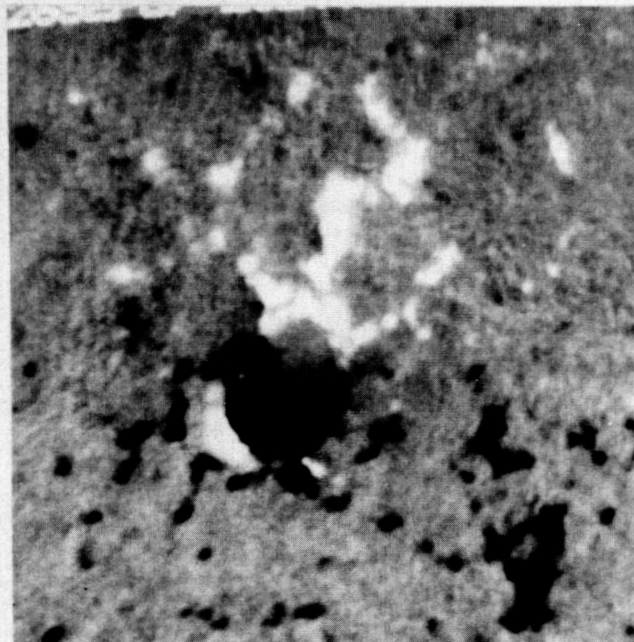
FIGURE 1



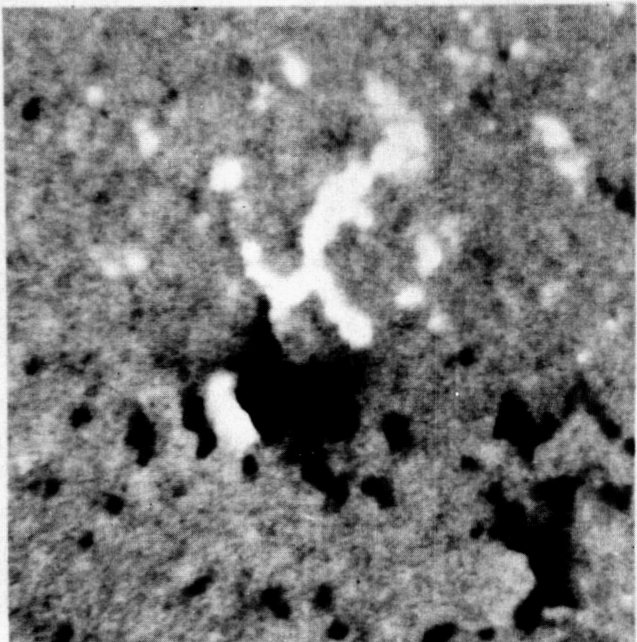
SEP 26 0808UT HUAIROU



SEP 26 1557 BBSO



SEP 26 2324 BBSO



SEP 27 0819 HUAIROU

FIGURE 2

ORIGINAL PAGE IS
OF POOR QUALITY

High-Resolution Digital Movies of Emerging Flux and Horizontal Flows in Active Regions on the Sun

K. Topka, S. Ferguson, Z. Frank, T. Tarbell, A. Title (Lockheed PARL)

Abstract

We present high-resolution observations of active regions in many wavelength bands obtained at the Vacuum Tower Telescope of NSO/Sunspot (Sacramento Peak). The SOUP tunable filter (50 - 100 mÅ bandwidth), HRSO 1024 × 1024 CCD camera, and a sunspot tracker for image stabilization were used. Subarrays of 512 × 512 pixels have been processed digitally and recorded on videodisk in movie format. We show movies with 0.5 - 1 arcsecond resolution of the following simultaneous (i.e., interlaced) observations: green continuum, longitudinal magnetogram, Doppler velocity, Fe I 5576 Å line center (mid-photosphere), H α wings (± 600 mÅ), and H α line center. The best set of movies show a 90 × 90 arcsecond field-of-view of an active region at S29, W11 (15:05 - 16:25 UT, 8/6/87). When viewed at speeds of a few thousand times real-time, the photospheric movies clearly show the active region fields being distorted by a remarkable combination of systematic flows and small eruptions of new flux. Flux emergence is most easily discovered in line center movies: an elongated dark feature (presumably a horizontal flux tube) appears first, followed soon after by bright points at one or both ends. A brief, strong upflow is seen when the dark feature first appears; downflow in the bright points persists much longer. The magnetic flux appears to increase gradually over this extended period. Some of the flux emergence events have been studied in detail, with measurements of horizontal and vertical velocities and magnetic flux vs. time within one footpoint of the loop.

This work was supported by Lockheed Independent Research Funds and NASA contracts NAS8-32805 (SOUP) and NAS5-26813 (HRSO).

Emergence of Magnetic Flux Tubes

The emergence of new magnetic flux through the photosphere is the first step in the formation of an active region (AR). Many emergence events have been observed at the moderate resolution of Big Bear and Kitt Peak magnetograms. Studies of these have produced a fairly clear understanding of the gross features of AR formation, such as flux emergence

rates, rates of polarity separation and areal growth, and distributions of frequency vs. total flux for AR's and ephemeral regions. The early chromospheric development of AR's has been observed even longer by spectroheliograph and filter movie techniques in H-alpha. However, very few if any events have been observed in great enough detail to study the MHD processes actually occurring during flux emergence. This requires not only very high spatial resolution over an extended period (tens of minutes to hours) but also simultaneous, cospatial measurements of magnetic fields, Doppler shifts, and intensities at several levels.

Theoretical models suggest that horizontal flux tubes should rise through the upper convection zone at speeds representing a balance between buoyancy and drag forces. When they reach the photosphere, the upper portions should expand rapidly into the chromosphere and corona, and the footpoints should become nearly vertical, due to buoyancy. The gas draining from the expanded upper part of the loop may trigger convective collapse, leading to constriction and amplification of the magnetic field strength.

Our observations of 6 August, 1987, show many examples of tiny flux tubes emerging through the surface. Although it is difficult to find one for which the seeing stays good throughout the event, so many events are seen in different phases that some general conclusions can be drawn. The first indications are dark striations in the continuum and line center intensity, suggestive of horizontal field lines rising through the surface; these are typically 1500 to 4000 km long. A strong upflow may be seen for a few minutes in the dark striation just after it appears. Bright points form at one or both ends of the dark feature a few minutes after it appears. Strong downflow and new magnetic flux appear in the bright points. The downflow may persist for an hour or more; the mass flux integrated over this time period would fill a tube roughly 3000 km long at photospheric densities, consistent with the initial footpoint separation. The magnetic flux appears to increase gradually over this whole period, instead of making an abrupt change when the bright point first appears. This result is very tentative, however, because the magnetograms are noisy and the conversion from polarization signal to flux is uncertain and may be time dependent.

Zwaan and Brants have also seen many of these features in an emerging flux region. It is clear that a modest increase in resolution and uniformity of seeing would permit meaningful comparisons with MHD models. Continued observations of this type at excellent sites, with assistance from active optics, or balloon flights of the SOUP instrument could provide such observations in the near future.

FIGURE CAPTIONS

Fig. 1. Snapshots of the active region in (a) continuum near 5576; (b) Fe I 5576, 30 mÅ blue; (c) H- α line center; (d) H- α wing, 600 mÅ red. All images in Figs. 1 and 2 were taken within 80 seconds of each other, in one cycle of the observing sequence. Field-of-view is 90×80 arcseconds, and ticks are at 2 arcsecond intervals.

Fig. 2. Same as Fig. 1, showing (a) Fe I 5576 line center, compensated for the local Doppler shift; (b) Doppler velocity measured from 4 images evenly spaced through 5576 ($g=0$ line); (c) H- α wing, 600 mÅ blue; (d) magnetogram made in blue wing of Fe I 6302 ($g=2.5$).

Fig. 3. Collages of frames from the movies, showing the emerging flux tube measured in Figs. 5 - 8 and many others: (a) 5576 line center; (b) 6302 magnetograms. Each frame is labelled with the time. Field-of-view is 25×25 arcseconds, and ticks are at 1 arcsecond intervals.

Fig. 4. Same as Fig. 3, showing (a) continuum near 5576; (b) Doppler velocity.

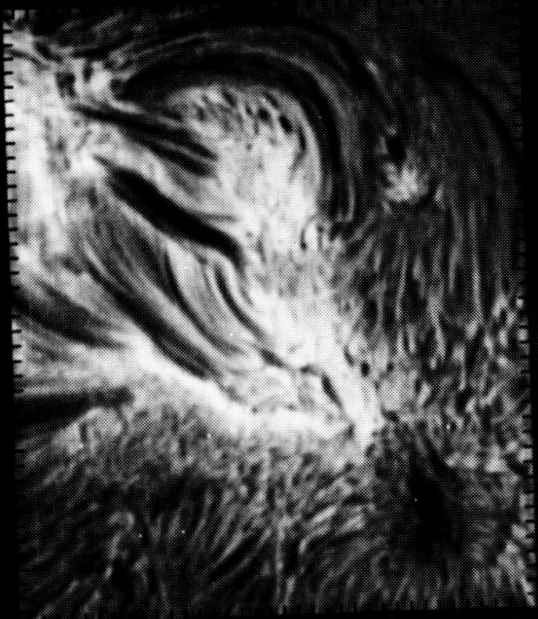
Fig. 5 Plot of velocity versus time in a small region between the footpoints of an emerging flux tube. The velocity is the mean in an irregular shaped area covering about 100 pixels of the Dopplergram movie. A strong upflow develops at the beginning of the emergence process and lasts about 200 seconds, suggestive of rising horizontal field lines.

Fig. 6 Plot of velocity versus time in a small region (about 70 pixels) centered on the footpoint of an emerging flux tube. The velocity starts near zero (with fluctuations due to 5-minute oscillations), and then a strong down flow develops that lasts about 1 hour.

Fig. 7 Plot of measured magnetic flux as a function of time in the footpoint of an emerging flux tube (same footpoint as Fig. 6). The data were computed from the magnetogram movie.

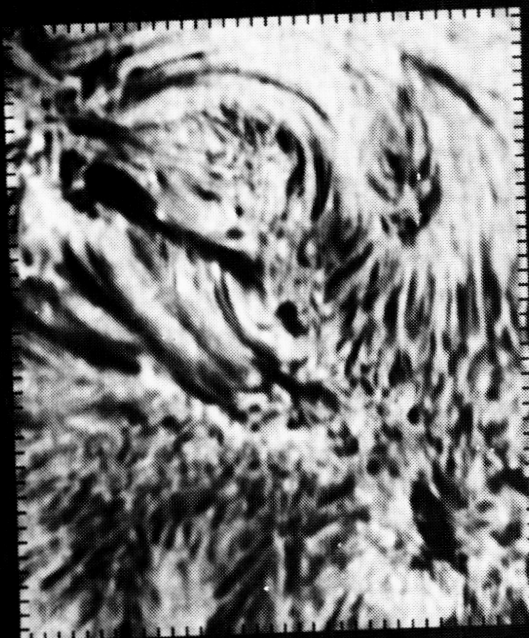
Fig. 8 Plot showing the motion of the footpoint of a new flux tube after emergence on the surface of the Sun (same footpoint as in Figs. 6 and 7). Crosses: measurements of the bright point visible on the line center movie. Squares: measurements of the corresponding small magnetic feature visible on the magnetogram movie. The footpoint moves away from its place of origin at 0.8 km/s.

ORIGINAL PAGE IS
OF POOR QUALITY



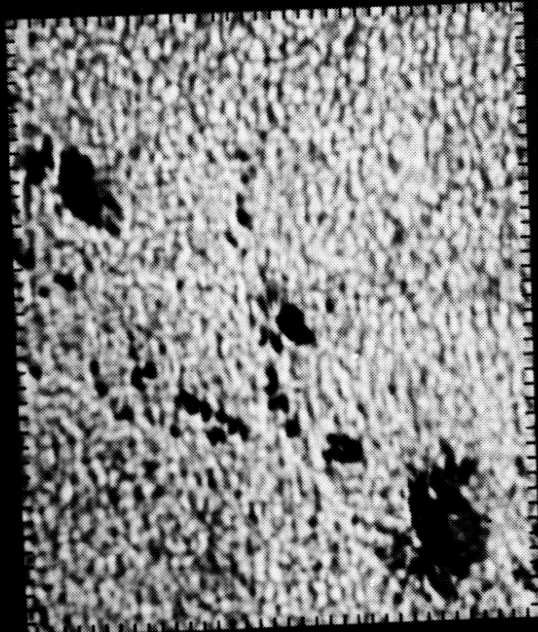
LPA RL

H-ALPHA 8/6/87 S29,W12



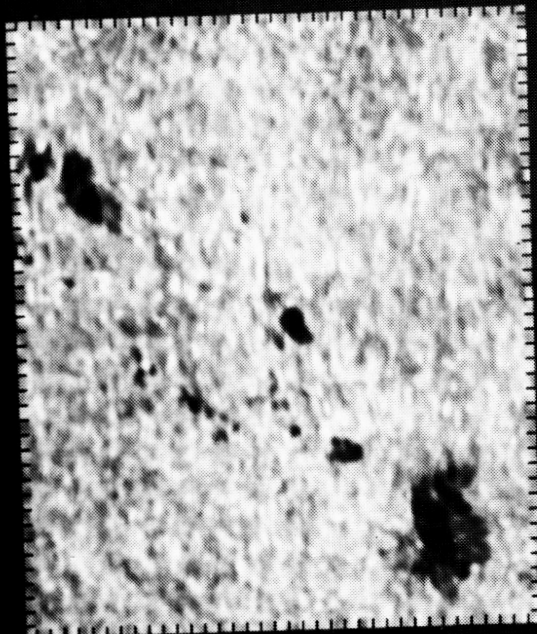
LPA RL

HA + 600 8/6/87 S29,W12



LPA RL

CONTINUUM 8/6/87 S29,W12



5576 - 30 8/6/87 S29,W12 LPA RL

FIG. 1

ORIGINAL PAGE IS
OF POOR QUALITY

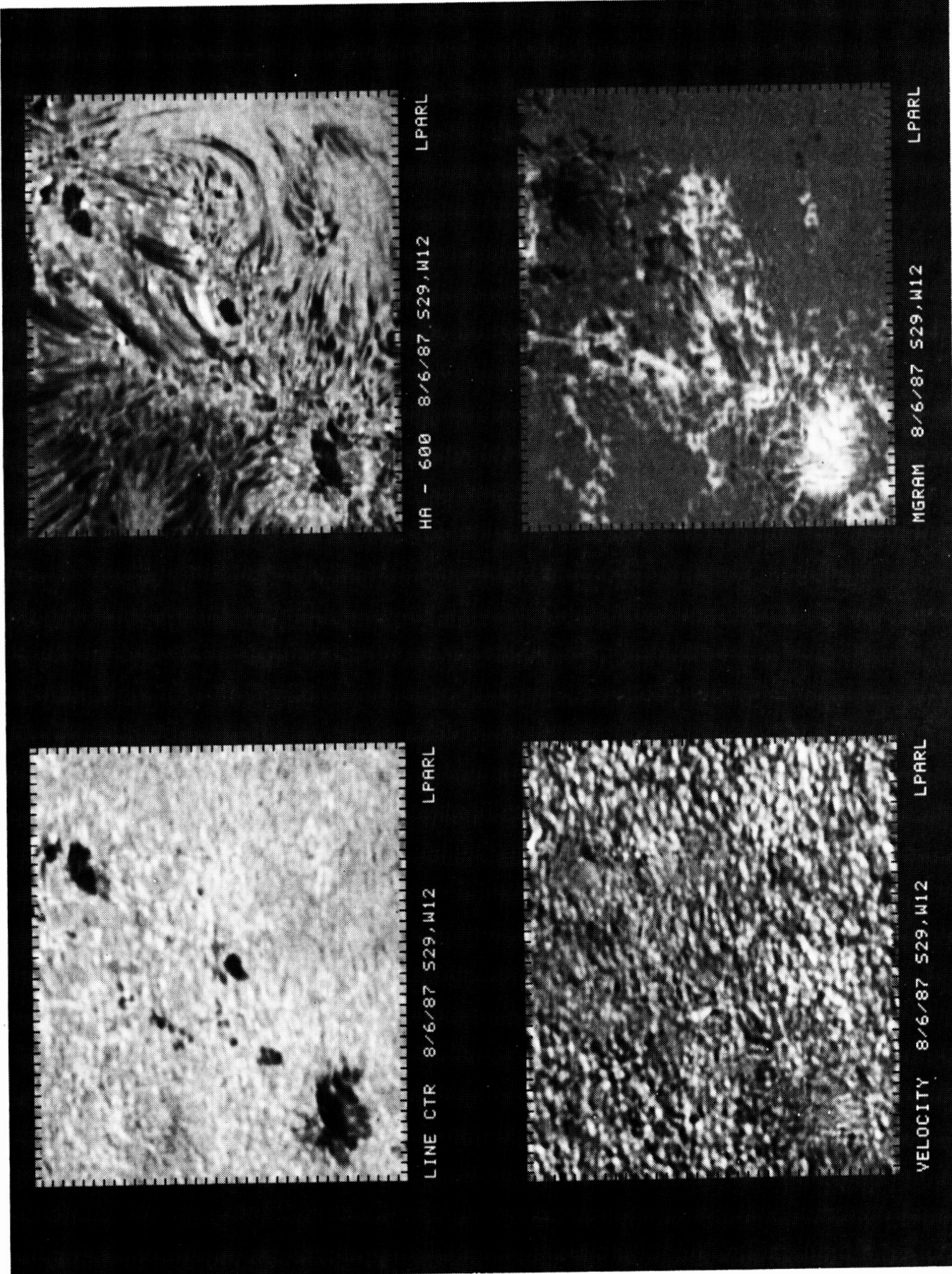


FIG. 2

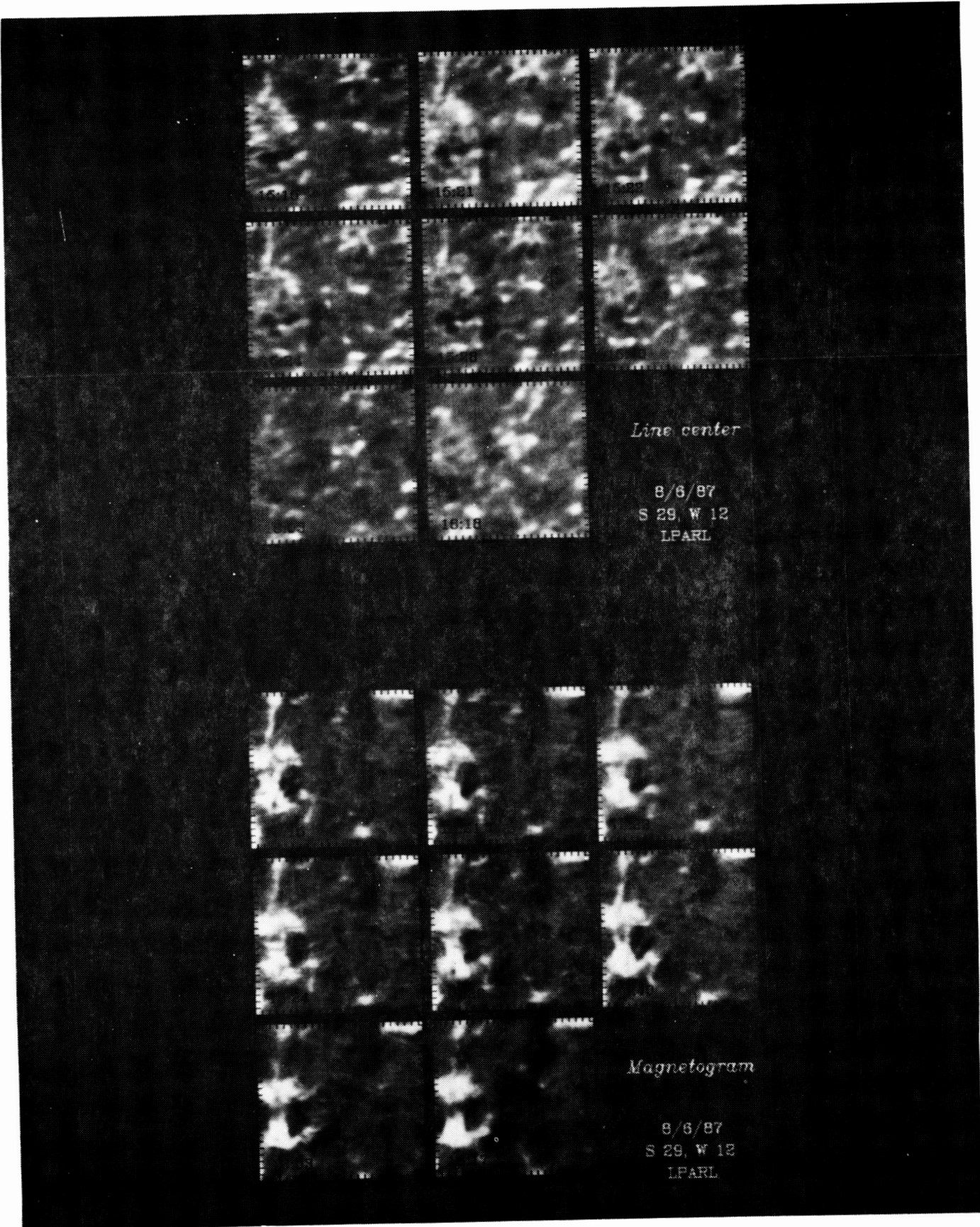
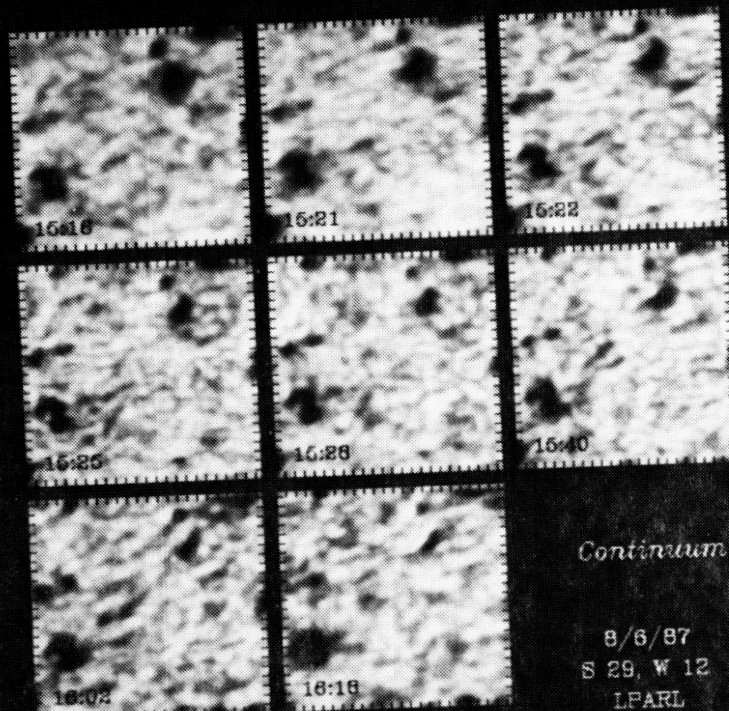
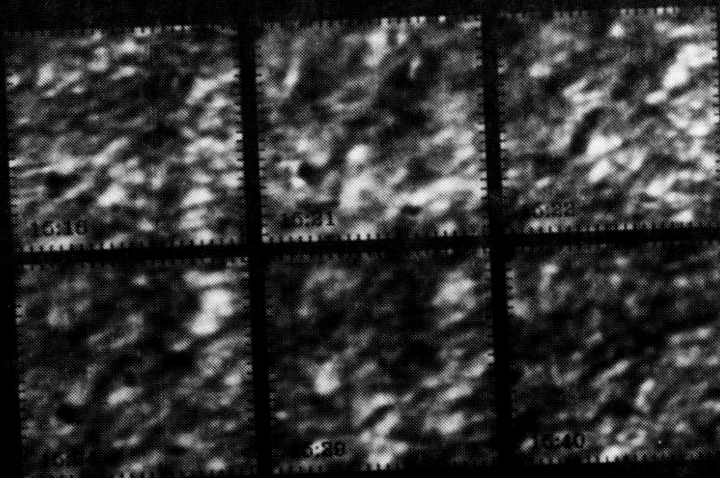


FIG.3

ORIGINAL PAGE IS
OF POOR QUALITY



8/6/87
S 29, W 12
LPA RL

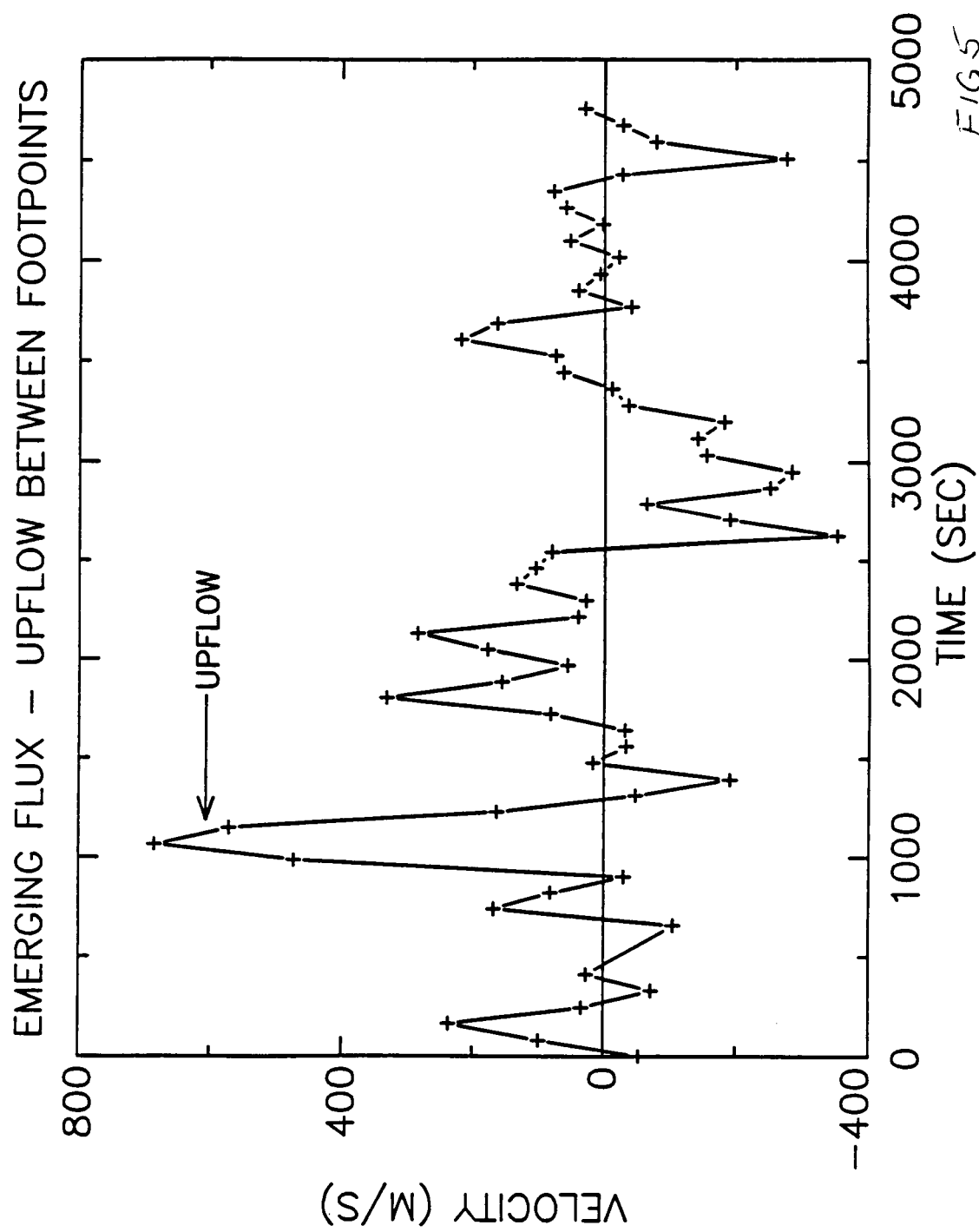


Velocity

8/6/87
S 29, W 12
LPA RL

FIG. 4

FIG. 5



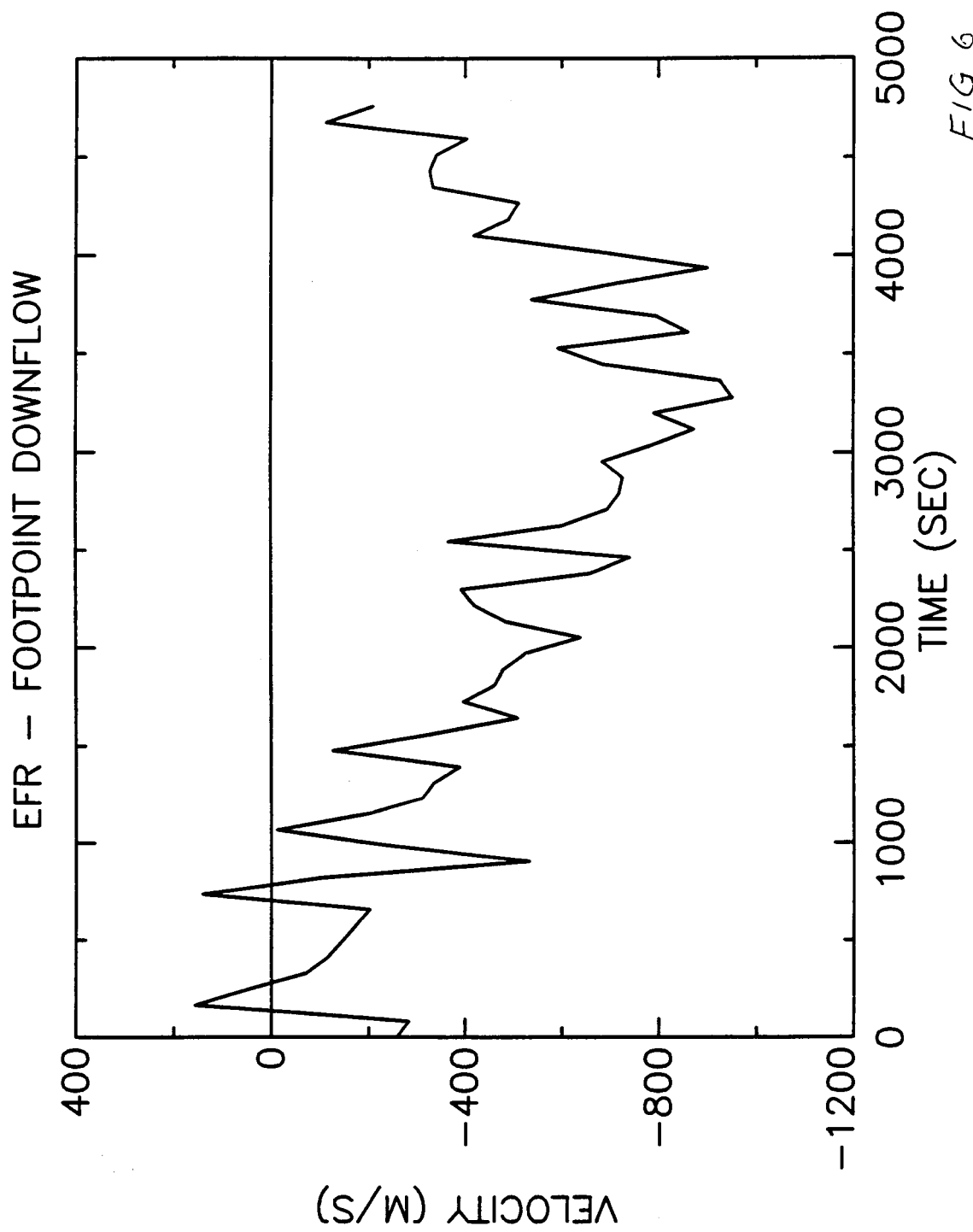
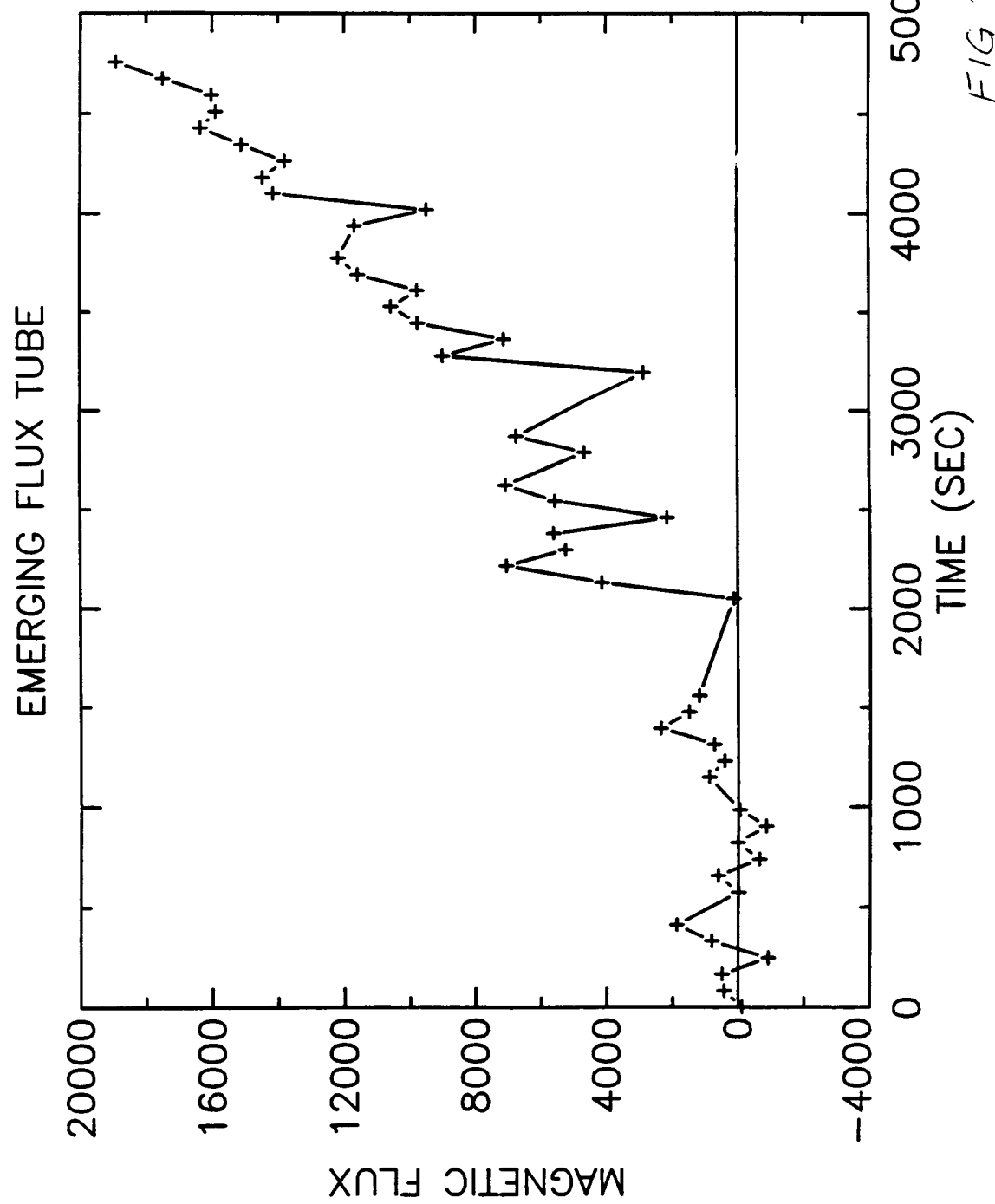
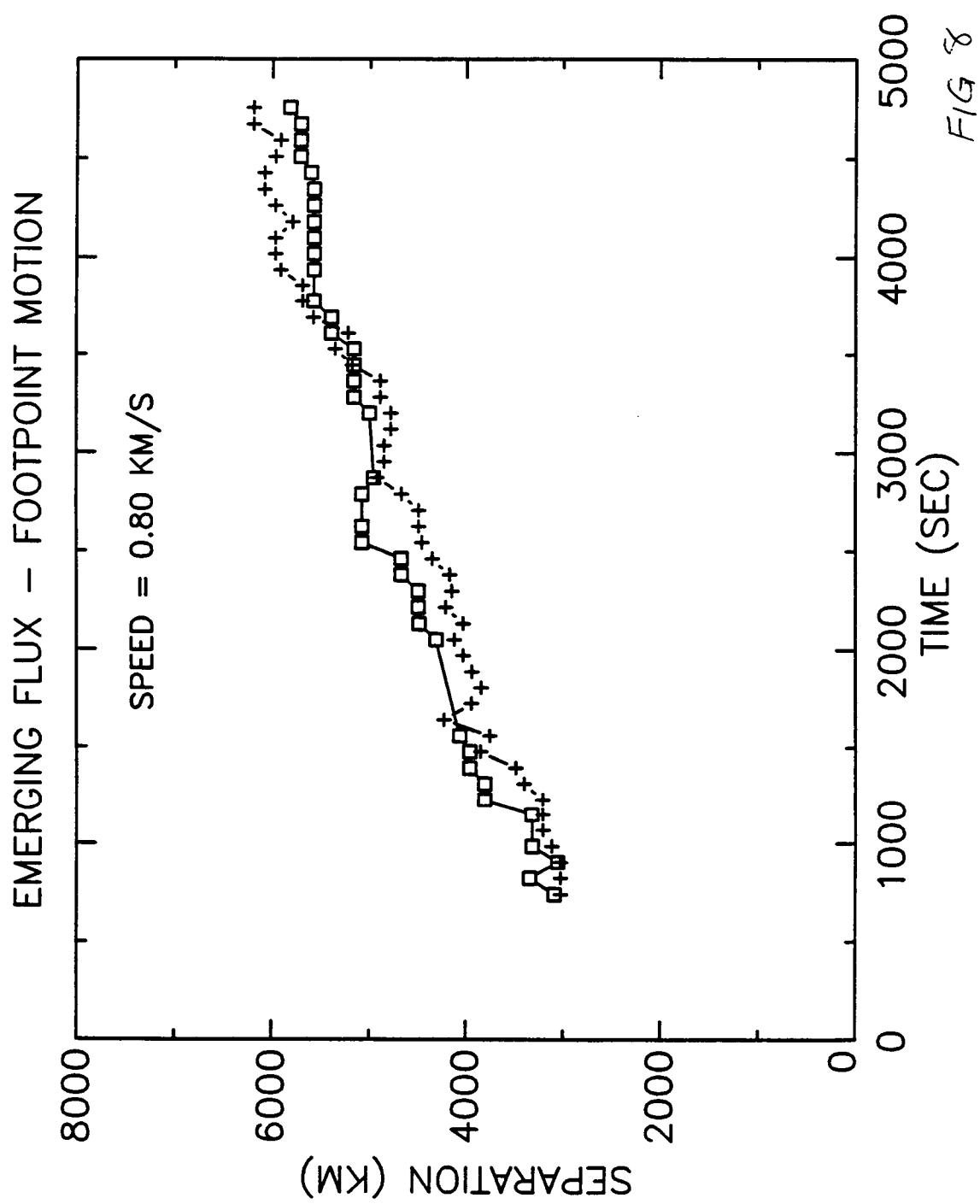


FIG 6





Statistical Properties of Solar Granulation from
the SOUP Instrument on Spacelab 2

K. Topka, A. Title, T. Tarbell, S. Ferguson, R. Shine (Lockheed PARL),

Abstract

The Solar Optical Universal Polarimeter (SOUP) on Spacelab 2 collected movies of solar granulation completely free from atmospheric blurring, and are not degraded by pointing jitter (the pointing stability was 0.003" root mean square). The movies illustrate that the solar five minute oscillation has a major role in the appearance of solar granulation and that exploding granules are a common feature of the granule evolution. Using 3-D Fourier filtering techniques we have been able to remove the oscillations and demonstrate that the autocorrelation lifetime of granulation is a factor of two greater in magnetic field regions than in field-free quiet sun. We have been able to measure horizontal velocities and observe flow patterns on the scale of meso- and supergranulation. In quiet regions the mean flow velocity is 370 m/s while in magnetic regions it is about 125 m/s. We have also found that the root mean square (rms) fluctuating horizontal velocity field is substantially greater in quiet sun than in strong magnetic field regions. By superimposing the location of exploding granules on the average flow maps we find that they appear almost exclusively in the center of mesogranulation size flow cells. Because of the non-uniformity of the distribution of exploding granules, the evolution of the granulation pattern in mesogranule cell centers and boundaries differs fundamentally. It is clear from this study there is neither a typical granule nor a typical granule evolution.

ANALYSIS and SUMMARY

The continuum intensity pattern of the solar photosphere is due to granulation (convective overshoot and turbulent flows), p- and f-mode oscillations, local internal gravity waves, and magnetic fields. From a single photograph it is impossible to separate these phenomenon. With the SOUP time sequences of images and 3-D Fourier filtering most of the effects of global oscillations, and some of the effects of waves, can be separated from the intensity pattern due to granulation. Simultaneous magnetograms have allowed us to isolate some of the effects of magnetic fields as well, and many of these results are presented here.

- On average granules are brighter in magnetic field areas than in quiet sun and the magnitude of the intensity increase is nearly independent of field strength until pores

form. Temporal intensity fluctuations are a maximum for quiet sun and decrease as magnetic flux in the local neighborhood increases. The fluctuations decrease monotonically with increasing field strength until pores form. The effects of magnetic fields on granulation extend well beyond (perhaps 2" – 4" or more) the boundaries of the individual magnetic flux tubes.

- The quasi steady component of the horizontal velocities of granules averages 370 m/s (with 4 arc second mask size) in quiet sun. The patterns in this flow are on the scale of meso- and supergranules. Magnetic fields strongly inhibit the average horizontal flow speeds of granules, to 275 m/s for weak fields, and to 100 m/s for strong fields.
- Attempts to directly measure the motion of individual granules by tracking the location of their centers during their lifetimes yields an average of about 1.0 km/sec. The shortest lived granules move some 30% - 40% faster than the longer lived ones.
- Measurements of the rms fluctuating horizontal velocities are strongly dependent on the type of solar region and the size of the aperture used for correlation tracking. In quiet sun these velocities go from about 0.45 to 1.4 km/s and in strong magnetic regions the increase is from 0.3 to 0.75 km/s as the measurement aperture decreases from 4 to 1 arc seconds. The velocities measured by the smallest apertures are on the order of velocities required for models of solar line widths. The rms velocities are lower in magnetic field areas by about 45%.
- Exploding granules tend to occur inside of mesogranules - in regions of positive divergence of the horizontal flow. Every 900 seconds, on average, all of the area within these cells has been affected at least once by the expansion fronts of an exploding granule. This also means that granules located within the network between mesogranules have a much different evolutionary history than those within the cells.

FIGURE CAPTIONS

Fig 1. SOUP Granulation Image. Quiet sun region. Contours reveal magnetic areas and are from a simultaneous Big Bear Solar Observatory magnetogram.

Fig 2. SOUP Granulation Image. Active region with pores. Superimposed are magnetic field strength contours.

Fig 3. Mean Intensity Image. Mean intensity image of the pore region is formed by averaging all 166 frames (28 minutes) of the sequence. On average the continuum appears brighter inside the magnetic areas.

Fig 4. Mean Intensity vs. Magnetic Field. The mean continuum intensity outside of magnetic areas is normalized to 100. On average the mean intensity inside magnetic areas is greater than that outside, and is nearly independent of field strength between 0 and -275 G. After this the mean intensity drops quickly because pores form.

Fig 5. RMS Map. The root-mean-square (RMS, black=small RMS, white=large RMS) of the continuum intensity during the observing period for the pore region (fig. 2). Magnetic contours are shown superimposed.

Fig 6. RMS vs. Magnetic Field. The mean RMS in intensity is plotted versus magnetic field strength for the pore region shown in figure 2. Solid - raw data, dashed - filtered to remove 5-minute oscillations. The diamonds plotted at 0 Gauss are the mean RMS intensity from the quiet sun sequence (fig. 1). The magnetic field suppresses the continuum intensity RMS until pores start to form at -275 G.

Fig 7. Horizontal Flow Speeds. Measured from local correlation tracking in both the quiet sun (fig. 1) and pore regions (fig 2).

Fig 8. Flow Speed vs. Magnetic Field. Scatter plot showing flow speed versus magnetic field strength. The solid line shows the mean flow speed. The mean speed in the quiet sun region is also plotted (dot labelled "QS" at 0 Gauss).

Fig 9. Transferse Velocity vs. Spatial Resolution. The RMS horizontal velocity is shown plotted as a function of FWHM of the gaussian used by the correlation tracker for 4 different regions of the Sun. As the magnetic field strength and spatial resolution increase, so does the RMS velocity.

Fig 10. Divergence and Exploding Granules. The divergence of the flow field in quiet sun (fig. 1, red - positive divergence or upflows blue - negative divergence or downflows) with the location of 41 exploding granules superimposed. Exploding granules tend to occur at or near areas of positive divergence.

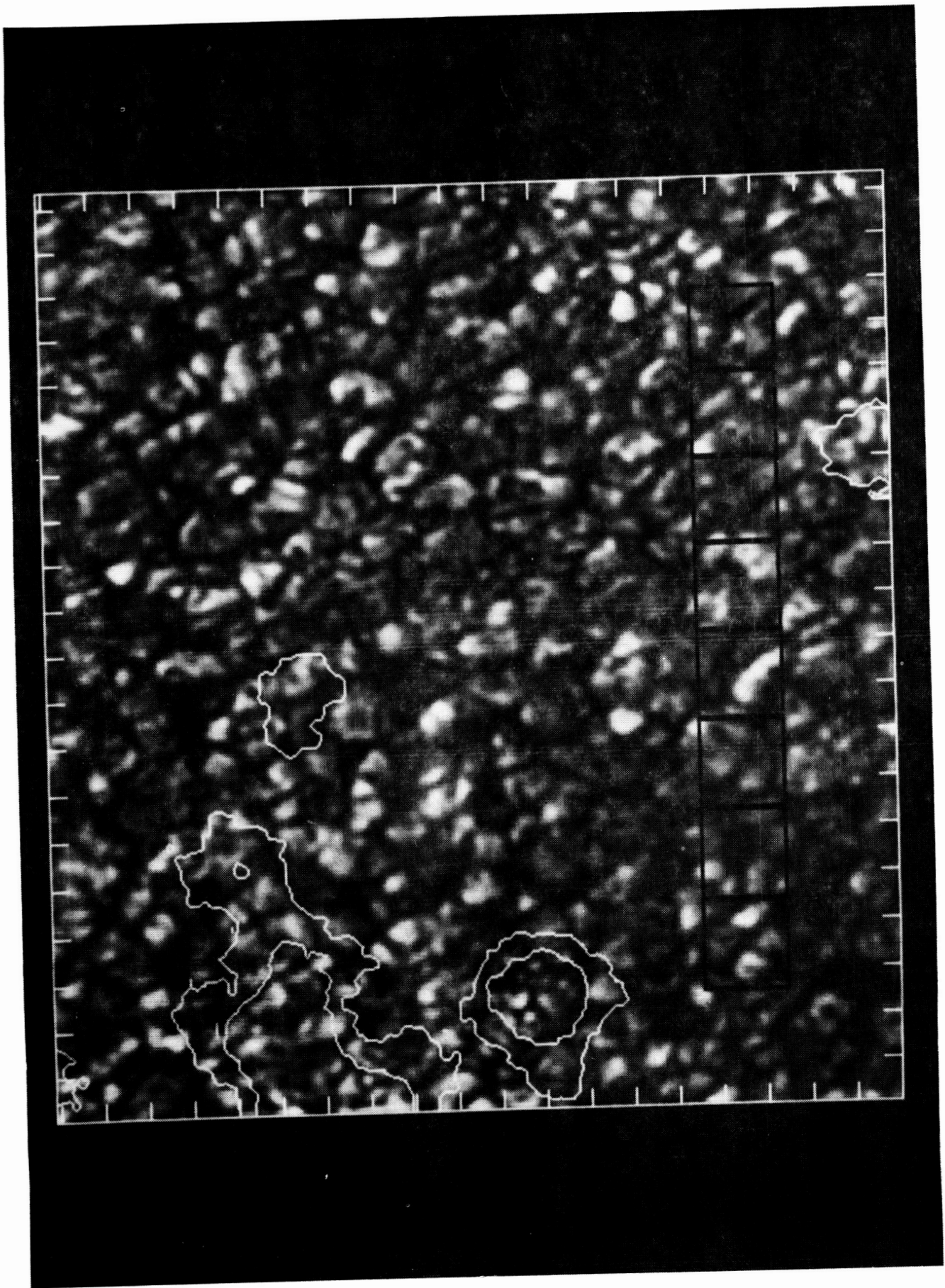


FIG. 1

ORIGINAL PAGE IS
OF POOR QUALITY

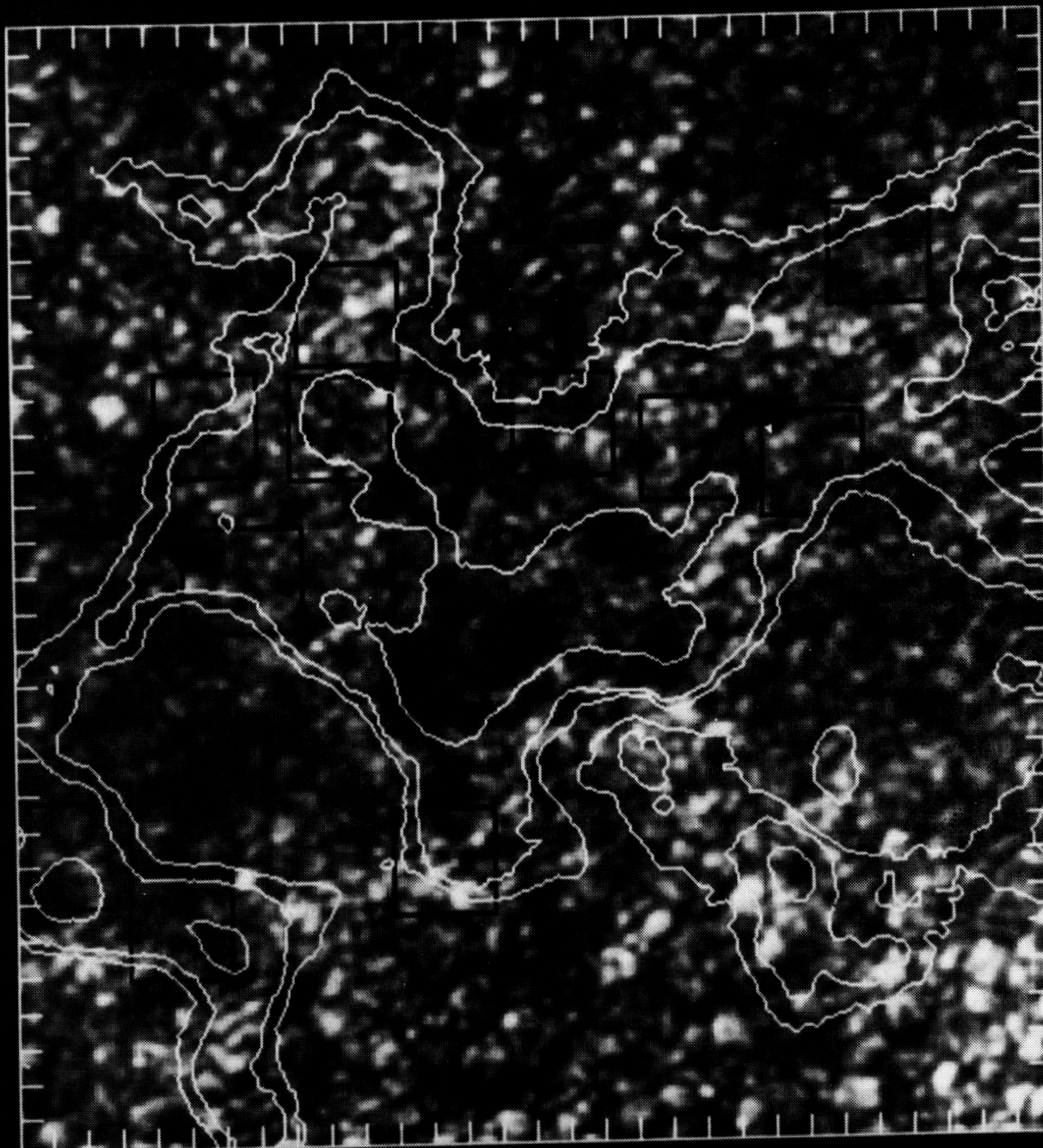


FIG. 2

ORIGINAL PAGE IS
OF POOR QUALITY

FIG. 3

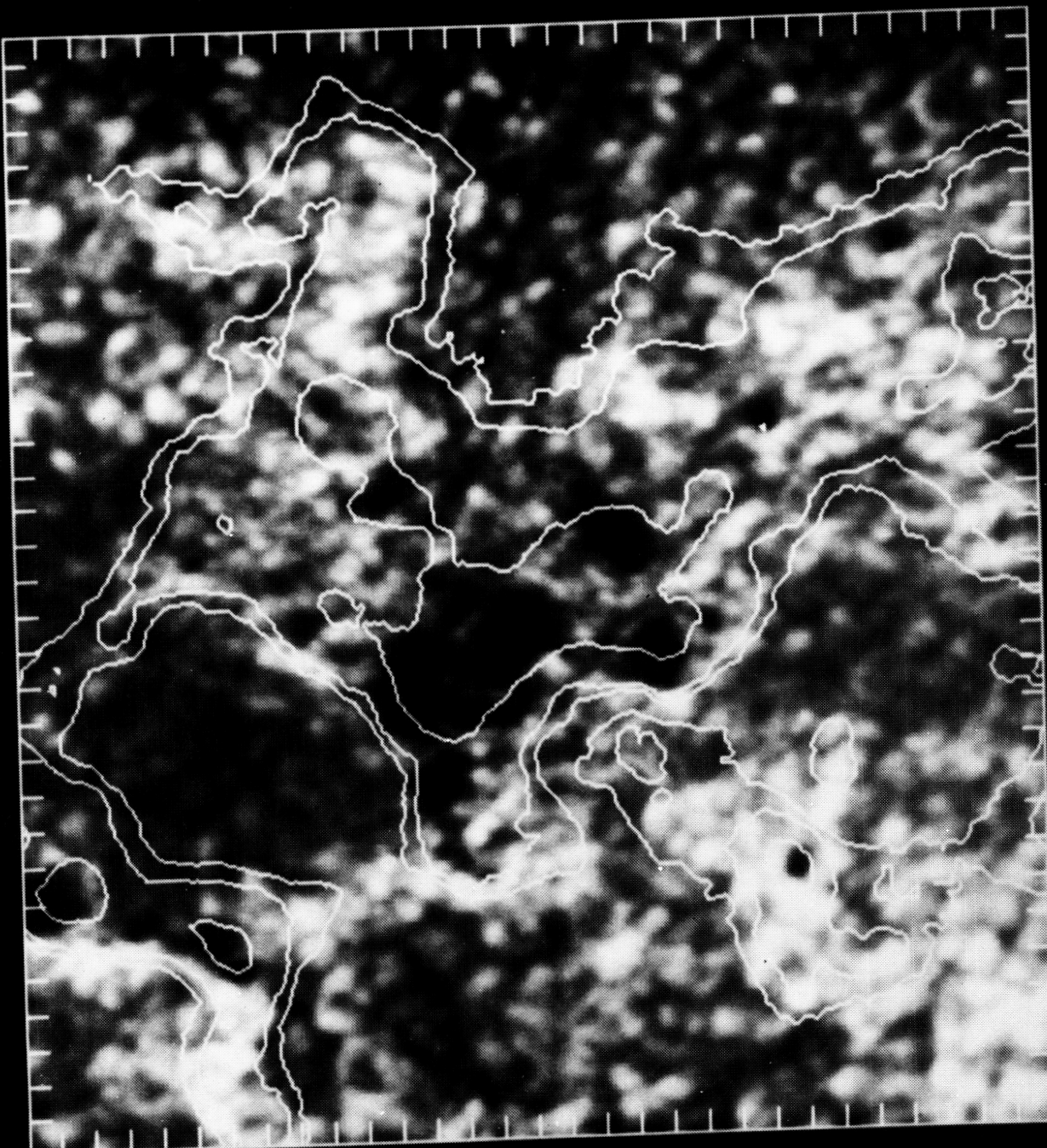
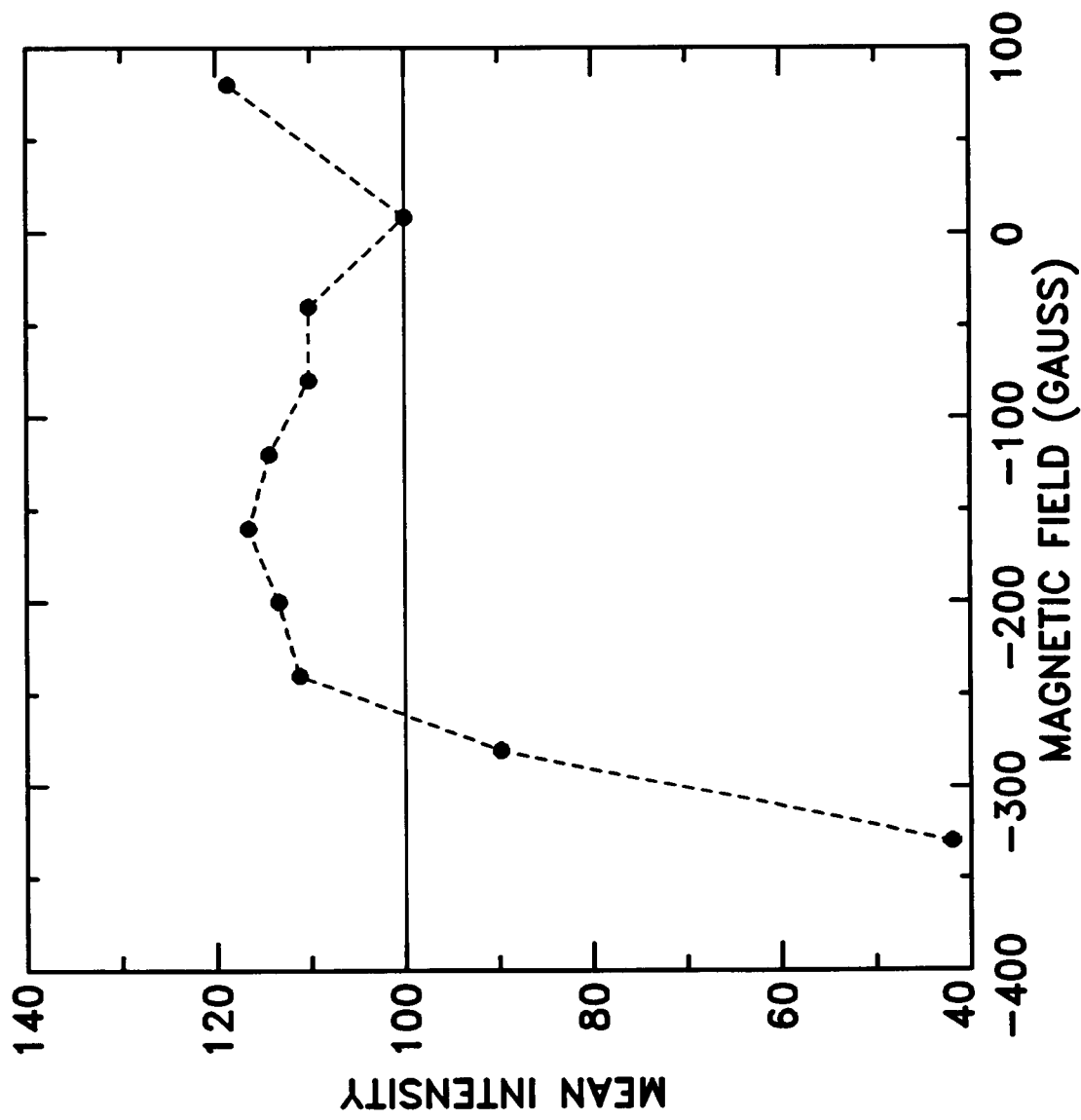


FIG 4



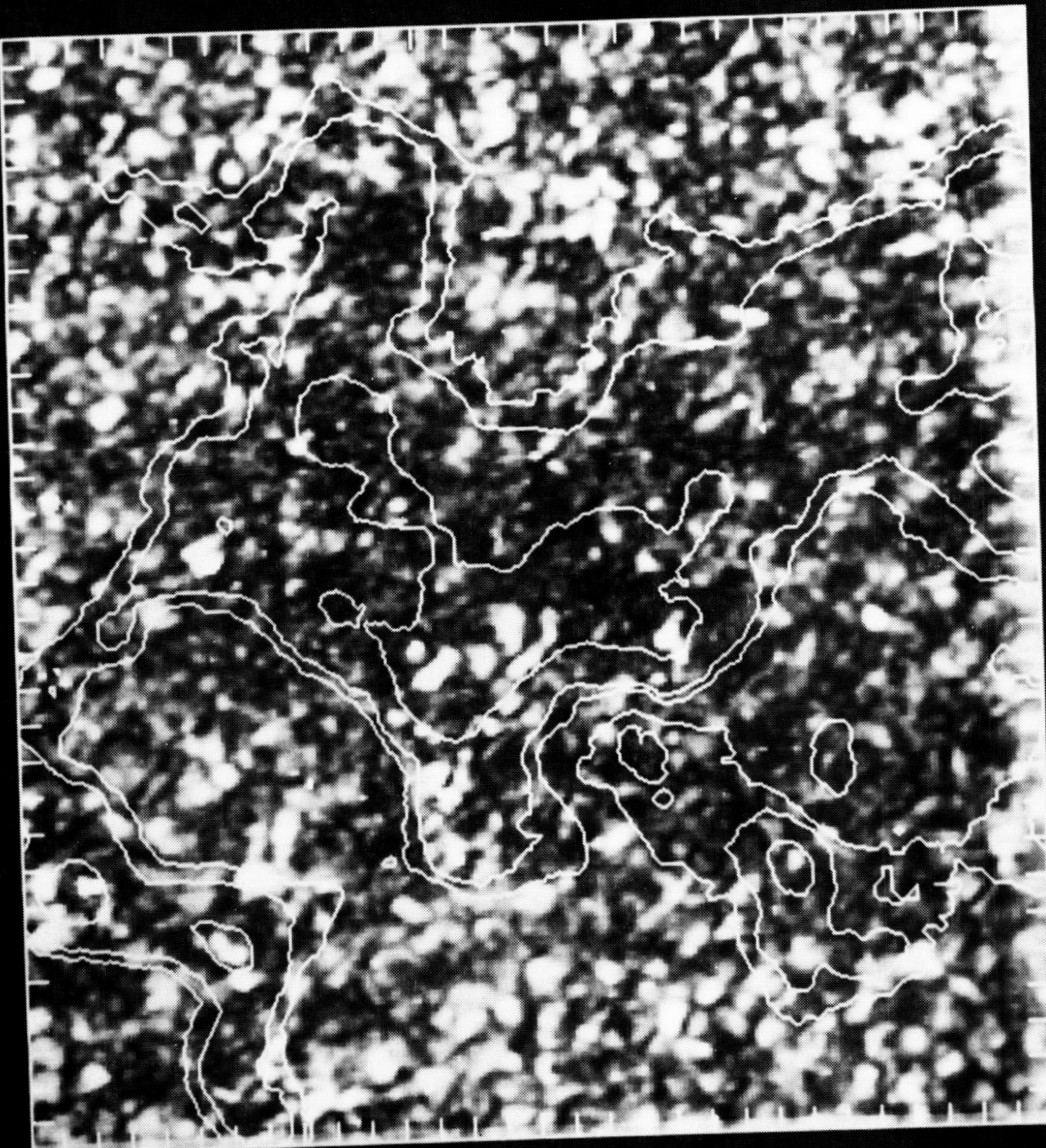
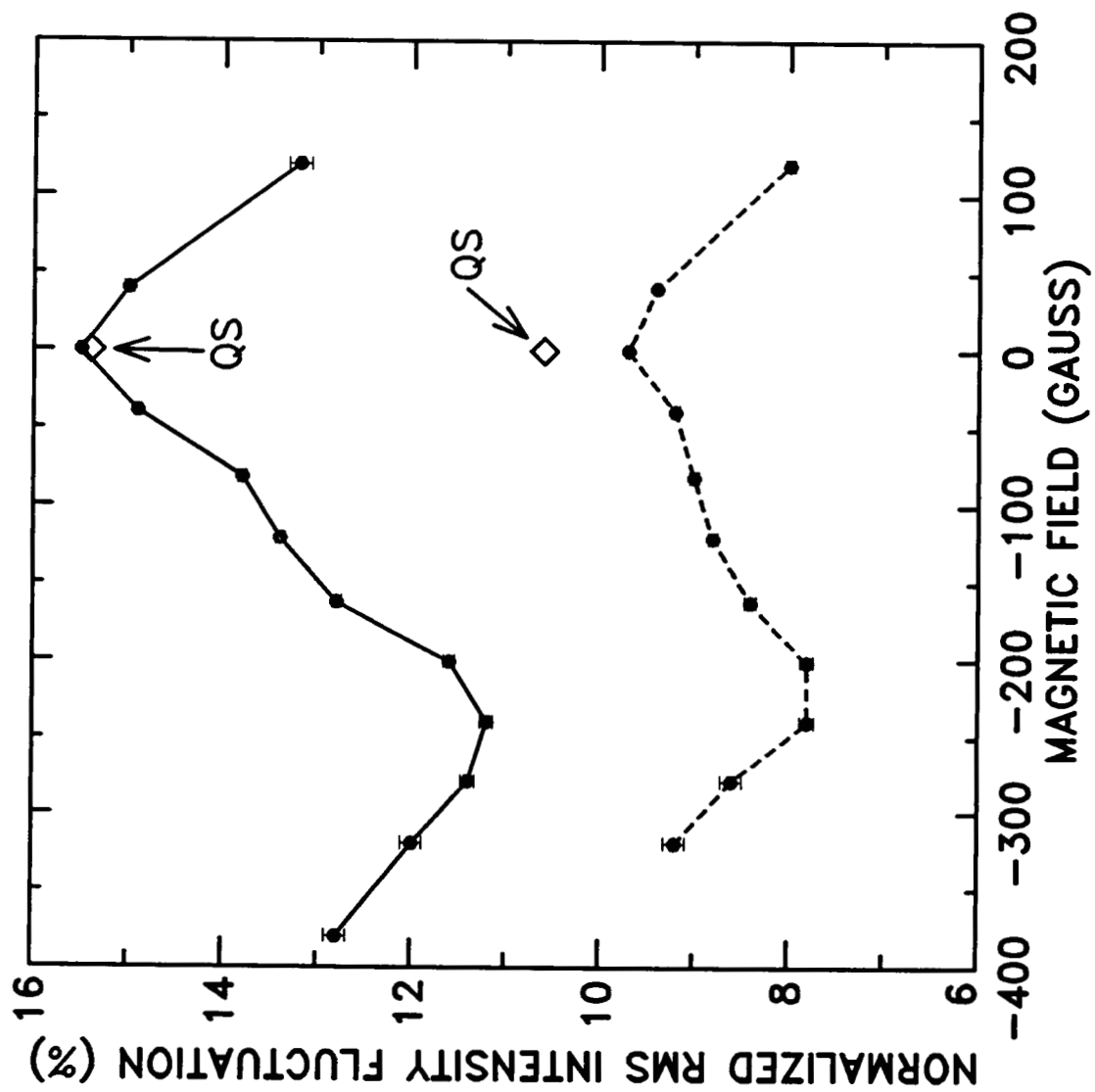


FIG 6



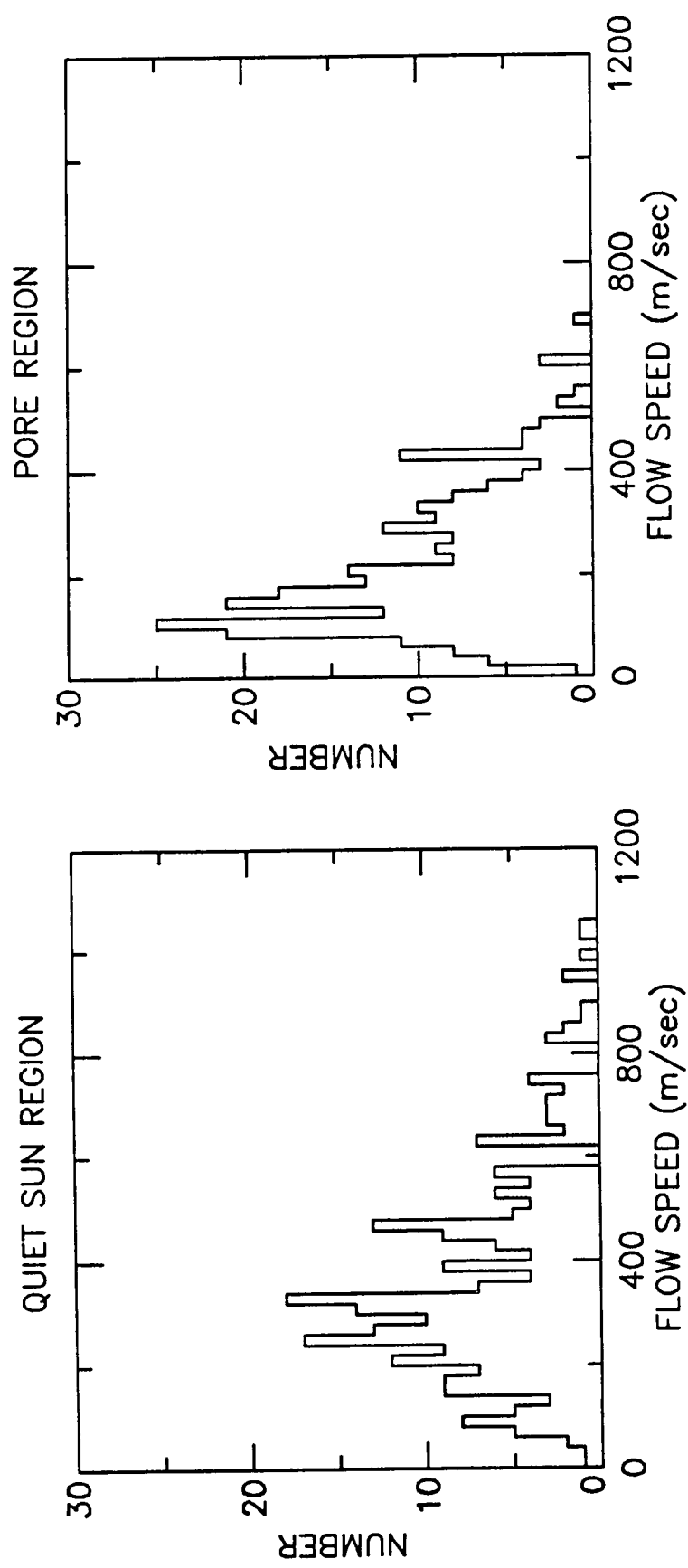
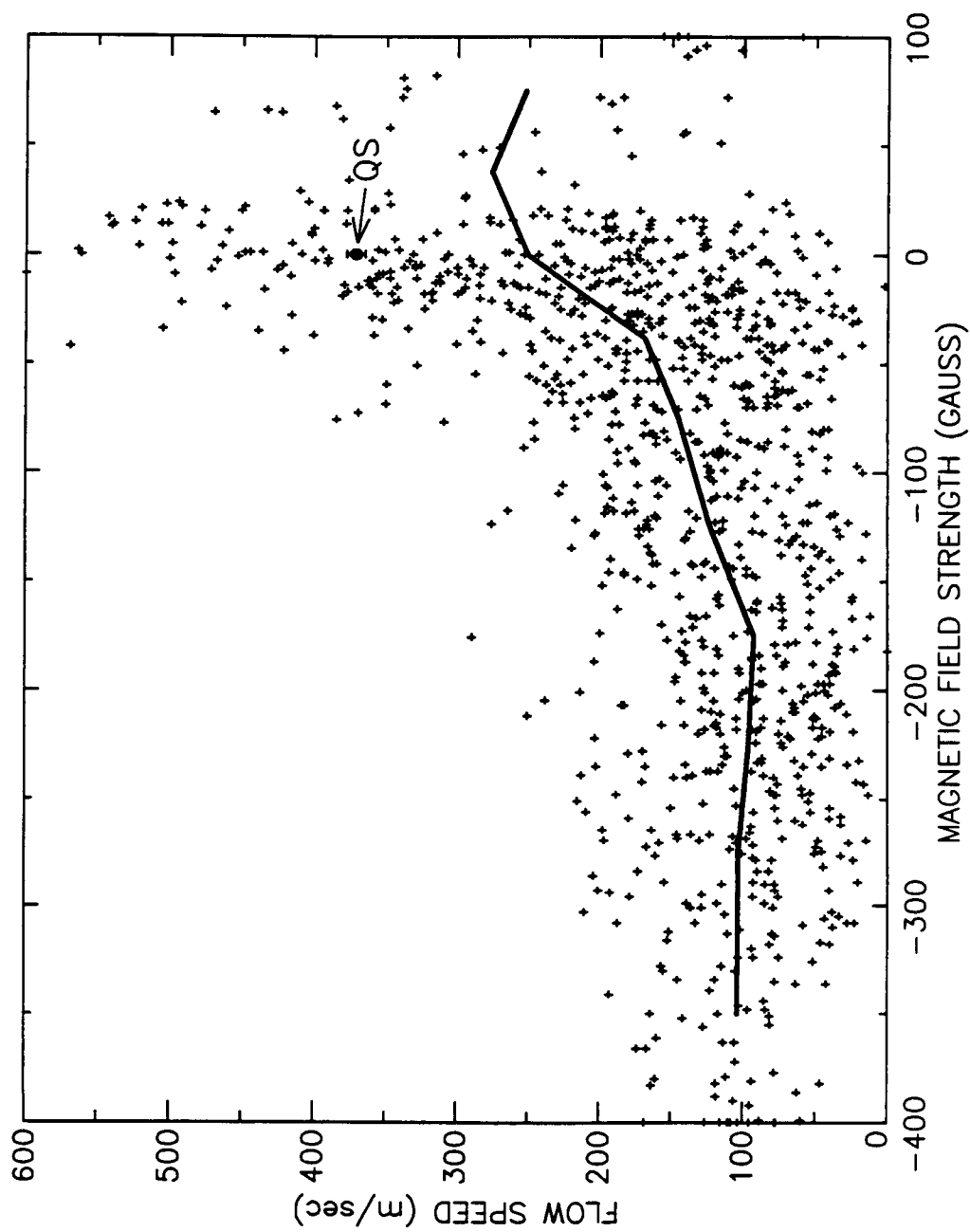


FIG. 8



TRANSVERSE VELOCITY vs. SPATIAL RESOLUTION

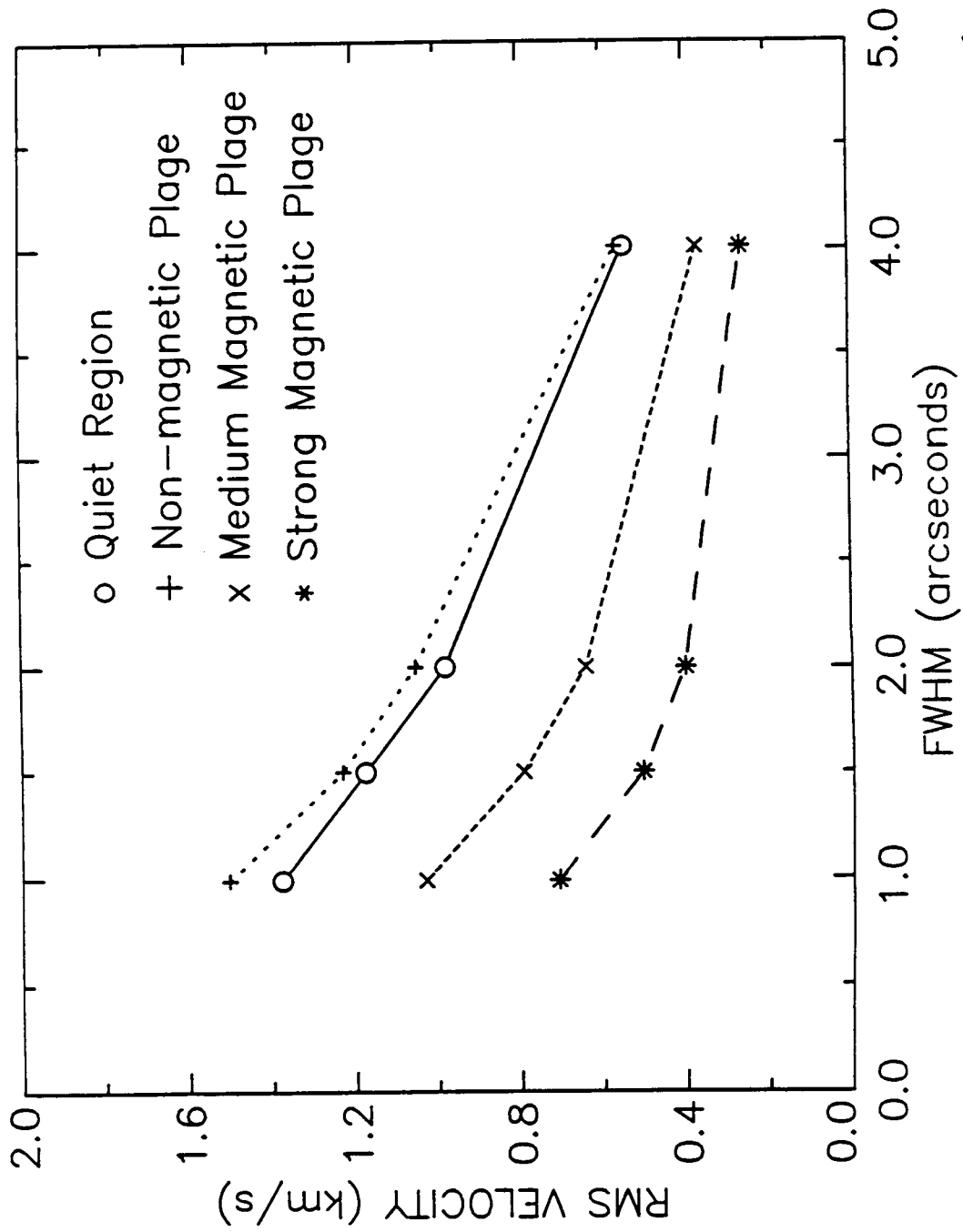


FIG 9

ORIGINAL PAGE IS
OF POOR QUALITY

FIG. 10

